Mechanics of the acoustic radiation force in tissue-like solids

A DISSERTATION
SUBMITTED TO THE FACULTY OF THE GRADUATE SCHOOL
OF THE UNIVERSITY OF MINNESOTA
BY

Egor V. Dontsov

IN PARTIAL FULFILLMENT OF THE REQUIREMENTS
FOR THE DEGREE OF
Doctor of Philosophy

Bojan B. Guzina

November, 2012

Acknowledgements

First of all, I would like to thank my adviser, Prof. Bojan Guzina for his tremendous support during the Ph.D. program. Starting from the beginning, he guided me through strenuous way of the education, helped to achieve deeper understanding of the problems, which eventually lead to the successful results.

I would like to acknowledge S. Chen, M. Urban, R. Kinnick, and M. Fatemi from the Mayo Clinic College of Medicine (Rochester, MN) for useful discussions on the testing aspects of my research and the experimental data which are used in the dissertation.

In addition, I am grateful to all my instructors from the high school, Novosibirsk State University and, finally, the University of Minnesota for providing the essential knowledge, without which this dissertation would not be written.

The effort of the committee members, namely Professors R. Ballarini, E. Detournay and F. Reitich is greatly appreciated.

The financial support during my doctoral studies was provided by the Sommerfeld Fellowship, the Shimizu Professorship and the Doctoral Dissertation Fellowship from the University of Minnesota.

Dedication

This work is dedicated to my father, Vladimir E. Dontsov, for introducing me to the beauty and significance of scientific research.

Abstract

The main objectives of this study include: i) the physics and mechanics of the acoustic radiation force (ARF) in fluids and tissue-like solids generated respectively by the plane wave and focused ultrasound fields in situations when the latter are modulated by a low-frequency signal; ii) simulation of nonlinear acoustic wave propagation when the amplitude of the focused ultrasound field is modulated by a low-frequency signal, and iii) modeling of the ARF-induced motion in soft tissues for the purpose of quantifying their nonlinear elasticity via the radiation force.

Mechanics and physics of the ARF. In the context of the ARF analyses, the key feature of the proposed study revolves around the dual-time scale treatment of the temporal variable, which allows one to parse out the contribution of ultrasound and its modulation in the nonlinear solution. In this way the ARF, giving rise to the mean motion, is exacted by computing the "fast" time average of the germane field equations. On developing a finite difference solution to the "mother" plane-wave problem, it is further shown that the featured "fast" time average can be computed as a double "ordinary" time average of the simulated nonlinear response. The proposed framework of analysis is illustrated by the analytical solution for a sinusoidal modulation envelope with quiescent past, which both exposes the limitations of earlier treatments and highlights the generation of the ARF in a lossless fluid when a modulated, high-intensity sound field is propagated through it. In the context of the focused beam configuration, a comparison with the existing theory reveals a number of key features that are brought to light by the new formulation, including the contributions to the ARF of ultrasound modulation and thermal expansion, as well as the precise role of constitutive nonlinearities in generating the sustained body force in tissue-like solids by a focused ultrasound beam.

Nonlinear acoustic solution. A key prerequisite for computing the ARF, as a spatially varying body force, is the knowledge of the nonlinear acoustic solution generated by the focused ultrasound beam. In this setting, the underpinning (nonlinear)

acoustic solution is effectively solved via a dual-time scale approach. In particular, the Westervelt-type equation, which governs the nonlinear acoustics of focused ultrasound beams, is effectively solved using hybrid time-frequency domain algorithm for any (sufficiently smooth) transient modulation envelope. To verify the proposed analytical and computational framework, the Khokhlov-Zabolotskaya-Kuznetsov (or the reduced Westervelt equation) equation is solved via finite differences in the time domain for an example pressure profile on the boundary of the ultrasound transducer. A comparison between the time-domain and hybrid calculations demonstrates that the latter is notably faster, requires significantly less memory, and has satisfactory accuracy for ratios between the modulation and carrier ultrasound frequencies below 0.1.

ARF-generated shear waves in a tissue. Regarding the third objective, namely the simulation of the ARF-induced motion in soft tissues, the linear equations of incompressible linear viscoelasticity with the ARF as the body force are solved using three-dimensional Fourier transform in the spatial domain. Thus developed viscoelastodynamic solution is used to simulate the ultrasound measurements of the ARF-induced shear wave motion in tissue-mimicking phantoms performed at the Mayo Clinic. As one key development of this dissertation, it was found that comparison between the experiment and model permits the estimation of a particular coefficient of nonlinear tissue elasticity (coupling the volumetric and deviatoric modes of deformation) from the amplitude of the ARF-generated shear waves. For completeness, the ARF estimates of this coefficient are verified via an established technique known as acoustoelasticity.

Contents

List of Tables

List of Figures

Chapter 1

Introduction

Garnering keen interest since its first observation by Faraday [1] who detected the circulation of air caused by a vibrating plate, the radiation force of sound is a phenomenon that has been intensely studied for over a century [2, 3, 4, 5, 6, 7]. In simple terms, the concept of the acoustic radiation force (ARF) describes the generation of "low"-frequency mean motion in the medium when a "high"-frequency, time-harmonic field of sufficient intensity is propagated through it. This downward leakage of energy across the frequency spectrum, brought about by an intricate interplay between the (kinematic and constitutive) nonlinearities of the problem and dissipative and/or heterogeneous nature of the propagation medium, has been known to cause both streaming in fluids [1, 8] and sustained deformation in soft, tissue-like solids [9, 10, 11].

Among the aforesaid diversity of biomedical applications of the ARF, perhaps the most widespread – and the one that motivates this study – deals with tissue (visco-)elasticity imaging where an elevated-intensity, focused ultrasound field (Mach number $= O(10^{-3})$) is used to "push" inside the tissue and thus achieve non-invasive internal palpation [12, 13, 10, 14, 15, 16]. In this class of diagnostic ultrasound techniques, the carrier signal (MHz rate) is often *modulated* by a low-frequency envelope (kHz rate) [17, 10, 12, 18, 15] both to facilitate the motion measurements and to confine their support to a neighborhood of the focal point which simplifies interpretation. In the landmark study of the effects of ultrasound modulation on the ARF [9], the germane radiation force in a tissue-like solid was approximated as a *product* between the non-modulated expression for the ARF (computed for a viscous fluid) and the squared modulation envelope. Unfortunately, such "separation" approach becomes inadequate when the modulation frequencies reach kHz range (assuming ultrasound frequencies on the order of MHz) as demonstrated in [19] and [20]. Furthermore, the ARF generated in a tissue-like solid may not be representable by that induced in a viscous fluid owing to irreconcilable differences between the respective (nonlinear) constitutive behaviors. Recognizing the latter discrepancy, the studies in [21, 22] offer a preliminary investigation of the ARF in a nonlinear soft solid assuming i) no effects of ultrasound modulation, and ii) an *ad hoc*, trial variation of the ultrasound-scale displacement field as a tool to illustrate the role of the Landau's third-order moduli [23] in the generation of the ARF.

The complete modeling of the ARF-generated shear motion, which is relevant for tissue imaging and diagnostic applications, can be split into three independent tasks: i) computation of the ultrasound-scale acoustic solution, ii) derivation of the formula for the ARF, that allows the computation of the body force distribution from a given ultrasound field, and iii) solution of the linear viscoelastic problem in a tissue-like solid with the ARF as the body force. This study covers all three aspects. However the second task, i.e. the derivation of the formula for the ARF in fluids and tissue-like solids due to modulated ultrasound, is the key contribution of this thesis and is accordingly examined in greater detail.

When dealing with the modeling of the ARF, the modulation effects enter the simulations both via i) modulation-corrected expression for the body force, and ii) computation of the intensity distribution, as shown in [19] for the case of plane waves and in [20] for the case of focused ultrasound beams. To account for situations when the pressure amplitudes in the focal region are sufficient to produce meaningful nonlinear distortion of the signal, one's ability to model the propagation of finite-amplitude waves is essential. One such approach is to solve the so-called Khokhlov-Zabolotskaya-Kuznetsov (KZK) equation, proposed in [24, 25], and used later by [26, 27, 28, 29] in a variety of applications. Alternatively, the Westervelt equation [30], which does not rely on the parabolic approximation, can be solved. A variant of the latter approach (as it voids the use of the parabolic approximation) is introduced in [31] to model short pulses in the time domain. To describe the propagation of *modulated* nonlinear ultrasound (via either the KZK or Westervelt equation), three approaches could be employed: i) quasi-static approximation, ii) time-domain solution, and iii) the dual-time approach. The quasi-static approximation assumes that the modulation frequency is very small, so that the dimensions of the sound beam are significantly smaller than the wavelength affiliated with the (dominant) modulation frequency. This is the most common approach to dealing with the effects of ultrasound modulation [9, 15]; unfortunately, this technique becomes inaccurate for higher modulation frequencies. On the other hand, the time-domain method is usually applied to simulate short pulses [28, 31] as it becomes computationally expensive for long signals (i.e. long modulation envelopes). The third technique, herein referred to as the dual-time approach, was conceptually proposed in [32]; it represents an intermediate method designed to deal specifically with modulated sound beams. In this work, it is shown that the dual-time approach bears similar computational effort as the quasi-static approximation, while being applicable to a much wider spectrum of modulation frequencies and moderately short pulses whose duration is on the order of several oscillation periods.

Having the radiation body force computed, the last step is to calculate the ARF-induced shear motion. As shown in [20], the magnitude of the ARF is proportional to one elastic nonlinearity parameter, which has not been studied extensively in the context of soft tissues and tissue-mimicking phantoms. To fill the gap, the last part of this work deals with the measurement of such third-order elastic modulus through the magnitude of the ARF-induced motion. To verify the approach, acoustoelasticity [33, 34, 7, 35], an alternative technique for measurement the elastic nonlinearity parameters, is utilized. Acoustoelasticity is a technique that allows quantification of the elastic nonlinearity coefficients of a material by measuring the variation of the sound speed in different directions (and/or polarizations) versus the applied uniaxial static stress. When dealing with nominally isotropic solids, the variation of the shear wave speed in two orthogonal directions with the applied stress permits the computation of two out of three independent nonlinearity coefficients. For consistency, the values of elastic nonlinearity obtained from the acoustoelasticity experiment are compared to those deduced from the shear wave amplitude via its relationship to the magnitude of the ARF used to generate the shear wave.

- **Chapter 2** introduces the dimensional platform and notation that are used throughout the dissertation.

- **Chapter 3** covers the most important part of this work – the derivation of the formula for the acoustic radiation force. The governing nonlinear equations (balance laws and constitutive response) that describe the tissue motion are introduced in the beginning, assuming both Eulerian and Lagrangian descriptions. The general formulation is then simplified by accounting for the specific geometry of the focused ultrasound problem, which leads to the so-called quasi-plane wave approximation. The scaling of problem quantities, affiliated with both the geometry of the problem and the dual-time nature of the modulated ultrasound beam is introduced next. The derivation of the radiation force is split into two major parts: i) plane wave analysis in Newtonian fluids, and ii) examination of the focused beam problem in nonlinear elastic material with heat conduction and viscosity (which is taken as constitutive model for soft tissues). The first part avoids massive calculations, shows the features of Eulerian and Lagrangian approaches, and allows for the verification of the proposed dual-time approach via finite-difference simulations. The second part, however, solves the problem that is relevant for the ARF-based imaging applications in medical diagnosis and highlights the role of tissue's constitutive nonlinearities on the generation of the ARF.

- **Chapter 4** is devoted to an effective calculation of the acoustic, i.e. ultrasound-scale solution for a given problem of *modulated* (focused) ultrasound. This step is a prerequisite for computing the ARF, since the latter typically depends on the acoustic intensity (see e.g. [9]). The governing equation, which accounts for the diffraction, nonlinear distortion and dissipation of acoustic waves generated by a focused ultrasound source is introduced in the beginning. The key feature of the proposed equation, which caters for efficient numerical calculations, lies in the dual-time paradigm which mimics that used for the calculations of the ARF. The numerical algorithm for solving the nonlinear wave-type equation is presented next. Finally, the accuracy and limitations of the proposed dual-time treatment are verified by comparing the results to the conventional (finite-difference) modeling in time domain.

- **Chapter 5** combines several topics, which all serve one goal – measuring the particular coefficient of tissue elasticity (featured in the newly obtained formula for the ARF) by way of the radiation force. The first part of this chapter introduces the concept of acoustoelasticity, a technique that allows for the measurement of nonlinear elasticity parameters through the dependence of shear wave speed on the level of applied (static) stress. This method is used to test for the elastic nonlinearity parameters of different tissue-mimicking phantoms (the experiments were performed at the Mayo Clinic). Then, the numerical model for the ARF-induced shear wave motion in a tissue-like solid, based on the use of triple spatial Fourier transform, is described. A comparison between the simulated and experimentally-measured displacement fields in tissue-mimicking phantoms permitted measurement of the nonlinear elasticity coefficient featured in the ARF formula. The values of this nonlinearity coefficient, calculated from the ARF measurements and obtained independently through acoustoelasticity measurements showed a good agreement, verifying the newly obtained formula for the ARF and opening an interesting possibility of measuring (and imaging) the nonlinear elastic properties of soft tissues by way of the ARF.

- **Chapter 6** concludes the dissertation with a final summary and discussion of the analyses presented in the thesis.

Published papers

[19] E. Dontsov and B. B. Guzina. Effect of low-frequency modulation on the acoustic radiation force in newtonian fluids. *SIAM J. Appl. Math.*, 71:356-378, 2011.

[20] E.V. Dontsov and B.B. Guzina. Acoustic radiation force in tissue-like solids due to modulated sound field. *J. Mech. Phys. Solids*, 60:1791-1813, 2012.

Papers in review and preparation

[32] E. Dontsov and B. B. Guzina. On the nonlinear parabolic wave equation for modulated ultrasound fields. Submitted to *Wave Motion*

[36] E. Dontsov and B. B. Guzina. Dual-time approach to the numerical simulation of modulated nonlinear ultrasound fields. In preparation.

Chapter 2

Dimensional platform and notation

For compact analysis, the problem variables and parameters are conveniently scaled by the mass density ϱ_o and absolute temperature $\mathcal{T}_\mathrm{o}$ of a material at rest; the small-amplitude *compressional* wave speed c_o, and the (carrier) ultrasound frequency Ω as indicated in Table 2.1. In this setting, all parameters and variables (other than four above that are used for the normalization) are assumed to be dimensionless, unless explicitly stated otherwise.

Several conventions are used in the dissertation: the Einstein summation convention for repeated indices; the gradient operator ∇ denotes the gradient "to the right", i.e. $(\nabla \boldsymbol{u})_\mathrm{ij} = \partial u_\mathrm{j}/\partial x_\mathrm{i}$ for vector field $\boldsymbol{u}$ and $(\nabla \cdot \boldsymbol{\sigma})_\mathrm{i} = \partial \sigma_\mathrm{ji}/\partial x_\mathrm{j}$ for tensor $\boldsymbol{\sigma}$; the double contraction product is defined as $\boldsymbol{A}:\boldsymbol{B} = \mathrm{tr}(\boldsymbol{A}\cdot\boldsymbol{B}^\mathrm{T})$ for second-order tensors $\boldsymbol{A}$ and $\boldsymbol{B}$.

Both Eulerian and Lagrangian descriptions are used in this work. To distinguish the quantities written in Lagrangian description, they are amended with the "hat" accent, i.e. $\hat{\boldsymbol{u}}$ is considered to be a function of Lagrangian coordinates, while $\boldsymbol{u}$ is the same quantity, but written in Eulerian coordinates. Also, the Lagrangian coordinates feature the "$_\mathrm{o}$" subscript, i.e $\boldsymbol{x}_\mathrm{o}$ denotes the position vector in Lagrangian coordinate system, while $\boldsymbol{x}$ is its analog in the current (Eulerian) configuration.

To shorten the notation for the approximation accuracy, "$\overset{\varepsilon^n}{=}$" is used to denote approximation with an $O(\varepsilon^n)$ residual.

Symbol	**Scale**	**Quantity**
t	$1/\Omega$	Time
$\boldsymbol{x} = (x, y, z)$	c_o/Ω	Position vector (Eulerian)
$\boldsymbol{x}_\mathrm{o} = (x_\mathrm{o}, y_\mathrm{o}, z_\mathrm{o})$	c_o/Ω	Position vector (Lagrangian)
$\boldsymbol{u} = (u_x, u_y, u_z)$	c_o/Ω	Displacement vector
$\boldsymbol{v} = (v_x, v_y, v_z)$	c_o	Particle velocity vector
ρ	ϱ_o	Mass density
p	$\varrho_\mathrm{o} c_\mathrm{o}^2$	Pressure
T	$\mathcal{T}_\mathrm{o}$	Absolute temperature
S	$c_\mathrm{o}^2/\mathcal{T}_\mathrm{o}$	Specific entropy
$\boldsymbol{\sigma}, \boldsymbol{P}$	$\varrho_\mathrm{o} c_\mathrm{o}^2$	Cauchy and first Piola-Kirchhoff stress tensors
G, K	$\varrho_\mathrm{o} c_\mathrm{o}^2$	Shear and bulk moduli
B, C, D	$\varrho_\mathrm{o} c_\mathrm{o}^2$	Third-order elastic moduli
μ, μ_B	$\varrho_\mathrm{o} c_\mathrm{o}^2/\Omega$	Shear and bulk viscosities
κ	$\varrho_\mathrm{o} c_\mathrm{o}^4/(\Omega\, \mathcal{T}_\mathrm{o})$	Thermal conductivity
α	Ω/c_o	Attenuation coefficient
α_T	$1/\mathcal{T}_\mathrm{o}$	Volumetric coefficient of thermal expansion
$\mathrm{c_p}$	$c_\mathrm{o}^2/\mathcal{T}_\mathrm{o}$	Heat capacity
$\mathcal{I}_\mathrm{max}$	$\varrho_\mathrm{o} c_\mathrm{o}^3$	Maximum wavefield intensity
ω_m	Ω	Modulation frequency

Table 2.1: Notation and scaling scheme

Chapter 3

Acoustic radiation force in viscous fluids and tissue-like solids due to modulated ultrasound

3.1 Introduction

Since the nineteenth century, it has been known that the propagation of elevated-intensity, time-harmonic sound waves in fluid may give rise to *aperiodic* motion [1, 8] due to intimate interplay between medium dissipation and nonlinearity of the problem [2]. The resulting mean i.e. "backbone" fluid motion, that is of primary interest in many applications, can be effectively computed [2, 3, 4, 5, 6] via an asymptotic treatment that a) makes an assumption on the smallness of the Mach number; b) formulates the problem in terms of the *mean* acoustic quantities, computed over the period of sound vibrations; and c) synthesizes the non-linear effects via an effective body-force term, the so-called acoustic radiation force (ARF). As the key simplifying step the latter is obtained, up to the leading order, by averaging a bi-linear form featuring the small-signal acoustic solution.

On the medical forefront, the phenomenon of the ARF has been increasingly exploited by way of elevated-intensity, focused ultrasound beams toward a broad spectrum of applications including tissue elasticity and viscoelasticity imaging, targeted drug delivery, monitoring ablation therapy, and acoustic tweezers [22, 16]. In a number of these applications, the focused ultrasound field is modulated with either transient or steady-state signal to: i) facilitate the observations of the ARF-induced tissue motion [10, 14], ii) expose the rate effects in tissue's constitutive response [11, 37], and iii) minimize the risk of tissue damage from local heating effects [9, 38]. For clarity, it is noted that the term "ARF" is in the literature used to denote two distinct phenomena affiliated with the propagation of elevated-intensity sound, namely that of a sustained i.e. mean body force in a homogeneous propagation medium [2, 3, 5, 39], and the mean force on a heterogeneity i.e. obstacle caused by the nonlinear scattering effects [40, 41, 21]. To provide a focus for the discussion, the remainder of the thesis deals exclusively with the generation of the ARF in *homogeneous media*.

In the above class of medical diagnosis applications, the MHz-rate ultrasound field used to generate the ARF is often *modulated* by frequencies on the order of kHz [17, 42, 18, 15] to both facilitate the motion measurements and help localize the motion of a tissue. At present, however, there are no fundamental theories describing the effect of sound modulation on the ARF and consequent (mean) motion. To address the problem this study begins, prompted by the available data [9], with hypothesis that the *ratio* between the (dominant) modulation frequency and ultrasound frequency is: i) small compared to unity, and ii) on the same order as the Mach number. The analysis proceeds with both plane wave and focused beam frameworks, and makes a critical split of the temporal variable into "slow" i.e. modulation time and "fast" i.e. ultrasound time. With such premise, it is shown that the resulting "fast" time averages of nonlinear acoustic fields permit elegant formulation in terms of a linear initial-boundary value problem featuring the ARF that, for the first time, rationally captures the effect of sound modulation. Recognizing the differences between the Eulerian and Lagrangian mean motion [6], the formulation is developed for both types of averages.

The proposed framework of analysis further exposes the possibility of the ARF generation, and thus the non-zero mean motion in a lossless (albeit non-linear) fluid or solid when a modulated, elevated-intensity ultrasound field is propagated through it.

The phenomenon of nontrivial mean motion in a lossless fluid generated via elevated-intensity, harmonically-modulated sound field has been demonstrated experimentally in [43], who employed a pair of acoustic beams with differing frequencies to study the so-called *difference-frequency* component of induced pressure fluctuations. Despite the maturity of the theoretical analysis developed to tackle the latter phenomenon, that builds upon the method of successive approximations [43, 30, 7, 44], to date there are no attempts to deal with the problem of difference-frequency signal generation via the concept of the ARF. The key advantage and utility of the latter approach which, for a specific *steady-state* modulation envelope, can be shown to be in agreement with earlier difference-frequency treatments [43, 7], rests in its ability to provide and in-depth yet compact analysis of mean motion for an *arbitrary* (e.g. transient) modulation envelope, built within the confines of envelope smoothness and smallness of its dominant frequency.

Regarding the plane wave analysis, where the tissue is modeled by a Newtonian fluid, included in the presentation is the analytical solution for sinusoidal modulation envelope which demonstrates that the previous "quasi-static" treatment [45, 46, 39, 9] of modulated elevated-intensity ultrasound problem may result in significant discrepancies and underestimation of the magnitude of the ARF for modulation frequencies on the order of kHz. For completeness, the new methodology is verified via the development of a custom finite-difference solution to the original (i.e. non-averaged) nonlinear problem that includes the necessary error estimates. An in-depth analysis of the latter solution reveals that the featured "fast" time averages of acoustic quantities can, to the leading order, be computed numerically via *double* (i.e. repeated) temporal averaging of the finite-difference simulations, thus paving the way for the use of "fast" time averaging in an experimental setting.

For the case of the focused ultrasound beam configuration, where the constitutive behavior of soft tissues is approximated by a nonlinear material with heat conduction and viscosity, the radiation body force is shown to have two qualitatively different parts: i) potential (which is responsible for the compressional wave) and ii) directional (which generates predominantly shear waves). Results demonstrate, that the proposed formulation, compared to the result of the existing theory [9], in addition accounts for the effects of the ultrasound modulation and thermal expansion, as well as for the constitutive nonlinearities in generating the sustained body force in a tissue-like solid by the focused ultrasound beam. The developments are illustrated via an analytical example, which provides clues into apparent discrepancies between the existing estimates of the ARF [9] and the obtained result.

3.2 Preliminaries

Two problem geometries are addressed in this Chapter – plane wave and focused ultrasound configurations. For briefness, the initial developments consider more general, focused geometry, while the plane wave is analyzed as a special reduced case. To help understand the transfer of momentum and energy from an elevated-intensity, ultrasound field – propagated through a soft tissue – to the later, this section recalls the underpinning balance laws and establishes the necessary constitutive model for soft tissues. Due to the fact that such generated motion may entail significant strains in a tissue near the focus of the beam, the problem is for generality considered from both Lagrangian and Eulerian viewpoints.

3.2.1 Balance laws

In what follows, let $\boldsymbol{x}$ and $\boldsymbol{x}_\mathrm{o}$ denote the current and reference position of a material point whereby

$$\hat{\boldsymbol{u}}(\boldsymbol{x}_\mathrm{o},t) \;=\; \boldsymbol{x}-\boldsymbol{x}_\mathrm{o} \tag{3.1}$$

is the displacement of a tissue. With such notation, all thermomechanical quantities of interest can be alternatively written in the Eulerian or Lagrangian frame of reference, the latter being indicated by the "hat" symbol. In terms of the displacement and velocity fields, one accordingly has

$$\boldsymbol{u}(\boldsymbol{x},t) \;=\; \hat{\boldsymbol{u}}(\boldsymbol{x}_\mathrm{o},t), \qquad \boldsymbol{v}(\boldsymbol{x},t) \;=\; \hat{\boldsymbol{v}}(\boldsymbol{x}_\mathrm{o},t) \;=\; \frac{\partial \hat{\boldsymbol{u}}}{\partial t}. \tag{3.2}$$

Owing to the fact that the expression for the acoustic radiation force inherently depends on the choice of the reference frame [22], the ensuing developments aim to expose the effect of ultrasound modulation on the ARF in both descriptions.

Eulerian frame of reference

On letting $\nabla(\cdot)$ denote the gradient with respect to $\boldsymbol{x}$ "to the right" [47] (see also Chapter 2), one may write the balances of mass, linear momentum, and energy as

$$\begin{aligned} \frac{\partial \rho}{\partial t} + \nabla\cdot(\rho \boldsymbol{v}) &= 0, \\ \rho\Big(\frac{\partial \boldsymbol{v}}{\partial t} + \boldsymbol{v}\cdot\nabla \boldsymbol{v}\Big) &= \nabla\cdot\boldsymbol{\sigma}, \\ \rho\Big(\frac{\partial U}{\partial t} + \boldsymbol{v}\cdot\nabla U\Big) &= -\nabla\cdot\boldsymbol{q} + \boldsymbol{\sigma}:\nabla\boldsymbol{v}, \end{aligned} \tag{3.3}$$

in Eulerian coordinates, where ρ denotes the mass density; $\boldsymbol{\sigma}$ is the Cauchy stress tensor; U denotes the specific internal energy, and $\boldsymbol{q}$ is the heat flux.

Lagrangian frame of reference

The counterparts of (3.3) in the Lagrangian frame of reference [47] can be written as

$$\begin{aligned} \hat{\rho} &= \frac{1}{\det(\hat{\boldsymbol{F}})}, & \hat{\boldsymbol{F}} &= \boldsymbol{I} + \nabla^{\mathrm{T}}\hat{\boldsymbol{u}}, \\ \frac{\partial^2 \hat{\boldsymbol{u}}}{\partial t^2} &= \nabla\cdot\hat{\boldsymbol{P}}, & \hat{\boldsymbol{P}} &= \det(\hat{\boldsymbol{F}})\,\hat{\boldsymbol{F}}^{-1}\cdot\hat{\boldsymbol{\sigma}} \\ \frac{\partial \hat{U}}{\partial t} &= -\nabla\cdot\big(\det(\hat{\boldsymbol{F}})\,\hat{\boldsymbol{F}}^{-1}\cdot\hat{\boldsymbol{q}}\big) + \hat{\boldsymbol{P}}:\frac{\partial \hat{\boldsymbol{F}}^{\mathrm{T}}}{\partial t}, \end{aligned} \tag{3.4}$$

where $\nabla(\hat{\cdot})$ indicates differentiation with respect to $\boldsymbol{x}_{\mathrm{o}}$, $\hat{\boldsymbol{F}}$ is the deformation gradient, $\boldsymbol{I}$ is the second-order identity tensor, and $\hat{\boldsymbol{P}}$ denotes the first Piola-Kirchhoff stress tensor.

To close either system (3.3) or (3.4), one must provide the constitutive equations for $\boldsymbol{\sigma}$, U and $\boldsymbol{q}$ which are established next.

3.2.2 Thermo-viscoelastic constitutive framework for soft tissues

To study the transfer of momentum and energy from a modulated (elevated-intensity) ultrasound field to a soft tissue, it is convenient to approximate the latter as an *elastic* *material with heat conduction and viscosity* [48] whose constitutive behavior is determined in terms of five response functions: $U, T, \boldsymbol{\Sigma}, \boldsymbol{J}$ and $\boldsymbol{q}$, namely

$$\begin{aligned} U &= U(\boldsymbol{F}, S), \\ T &= T(\boldsymbol{F}, S), \\ \boldsymbol{\sigma} &= \boldsymbol{\Sigma}(\boldsymbol{F}, S) \,+\, \boldsymbol{J}(\boldsymbol{F}, S) \!:\! \nabla\boldsymbol{v}, \\ \boldsymbol{q} &= \boldsymbol{q}(\boldsymbol{F}, S, \nabla T), \end{aligned} \tag{3.5}$$

where S denotes the specific entropy, and T is the absolute temperature. Here it is noted that (3.5c) can be loosely affiliated with the Kelvin-Voigt mechanical analog due to the fact that $\boldsymbol{\Sigma}(\boldsymbol{F}, S)$ is the (nonlinear) thermoelastic part of the Cauchy stress tensor, while $\boldsymbol{J} : \nabla\boldsymbol{v}$ represents its viscous component, assumed to be linear in $\nabla\boldsymbol{v}$ for an assumption to the contrary would necessitate the inclusion of acceleration gradients in the argument list for $\boldsymbol{\sigma}$ [48]. To satisfy the Clausius-Duhem inequality, (3.5) must be such that

$$T = \left(\frac{\partial U}{\partial S}\right)_{\boldsymbol{F}}, \qquad \boldsymbol{\Sigma} = \rho \left(\frac{\partial U}{\partial \boldsymbol{F}}\right)_{S} \cdot \boldsymbol{F}^{\mathrm{T}}, \qquad \nabla\boldsymbol{v} : \boldsymbol{J} : \nabla\boldsymbol{v} \geqslant 0, \qquad \nabla T \cdot \boldsymbol{q} \leqslant 0, \tag{3.6}$$

assuming that the temperature relation is invertible [48].

Comment on the constitutive format. With regard to the particular structure of the postulated viscoelastic relationship (3.5c), it is worth noting that the nature of the rate-dependent constitutive behavior of soft tissues over a broad frequency spectrum (kHz to MHz range) is to date an open question. In the MHz frequency range, (linear) ultrasound studies indicate that the tissues' constitutive behavior in shear is consistent with that of the Kelvin-Voigt model, while their bulk response is more closely described by the Zener (i.e. standard linear solid) model [49, 50]. In the lower (quasi-static to kHz) frequency range, on the other hand, rate-dependent models for the constitutive response of soft tissues in shear vary widely [15, 51, 52, 53, 54, 55, 56], while the viscoelastic description of their bulk behavior is virtually nonexistent. In this setting, a generalization of (3.5c) that may be better suited for finely matching any particular set of constitutive observations at *both* (ultrasound and modulation) time scales can be formulated within the framework of materials with memory [57], wherein U, $\boldsymbol{\sigma}$ and $\boldsymbol{q}$ are assumed to depend on the time histories of $\boldsymbol{F}$, S and ∇T. An account for such behavior, however, would result in a integro-differential formulation that is not amenable to a compact analytical treatment. As a result the assumed viscoelastic framework, that is consistent with earlier ARF studies [39, 9], is deemed adequate for its tractability and the lack of comprehensive (broadband) experimental data on the rate-dependent behavior of soft tissues.

Isotropic solid. Owing to the fact that the isotropic solids contain $-\boldsymbol{I}$ in their symmetry group [58], it can be shown [48] that (3.5d) is subject to an additional constraint of antisymmetry with respect to ∇T, namely

$$\boldsymbol{q}(\boldsymbol{F},S,\nabla T) \;=\; \boldsymbol{q}(\boldsymbol{F},S,-\nabla T). \tag{3.7}$$

Under the premise of material isotropy, one may further reduce (3.5a) as

$$U \;=\; \bar{U}\big(I_1(\boldsymbol{E}),I_2(\boldsymbol{E}),I_3(\boldsymbol{E}),S\big), \tag{3.8}$$

where

$$I_1(\boldsymbol{E})=\mathrm{tr}(\boldsymbol{E}), \qquad I_2(\boldsymbol{E})=\tfrac{1}{2}\big[(\mathrm{tr}(\boldsymbol{E}))^2-\mathrm{tr}(\boldsymbol{E}^2)\big], \qquad I_3(\boldsymbol{E})=\det(\boldsymbol{E}), \tag{3.9}$$

denote respectively the first, the second, and the third invariant of the Green-Lagrangian strain tensor

$$\boldsymbol{E}=\tfrac{1}{2}(\boldsymbol{F}^{\mathrm{T}}\!\cdot\boldsymbol{F}-\boldsymbol{I}).$$

On substituting (3.8) in (3.6), one finds

$$T=\frac{\partial\bar{U}}{\partial S}, \quad \boldsymbol{\Sigma}=\rho\boldsymbol{F}\cdot\left[\frac{\partial\bar{U}}{\partial I_1}\boldsymbol{I}+\frac{\partial\bar{U}}{\partial I_2}\Big(I_1(\boldsymbol{E})\boldsymbol{I}-\boldsymbol{E}\Big)+\frac{\partial\bar{U}}{\partial I_3}\Big(I_2(\boldsymbol{E})\boldsymbol{I}-I_1(\boldsymbol{E})\boldsymbol{E}+\boldsymbol{E}^2\Big)\right]\cdot\boldsymbol{F}^{\mathrm{T}}, \tag{3.10}$$

where the dependence on entropy is embedded in the derivatives of $\bar{U}$. To facilitate the specification of $\bar{U}$, it can be shown on the basis of (3.10) and basic thermodynamic considerations as in Appendix A.1 that the mixed derivative of specific internal energy at the initial (equilibrium) state "o" permits representation

$$\left(\frac{\partial^2\bar{U}}{\partial S\partial\boldsymbol{E}}\right)_{\!\mathrm{o}} = \left(\frac{\partial T}{\partial\boldsymbol{E}}\right)_{\!S,\mathrm{o}} = \left(\frac{\partial[\rho^{-1}\boldsymbol{F}^{-1}\!\cdot\boldsymbol{\Sigma}\cdot\boldsymbol{F}^{-\mathrm{T}}]}{\partial S}\right)_{\!\boldsymbol{E},\mathrm{o}} = -\frac{\beta_{\mathrm{T}}}{\mathrm{c_p}}\boldsymbol{I}, \qquad \beta_{\mathrm{T}}=\alpha_{\mathrm{T}}K, \tag{3.11}$$

where α_{T} is the coefficient of volumetric thermal expansion, K denotes the linear elastic bulk modulus, and $\mathrm{c_p}$ is the specific heat capacity at constant stress. From (3.11), one finds that the linearization of the second of (3.10) results in a linear thermoelastic relationship

$$\boldsymbol{\Sigma} - \boldsymbol{\sigma}_{\rm o} \;=\; (K - \tfrac{2}{3}G)(\nabla\cdot\boldsymbol{u})\boldsymbol{I} \,+\, G(\nabla\boldsymbol{u} + \nabla^{\rm T}\boldsymbol{u}) \,-\, \frac{\beta_{\rm T}}{{\rm c_p}}(S - S_{\rm o})\,\boldsymbol{I}, \tag{3.12}$$

where $K = 1 - \frac{4}{3}G$ and G denote respectively the tissue's bulk and shear modulus (see the scaling scheme in Table 2.1), while $S_{\rm o}$ and $\boldsymbol{\sigma}_{\rm o}$ are respectively the specific entropy and Cauchy stress tensor evaluated at the initial state. To preserve the isotropy of the material in a prestressed reference configuration, it is hereon assumed that $\boldsymbol{\sigma}_{\rm o} = -p_{\rm o}\boldsymbol{I}$, i.e. that the initial state of stress is hydrostatic. For completeness, it is noted from (3.12) that K signifies the bulk modulus at constant entropy, as opposed to the bulk modulus at constant temperature ($K_{\rm T}$) as is usually assumed in linear thermoelasticity [47]. The difference between the two definitions is, however, typically small since $K/K_{\rm T} = {\rm c_p}/{\rm c_v} \approx 1$ where ${\rm c_v}$ is the specific heat capacity at constant strain.

3.3 Governing equations for small Mach number

With reference to the scaling scheme in Table 2.1, one may introduce the Mach number associated with the ultrasound wave in a soft tissue as

$$\varepsilon \;=\; v_{\rm max} \;\approx\; \sqrt{2}\,\mathcal{I}_{\rm max}^{1/2}, \tag{3.13}$$

where $v_{\rm max}$ is the maximum (dimensionless) particle velocity, and $\mathcal{I}_{\rm max}$ is the associated wavefield intensity.

3.3.1 Smallness of problem parameters

In ultrasound imaging applications involving the acoustic radiation force, the Mach number is typically on the order of 10^{-3} [9] which supports the hypothesis $\varepsilon \ll 1$ commonly made in the ARF analyses [45, 46, 39, 9]. In the context of nonlinear solid mechanics, one finds that $\boldsymbol{E} = O(\varepsilon)$ (see Section 3.3.4) which implies that the maximum strain generated by the ultrasound wave is on the order of 0.1%. While this level of strain normally does not warrant the deployment of finite-deformation kinematics in the context of static and quasi-static processes, numerous experimental studies have demonstrated that $\varepsilon = O(10^{-3})$ is sufficient to produce observable nonlinear effects in ultrasound wave propagation [9].

For an effective asymptotic analysis of (3.4)–(3.10) when $\varepsilon \ll 1$, one may note (assuming the carrier ultrasound frequencies of at least 1 MHz) that the dimensionless attenuation coefficient α in soft tissues can be estimated as $(0.5 \div 5) \times 10^{-3}$ [59, 50], and therefore assumed to behave as $O(\varepsilon)$. To cater for medical imaging applications where the ultrasound modulation frequency is regularly on the order of kHz [17], the proposed analysis further assumes $\omega_{\rm m} = O(\varepsilon)$ for this key parameter, considered to be $o(\varepsilon)$ in previous treatments [5]. With such hypotheses, one may rescale the attenuation coefficient and modulation frequency as

$$\tilde{\alpha} := \frac{\alpha}{\varepsilon} = O(1), \qquad \tilde{\omega}_{\rm m} := \frac{\omega_{\rm m}}{\varepsilon} = O(1), \qquad \varepsilon \ll 1. \tag{3.14}$$

Recalling (3.5), it is noted that the assumption about the smallness of α further implies that the combined dissipation effect due to viscosity and heat conduction must be $O(\varepsilon)$. Accordingly, one may tentatively set

$$\tilde{\boldsymbol{J}}(\boldsymbol{F}, S) := \frac{\boldsymbol{J}(\boldsymbol{F}, S)}{\varepsilon} = O(1), \tag{3.15}$$

a hypothesis that will be substantiated later once the constitutive model for soft tissues, synthesized via $\boldsymbol{\Sigma}$ and $\boldsymbol{J}$, is specified.

In the context of (3.12), estimates of the linear-elastic shear modulus in soft tissues vary widely and have been reported in the range $10^3 \div 10^6$ Pa [9, 54, 55]. Given the fact that the compressional-wave modulus of soft tissues, $\varrho_{\rm o} c_{\rm o}^2$, is close to the bulk modulus of water (2.2×10^9 Pa), it follows on the basis of the assumed scaling scheme, Table 2.1, that G does not exceed $O(\varepsilon)$. As a result, one may safely accompany (3.14) and (3.15) by introducing the rescaled shear modulus

$$\tilde{G} := \frac{G}{\varepsilon} \leqslant O(1). \tag{3.16}$$

In this setting, situations where $\tilde{G} \ll 1$ can be treated by simply neglecting the terms containing $\tilde{G}$.

For an in-depth analysis of the thermomechanical problem at hand, it is further noted with reference to Table 2.1 that the coefficient of thermal conductivity, featured in the Fourier law (i.e. the leading-order approximation of (3.5d)), is normally $\kappa \approx$

$3\times10^{-7}=O(\varepsilon^2)$ in soft tissues [60]. In the context of (3.3c), (3.5), (3.6) and (3.15), this implies that the dissipation due to heat conduction is small relative to that induced by material viscosity. This is in contrast to the customary hypothesis underpinning the analysis of nonlinear wave propagation in fluids [7], that is the basis for the existing theories of the ARF [5, 39], stating that the two dissipation mechanisms are of the of the same order. To effectively build upon the ARF solution for non-modulated ultrasound beams [5, 39], it is hereon assumed that

$$\tilde{\kappa} \;:=\; \frac{\kappa}{\varepsilon} \;\leqslant O(1), \tag{3.17}$$

which allows one to *formally retain* the terms affiliated with heat conduction (and thus induced energy dissipation) in the asymptotic analysis of the thermomechanical system. In Section 3.6, this hypothesis will be critical for the correct expansion of the *averaged* balance equations which demonstrate that, when $\kappa=O(\varepsilon^2)$, the order of the averaged entropy is $1/\varepsilon$ times larger than that of its ultrasound fluctuation counterpart – a fact which requires the retention of seemingly negligible terms (associated with entropy) in the non-averaged system of equations (3.3). Of course, once the final expression for the ARF is obtained, (3.17) does not preclude substituting a realistic value for κ. With (3.14)–(3.17) in place, the assumptions on the order of problem parameters can be completed by postulating the initial hydrostatic stress, $\boldsymbol{\sigma}_{\rm o}=-p_{\rm o}\boldsymbol{I}$ in (3.12) to be commensurate with the atmospheric pressure whereby $\tilde{p}_{\rm o}:=p_{\rm o}/\varepsilon\leqslant O(1)$, and taking the specific heat capacity $\mathrm{c_p}$ and the volumetric coefficient of thermal expansion $\alpha_{\rm T}$ to be $O(1)$ (e.g. $\mathrm{c_p}\approx0.7$ and $\alpha_{\rm T}\approx0.1$ at 37$^{\rm o}$C for water).

3.3.2 Eulerian description

To aid the asymptotic treatment of the ARF generated by a modulated ultrasound wave with $\varepsilon\ll1$, consider the small-amplitude perturbations of the reference (thermodynamic equilibrium) state in terms of the displacement vector $\boldsymbol{u}$, particle velocity $\boldsymbol{v}$, heat flux $\boldsymbol{q}$, mass density ρ, Cauchy stress tensor $\boldsymbol{\sigma}$, absolute temperature T, and specific entropy S written as

$$\begin{gathered}\boldsymbol{u} \,=\, \varepsilon\tilde{\boldsymbol{u}}, \qquad \boldsymbol{v} \,=\, \varepsilon\tilde{\boldsymbol{v}}, \qquad \boldsymbol{q} \,=\, \varepsilon^2\tilde{\boldsymbol{q}}, \\ \rho \,=\, 1+\varepsilon\tilde{\rho}, \qquad \boldsymbol{\sigma} \,=\, \boldsymbol{\sigma}_{\rm o}+\varepsilon\tilde{\boldsymbol{\sigma}}, \qquad T \,=\, 1+\varepsilon\tilde{T}, \qquad S \,=\, S_{\rm o}+\varepsilon^2\tilde{S},\end{gathered} \tag{3.18}$$

where constants $\boldsymbol{\sigma}_{\rm o}$ and $S_{\rm o}$ signify respectively the equilibrium (initial) values of the stress tensor and specific entropy. By virtue of (3.1), (3.2) and (3.18), the scaled system kinematics takes the form

$$\varepsilon\tilde{\boldsymbol{u}} \;=\; \boldsymbol{x}-\boldsymbol{x}_{\rm o}, \qquad \tilde{\boldsymbol{v}} \;=\; \big(\boldsymbol{I}-\varepsilon\nabla^{\rm T}\tilde{\boldsymbol{u}}\big)^{-1}\cdot\frac{\partial\tilde{\boldsymbol{u}}}{\partial t}. \tag{3.19}$$

On the basis of (3.5), (3.6), (3.18) and (3.19), balance laws (3.3) can be rewritten as

$$\begin{aligned} \frac{\partial\tilde{\rho}}{\partial t}+\nabla\cdot\big((1+\varepsilon\tilde{\rho})\tilde{\boldsymbol{v}}\big) \;&=\; 0,\\ (1+\varepsilon\tilde{\rho})\Big(\frac{\partial\tilde{\boldsymbol{v}}}{\partial t}+\varepsilon\tilde{\boldsymbol{v}}\cdot\nabla\tilde{\boldsymbol{v}}\Big) \;&=\; \nabla\cdot\tilde{\boldsymbol{\sigma}},\\ (1+\varepsilon\tilde{\rho})(1+\varepsilon\tilde{T})\Big(\frac{\partial\tilde{S}}{\partial t}+\varepsilon\tilde{\boldsymbol{v}}\cdot\nabla\tilde{S}\Big) \;&=\; -\nabla\cdot\tilde{\boldsymbol{q}}\;+\;\varepsilon\,\nabla\tilde{\boldsymbol{v}}:\boldsymbol{J}:\nabla\tilde{\boldsymbol{v}}. \end{aligned} \tag{3.20}$$

Order of the perturbation quantities. From the definition of the Mach number in (3.13), it is clear that $\tilde{\boldsymbol{v}}=O(1)$. Comparing the leading terms in (3.19)–(3.20), one consequently finds that $\tilde{\boldsymbol{u}}=O(1)$, $\tilde{\rho}=O(1)$ and $\tilde{\boldsymbol{\sigma}}=O(1)$. In Sec. 3.3.4, it will be further shown that likewise $\tilde{T}=O(1)$. Under the latter restriction and hypothesis (3.17), it will also be demonstrated that $\tilde{\boldsymbol{q}}\leqslant O(1)$ and consequently $\tilde{S}\leqslant O(1)$ by way of (3.20c). In this setting, one may safely proceed with the asymptotic analysis by considering all (scaled) perturbation quantities in (3.18) to be on the order of unity.

3.3.3 Lagrangian description

On the basis of (3.4), (3.5), (3.6) and (3.18), the counterparts of (3.19) and (3.20) in the Lagrangian frame of reference can be written as

$$\varepsilon\hat{\tilde{\boldsymbol{u}}} \;=\; \boldsymbol{x}-\boldsymbol{x}_{\rm o}, \qquad \hat{\tilde{\boldsymbol{v}}} \;=\; \frac{\partial\hat{\tilde{\boldsymbol{u}}}}{\partial t}, \tag{3.21}$$

and

$$\begin{aligned} 1+\varepsilon\hat{\tilde{\rho}} \;&=\; \frac{1}{\det(\hat{\boldsymbol{F}})}, \qquad \hat{\boldsymbol{F}} \;=\; \boldsymbol{I}+\varepsilon\nabla^{\rm T}\hat{\tilde{\boldsymbol{u}}},\\ \frac{\partial^2\hat{\tilde{\boldsymbol{u}}}}{\partial t^2} \;&=\; \nabla\cdot\hat{\tilde{\boldsymbol{P}}}, \qquad \hat{\tilde{\boldsymbol{P}}} \;=\; \det(\hat{\boldsymbol{F}})\hat{\boldsymbol{F}}^{\text{-1}}\cdot\hat{\tilde{\boldsymbol{\sigma}}},\\ (1+\varepsilon\hat{\tilde{T}})\frac{\partial\hat{\tilde{S}}}{\partial t} \;&=\; -\nabla\cdot\big(\det(\hat{\boldsymbol{F}})\,\hat{\boldsymbol{F}}^{\text{-1}}\cdot\hat{\tilde{\boldsymbol{q}}}\big)\;+\;\varepsilon\,\det(\hat{\boldsymbol{F}})\,\big(\hat{\boldsymbol{F}}^{-\rm T}\cdot\nabla\hat{\tilde{\boldsymbol{v}}}\big):\hat{\tilde{\boldsymbol{J}}}:\big(\hat{\boldsymbol{F}}^{-\rm T}\cdot\nabla\hat{\tilde{\boldsymbol{v}}}\big), \end{aligned} \tag{3.22}$$

By employing the reasoning as in Sec. 3.3.2, it can be similarly shown that all perturbation quantities (and thus the leading terms) in (3.22) are, at most, on the order of unity – a feature that is critical in exposing the second-order behavior of the system (underpinning the generation of the ARF) when $\varepsilon \ll 1$.

3.3.4 Approximation of the constitutive behavior

Eulerian frame of reference. For a meaningful treatment of (3.20), it is critical to *specify* the response functions in (3.5), characterizing the isotropic elastic material with heat conduction and viscosity. Owing to the fact that the internal energy does not appear explicitly in the rescaled field equations, the focus is hereon made on (3.5b)–(3.5d). In the context of the featured asymptotic analysis, such specification can be effected without loss of generality by recalling (3.8)–(3.11) and expanding (3.5b)–(3.5d), up to a suitable order, with respect to ε. To this end, let

$$\begin{aligned} \tilde{\boldsymbol{E}} \; &:= \; \frac{\boldsymbol{E}}{\varepsilon} \; = \; \tfrac{1}{2}\Big(\boldsymbol{F}^{\mathrm{T}}\!\cdot\nabla\tilde{\boldsymbol{u}} + \nabla^{\mathrm{T}}\tilde{\boldsymbol{u}}\!\cdot\!\boldsymbol{F} + \varepsilon\,\boldsymbol{F}^{\mathrm{T}}\!\cdot\nabla\tilde{\boldsymbol{u}}\!\cdot\!\nabla^{\mathrm{T}}\tilde{\boldsymbol{u}}\!\cdot\!\boldsymbol{F}\Big) = O(1), \\ \boldsymbol{F} \; &= \; (\boldsymbol{I} - \varepsilon\nabla^{\mathrm{T}}\tilde{\boldsymbol{u}})^{-1} = O(1), \end{aligned} \tag{3.23}$$

denote the scaled Green-Lagrangian strain tensor and deformation gradient expressed in terms of Eulerian quantities so that, by virtue of (3.9), one has

$$I_n(\tilde{\boldsymbol{E}}) \; = \; \frac{I_n(\boldsymbol{E})}{\varepsilon^n} \; = \; O(1), \qquad n = 1,2,3. \tag{3.24}$$

In what follows, an implicit assumption is made that the response functions in (3.5) are *well behaved* in the sense that the partial derivatives of each constitutive relationship, computed at the initial (equilibrium) state, are continuous and such that

$$\left|\left(\frac{\partial^{m+n}\mathbb{F}}{\partial\mathcal{X}^m\partial\mathcal{Y}^n}\right)_{\!\mathrm{o}}\right| \leqslant O\Big(\max_{\mathcal{X}}\Big(\frac{\partial\mathbb{F}}{\partial\mathcal{X}}\Big)_{\!\mathrm{o}}\Big), \qquad \mathbb{F} = U, T, \boldsymbol{\sigma}, \boldsymbol{q}, \qquad \mathcal{X},\mathcal{Y} = \boldsymbol{F}, S, \nabla\boldsymbol{v}, \nabla T, \tag{3.25}$$

for $m+n \geqslant 2$ as applicable. With reference to (3.6a) and (3.8), this in particular implies that all derivatives of $\bar{U}$ with respect to its arguments at the equilibrium state are at most $O(T) = O(1)$. Physically, hypothesis (3.25) ensures that the higher-order derivatives in (3.25), multiplying the nonlinear terms in the asymptotic expansion, are bounded *in order* by the leading term which guarantees that the response of the system is predominantly linear under small perturbations about the equilibrium state.

Since the acoustic radiation force is known to stem from the quadratic (and bi-linear) terms featuring the perturbation quantities [5], one may first invoke (3.8), (3.10a), (3.11), (3.18) and (3.23) and expand scaled (3.5b) in ε, up to the linear terms, as

$$\begin{aligned}
\tilde{T} &\overset{\varepsilon^2}{=} \left(\frac{\partial^2 \bar{U}}{\partial S \partial \boldsymbol{E}}\right)_{\!\mathrm{o}} \!:\! \tilde{\boldsymbol{E}} \;+\; \varepsilon \left(\frac{\partial^2 \bar{U}}{\partial S^2}\right)_{\!\mathrm{o}} \tilde{S} \;+\; \varepsilon\, \tilde{\boldsymbol{E}} \!:\! \left(\frac{\partial^3 \bar{U}}{\partial S \partial \boldsymbol{E}^2}\right)_{\!\mathrm{o}} \!:\! \tilde{\boldsymbol{E}} \\
&\overset{\varepsilon^2}{=} -\frac{\beta_{\mathrm{T}}}{\mathrm{c_p}} \nabla\cdot\tilde{\boldsymbol{u}} \;-\; \varepsilon \left(\frac{\beta_{\mathrm{T}}}{2\mathrm{c_p}}\right) \nabla\tilde{\boldsymbol{u}} \!:\! \nabla^{\mathrm{T}}\tilde{\boldsymbol{u}} \;+\; \varepsilon \left[\left(\frac{\partial^3 \bar{U}}{\partial S \partial I_1^2}\right)_{\!\mathrm{o}} + \left(\frac{\partial^2 \bar{U}}{\partial S \partial I_2}\right)_{\!\mathrm{o}}\right] (\nabla\cdot\tilde{\boldsymbol{u}})^2 \\
&- \;\varepsilon \left[\frac{\beta_{\mathrm{T}}}{\mathrm{c_p}} + \left(\frac{\partial^2 \bar{U}}{\partial S \partial I_2}\right)_{\!\mathrm{o}}\right] \nabla^{\mathrm{S}}\tilde{\boldsymbol{u}} \!:\! \nabla^{\mathrm{S}}\tilde{\boldsymbol{u}} \;+\; \varepsilon \left(\frac{\partial^2 \bar{U}}{\partial S^2}\right)_{\!\mathrm{o}} \tilde{S},
\end{aligned} \tag{3.26}$$

where $\nabla^{\mathrm{S}}\tilde{\boldsymbol{u}} := \frac{1}{2}(\nabla\tilde{\boldsymbol{u}} + \nabla^{\mathrm{T}}\tilde{\boldsymbol{u}})$ (see Chapter 2 for definition of "$\overset{\varepsilon^n}{=}$"). Clearly, (3.26) verifies the claim that $\tilde{T} = O(1)$ made in Section 3.3.2.

Similarly, (3.10b) can be scaled up to $O(1)$ and expanded in ε, by virtue of (3.23) and (3.24), up to the linear terms as

$$\begin{aligned}
\tilde{\boldsymbol{\Sigma}} := \frac{\boldsymbol{\Sigma} - \boldsymbol{\sigma}_{\mathrm{o}}}{\varepsilon} &\overset{\varepsilon^2}{=} \big(1 - 2\varepsilon\tilde{G}\big)\nabla\cdot\tilde{\boldsymbol{u}}\,\boldsymbol{I} \;+\; 2\varepsilon\tilde{G}\nabla^{\mathrm{S}}\tilde{\boldsymbol{u}} \;+\; \varepsilon\Big[\tfrac{1}{2}(B{+}3C{+}D{-}2)(\nabla\cdot\tilde{\boldsymbol{u}})^2 \\
&- \;\tfrac{1}{2}(C{+}D)\nabla^{\mathrm{S}}\tilde{\boldsymbol{u}} \!:\! \nabla^{\mathrm{S}}\tilde{\boldsymbol{u}} + \nabla\tilde{\boldsymbol{u}} \!:\! \nabla^{\mathrm{T}}\tilde{\boldsymbol{u}} + \tfrac{1}{2}\nabla\tilde{\boldsymbol{u}} \!:\! \nabla\tilde{\boldsymbol{u}} - \frac{\beta_{\mathrm{T}}}{\mathrm{c_p}}\tilde{S}\Big]\boldsymbol{I} \\
&- \;\varepsilon\Big[(C{+}D{-}2)\,\nabla\cdot\tilde{\boldsymbol{u}}\,\boldsymbol{I} - D\nabla^{\mathrm{S}}\tilde{\boldsymbol{u}}\Big]\cdot\nabla^{\mathrm{S}}\tilde{\boldsymbol{u}}
\end{aligned} \tag{3.27}$$

where

$$B := \left(\frac{\partial^3 \bar{U}}{\partial {I_1}^3}\right)_{\!\mathrm{o}}, \qquad C := \left(\frac{\partial^2 \bar{U}}{\partial I_1 \partial I_2}\right)_{\!\mathrm{o}}, \qquad D := \left(\frac{\partial \bar{U}}{\partial I_3}\right)_{\!\mathrm{o}}, \tag{3.28}$$

as shown in Appendix A.2. Note that the expansions of hyperelastic constitutive relationships similar to (3.27) (albeit without the entropy contribution) can be found elsewhere in the literature [7, 21], featuring the so-called Landau's third-order moduli A^{Lan}, B^{Lan}, and C^{Lan} [23]. The featured nonlinearity parameters B, C and D can be related to the Landau's third-order moduli as

$$B \;=\; 2A^{\mathrm{Lan}} + 6B^{\mathrm{Lan}} + 2C^{\mathrm{Lan}}, \qquad C \;=\; -A^{\mathrm{Lan}} - 2B^{\mathrm{Lan}}, \qquad D \;=\; A^{\mathrm{Lan}}.$$

By way of (3.15), (3.18) and (3.27), constitutive relationship (3.5c) reads

$$\tilde{\boldsymbol{\sigma}} \;=\; \tilde{\boldsymbol{\Sigma}}(\boldsymbol{F}, S) \;+\; \varepsilon\,\tilde{\boldsymbol{J}}(\boldsymbol{F}, S) \!:\! \nabla\tilde{\boldsymbol{v}}, \tag{3.29}$$

which demonstrates that $\tilde{\boldsymbol{\sigma}}$ can be approximated with accuracy $O(\varepsilon^2)$ by retaining only the leading term in the expansion of $\tilde{\boldsymbol{J}}$. To this end, one may invoke the premise of material isotropy whereby the leading-order expansion of the viscosity term in (3.29) becomes

$$\tilde{\boldsymbol{J}}(\boldsymbol{F},S)\!:\!\nabla\tilde{\boldsymbol{v}} \;\overset{\varepsilon}{=}\; (\tilde{\mu}_{\mathrm{B}} - \tfrac{2}{3}\tilde{\mu})(\nabla\!\cdot\!\tilde{\boldsymbol{v}})\,\boldsymbol{I} \;+\; 2\tilde{\mu}\nabla^{\mathrm{S}}\tilde{\boldsymbol{v}}, \qquad \tilde{\mu}_{\mathrm{B}} := \frac{\mu_{\mathrm{B}}}{\varepsilon}, \quad \tilde{\mu} := \frac{\mu}{\varepsilon}, \tag{3.30}$$

where constants $\mu_{\mathrm{B}} \geqslant 0$ and $\mu \geqslant 0$ denote respectively the viscosities of the solid in bulk and shear [48]. In support of (3.15) and (3.30), it is noted that the studies of ultrasound wave dispersion and attenuation in soft tissues [49, 50] indicate that $\tilde{\mu}_{\mathrm{B}} = O(1)$ and $\tilde{\mu} \leqslant O(1)$ as implied by the referenced formulas.

On recalling (3.7), the heat flux relationship (3.5d) can next be expanded with respect to its arguments by retaining *only* the terms that contain the odd powers of ∇T. Within the framework of material isotropy and (3.25), such expansion yields

$$\tilde{\boldsymbol{q}} \;\overset{\varepsilon^2}{=}\; -\,\nabla\tilde{T}\cdot\Big[\tilde{\kappa}\boldsymbol{I} - \varepsilon\,\nabla^{\mathrm{T}}\tilde{\boldsymbol{u}}\!:\!\tilde{\boldsymbol{A}}\Big] \tag{3.31}$$

where, consistent with the definition of the scaled coefficient of thermal conductivity as in (3.17), one has

$$\tilde{\kappa}\boldsymbol{I} := \;-\frac{1}{\varepsilon}\left(\frac{\partial\boldsymbol{q}}{\partial\nabla T}\right)_{\!\mathrm{o}}, \qquad \tilde{\boldsymbol{A}} := \;\frac{1}{\varepsilon}\left(\frac{\partial^2\boldsymbol{q}}{\partial\boldsymbol{F}\partial\nabla T}\right)_{\!\mathrm{o}}, \tag{3.32}$$

under the constraint that $|\tilde{\boldsymbol{A}}| \leqslant O(\tilde{\kappa})$. In support of the latter restriction, it is noted that assuming $|\tilde{\boldsymbol{A}}| > O(\tilde{\kappa})$ would violate not only (3.25), but also the Clausius-Duhem inequality for the second-order tensor within the square brackets in (3.31) could not be guaranteed to be positive-definite under an arbitrary choice of $\nabla^{\mathrm{T}}\tilde{\boldsymbol{u}}$. On the basis of (3.17), (3.26) and (3.31) it now follows that $\tilde{\boldsymbol{q}} \leqslant O(1)$ and, by way of (3.20c), that $\tilde{S} \leqslant O(1)$ as asserted in Section 3.3.2.

In concluding the asymptotic treatment of (3.5), one may note that (3.20), (3.26), (3.27)–(3.30) and (3.31) yield a closed system of equations, each expanded up to the second order, with an explicit set of constitutive equations in terms of $\tilde{T}$, $\tilde{\boldsymbol{\sigma}}$ and $\tilde{\boldsymbol{q}}$ that is applicable to a generic (isotropic) elastic solid with heat conduction and viscosity [48].

Lagrangian frame of reference. To close the system of field equations (3.21)–(3.22), it is necessary to provide the Lagrangian analogues of (3.26), (3.27)–(3.30) and (3.31). To this end, one finds from (3.23) that

$$\hat{\tilde{\boldsymbol{E}}} \;:=\; \frac{\hat{\boldsymbol{E}}}{\varepsilon} \;=\; \tfrac{1}{2}\Big(\nabla\hat{\tilde{\boldsymbol{u}}} + \nabla^{\mathrm{T}}\hat{\tilde{\boldsymbol{u}}} + \varepsilon\,\nabla\hat{\tilde{\boldsymbol{u}}}\!\cdot\!\nabla^{\mathrm{T}}\hat{\tilde{\boldsymbol{u}}}\Big) \;=\; O(1), \tag{3.33}$$

whose invariants obey scaling equivalent to that in (3.24). In this setting, temperature expansion (3.26) can be rewritten using (3.33) and (3.23) as

$$\begin{aligned}\hat{\hat{T}} \;&\overset{\varepsilon^2}{=}\; -\frac{\beta_{\mathrm{T}}}{\mathrm{c_p}}\nabla\cdot\hat{\hat{\boldsymbol{u}}} \;+\; \varepsilon\left(\frac{\beta_{\mathrm{T}}}{2\mathrm{c_p}}\right)\nabla\hat{\hat{\boldsymbol{u}}}\!:\!\nabla^{\mathrm{T}}\hat{\hat{\boldsymbol{u}}} \;+\; \varepsilon\left[\left(\frac{\partial^3\bar{U}}{\partial S\partial I_1^2}\right)_{\!\mathrm{o}} + \left(\frac{\partial^2\bar{U}}{\partial S\partial I_2}\right)_{\!\mathrm{o}}\right](\nabla\cdot\hat{\hat{\boldsymbol{u}}})^2 \\ &-\; \varepsilon\left[\frac{\beta_{\mathrm{T}}}{\mathrm{c_p}} + \left(\frac{\partial^2\bar{U}}{\partial S\partial I_2}\right)_{\!\mathrm{o}}\right]\nabla^{\mathrm{S}}\hat{\hat{\boldsymbol{u}}}\!:\!\nabla^{\mathrm{S}}\hat{\hat{\boldsymbol{u}}} \;+\; \varepsilon\left(\frac{\partial^2\bar{U}}{\partial S^2}\right)_{\!\mathrm{o}}\hat{\hat{S}} \end{aligned} \qquad (3.34)$$

Similarly, the first Piola-Kirchhoff stress tensor featured in (3.22b) can be expanded with reference to (3.29) as

$$\hat{\hat{\boldsymbol{P}}} \;=\; \hat{\hat{\boldsymbol{\Pi}}} \;+\; \varepsilon\det(\hat{\boldsymbol{F}})\,\hat{\boldsymbol{F}}^{-1}\!\cdot\hat{\hat{\boldsymbol{J}}}(\hat{\boldsymbol{F}},\hat{S})\!:\!(\hat{\boldsymbol{F}}^{-\mathrm{T}}\!\cdot\nabla\hat{\hat{\boldsymbol{v}}}), \qquad (3.35)$$

where $\hat{\hat{\boldsymbol{\Pi}}}:=\det(\hat{\boldsymbol{F}})\,\hat{\boldsymbol{F}}^{-1}\!\cdot\hat{\hat{\boldsymbol{\Sigma}}}$ is given by

$$\begin{aligned}\hat{\hat{\boldsymbol{\Pi}}} \;&\overset{\varepsilon^2}{=}\; \big(1-2\varepsilon\tilde{G}\big)\nabla\cdot\hat{\hat{\boldsymbol{u}}}\,\boldsymbol{I} \;+\; 2\varepsilon\tilde{G}\nabla^{\mathrm{S}}\hat{\hat{\boldsymbol{u}}} \;+\; \varepsilon\Big[\tfrac{1}{2}(B{+}3C{+}D)(\nabla\cdot\hat{\hat{\boldsymbol{u}}})^2 - \tfrac{1}{2}(C{+}D)\nabla^{\mathrm{S}}\hat{\hat{\boldsymbol{u}}}\!:\!\nabla^{\mathrm{S}}\hat{\hat{\boldsymbol{u}}} \\ &+ \tfrac{1}{2}\nabla\hat{\hat{\boldsymbol{u}}}\!:\!\nabla\hat{\hat{\boldsymbol{u}}} - \frac{\beta_{\mathrm{T}}}{\mathrm{c_p}}\hat{\hat{S}}\Big]\boldsymbol{I} \;-\; \varepsilon\Big[(C{+}D)\,\nabla\cdot\hat{\hat{\boldsymbol{u}}}\,\boldsymbol{I} - D\nabla^{\mathrm{S}}\hat{\hat{\boldsymbol{u}}}\Big]\cdot\nabla^{\mathrm{S}}\hat{\hat{\boldsymbol{u}}} \;+\; \varepsilon\nabla\cdot\hat{\hat{\boldsymbol{u}}}\,\nabla\hat{\hat{\boldsymbol{u}}}, \end{aligned} \qquad (3.36)$$

as shown in Appendix A.2, and

$$\det(\hat{\boldsymbol{F}})\hat{\boldsymbol{F}}^{-1}\!\cdot\hat{\hat{\boldsymbol{J}}}(\hat{\boldsymbol{F}},\hat{S})\!:\!(\hat{\boldsymbol{F}}^{-\mathrm{T}}\!\cdot\nabla\hat{\hat{\boldsymbol{v}}}) \;\overset{\varepsilon}{=}\; (\tilde{\mu}_{\mathrm{B}} - \tfrac{2}{3}\tilde{\mu})(\nabla\cdot\hat{\hat{\boldsymbol{v}}})\,\boldsymbol{I} \;+\; 2\tilde{\mu}\,\nabla^{\mathrm{S}}\hat{\hat{\boldsymbol{v}}}, \qquad (3.37)$$

see also (3.30). Finally, expansion of the heat flux (3.31) can be rewritten in the Lagrangian frame of reference as

$$\hat{\hat{\boldsymbol{q}}} \;\overset{\varepsilon^2}{=}\; -\nabla\hat{\hat{T}}\cdot\Big[\tilde{\kappa}\boldsymbol{I} - \varepsilon\,\nabla^{\mathrm{T}}\hat{\hat{\boldsymbol{u}}}\!:\!\big(\boldsymbol{I}_4 + \tilde{\boldsymbol{A}}\big)\Big], \qquad (3.38)$$

where $\boldsymbol{I}_4$ is the fourth-order identity tensor and $\tilde{\boldsymbol{A}}$ is given by (3.32).

Limiting case of (3.29) for a Newtonian fluid. To facilitate the comparison of the results for focused beam geometry with those obtained for fluids under the premise of plane-wave propagation, it is instructive to consider the degenerate case of (3.29) for a Newtonian fluid. Assuming that $\beta_{\mathrm{T}}, \mathrm{c_p}, \tilde{\mu}_{\mathrm{B}}$ and $\tilde{\mu}$ characterizing the elastic solid (with heat conduction and viscosity) can be assigned to the Newtonian fluid, the question remains as to the choice of constants $\tilde{G}, B, C$ and D that would permit such degeneration. To this end, it is first noted that the thermoelastic part of the Cauchy stress tensor in fluids is spherical and related to the thermodynamic pressure $p=\varepsilon\tilde{p}$ as $\tilde{\boldsymbol{\Sigma}}_{\text{FL}}=-\tilde{p}\boldsymbol{I}$ [7], which allows one to deduce from (3.27) that

$$\tilde{G}=0, \qquad C=2, \qquad D=0. \tag{3.39}$$

Since the constitutive relationship for fluids typically entails mass density perturbations (as opposed to displacements), one may conveniently expand (3.22a) in Taylor series to obtain

$$\hat{\tilde{\rho}} \overset{\varepsilon^2}{=} -\nabla\cdot\hat{\tilde{\boldsymbol{u}}} \;+\; \tfrac{1}{2}\varepsilon(\nabla\cdot\hat{\tilde{\boldsymbol{u}}})^2 \;+\; \tfrac{1}{2}\varepsilon\nabla\hat{\tilde{\boldsymbol{u}}}\colon\nabla^{\text{T}}\hat{\tilde{\boldsymbol{u}}},$$

which can be rewritten in the Eulerian frame of reference as

$$\tilde{\rho} \overset{\varepsilon^2}{=} -\nabla\cdot\tilde{\boldsymbol{u}} \;+\; \tfrac{1}{2}\varepsilon(\nabla\cdot\tilde{\boldsymbol{u}})^2 \;-\; \tfrac{1}{2}\varepsilon\nabla\tilde{\boldsymbol{u}}\colon\nabla^{\text{T}}\tilde{\boldsymbol{u}}. \tag{3.40}$$

On substituting (3.39) into (3.27), one finds by virtue of (3.30) that (3.29) degenerates to the well-known constitutive format for Newtonian fluids, namely

$$\begin{aligned}\tilde{\boldsymbol{\sigma}}_{\text{FL}} &\overset{\varepsilon^2}{=} -\tilde{p}\boldsymbol{I} \;+\; \varepsilon\big(\tilde{\mu}_{\text{B}}-\tfrac{2}{3}\tilde{\mu}\big)\nabla\cdot\tilde{\boldsymbol{v}}\,\boldsymbol{I} \;+\; 2\varepsilon\tilde{\mu}\nabla^{\text{S}}\tilde{\boldsymbol{v}},\\ \tilde{p} &= \tilde{\rho} \;+\; \varepsilon(\beta-1)\tilde{\rho}^2 \;+\; \varepsilon\frac{\beta_{\text{T}}}{\text{c}_{\text{p}}}\tilde{S}, \qquad \beta:=-\tfrac{1}{2}(B+3)\end{aligned} \tag{3.41}$$

where $\tilde{p}$ is the scaled thermodynamic pressure, and β is the coefficient of acoustic nonlinearity [7]. This result indeed demonstrates that the sought degeneration can be effected by complementing (3.39) with

$$B=-(2\beta+3). \tag{3.42}$$

3.4 Formulation and scaling of the focused beam problem

To understand the effect of low-frequency modulation on the generation of the ARF, the next step is to formulate the boundary value problem that is consistent with relevant applications of elevated-intensity ultrasound [61, 17] toward remote palpation of soft tissues. For simplicity, this is accomplished by making reference to the Cartesian coordinate system (x_1,x_2,z) whose z-axis coincides with that of the ultrasound transducer as in Fig. 3.2. On denoting the featured transverse coordinates jointly by $x_{\mathfrak{i}}$, $\mathfrak{i}=1,2$, the geometry of a focused ultrasound transducer with shape Γ can accordingly be synthesized via its focal distance d (i.e. the radius of curvature) and transverse dimensions

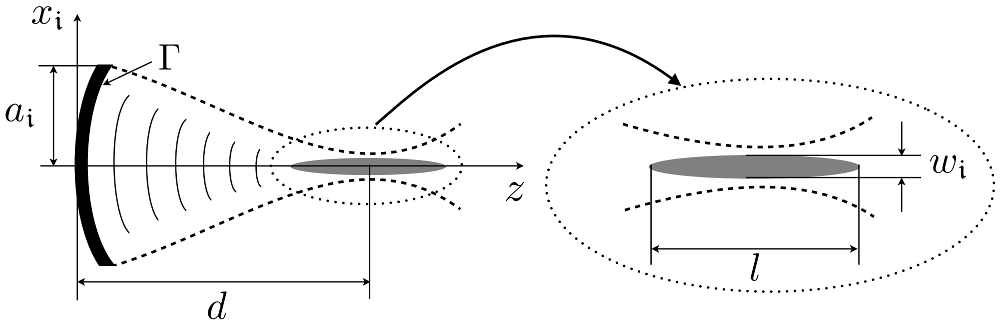

Figure 3.1: Schematics of a transducer used to generate the focused ultrasound field (left), which in turn gives rise to the ARF within the focal region (right).

a_i as indicated in Fig. 3.2. In this setting, the transducer's action can be formulated, in the Lagrangian frame of reference, via Dirichlet boundary condition

$$\hat{\tilde{\boldsymbol{u}}}\big|_{\Gamma} \;=\; \boldsymbol{\Lambda}(\boldsymbol{x}_o)\,\mathcal{M}(\varepsilon t)\,\sin(t), \qquad \boldsymbol{x}_o \in \Gamma, \tag{3.43}$$

where $\hat{\tilde{\boldsymbol{u}}}$ is the scaled displacement vector, see (3.18); Γ denotes the surface of a transducer; prescribed function $\boldsymbol{\Lambda}$ signifies the so-called profile of the beam; and $\mathcal{M}=O(1)$ is the ultrasound *modulation envelope* such that

$$\mathcal{M} \equiv 0 \quad \text{for} \quad t \leqslant 0 \qquad \text{and} \qquad \frac{d\mathcal{M}(\varepsilon t)}{d(\varepsilon t)} = O(1) \quad \text{for} \quad t>0, \tag{3.44}$$

i.e. $\mathcal{M}$ is a smooth modulation signal with quiescent past and dominant (dimensionless) frequency $\omega_m = O(\varepsilon)$. Here it is assumed that the oscillating transducer is the sole source of excitation for the problem, whereby the "left" boundary condition (3.43) is complemented by the radiation condition at $z = \infty$. For a comprehensive study of the featured thermomechanical problem, it is further assumed that the transducer's boundary is thermally insulated, i.e. that

$$\hat{\tilde{\boldsymbol{q}}}\big|_{\Gamma} \;=\; 0, \tag{3.45}$$

where $\hat{\tilde{\boldsymbol{q}}}$ denotes the scaled heat flux. In the sequel it will be shown that (3.45), while not being essential for the computation of the ARF, may be useful for the analysis of (averaged) temperature distribution generated by the absorption of an elevated-intensity ultrasonic field by the tissue.

Plane wave problem. Note that the reduced plane wave problem will also be examined in this study. For the latter configuration, the boundary condition (3.43) reduces to

$$\hat{\hat{u}}_z\big|_{z_\text{o}=0} \;=\; \mathcal{M}(\varepsilon t)\,\sin(t), \tag{3.46}$$

while the thermal boundary condition (3.45) simplifies to

$$\hat{\hat{q}}_z\big|_{z_\text{o}=0} \;=\; 0. \tag{3.47}$$

3.4.1 Scaling affiliated with geometry of the beam

Since the dimensionless ultrasound frequency in this study equals unity (see Table 2.1), the geometry of a focused ultrasound beam in Fig. 3.2 is governed only by three dimensionless parameters, namely $a_\mathfrak{i}$ ($\mathfrak{i}=1,2$) and d, or alternatively, by $f_\mathfrak{i} := d/(2a_\mathfrak{i})$ and d, where $f_\mathfrak{i}$ is the so-called *focal ratio* computed with respect to $a_\mathfrak{i}$. For an effective asymptotic treatment of the featured boundary value problem, it is noted that the ultrasound transducers used to generate the ARF typically have the aperture i.e. diameter between 1 and 4.5 cm, focal distance $2\div 9$ cm and carrier frequency $1\div 5$ MHz [17, 13, 61, 62, 63]. In this setting, one finds that the focal ratios affiliated with ARF-generating transducers are normally $f = 1.5 \div 5$, while their dimensionless focal distances (referring to the length scale as in Table 2.1) are in the range $d = 300 \div 1500$ [17, 13, 61, 62, 63].

Focal region. In theory and applications of the acoustic radiation force [9], of critical interest is the "cigar"-shaped zone D of coalescence of ultrasound waves (indicated by the shaded area in Fig. 3.2), where the Mach number reaches sufficiently high values so that the sought nonlinear effect is significant. Given possible disproportionality of the size of this region relative to other characteristic length scales of the problem, however, it is essential to moderate its dimensions by a suitable power of the Mach number in a way similar to transformation (3.18).

Assuming axisymmetric transducer geometry, one may estimate the *half-width* and *half-length* of the focal zone respectively as

$$w \approx 2\pi f, \qquad l \approx 14\pi f^2, \tag{3.48}$$

as shown in Appendix A.4. On recalling the premise that $\varepsilon = O(10^{-3})$ in the focal region, its half-width can be accordingly scaled as

$$\tilde{w_{\mathrm{i}}} \;=\; \varepsilon^{\lambda} w_{\mathrm{i}} \;=\; O(1), \qquad \lambda = \frac{\log(2\pi f)}{-\log\varepsilon} > \frac{1}{4}, \qquad \mathrm{i}=1,2, \tag{3.49}$$

for focal numbers $f \geqslant 1$. Here it is noted that the lower bound on λ in (3.49) is critical for the development of a compact expression for the ARF. In particular, it will be shown that the relative approximation error of the ARF behaves as $O(\varepsilon^{\min\{1,4\lambda-1\}})$, whereby $\lambda=\frac{1}{4}$ is a threshold beyond which a simple expression for the ARF ceases to apply.

Scaling of transverse coordinates. In the analysis of focusing effects such as those of interest in this study, it is next reasonable to assume that inside D, the partial derivatives of any thermomechanical quantity with respect to transverse coordinates x_{i} scale with *the width* of the focal region. On denoting the compound state vector solving (3.21)–(3.22) as

$$\boldsymbol{Q}(x_{\mathrm{i}},z,t) \;:=\; \big(\tilde{\rho},\tilde{\boldsymbol{u}},\tilde{\boldsymbol{v}},\tilde{\boldsymbol{\sigma}},\tilde{\boldsymbol{q}},\tilde{T},\tilde{S}\big)(x_{\mathrm{i}},z,t), \tag{3.50}$$

this in particular implies that

$$\frac{\partial\boldsymbol{Q}}{\partial(x_{\mathrm{i}}/w_{\mathrm{i}})} = O(\boldsymbol{Q}), \qquad \boldsymbol{x}\in D. \tag{3.51}$$

Outside D, on the other hand, one may expect the same derivatives to diminish due to widening of the beam (see e.g. the top panel in Fig. A.1), whereby

$$\frac{\partial\boldsymbol{Q}}{\partial(x_{\mathrm{i}}/w_{\mathrm{i}})} \leqslant O(\boldsymbol{Q}), \qquad \boldsymbol{x}\notin D. \tag{3.52}$$

On the basis of (3.49)–(3.52), the scaled transverse coordinates (in Eulerian formulation) can be introduced as

$$\chi_{\mathrm{i}} := \varepsilon^{\lambda} x_{\mathrm{i}}, \qquad \frac{\partial\boldsymbol{Q}}{\partial\chi_{\mathrm{i}}} \leqslant O(\boldsymbol{Q}). \tag{3.53}$$

Note that scaling (3.53) with $\lambda=\frac{1}{2}$ coincides with that underpinning the Khokhlov-Zabolotskaya-Kuznetsov (KZK) equation [39, 9, 7], which is commonly used to describe focused ultrasound beams. As a rule, the latter analyses postulate the so-called “narrow beam” geometry that can be affiliated with focal number $f\approx 5$. In contrast, the present framework caters for configurations with $f \geqslant 1$ that are more representative of the ARF transducers reported in the literature. For generality one should also observe that conditions (3.53) imply that the featured thermomechanical quantities vary slowly perpendicular to the beam axis (over distances of one ultrasound wavelength); in this context, such waves are sometimes referred to as the *quasi-plane* waves [7].

In light of (3.53), one finds that the right-hand side of the balance of linear momentum (3.20b) is, to the leading order, $\nabla\cdot\tilde{\boldsymbol{\sigma}} = \nabla\nabla\cdot\tilde{\boldsymbol{u}} = (O(\varepsilon^\lambda), O(\varepsilon^\lambda), O(1))$. This in turn implies that $\tilde{\boldsymbol{v}}$, and thus $\tilde{\boldsymbol{u}}$, are vector fields whose components in the (x_1, x_2, z) coordinate frame behave respectively as $(O(\varepsilon^\lambda), O(\varepsilon^\lambda), O(1))$. Accordingly, the ensuing asymptotic analysis can be facilitated by writing

$$\begin{aligned} \tilde{\boldsymbol{u}} &= (\tilde{u}_{\mathrm{i}}, \tilde{u}_z)(x_{\mathrm{i}}, z, t) := (\varepsilon^\lambda \tilde{\mathrm{u}}_{\mathrm{i}}, \tilde{\mathrm{u}}_z)(\chi_{\mathrm{i}}, z, t), \qquad \tilde{\mathrm{u}}_{\mathrm{i}}, \tilde{\mathrm{u}}_z = O(1), \\ \tilde{\boldsymbol{v}} &= (\tilde{v}_{\mathrm{i}}, \tilde{v}_z)(x_{\mathrm{i}}, z, t) := (\varepsilon^\lambda \tilde{\mathrm{v}}_{\mathrm{i}}, \tilde{\mathrm{v}}_z)(\chi_{\mathrm{i}}, z, t), \qquad \tilde{\mathrm{v}}_{\mathrm{i}}, \tilde{\mathrm{v}}_z = O(1), \end{aligned} \tag{3.54}$$

where $\tilde{u}_{\mathrm{i}}$ stands for the *ordered pair* $(\tilde{u}_1, \tilde{u}_2)$, $\tilde{\mathrm{u}}_{\mathrm{i}}$ for $(\tilde{\mathrm{u}}_1, \tilde{\mathrm{u}}_2)$, and so on. An important restriction on (3.53) and (3.54) is that they strictly apply to the quantities associated with the ultrasound time scale and, in general, may not be applicable to the mean motion induced by the ARF.

In preparation of the ensuing discussion, it is noted the counterparts of (3.50)–(3.54) in the Lagrangian frame of reference can be obtained by superseding $\{x_{\mathrm{i}}, z, \chi_{\mathrm{i}}, \boldsymbol{Q}, \tilde{\mathrm{u}}_{\mathrm{i}}, \tilde{\mathrm{u}}_z, \tilde{\mathrm{v}}_{\mathrm{i}}, \tilde{\mathrm{v}}_z\}$ respectively by $\{x_{\mathrm{io}}, z_{\mathrm{o}}, \chi_{\mathrm{io}}, \hat{\boldsymbol{Q}}, \hat{\tilde{\mathrm{u}}}_{\mathrm{i}}, \hat{\tilde{\mathrm{u}}}_z, \hat{\tilde{\mathrm{v}}}_{\mathrm{i}}, \hat{\tilde{\mathrm{v}}}_z\}$, where $\hat{\boldsymbol{Q}} := \big(\hat{\tilde{\rho}}, \hat{\tilde{\boldsymbol{u}}}, \hat{\tilde{\boldsymbol{v}}}, \hat{\tilde{\boldsymbol{\sigma}}}, \hat{\tilde{\boldsymbol{q}}}, \hat{\tilde{T}}, \hat{\tilde{S}}\big)$.

3.4.2 "Slow" time variable

The key difficulty in exposing the time-averaged behavior of the state vector $\boldsymbol{Q}$ or $\hat{\boldsymbol{Q}}$ for the modulated ultrasound problem resides in the presence of disparate time scales in the boundary condition (3.43). To tackle the problem, consider the reparameterized Lagrangian state vector

$$\hat{\boldsymbol{Q}}(\chi_{\mathrm{io}}, z_{\mathrm{o}}, t) \;:=\; \hat{\boldsymbol{Q}}(x_{\mathrm{io}}, z_{\mathrm{o}}, t) \tag{3.55}$$

which solves (3.22) and (3.34)–(3.38) subject to boundary conditions (3.43)–(3.45) and the radiation condition at infinity. Recalling that (3.43) is the sole source of excitation for the problem, consider next the *phase-shifted* solution $\hat{\boldsymbol{Q}}_\phi(\chi_{\mathrm{io}}, z_{\mathrm{o}}, t)$ which is affiliated with the perturbed boundary condition

$$\hat{\boldsymbol{Q}}^{\boldsymbol{u}}_\phi(\chi_{\mathrm{io}}, z_{\mathrm{o}}, t)\big|_\Gamma \;=\; \boldsymbol{\Lambda}(\boldsymbol{x}_{\mathrm{o}})\, \mathcal{M}(\varepsilon t)\, \sin(t+\phi), \qquad \boldsymbol{x}_{\mathrm{o}} \in \Gamma, \tag{3.56}$$

where $\hat{\boldsymbol{Q}}^{\boldsymbol{u}} = \hat{\hat{\boldsymbol{u}}}$ is the $\hat{\hat{\boldsymbol{u}}}$-component of the state vector $\hat{\boldsymbol{Q}}$, and ϕ is the phase-shift parameter applied to the carrier ultrasound signal. To help parse out the "ultrasound" time in the solution, one may introduce the so-called "slow" time variable

$$\tau \;:=\; \varepsilon t \tag{3.57}$$

and auxiliary vector function $\hat{\boldsymbol{G}}(\chi_{\text{io}}, z_{\text{o}}, \tau, t)$ such that

$$\hat{\boldsymbol{G}}(\chi_{\text{io}}, z_{\text{o}}, \tau, t+\phi) \;:=\; \hat{\boldsymbol{Q}}_{\phi}(\chi_{\text{io}}, z_{\text{o}}, t), \qquad \phi \geqslant 0 \tag{3.58}$$

holds everywhere in space and time, see also [19] in the context of modulated plane waves. On the basis of (3.56) and (3.58), one finds that

$$\hat{\boldsymbol{G}}^{\boldsymbol{u}}(\chi_{\text{io}}, z_{\text{o}}, \tau, t+\phi)\big|_{\Gamma} \;=\; \boldsymbol{\Lambda}(\boldsymbol{x}_{\text{o}})\,\mathcal{M}(\varepsilon t)\,\sin(t+\phi), \qquad \boldsymbol{x}_{\text{o}} \in \Gamma, \tag{3.59}$$

where $\hat{\boldsymbol{G}}^{\boldsymbol{u}} = \hat{\hat{\boldsymbol{u}}}$. On the basis of (3.59) and premise $d\mathcal{M}(\tau)/d\tau = O(1)$ as in (3.44), one finds that $\partial\hat{\boldsymbol{G}}^{\boldsymbol{u}}/\partial\tau = O(1)$ on the boundary. Even though the governing field equations (3.22) are nonlinear, one can safely assume that the overall solution retains such smoothness throughout the domain, i.e. that $\partial\hat{\boldsymbol{G}}/\partial\tau = O(1)$ *everywhere* due to the facts that the problem is mildly nonlinear ($\varepsilon \ll 1$) and that the material is dissipative which precludes the existence of characteristic surfaces, i.e. shocks. As a result, it follows from (3.59) that $\hat{\boldsymbol{G}}$ is periodic in "fast" time t, i.e. that

$$\hat{\boldsymbol{G}}(\chi_{\text{io}}, z_{\text{o}}, \tau, t+2\pi) \;=\; \hat{\boldsymbol{G}}(\chi_{\text{io}}, z_{\text{o}}, \tau, t). \tag{3.60}$$

Here one may note that reparameterization (3.58) amounts to the method of dual-time scales that is used toward the asymptotic treatment of differential equations involving "fast" and "slow" processes, see e.g. [64] in the context of nonlinear wave problems and [65] with reference to time-averaged diffusion processes.

3.4.3 "Slow" space variable

Under the quasi-plane wave assumption (3.53), the displacement response of the featured (tissue-like) solid due to focused ultrasound beam is dominated by its axial component, $\hat{\hat{\text{u}}}_z$, as indicated via (3.54). In this setting it can be shown from (3.21), (3.22a), and (3.35)–(3.37) that the balance of linear momentum (3.22b) (that is central to the definition of the ARF) can be written, to the leading order, as

$$\frac{\partial^2 \hat{\hat{\mathrm{u}}}_z}{\partial t^2} - \frac{\partial^2 \hat{\hat{\mathrm{u}}}_z}{\partial z_\mathrm{o}^2} = O(\varepsilon^{\vartheta}), \qquad \vartheta = \min\{1, 2\lambda\}. \tag{3.61}$$

In light of (3.57) and (3.58), wave equation (3.61) now reads

$$\frac{\partial^2 \hat{\boldsymbol{G}}^{\mathrm{u}_z}}{\partial t^2} + 2\varepsilon \frac{\partial^2 \hat{\boldsymbol{G}}^{\mathrm{u}_z}}{\partial t \partial \tau} + \varepsilon^2 \frac{\partial^2 \hat{\boldsymbol{G}}^{\mathrm{u}_z}}{\partial \tau^2} - \frac{\partial^2 \hat{\boldsymbol{G}}^{\mathrm{u}_z}}{\partial z_\mathrm{o}^2} = O(\varepsilon^{\vartheta}), \tag{3.62}$$

where $\hat{\boldsymbol{G}}^{\mathrm{u}_z} = \hat{\hat{\mathrm{u}}}_z$ is the $\hat{\hat{\mathrm{u}}}_z$-component of the state vector $\hat{\boldsymbol{G}}$. An effective way to cancel the $O(1)$-terms in (3.62) and thus aid its $O(\varepsilon)$-asymptotic analysis is to introduce the "slow" axial coordinate

$$\zeta_\mathrm{o} := \varepsilon^{\vartheta} z_\mathrm{o} \tag{3.63}$$

and an assistant function

$$\hat{\boldsymbol{R}}(\chi_\mathrm{io}, \zeta_\mathrm{o}, z_\mathrm{o}, \tau, t) := \hat{\boldsymbol{G}}(\chi_\mathrm{io}, z_\mathrm{o}, \tau, t) = \hat{\boldsymbol{Q}}(\chi_\mathrm{io}, z_\mathrm{o}, t), \tag{3.64}$$

that is subject to the one-way-wave-equation constraint

$$\frac{\partial \hat{\boldsymbol{R}}}{\partial z_\mathrm{o}} = -\frac{\partial \hat{\boldsymbol{R}}}{\partial t}. \tag{3.65}$$

With reference to (3.60) and (3.62), the new function is clearly periodic in "fast" time t, namely

$$\hat{\boldsymbol{R}}(\chi_\mathrm{io}, \zeta_\mathrm{o}, z_\mathrm{o}, \tau, t{+}2\pi) = \hat{\boldsymbol{R}}(\chi_\mathrm{io}, \zeta_\mathrm{o}, z_\mathrm{o}, \tau, t), \tag{3.66}$$

and is such that $\hat{\boldsymbol{R}}^{\mathrm{u}_z} = \hat{\hat{\mathrm{u}}}_z$ satisfies the governing equation

$$2\varepsilon \frac{\partial^2 \hat{\boldsymbol{R}}^{\mathrm{u}_z}}{\partial t \partial \tau} - 2\varepsilon^{\vartheta} \frac{\partial^2 \hat{\boldsymbol{R}}^{\mathrm{u}_z}}{\partial z_\mathrm{o} \partial \zeta_\mathrm{o}} + \varepsilon^2 \frac{\partial^2 \hat{\boldsymbol{R}}^{\mathrm{u}_z}}{\partial \tau^2} - \varepsilon^{2\vartheta} \frac{\partial^2 \hat{\boldsymbol{R}}^{\mathrm{u}_z}}{\partial \zeta_\mathrm{o}^2} = O(\varepsilon^{\vartheta}). \tag{3.67}$$

From (3.67) one may note that the introduction of the "slow" space variable via (3.63) and (3.65), commonly used in deriving the Khokhlov-Zabolotskaya-Kuznetsov (KZK) equation of nonlinear acoustics [7] (under the premises of no modulation and "narrow" beam geometry for which $\lambda = \frac{1}{2} \Rightarrow \vartheta = 1$), helps balance the leading terms as it eliminates the $O(1)$-entries from the balance of linear momentum (3.62).

For clarity of exposition, it is recalled that the "slow" spatiotemporal coordinates in (3.64) are given by

$$\chi_{\rm io} = \varepsilon^{\lambda} x_{\rm io}, \qquad \zeta_{\rm o} = \varepsilon^{\vartheta} z_{\rm o}, \qquad \tau = \varepsilon t, \qquad \lambda = \frac{\log(2\pi f)}{-\log\varepsilon}, \qquad \vartheta = \min\{1, 2\lambda\}, \tag{3.68}$$

where $f \geqslant 1$ is the focal number of the ultrasound beam. A comparison between the argument lists of $\hat{\boldsymbol{R}}$ and $\hat{\boldsymbol{Q}}$ in (3.64) also reveals that $\hat{\boldsymbol{R}}$ splits *both* axial and temporal coordinate into their "slow" i.e. *macro* $(\zeta_{\rm o}, \tau)$ and "fast" i.e. *micro* $(z_{\rm o}, t)$ components. This is in contrast to the treatment of the KZK equation [7] that entails neither splitting nor scaling of the temporal coordinate. Here it is also useful to observe that the scaling of "slow" spatial coordinates $(\chi_{\rm io}, \zeta_{\rm o})$ given by (3.68) is transversely isotropic. This particular feature of the scaled solution is driven by: i) axially-symmetric estimate (3.49) of the width of the focal zone, and ii) "cigar" shape of the focal region, see Figs. 3.2 and A.1.

Eulerian formulation. As indicated earlier, the expression for the ARF is strongly dependent on the choice of the reference frame. To expose the differences between the material and spatial description of the problem, the Lagrangian state vector $\hat{\boldsymbol{R}}$ can alternatively be recast in terms of its Eulerian companion $\boldsymbol{R}$ as

$$\boldsymbol{R}(\chi_{\rm i}, \zeta, z, \tau, t) \;=\; \hat{\boldsymbol{R}}(\chi_{\rm io}, \zeta_{\rm o}, z_{\rm o}, \tau, t), \qquad \chi_{\rm i} = \varepsilon^{\lambda} x_{\rm i}, \quad \zeta = \varepsilon^{\vartheta} z, \quad \tau = \varepsilon t, \tag{3.69}$$

which relates to the Eulerian state vector (3.55) as

$$\boldsymbol{R}(\chi_{\rm i}, \zeta, z, \tau, t) \;=\; \boldsymbol{Q}(\chi_{\rm i}, z, t). \tag{3.70}$$

As shown in Appendix A.3, $\boldsymbol{R}$ preserves the reciprocity and periodicity properties of $\hat{\boldsymbol{R}}$, namely

$$\frac{\partial \boldsymbol{R}}{\partial z} = -\frac{\partial \boldsymbol{R}}{\partial t}, \tag{3.71}$$

and

$$\boldsymbol{R}(\chi_{\rm i}, \zeta, z, \tau, t+2\pi) \;=\; \boldsymbol{R}(\chi_{\rm i}, \zeta, z, \tau, t). \tag{3.72}$$

On the basis of (3.69) and Taylor expansion of $\boldsymbol{R}$ around $(\chi_{\rm io}, \zeta_{\rm o}, z_{\rm o}, \tau, t)$, it is noted for future reference that

$$\begin{aligned} \hat{\boldsymbol{R}}(\chi_{\rm io}, \zeta_{\rm o}, z_{\rm o}, \tau, t) \;&=\; \boldsymbol{R}(\chi_{\rm io} + \varepsilon^{1+2\lambda}\hat{\rm u}_{\rm i},\, \zeta_{\rm o} + \varepsilon^{1+\vartheta}\hat{\hat{\rm u}}_z,\, z_{\rm o} + \varepsilon\hat{\rm u}_z,\, \tau,\, t) \\ &\overset{\varepsilon}{=}\; \boldsymbol{R}(\chi_{\rm io}, \zeta_{\rm o}, z_{\rm o}, \tau, t). \end{aligned} \tag{3.73}$$

3.4.4 “Fast” time averages

With the above definitions, the Eulerian and Lagrangian “fast” time averages of the state vector (3.69) can be respectively introduced as

$$\begin{aligned} \langle \boldsymbol{R} \rangle_{\mathrm{E}}(\chi_{\mathrm{i}}, \zeta, \tau) \ &:= \ \frac{1}{2\pi} \int_{t-\pi}^{t+\pi} \boldsymbol{R}(\chi_{\mathrm{i}}, \zeta, z, \tau, t') \ dt', \\ \langle \hat{\boldsymbol{R}} \rangle_{\mathrm{L}}(\chi_{\mathrm{io}}, \zeta_{\mathrm{o}}, \tau) \ &:= \ \frac{1}{2\pi} \int_{t-\pi}^{t+\pi} \hat{\boldsymbol{R}}(\chi_{\mathrm{io}}, \zeta_{\mathrm{o}}, z_{\mathrm{o}}, \tau, t') \ dt'. \end{aligned} \tag{3.74}$$

To justify the reduced argument list on the left-hand sides of (3.74a) and (3.74b), it is noted using (3.65), (3.66), (3.71) and (3.72) that

$$\begin{aligned} \frac{\partial \langle \boldsymbol{R} \rangle_{\mathrm{E}}}{\partial z} \ &= \ \frac{1}{2\pi} \int_{t-\pi}^{t+\pi} \frac{\partial \boldsymbol{R}}{\partial z}(\chi_{\mathrm{i}}, \zeta, z, \tau, t') \ dt' \ = \ -\frac{1}{2\pi} \int_{t-\pi}^{t+\pi} \frac{\partial \boldsymbol{R}}{\partial t'}(\chi_{\mathrm{i}}, \zeta, z, \tau, t') \ dt' \ = \ 0, \\ \frac{\partial \langle \hat{\boldsymbol{R}} \rangle_{\mathrm{L}}}{\partial z_{\mathrm{o}}} \ &= \ \frac{1}{2\pi} \int_{t-\pi}^{t+\pi} \frac{\partial \hat{\boldsymbol{R}}}{\partial z_{\mathrm{o}}}(\chi_{\mathrm{io}}, \zeta_{\mathrm{o}}, z_{\mathrm{o}}, \tau, t') \ dt' \ = \ -\frac{1}{2\pi} \int_{t-\pi}^{t+\pi} \frac{\partial \hat{\boldsymbol{R}}}{\partial t'}(\chi_{\mathrm{io}}, \zeta_{\mathrm{o}}, z_{\mathrm{o}}, \tau, t') \ dt' \ = \ 0, \end{aligned}$$

and

$$\begin{aligned} \frac{\partial \langle \boldsymbol{R} \rangle_{\mathrm{E}}}{\partial t} &= \frac{1}{2\pi} \Big(\boldsymbol{R}(\chi_{\mathrm{i}}, \zeta, z, \tau, t + \pi) - \boldsymbol{R}(\chi_{\mathrm{i}}, \zeta, z, \tau, t - \pi) \Big) = 0, \\ \frac{\partial \langle \hat{\boldsymbol{R}} \rangle_{\mathrm{L}}}{\partial t} &= \frac{1}{2\pi} \Big(\hat{\boldsymbol{R}}(\chi_{\mathrm{io}}, \zeta_{\mathrm{o}}, z_{\mathrm{o}}, \tau, t + \pi) - \hat{\boldsymbol{R}}(\chi_{\mathrm{io}}, \zeta_{\mathrm{o}}, z_{\mathrm{o}}, \tau, t - \pi) \Big) = 0. \end{aligned}$$

With reference to the instantaneous relationships (3.64) and (3.70), the Eulerian and Lagrangian “fast” time averages of the “mother” state vector $\boldsymbol{Q}(\chi_{\mathrm{i}}, z, t) = \hat{\boldsymbol{Q}}(\chi_{\mathrm{io}}, z_{\mathrm{o}}, t)$ can be computed respectively as

$$\langle \boldsymbol{Q} \rangle_{\mathrm{E}} \ = \ \langle \boldsymbol{R} \rangle_{\mathrm{E}}, \qquad \langle \hat{\boldsymbol{Q}} \rangle_{\mathrm{L}} \ = \ \langle \hat{\boldsymbol{R}} \rangle_{\mathrm{L}}. \tag{3.75}$$

By virtue of (3.70), (3.71), periodicity condition (3.72), and (3.75), the Eulerian time averages of $\partial \boldsymbol{Q}/\partial x_{\mathrm{i}}$, $\partial \boldsymbol{Q}/\partial z$ and $\partial \boldsymbol{Q}/\partial t$ can next be shown to permit respective representations

$$\begin{aligned} \left\langle \frac{\partial \boldsymbol{Q}}{\partial x_{\mathrm{i}}} \right\rangle_{\mathrm{E}} \ &= \ \varepsilon^{\lambda} \left\langle \frac{\partial \boldsymbol{Q}}{\partial \chi_{\mathrm{i}}} \right\rangle_{\mathrm{E}} \ = \ \varepsilon^{\lambda} \left\langle \frac{\partial \boldsymbol{R}}{\partial \chi_{\mathrm{i}}} \right\rangle_{\mathrm{E}} \ = \ \varepsilon^{\lambda} \frac{\partial \langle \boldsymbol{Q} \rangle_{\mathrm{E}}}{\partial \chi_{\mathrm{i}}}, \\ \left\langle \frac{\partial \boldsymbol{Q}}{\partial z} \right\rangle_{\mathrm{E}} \ &= \ \left\langle -\frac{\partial \boldsymbol{R}}{\partial t} + \varepsilon^{\vartheta} \frac{\partial \boldsymbol{R}}{\partial \zeta} \right\rangle_{\mathrm{E}} \ = \ \varepsilon^{\vartheta} \frac{\partial \langle \boldsymbol{R} \rangle_{\mathrm{E}}}{\partial \zeta} \ = \ \varepsilon^{\vartheta} \frac{\partial \langle \boldsymbol{Q} \rangle_{\mathrm{E}}}{\partial \zeta}, \\ \left\langle \frac{\partial \boldsymbol{Q}}{\partial t} \right\rangle_{\mathrm{E}} \ &= \ \left\langle \frac{\partial \boldsymbol{R}}{\partial t} + \varepsilon \frac{\partial \boldsymbol{R}}{\partial \tau} \right\rangle_{\mathrm{E}} \ = \ \varepsilon \frac{\partial \langle \boldsymbol{R} \rangle_{\mathrm{E}}}{\partial \tau} \ = \ \varepsilon \frac{\partial \langle \boldsymbol{Q} \rangle_{\mathrm{E}}}{\partial \tau}. \end{aligned} \tag{3.76}$$

Similarly, the use of (3.64)–(3.66) and (3.75) yields the Lagrangian counterparts of (3.76) as

$$\begin{aligned}
\left\langle \frac{\partial \hat{\boldsymbol{Q}}}{\partial x_{\rm io}} \right\rangle_{\rm L} &= \varepsilon^{\lambda} \left\langle \frac{\partial \hat{\boldsymbol{R}}}{\partial \chi_{\rm io}} \right\rangle_{\rm L} = \varepsilon^{\lambda} \frac{\partial \langle \hat{\boldsymbol{Q}} \rangle_{\rm L}}{\partial \chi_{\rm io}}, \\
\left\langle \frac{\partial \hat{\boldsymbol{Q}}}{\partial z_{\rm o}} \right\rangle_{\rm L} &= \left\langle -\frac{\partial \hat{\boldsymbol{R}}}{\partial t} + \varepsilon^{\vartheta} \frac{\partial \hat{\boldsymbol{R}}}{\partial \zeta_{\rm o}} \right\rangle_{\rm L} = \varepsilon^{\vartheta} \frac{\partial \langle \hat{\boldsymbol{Q}} \rangle_{\rm L}}{\partial \zeta_{\rm o}}, \\
\left\langle \frac{\partial \hat{\boldsymbol{Q}}}{\partial t} \right\rangle_{\rm L} &= \left\langle \frac{\partial \hat{\boldsymbol{R}}}{\partial t} + \varepsilon \frac{\partial \hat{\boldsymbol{R}}}{\partial \tau} \right\rangle_{\rm L} = \varepsilon \frac{\partial \langle \hat{\boldsymbol{Q}} \rangle_{\rm L}}{\partial \tau}.
\end{aligned} \tag{3.77}$$

In what follows, it is shown that the use of the "fast" temporal averages (3.74) is critical for obtaining a meaningful expression for the ARF due to a modulated ultrasound field.

Remark. From (3.74), one may note that the Eulerian and Lagrangian "fast" time averages of any thermomechanical quantity g can be affiliated with respective transformations

$$\begin{aligned}
\langle g(\cdot, z, t) \rangle_{\rm E} &\implies \langle g \rangle_{\rm E}(\cdot, \zeta, \tau), \qquad \zeta = \varepsilon^{\vartheta} z, \quad \tau = \varepsilon t, \\
\langle \hat{g}(\cdot, z_{\rm o}, t) \rangle_{\rm L} &\implies \langle \hat{g} \rangle_{\rm L}(\cdot, \zeta_{\rm o}, \tau), \qquad \zeta_{\rm o} = \varepsilon^{\vartheta} z_{\rm o}, \quad \tau = \varepsilon t,
\end{aligned}$$

where z, $z_{\rm o}$ and t denote the virgin axial and temporal coordinates. Consistent with this observation, all ensuing occurrences of z, $z_{\rm o}$ and t are understood in the sense of *virgin* time and space unless explicitly stated otherwise.

3.5 Acoustic radiation force: plane wave

First, the fundamental case of a plane wave excitation is considered, while the focused geometry is examined later in Section 3.6. The advantage of this one-dimensional case lies in the simplicity, which is not overwhelmed with the long algebraic derivations, but highlights many features of the acoustic radiation force. To this end let

$$\frac{\partial(\cdot)}{\partial x_{\rm i}} = \frac{\partial(\cdot)}{\partial \chi_{\rm i}} = 0, \qquad \tilde{\rm u}_{\rm i} = \tilde{\rm v}_{\rm i} = 0, \qquad \mathfrak{i} = 1, 2, \tag{3.78}$$

so that the ultrasound waves propagate in the positive z direction having only z component of the displacement. Also note that $\vartheta = 1$ (see Section 3.4.3) and $\zeta = \varepsilon z$ for the plane wave case. The constitutive model is taken as for the Newtonian fluid (3.41), and the velocity and mass density perturbations are accordingly chosen as the problem variables. Note, however, that both considered viscoelastic model and Newtonian fluid behave similarly under a plane wave excitation, so that the difference in the description is synthesized only by a choice of problem variables.

3.5.1 Eulerian formulation

To obtain an expression for the ARF due to modulated ultrasound excitation, consider first the balance laws (3.20) which, reduced to the plane-wave problem, read

$$\begin{aligned} \frac{\partial \tilde{\rho}}{\partial t} + \frac{\partial((1+\varepsilon\tilde{\rho})\tilde{v}_z)}{\partial z} &= 0, \\ (1+\varepsilon\tilde{\rho})\left(\frac{\partial \tilde{v}_z}{\partial t} + \frac{1}{2}\varepsilon\frac{\partial \tilde{v}_z^2}{\partial z}\right) &= \frac{\partial \sigma_{zz}}{\partial z}, \\ (1+\varepsilon\tilde{\rho})(1+\varepsilon\tilde{T})\left(\frac{\partial \tilde{S}}{\partial t} + \varepsilon\tilde{v}_z\frac{\partial \tilde{S}}{\partial z}\right) &= -\frac{\partial \tilde{q}_z}{\partial z} + \varepsilon\tilde{J}_{zzzz}\left(\frac{\partial \tilde{v}_z}{\partial z}\right)^2. \end{aligned} \tag{3.79}$$

On taking the "fast" time average (3.74) of (3.79a), one finds that

$$\frac{\partial\langle\tilde{\rho}\rangle_{\mathrm{E}}}{\partial\tau} + \frac{\partial\langle\tilde{j}_z\rangle_{\mathrm{E}}}{\partial\zeta} = 0, \tag{3.80}$$

where

$$\langle\tilde{j}_z\rangle_{\mathrm{E}} := \langle\tilde{v}_z(1+\varepsilon\tilde{\rho})\rangle_{\mathrm{E}} \tag{3.81}$$

is the averaged mass flux. For problems with no acoustic streaming such as that investigated in this study the ARF, hereon denoted by $\tilde{f}_{\mathrm{E}}$, can be defined as the time average of the leading non-linear terms in the balance of linear momentum [5]. For its evaluation, one may employ the expanded constitutive relation (3.41) and compute the "fast" time average of (3.79b) to arrive at the *linearized* balance of linear momentum in terms of $\langle\tilde{j}_z\rangle_{\mathrm{E}}$, $\langle\tilde{\rho}\rangle_{\mathrm{E}}$ and $\langle\tilde{S}\rangle_{\mathrm{E}}$ as

$$\frac{\partial\langle\tilde{j}_z\rangle_{\mathrm{E}}}{\partial\tau} + \frac{\partial\langle\tilde{\rho}\rangle_{\mathrm{E}}}{\partial\zeta} + \varepsilon\frac{\beta_{\mathrm{T}}}{\mathrm{c_p}}\frac{\partial\langle\tilde{S}\rangle_{\mathrm{E}}}{\partial\zeta} = \tilde{f}_z^{\mathrm{E}}, \tag{3.82}$$

where

$$\tilde{f}_z^{\mathrm{E}} \overset{\varepsilon^2}{=} \left\langle \tilde{v}_z\frac{\partial\tilde{\rho}}{\partial t} - \frac{1}{2}(1+\varepsilon\tilde{\rho})\frac{\partial\tilde{v}_z^2}{\partial z} - (\beta-1)\frac{\partial\tilde{\rho}^2}{\partial z}\right\rangle_{\mathrm{E}} \tag{3.83}$$

is the sought acoustic radiation force. In what follows, it will be shown that $\langle\tilde{j}_z\rangle_{\mathrm{E}}$, $\langle\tilde{\rho}\rangle_{\mathrm{E}}$ and $\tilde{f}_z^{\mathrm{E}}$ are all $O(\varepsilon)$ whereas the averaged entropy perturbation, $\langle\tilde{S}\rangle_{\mathrm{E}}$, is $O(1)$ which is the reason for retaining the entropy term in (3.82). By virtue of (3.79a), the ARF (3.83) can be rewritten as

$$\begin{aligned} \tilde f_z^{\mathrm{E}} &\overset{\varepsilon^2}{=} \left\langle \tilde v_z \left(-\frac{\partial \tilde v_z}{\partial z} - \varepsilon \frac{\partial(\tilde\rho \tilde v_z)}{\partial z} \right) - \frac{1}{2}(1+\varepsilon\tilde\rho)\frac{\partial \tilde v_z^2}{\partial z} - (\beta-1)\frac{\partial \tilde\rho^2}{\partial z} \right\rangle_{\mathrm{E}} \\ &\overset{\varepsilon^2}{=} -\varepsilon\, \frac{\partial \langle \tilde v_z^2\rangle_{\mathrm{E}}}{\partial \zeta} - \varepsilon(\beta-1)\, \frac{\partial \langle \tilde\rho^2\rangle_{\mathrm{E}}}{\partial \zeta}, \end{aligned} \tag{3.84}$$

which demonstrates that $\tilde f_z^{\mathrm{E}}$ is indeed $O(\varepsilon)$. On exercising the relationship

$$\tilde v_z \overset{\varepsilon}{=} \tilde\rho, \tag{3.85}$$

established in Appendix A.5 for the problem under consideration, one may further reduce (3.84) to

$$\tilde f_z^{\mathrm{E}} \overset{\varepsilon^2}{=} -\varepsilon\, \beta\, \frac{\partial \tilde I_{\mathrm{E}}}{\partial \zeta},$$

where

$$\tilde I_{\mathrm{E}}(\tau,\zeta) \;:=\; \langle \tilde\rho^2\rangle_{\mathrm{E}} \overset{\varepsilon}{=} \langle \tilde p\, \tilde v_z\rangle_{\mathrm{E}}, \tag{3.86}$$

is an $O(1)$-approximation of the *intensity* of the ultrasound beam.

To close the system of equations in terms of $\langle \tilde j_z\rangle_{\mathrm{E}}$, $\langle \tilde\rho\rangle_{\mathrm{E}}$ and $\langle \tilde S\rangle_{\mathrm{E}}$, the "fast" time average of the balance of energy (3.79c) can be computed as

$$\varepsilon \frac{\partial \langle \tilde S\rangle_{\mathrm{E}}}{\partial \tau} + \varepsilon \left\langle \tilde v_z \frac{\partial \tilde S}{\partial z} \right\rangle_{\mathrm{E}} \overset{\varepsilon^2}{=} -\varepsilon\tilde\kappa \left\langle (\tilde\rho + \tilde T)\frac{\partial^2 \tilde T}{\partial z^2} \right\rangle_{\mathrm{E}} + \varepsilon\Big(\tilde\mu_{\mathrm{B}} + \tfrac{4}{3}\tilde\mu\Big) \left\langle \left(\frac{\partial \tilde v_z}{\partial z}\right)^2 \right\rangle_{\mathrm{E}}, \tag{3.87}$$

The convection term on the left-hand side of (3.87) can be transformed via (3.79a) and (3.79c) as

$$\left\langle \tilde v_z \frac{\partial \tilde S}{\partial z} \right\rangle_{\mathrm{E}} \overset{\varepsilon}{=} -\left\langle \frac{\partial \tilde v_z}{\partial z} \tilde S \right\rangle_{\mathrm{E}} \overset{\varepsilon}{=} \left\langle \frac{\partial \tilde\rho}{\partial t} \tilde S \right\rangle_{\mathrm{E}} \overset{\varepsilon}{=} -\left\langle \tilde\rho \frac{\partial \tilde S}{\partial t} \right\rangle_{\mathrm{E}} \overset{\varepsilon}{=} -\tilde\kappa \left\langle \tilde\rho \frac{\partial^2 \tilde T}{\partial z^2} \right\rangle_{\mathrm{E}},$$

which reduces (3.176) to

$$\frac{\partial \langle \tilde S\rangle_{\mathrm{E}}}{\partial \tau} \overset{\varepsilon}{=} -\tilde\kappa \left\langle \tilde T \frac{\partial^2 \tilde T}{\partial z^2} \right\rangle_{\mathrm{E}} + \Big(\tilde\mu_{\mathrm{B}} + \tfrac{4}{3}\tilde\mu\Big) \left\langle \left(\frac{\partial \tilde v_z}{\partial z}\right)^2 \right\rangle_{\mathrm{E}}. \tag{3.88}$$

Similarly, the first term on the right side of (3.88) can be simplified via (3.26), (3.93) and (3.85) as

$$\frac{\mathrm{c}_{\mathrm{P}}^2}{\beta_{\mathrm{T}}^2} \left\langle \tilde T \frac{\partial^2 \tilde T}{\partial z^2} \right\rangle_{\mathrm{E}} \overset{\varepsilon}{=} \left\langle \tilde\rho \frac{\partial^2 \tilde\rho}{\partial z^2} \right\rangle_{\mathrm{E}} \overset{\varepsilon}{=} \left\langle \tilde v_z \frac{\partial^2 \tilde v_z}{\partial z^2} \right\rangle_{\mathrm{E}} \overset{\varepsilon}{=} -\left\langle \left(\frac{\partial \tilde v_z}{\partial z}\right)^2 \right\rangle_{\mathrm{E}},$$

which, by way of (3.79a), allows one to reduce the averaged energy balance as

$$\frac{\partial\langle\tilde{S}\rangle_{\mathrm{E}}}{\partial\tau} \overset{\varepsilon}{=} \tilde{\delta}\tilde{I}^{*}_{\mathrm{E}}, \qquad \tilde{I}^{*}_{\mathrm{E}} = \left\langle\left(\frac{\partial\tilde{\rho}}{\partial t}\right)^{2}\right\rangle_{\mathrm{E}}, \tag{3.89}$$

where

$$\tilde{\delta} \;:=\; \tilde{\mu}_{\mathrm{B}} + \frac{4}{3}\tilde{\mu} + \tilde{\kappa}\frac{\beta_{\mathrm{T}}^{2}}{\mathrm{c}_{\mathrm{p}}^{2}}$$

is the so-called *diffusivity of sound* [7] which signifies dissipation of acoustic waves due to viscosity and heat conduction. As can be seen from (3.89), the entropy fluctuation is $O(1)$ as postulated earlier. From this result, an earlier observation that $\tilde{f}^{\mathrm{E}}_{z}$ is $O(\varepsilon)$, and the fact that the effective excitation to the linear system (3.80) and (3.82) (with homogeneous boundary conditions) is given by $\tilde{f}^{\mathrm{E}}_{z} - \varepsilon\frac{\beta_{\mathrm{T}}}{\mathrm{c}_{\mathrm{p}}}\partial\langle\tilde{S}\rangle_{\mathrm{E}}/\partial\zeta$, one finds that $\langle\tilde{j}_{z}\rangle_{\mathrm{E}}$ and $\langle\tilde{\rho}\rangle_{\mathrm{E}}$ are indeed $O(\varepsilon)$.

Initial-boundary value problem

To summarize, the "fast" time averages of the nonlinear balance equations (3.79) can be reduced to the linear system

$$\begin{aligned}
\frac{\partial\langle\tilde{\rho}\rangle_{\mathrm{E}}}{\partial\tau} + \frac{\partial\langle\tilde{j}_{z}\rangle_{\mathrm{E}}}{\partial\zeta} \;&=\; 0,\\
\frac{\partial\langle\tilde{j}_{z}\rangle_{\mathrm{E}}}{\partial\tau} + \frac{\partial\langle\tilde{\rho}\rangle_{\mathrm{E}}}{\partial\zeta} + \varepsilon\frac{\beta_{\mathrm{T}}}{\mathrm{c}_{\mathrm{p}}}\frac{\partial\langle\tilde{S}\rangle_{\mathrm{E}}}{\partial\zeta} \;&\overset{\varepsilon^{2}}{=}\; -\,\varepsilon\beta\,\frac{\partial\tilde{I}_{\mathrm{E}}}{\partial\zeta},\\
\frac{\partial\langle\tilde{S}\rangle_{\mathrm{E}}}{\partial\tau} \;&\overset{\varepsilon}{=}\; \tilde{\delta}\tilde{I}^{*}_{\mathrm{E}},
\end{aligned} \tag{3.90}$$

in terms of $\langle\tilde{\rho}\rangle_{\mathrm{E}}$, $\langle\tilde{j}_{z}\rangle_{\mathrm{E}}$ and $\langle\tilde{S}\rangle_{\mathrm{E}}$, assuming that $\tilde{I}_{\mathrm{E}}$ and $\tilde{I}^{*}_{\mathrm{E}}$ can be computed *a priori* – a hypothesis that will be dealt with in Section 3.5.4. A salient feature of (3.90) is that $\langle\tilde{S}\rangle_{\mathrm{E}}$ is only *semi-coupled* with the rest of the system in that (3.90c), given $\tilde{I}^{*}_{\mathrm{E}}$, can be solved independently as an initial value problem. With the solution for $\langle\tilde{S}\rangle_{\mathrm{E}}$ at hand, (3.90a) and (3.90b) can be deemed to form a closed system in terms of $\langle\tilde{\rho}\rangle_{\mathrm{E}}$ and $\langle\tilde{j}_{z}\rangle_{\mathrm{E}}$ whose treatment, beyond the quiescent-past hypothesis, requires appropriate (mechanical) boundary conditions that are established next.

Equations(3.90a) and (3.90b) are accompanied by the radiation condition at infinity i.e.

$$\frac{\partial\langle\tilde{\rho}\rangle_{\mathrm{E}}}{\partial\tau} = -\frac{\partial\langle\tilde{\rho}\rangle_{\mathrm{E}}}{\partial\zeta}, \qquad \zeta\to\infty, \tag{3.91}$$

which ensures that the solution propagates in the positive ζ-direction. Since the "left" boundary condition (3.46) (reduced to a planar transducer) at the transducer boundary is inherently given in Lagrangian coordinates, its "fast" time average can be written as

$$\langle \tilde{v}_z \rangle_{\mathrm{L}}(\tau, 0) \;=\; \varepsilon \frac{\partial \langle \tilde{u}_z \rangle_{\mathrm{L}}}{\partial \tau}(\tau, 0) \;=\; 0. \tag{3.92}$$

To express (3.92) in terms of $\langle \tilde{j}_z \rangle_{\mathrm{E}}$, one finds from the plane-wave balance of mass (3.4) that

$$1 + \varepsilon \tilde{\rho} \;=\; \frac{\partial z_{\mathrm{o}}}{\partial z} \;=\; 1 - \varepsilon \frac{\partial \tilde{u}_z}{\partial z} \quad\Longrightarrow\quad \tilde{\rho} \;=\; -\frac{\partial \tilde{u}_z}{\partial z}, \tag{3.93}$$

whereby the averaged mass flux becomes

$$\langle \tilde{j}_z \rangle_{\mathrm{E}} \overset{\varepsilon^2}{=} \left\langle \frac{\partial \tilde{u}_z}{\partial t} + \varepsilon \tilde{v}_z \frac{\partial \tilde{u}_z}{\partial z} + \varepsilon \tilde{v}_z \tilde{\rho} \right\rangle_{\mathrm{E}} \overset{\varepsilon^2}{=} \varepsilon \frac{\partial \langle \tilde{u}_z \rangle_{\mathrm{E}}}{\partial \tau}. \tag{3.94}$$

To establish the connection between the Eulerian and Lagrangian "fast" time averages, one may note with reference to (3.71)–(3.75) and relationships $z = z_{\mathrm{o}} + \varepsilon \hat{\tilde{u}}_z$ and $\zeta = \zeta_{\mathrm{o}} + \varepsilon^2 \hat{\tilde{u}}_z$ that

$$\begin{aligned}
\langle \tilde{u}_z \rangle_{\mathrm{L}}(\tau, \zeta_{\mathrm{o}}) \;&:=\; \frac{1}{2\pi} \int_{t-\pi}^{t+\pi} \hat{R}^{u_z}(t', z_{\mathrm{o}}, \tau, \zeta_{\mathrm{o}}) \; dt' \\
&=\; \frac{1}{2\pi} \int_{t-\pi}^{t+\pi} R^{u_z}\big(t', z_{\mathrm{o}} + \varepsilon \hat{R}^{u_z}(t', z_{\mathrm{o}}, \tau, \zeta_{\mathrm{o}}), \tau, \zeta_{\mathrm{o}} + \varepsilon^2 \hat{R}^{u_z}(t', z_{\mathrm{o}}, \tau, \zeta_{\mathrm{o}})\big) \; dt' \\
&\overset{\varepsilon^2}{=}\; \langle \tilde{u}_z \rangle_{\mathrm{E}}(\tau, \zeta_{\mathrm{o}}) + \frac{\varepsilon}{2\pi} \int_{t-\pi}^{t+\pi} \frac{\partial R^{u_z}}{\partial z}(t', z_{\mathrm{o}}, \tau, \zeta_{\mathrm{o}}) \, \hat{R}^{u_z}(t', z_{\mathrm{o}}, \tau, \zeta_{\mathrm{o}}) \; dt' \qquad (3.95) \\
&\overset{\varepsilon^2}{=}\; \langle \tilde{u}_z \rangle_{\mathrm{E}}(\tau, \zeta_{\mathrm{o}}) - \frac{\varepsilon}{4\pi} \int_{t-\pi}^{t+\pi} \frac{\partial (R^{u_z})^2}{\partial t'}(t', z_{\mathrm{o}}, \tau, \zeta_{\mathrm{o}}) \; dt' \;\overset{\varepsilon^2}{=}\; \langle \tilde{u}_z \rangle_{\mathrm{E}}(\tau, \zeta_{\mathrm{o}}),
\end{aligned}$$

where $\langle \tilde{u}_z \rangle_{\mathrm{E}}(\tau, \zeta_{\mathrm{o}})$ signifies $\langle \tilde{u}_z \rangle_{\mathrm{E}}(\tau, \zeta = \zeta_{\mathrm{o}})$, and $\partial R^{u_z}/\partial z$ indicates differentiation with respect to the second argument. In a similar fashion it can be shown that $\langle \tilde{v}_z \rangle_{\mathrm{L}} \overset{\varepsilon^2}{=} \langle \tilde{v}_z \rangle_{\mathrm{E}} + \varepsilon \tilde{I}_{\mathrm{E}}$, which is consistent with the result in [6] exposing the difference between the Lagrangian and Eulerian mean velocities due to time-harmonic plane wave. On the basis of (3.94) and (3.95), (3.92) can now be rewritten as

$$\langle \tilde{j}_z \rangle_{\mathrm{E}}(\tau, 0) \;\overset{\varepsilon^2}{=}\; \varepsilon \frac{\partial \langle \tilde{u}_z \rangle_{\mathrm{L}}}{\partial \tau}(\tau, 0) \;\overset{\varepsilon^2}{=}\; 0, \tag{3.96}$$

which is the "left" boundary condition for (3.90a) and (3.90b). In concluding this section, it is noted by comparing (3.90) to (3.79) that the zero-heat-flux boundary condition (3.47) is not required for the computation of the "fast" time averages $\langle \tilde{\rho} \rangle_{\mathrm{E}}$, $\langle \tilde{j}_z \rangle_{\mathrm{E}}$

and $\langle\tilde{S}\rangle_{\text{E}}$ owing to the particular (semi-coupled) structure of (3.90). In Section 3.5.5, however, this thermal boundary condition will be required (and used) toward the numerical solution of the "mother" nonlinear system (3.79), employed as a tool to verify the proposed developments.

Eulerian intensity

In dealing with the initial-boundary value problem specified by (3.90)–(3.91), (3.96), and the quiescent-past condition, the question remains how to compute the $O(1)$-distribution of the ultrasound intensity (3.86) and its companion $\tilde{I}_{\text{E}}^{*}$, see (3.89), which furnish excitation for the problem. In general the latter task entails the knowledge of the plane-wave solution, in terms of $\tilde{\rho}$, to the "mother" nonlinear problem governed by (3.79). For the purpose of computing the radiation force, the latter solution is typically approximated via its leading *linear* term [7]. In certain situations, however, the computation of $\tilde{I}_{\text{E}}$ and $\tilde{I}_{\text{E}}^{*}$ can be further simplified by employing an auxiliary differential relationship that is established next.

On multiplying (3.79a) and (3.79b) respectively by $\tilde{v}_z$ and $\tilde{\rho}$, one finds

$$\begin{aligned}
\tilde{v}_z\frac{\partial\tilde{\rho}}{\partial t}+\tilde{v}_z\frac{\partial\tilde{v}_z}{\partial z} &= -\,\varepsilon\tilde{v}_z\frac{\partial(\tilde{\rho}\tilde{v}_z)}{\partial z},\\
\tilde{\rho}\frac{\partial\tilde{v}_z}{\partial t}+\tilde{\rho}\frac{\partial\tilde{\rho}}{\partial z} &\overset{\varepsilon^2}{=} -\,\varepsilon\tilde{\rho}(\beta-1)\frac{\partial\tilde{\rho}^2}{\partial z}-\varepsilon\frac{\beta_{\text{T}}}{\text{c}_{\text{p}}}\tilde{\rho}\frac{\partial\tilde{S}}{\partial z}+\varepsilon\Big(\tilde{\mu}_{\text{B}}+\tfrac{4}{3}\tilde{\mu}\Big)\tilde{\rho}\frac{\partial^2\tilde{v}_z}{\partial z^2}.
\end{aligned}\tag{3.97}$$

By virtue of (3.85), the summation of (3.97a) and (3.97b) gives

$$\frac{\partial(\tilde{\rho}\,\tilde{v}_z)}{\partial t}+\frac{1}{2}\frac{\partial(\tilde{\rho}^2+\tilde{v}_z^2)}{\partial z} \overset{\varepsilon^2}{=} -\frac{2\varepsilon}{3}\beta\frac{\partial\tilde{\rho}^3}{\partial z}-\varepsilon\frac{\beta_{\text{T}}}{\text{c}_{\text{p}}}\tilde{\rho}\frac{\partial\tilde{S}}{\partial z}+\varepsilon\Big(\tilde{\mu}_{\text{B}}+\tfrac{4}{3}\tilde{\mu}\Big)\tilde{\rho}\frac{\partial^2\tilde{\rho}}{\partial z^2}.\tag{3.98}$$

On the basis of (3.79a) and (3.79b), it can be shown that

$$\Big\langle\tilde{\rho}\frac{\partial^2\tilde{\rho}}{\partial z^2}\Big\rangle_{\text{E}}\overset{\varepsilon}{=}-\Big\langle\tilde{\rho}\frac{\partial^2\tilde{v}_z}{\partial t\partial z}\Big\rangle_{\text{E}}\overset{\varepsilon}{=}\Big\langle\tilde{\rho}\frac{\partial^2\tilde{\rho}}{\partial t^2}\Big\rangle_{\text{E}}\overset{\varepsilon}{=}\Big\langle\frac{\partial}{\partial t}\Big(\tilde{\rho}\frac{\partial\tilde{\rho}}{\partial t}\Big)\Big\rangle_{\text{E}}-\Big\langle\Big(\frac{\partial\tilde{\rho}}{\partial t}\Big)^2\Big\rangle_{\text{E}}\overset{\varepsilon}{=}-\Big\langle\Big(\frac{\partial\tilde{\rho}}{\partial t}\Big)^2\Big\rangle_{\text{E}}.\tag{3.99}$$

Similarly from (3.26), (3.93), (3.79b), (3.79c), (3.85) and (3.99) one finds

$$\begin{aligned}
\Big\langle\tilde{\rho}\frac{\partial\tilde{S}}{\partial z}\Big\rangle_{\text{E}} &\overset{\varepsilon}{=} -\Big\langle\frac{\partial\tilde{\rho}}{\partial z}\tilde{S}\Big\rangle_{\text{E}} \overset{\varepsilon}{=} \Big\langle\frac{\partial\tilde{v}_z}{\partial t}\tilde{S}\Big\rangle_{\text{E}} \overset{\varepsilon}{=} -\Big\langle\tilde{v}_z\frac{\partial\tilde{S}}{\partial t}\Big\rangle_{\text{E}}\\
&\overset{\varepsilon}{=} -\tilde{\kappa}\Big\langle\tilde{v}_z\frac{\partial^2\tilde{T}}{\partial z^2}\Big\rangle_{\text{E}} \overset{\varepsilon}{=} -\tilde{\kappa}\frac{\beta_{\text{T}}}{\text{c}_{\text{p}}}\Big\langle\tilde{\rho}\frac{\partial^2\tilde{\rho}}{\partial z^2}\Big\rangle_{\text{E}} \overset{\varepsilon}{=} \tilde{\kappa}\frac{\beta_{\text{T}}}{\text{c}_{\text{p}}}\Big\langle\Big(\frac{\partial\tilde{\rho}}{\partial t}\Big)^2\Big\rangle_{\text{E}},
\end{aligned}\tag{3.100}$$

whereby the Eulerian time average of (3.98) reduces to

$$\frac{\partial \tilde{I}_{\mathrm{E}}}{\partial \tau} + \frac{\partial \tilde{I}_{\mathrm{E}}}{\partial \zeta} + \tilde{\delta} \tilde{I}^{*}_{\mathrm{E}} \overset{\varepsilon}{=} 0, \qquad \tilde{I}_{\mathrm{E}} := \langle \tilde{\rho}^{2} \rangle_{\mathrm{E}}, \qquad \tilde{I}^{*}_{\mathrm{E}} := \left\langle \left(\frac{\partial \tilde{\rho}}{\partial t} \right)^{2} \right\rangle_{\mathrm{E}}. \tag{3.101}$$

For completeness, governing equation (3.101) can now be complemented by the the quiescent-past hypothesis and, with the use of (3.46) and (3.85), the boundary condition

$$\tilde{I}_{\mathrm{E}}(\tau, 0) \overset{\varepsilon}{=} \tfrac{1}{2} \mathcal{M}^{2}(\tau). \tag{3.102}$$

In Section 3.5.4, (3.101) and (3.102) will be used to obtain an explicit expression for $\tilde{I}_{\mathrm{E}}$ and $\tilde{I}^{*}_{\mathrm{E}}$, and consequently the analytical solution to (3.90) in strongly dissipative fluids.

3.5.2 Lagrangian formulation

To obtain the counterpart of (3.90)–(3.91) and (3.96) in the Lagrangian frame of reference, consider the balance laws (3.22) which, reduced to the plane-wave problem, read

$$\begin{aligned} 1 + \varepsilon \hat{\hat{\rho}} &= \Big(1 + \varepsilon \frac{\partial \hat{\hat{u}}_{z}}{\partial z_{\mathrm{o}}} \Big)^{-1}, \\ \frac{\partial \hat{\hat{v}}_{z}}{\partial t} &= \frac{\partial \hat{\hat{P}}_{zz}}{\partial z_{\mathrm{o}}}, \\ \Big(1 + \varepsilon \hat{\hat{T}} \Big) \frac{\partial \hat{\hat{S}}}{\partial t} &= -\frac{\partial \hat{\hat{q}}_{z}}{\partial z_{\mathrm{o}}} + \varepsilon (1 + \varepsilon \hat{\hat{\rho}}) \hat{\hat{J}}_{zzzz} \Big(\frac{\partial \hat{\hat{v}}_{z}}{\partial z_{\mathrm{o}}} \Big)^{2}. \end{aligned} \tag{3.103}$$

Expansion of (3.103a) in Taylor series yields

$$1 + \varepsilon \hat{\hat{\rho}} \overset{\varepsilon^{4}}{=} 1 - \varepsilon \frac{\partial \hat{\hat{u}}_{z}}{\partial z_{\mathrm{o}}} + \Big(\varepsilon \frac{\partial \hat{\hat{u}}_{z}}{\partial z_{\mathrm{o}}} \Big)^{2} - \Big(\varepsilon \frac{\partial \hat{\hat{u}}_{z}}{\partial z_{\mathrm{o}}} \Big)^{3}. \tag{3.104}$$

On differentiating (3.104) with respect to time and taking the Lagrangian "fast"-time average (3.74) of the resulting expression, one finds via (3.93) that

$$\frac{\partial \langle \tilde{\rho} \rangle_{\mathrm{L}}}{\partial \tau} + \frac{\partial \langle \tilde{v}_{z} \rangle_{\mathrm{L}}}{\partial \zeta_{\mathrm{o}}} \overset{\varepsilon^{2}}{=} \varepsilon \frac{\partial \tilde{I}_{\mathrm{L}}}{\partial \tau}, \qquad \tilde{I}_{\mathrm{L}} \;;=\; \langle \tilde{\rho}^{2} \rangle_{\mathrm{L}} \tag{3.105}$$

Similarly, the averaging of (3.103b) aided by (3.85) yields

$$\frac{\partial \langle \tilde{v}_{z} \rangle_{\mathrm{L}}}{\partial \tau} + \frac{\partial \langle \tilde{\rho} \rangle_{\mathrm{L}}}{\partial \zeta_{\mathrm{o}}} + \varepsilon \frac{\beta_{\mathrm{T}}}{\mathrm{c_p}} \frac{\partial \langle \tilde{S} \rangle_{\mathrm{L}}}{\partial \zeta_{\mathrm{o}}} = \tilde{f}^{\mathrm{L}}_{z}, \tag{3.106}$$

where

$$\tilde{f}_z^{\mathrm{L}} \overset{\varepsilon^2}{=} -\varepsilon(\beta-1)\frac{\partial \tilde{I}_{\mathrm{L}}}{\partial \zeta_{\mathrm{o}}}$$

is the sought ARF computed in the Lagrangian frame of reference. Analogous to the comment made earlier in the context of the Eulerian formulation, it is noted that the entropy term is retained in (3.106) for $\langle\tilde{S}\rangle_{\mathrm{L}}$ is $O(1)$ whereas $\langle\tilde{v}_z\rangle_{\mathrm{L}}, \langle\tilde{\rho}\rangle_{\mathrm{L}}$ and $\tilde{f}_z^{\mathrm{L}}$ are $O(\varepsilon)$ when $\varepsilon \ll 1$.

With reference to (3.105) and (3.106), the linearized system of governing equations in terms of $\langle\tilde{v}_z\rangle_{\mathrm{L}}$, $\langle\tilde{\rho}\rangle_{\mathrm{L}}$ and $\langle\tilde{S}\rangle_{\mathrm{L}}$ can now be closed by averaging (3.103c) which, by way of (3.103a), yields

$$\varepsilon\frac{\partial\langle\tilde{S}\rangle_{\mathrm{L}}}{\partial\tau} \overset{\varepsilon^2}{=} -\varepsilon\tilde{\kappa}\Big\langle \hat{\tilde{T}}\frac{\partial^2\hat{\tilde{T}}}{\partial z_{\mathrm{o}}^2}\Big\rangle_{\mathrm{L}} + \varepsilon\Big(\tilde{\mu}_{\mathrm{B}} + \tfrac{4}{3}\tilde{\mu}\Big)\Big\langle\Big(\frac{\partial\hat{\tilde{\rho}}}{\partial t}\Big)^2\Big\rangle_{\mathrm{L}}. \tag{3.107}$$

On the basis of (3.26), (3.93), (3.85) and (3.103a), one can show that

$$\frac{\mathrm{c}_{\mathrm{p}}^2}{\beta_{\mathrm{T}}^2}\Big\langle \hat{\tilde{T}}\frac{\partial^2\hat{\tilde{T}}}{\partial z_{\mathrm{o}}^2}\Big\rangle_{\mathrm{L}} \overset{\varepsilon}{=} \Big\langle \hat{\tilde{\rho}}\frac{\partial^2\hat{\tilde{\rho}}}{\partial z_{\mathrm{o}}^2}\Big\rangle_{\mathrm{L}} \overset{\varepsilon}{=} \Big\langle \hat{\tilde{v}}_z\frac{\partial^2\hat{\tilde{v}}_z}{\partial z_{\mathrm{o}}^2}\Big\rangle_{\mathrm{L}} \overset{\varepsilon}{=} -\Big\langle\Big(\frac{\partial\hat{\tilde{v}}_z}{\partial z_{\mathrm{o}}}\Big)^2\Big\rangle_{\mathrm{L}} \overset{\varepsilon}{=} -\Big\langle\Big(\frac{\partial\hat{\tilde{\rho}}}{\partial t}\Big)^2\Big\rangle_{\mathrm{L}},$$

which reduces (3.107) to

$$\frac{\partial\langle\tilde{S}\rangle_{\mathrm{L}}}{\partial\tau} \overset{\varepsilon}{=} \tilde{\delta}\tilde{I}_{\mathrm{L}}^*, \qquad \tilde{I}_{\mathrm{L}}^* := \Big\langle\Big(\frac{\partial\hat{\tilde{\rho}}}{\partial t}\Big)^2\Big\rangle_{\mathrm{L}}.$$

Initial-boundary value problem

Consistent with earlier discussion, the featured linear system

$$\begin{aligned}
\frac{\partial\langle\tilde{\rho}\rangle_{\mathrm{L}}}{\partial\tau} + \frac{\partial\langle\tilde{v}_z\rangle_{\mathrm{L}}}{\partial\zeta_{\mathrm{o}}} &\overset{\varepsilon^2}{=} \varepsilon\frac{\partial\tilde{I}_{\mathrm{L}}}{\partial\tau},\\
\frac{\partial\langle\tilde{v}_z\rangle_{\mathrm{L}}}{\partial\tau} + \frac{\partial\langle\tilde{\rho}\rangle_{\mathrm{L}}}{\partial\zeta_{\mathrm{o}}} + \varepsilon\frac{\beta_{\mathrm{T}}}{\mathrm{c}_{\mathrm{p}}}\frac{\partial\langle\tilde{S}\rangle_{\mathrm{L}}}{\partial\zeta_{\mathrm{o}}} &\overset{\varepsilon^2}{=} -\varepsilon(\beta-1)\frac{\partial\tilde{I}_{\mathrm{L}}}{\partial\zeta_{\mathrm{o}}},\\
\frac{\partial\langle\tilde{S}\rangle_{\mathrm{L}}}{\partial\tau} &\overset{\varepsilon}{=} \tilde{\delta}\tilde{I}_{\mathrm{L}}^*,
\end{aligned} \tag{3.108}$$

in terms of $\langle\tilde{\rho}\rangle_{\mathrm{L}}$, $\langle\tilde{v}_z\rangle_{\mathrm{L}}$ and $\langle\tilde{S}\rangle_{\mathrm{L}}$, is next complemented by the radiation condition

$$\frac{\partial\langle\tilde{\rho}\rangle_{\mathrm{L}}}{\partial\tau} = -\frac{\partial\langle\tilde{\rho}\rangle_{\mathrm{L}}}{\partial\zeta_{\mathrm{o}}}, \qquad \zeta_{\mathrm{o}}\to\infty, \tag{3.109}$$

which precludes waves incoming from infinity, and the "left" boundary condition

$$\langle \tilde{v}_z \rangle_{\mathrm{L}}(\tau, 0) \;=\; 0, \tag{3.110}$$

as given by (3.92).

To facilitate the comparison between the Eulerian formulation (3.90)and its Lagrangian counterpart (3.108), one may note by employing the reciprocity condition (3.71) and Taylor-series transformation as in (3.95) that

$$\langle \tilde{\rho} \rangle_{\mathrm{L}} \overset{\varepsilon^2}{=} \langle \tilde{\rho} \rangle_{\mathrm{E}} + \varepsilon \tilde{I}_{\mathrm{L}}, \qquad \langle \tilde{v}_z \rangle_{\mathrm{L}} \overset{\varepsilon^2}{=} \langle \tilde{j}_z \rangle_{\mathrm{E}}, \qquad \langle \tilde{S} \rangle_{\mathrm{L}} \overset{\varepsilon}{=} \langle \tilde{S} \rangle_{\mathrm{E}}, \tag{3.111}$$

recalling the fact that $\langle \tilde{\rho} \rangle_{\mathrm{L}}$, $\langle \tilde{v}_z \rangle_{\mathrm{L}}$, $\langle \tilde{\rho} \rangle_{\mathrm{E}}$ and $\langle \tilde{j}_z \rangle_{\mathrm{E}}$ are all $O(\varepsilon)$, while $\langle \tilde{S} \rangle_{\mathrm{L}}$ and $\langle \tilde{S} \rangle_{\mathrm{E}}$ are $O(1)$.

Lagrangian intensity

The above developments can be concluded by noting, again via (3.71) and manipulation as in (3.95) that

$$\tilde{I}_{\mathrm{L}} \;\overset{\varepsilon}{=}\; \tilde{I}_{\mathrm{E}}, \qquad \tilde{I}^*_{\mathrm{L}} \;\overset{\varepsilon}{=}\; \tilde{I}^*_{\mathrm{E}}. \tag{3.112}$$

Substitution of the above relationship into (3.101), together with the fact that $\partial\zeta_{\mathrm{o}}/\partial\zeta = 1+O(\varepsilon^2)$, immediately yields the differential relationship

$$\frac{\partial \tilde{I}_{\mathrm{L}}}{\partial \tau} + \frac{\partial \tilde{I}_{\mathrm{L}}}{\partial \zeta_{\mathrm{o}}} + \tilde{\delta} \tilde{I}^*_{\mathrm{L}} \overset{\varepsilon}{=} 0, \qquad \tilde{I}_{\mathrm{L}} \;:=\; \langle \tilde{\rho}^2 \rangle_{\mathrm{L}}, \qquad \tilde{I}^*_{\mathrm{L}} := \left\langle \left(\frac{\partial \hat{\tilde{\rho}}}{\partial t} \right)^2 \right\rangle_{\mathrm{L}}. \tag{3.113}$$

Similar to the remark made earlier, (3.113) can be used to obtain an explicit expression for $\tilde{I}_{\mathrm{L}}$ and $\tilde{I}^*_{\mathrm{L}}$, and consequently the analytical solution to (3.108) in highly dissipative fluids.

3.5.3 Comments on the solution

As exemplified via Eulerian formulation (3.90) the ARF can be defined, for problems precluding acoustic streaming, as an effective body force synthesizing the non-linear effects within the framework of a linearized system written in terms of suitable time-averaged acoustic quantities. As demonstrated in [5], the same definition can be extended to problems involving the *initiation* of acoustic streaming where the streaming and thus averaged velocities are sufficiently small. Synthesizing the treatment of the latter class of problems which assumes *non-modulated* ultrasound excitation [5, 39] one finds, using the present framework of analysis and Eulerian description, that the one-dimensional balance of linear momentum permits representation

$$\frac{\partial\langle\tilde{j}_z\rangle_{\mathrm{E}}}{\partial\tau}+\frac{\partial\langle\tilde{p}\rangle_{\mathrm{E}}}{\partial\zeta}\overset{\varepsilon^2}{=}\varepsilon\tilde{\delta}\tilde{I}^*_{\mathrm{E}}, \tag{3.114}$$

in terms of the averaged mass flux and pressure perturbations, $\langle\tilde{j}_z\rangle_{\mathrm{E}}$ and $\langle\tilde{p}\rangle_{\mathrm{E}}$. On employing (3.41) and (3.101), the *modulated* ultrasound counterpart of (3.114), namely (3.90b), can be written in terms of $\langle\tilde{j}_z\rangle_{\mathrm{E}}$ and $\langle\tilde{p}\rangle_{\mathrm{E}}$ as

$$\frac{\partial\langle\tilde{j}_z\rangle_{\mathrm{E}}}{\partial\tau}+\frac{\partial\langle\tilde{p}\rangle_{\mathrm{E}}}{\partial\zeta}\overset{\varepsilon^2}{=}\varepsilon\tilde{\delta}\tilde{I}^*_{\mathrm{E}}+\varepsilon\frac{\partial\tilde{I}_{\mathrm{E}}}{\partial\tau}, \tag{3.115}$$

which highlights the effect of ultrasound modulation on the acoustic radiation force, synthesized via term $\varepsilon\,\partial\tilde{I}_{\mathrm{E}}/\partial\tau$. By rule, previous treatments of the modulated ARF problem have made use of a "quasi-static" approach which utilizes (3.114) and assumes the ARF to take the form of a *product* between the *non-modulated expression*, $\varepsilon\tilde{\delta}\tilde{I}^*_{\mathrm{E}}$ and the *squared modulation envelope* $\mathcal{M}^2$, i.e. the modulation envelope for intensity. For completeness, one may also note that the ARF on the right-hand side of (3.115) can be interpreted as a negative divergence of the Reynolds stress tensor [6, 7], interpreted as the "*fast*" time average of the momentum flux tensor.

A comparison of (3.115) with (3.90) demonstrates that the expression for the ARF (identified as the body-force term on the right-hand side of the balance of linear momentum) is inherently dependent on the choice of the primary field quantities. This raises the question of the selection of $\langle\tilde{\rho}\rangle_{\mathrm{E}}$, $\langle\tilde{j}_z\rangle_{\mathrm{E}}$ and $\langle\tilde{S}\rangle_{\mathrm{E}}$, see (3.90)–(3.92), as the primary field quantities in lieu of $\langle\tilde{j}_z\rangle_{\mathrm{E}}$ and $\langle\tilde{p}\rangle_{\mathrm{E}}$ that are considered in [5]. For problems involving non-modulated ultrasound excitation, $\langle\tilde{j}_z\rangle_{\mathrm{E}}$ and $\langle\tilde{p}\rangle_{\mathrm{E}}$ are indeed uncoupled from the entropy perturbation $\langle\tilde{S}\rangle_{\mathrm{E}}$ as shown in the latter study. When modulation enters the problem, however, the problem becomes coupled; in particular, $\partial\langle\tilde{S}\rangle_{\mathrm{E}}/\partial\tau$ enters the *mass* balance when using $\langle\tilde{j}_z\rangle_{\mathrm{E}}$ and $\langle\tilde{p}\rangle_{\mathrm{E}}$, and *momentum* balance when using $\langle\tilde{j}_z\rangle_{\mathrm{E}}$ and $\langle\tilde{\rho}\rangle_{\mathrm{E}}$. As a result, there is no net gain in using $\langle\tilde{p}\rangle_{\mathrm{E}}$ in lieu of $\langle\tilde{\rho}\rangle_{\mathrm{E}}$. If either set of quantities is used, however, the "fast"-time averaging of (3.41) yields an auxiliary relationship

$$\langle\tilde{p}\rangle_{\mathrm{E}}\overset{\varepsilon^2}{=}\langle\tilde{\rho}\rangle_{\mathrm{E}}+\varepsilon\frac{\beta_{\mathrm{T}}}{\mathrm{c_p}}\langle\tilde{S}\rangle_{\mathrm{E}}+\varepsilon(\beta-1)\tilde{I}_{\mathrm{E}},$$

which permits straightforward conversion from one formulation to another.

ARF in a lossless fluid

An inspection of (3.90) and (3.101) in terms of the Eulerian formulation, and (3.108) and (3.113) in terms of the Lagrangian formulation reveals an interesting (and so far little understood) phenomenon of the *existence* of the ARF in a lossless fluid where $\tilde{\delta}=0$. From (3.101) and (3.113), one finds that this phenomenon is caused by the modulation of ultrasound whereby $\partial\tilde{I}_{\rm E}/\partial\tau$ and $\partial\tilde{I}_{\rm L}/\partial\tau$ are both non-zero, causing the right-hand sides in the balances of linear momentum (3.90) and (3.108) to remain non-trivial. In the case of a non-modulated ultrasound excitation ($\partial(\cdot)/\partial\tau=0$) these right-hand sides indeed vanish, see also (3.114), contributing to the present misconception that the ARF necessarily vanishes in a lossless homogeneous fluid (see [21]).

Relevance of the plane-wave solution to viscoelastic solids

Even though the present study considers wave motion in a Newtonian fluid, its conclusions are equally relevant to the understanding of like plane waves in a viscoelastic solid – a model that is commonly used to simulate the constitutive behavior of soft tissues [17, 42, 18, 15] due to the fact that there is no streaming in the current model. With the analogies between constitutive parameters of fluid and solid, discussed in Section 3.3.4, there is no fundamental difference between the plane-wave problem considered herein and its analogue for a viscoelastic solid.

To expose the utility of the ARF featured in (3.90) toward the (Eulerian) analysis of *time-averaged* wave motion in a viscoelastic solid generated by modulated elevated-intensity ultrasound, one may rewrite the balance of momentum (3.90b) using (3.90c), (3.93), (3.101) and (3.94) and, as

$$\frac{\partial^2\langle\tilde{u}_z\rangle_{\rm E}}{\partial\tau^2} - \frac{\partial^2\langle\tilde{u}_z\rangle_{\rm E}}{\partial\zeta^2} + \frac{\beta_{\rm T}}{\rm c_p}\frac{\partial\langle\tilde{S}\rangle_{\rm E}}{\partial\zeta} \overset{\varepsilon}{=} \beta\frac{\partial\tilde{I}_{\rm E}}{\partial\tau} + \beta\tilde{\delta}\tilde{I}^*_{\rm E} \tag{3.116}$$

where $\tilde{I}_{\rm E}$ is governed by (3.101). This *wave equation* in terms of the "fast" time-averaged axial displacement, $\langle\tilde{u}_z\rangle_{\rm E}$, demonstrates that the ARF in (3.90) as derived for fluids directly translates (apart from the factor of ε and thermal expansion term) into that for solids. Here it is noted that the P-wave speed in (3.116) equals unity due to adopted normalization scheme, whereas the viscosity term is negligible for it is $O(\varepsilon^2)$ in the averaged equation. For completeness, one may also observe that (3.116) can alternatively be obtained from (3.115), noting the ARF featured in the latter takes a notably different format i.e. that care must be taken when taking the ARF, derived for fluids, as an apparent body force acting on the solid as is usually done in medical ultrasound applications [12].

Relationship with difference-frequency signal generation

In an experimental setting, the postulated boundary condition (3.46) can be effected either via modulation of the incipient ultrasound field [14, 15] or, alternatively, via the use of two ultrasound fields with slightly different frequencies (e.g. [66]) which amounts to difference-frequency generation of the mean fluid motion [43, 30, 7]. To deal specifically with the latter case, boundary condition (3.46) (reduced to the plane wave) should be formally superseded by

$$\hat{\tilde{v}}_z(t, z_\mathrm{o}\!=\!0) \;=\; A_1 \sin\!\big((1+\omega_\mathrm{m})t + \varphi_1\big) + A_2 \sin(t+\varphi_2), \qquad (3.117)$$

where A_i and φ_i denote respectively the amplitude and phase of the ith sound field ($\mathrm{i}\!=\!1,2$), while $1+\omega_\mathrm{m},\ \omega_\mathrm{m}\!=\!O(\varepsilon)$ signifies the ratio between the larger and the smaller ultrasound frequency so that $\omega_\mathrm{m} > 0$. In terms of the featured ARF analysis which revolves around the initial-boundary value problem for the intensity of the sound field, this change in the kinematic boundary condition from (3.46) to (3.117) requires that the "left" boundary condition for intensity, (3.102), be replaced by

$$\tilde{I}_\mathrm{E}(\tau,0) \;\overset{\varepsilon}{=}\; \frac{1}{2}\Big(A_1^2 + A_2^2 + 2A_1A_2\cos\!\big(\tilde{\omega}_\mathrm{m}\tau + \varphi_1 - \varphi_2\big)\Big), \qquad \tilde{\omega}_\mathrm{m} = \frac{\omega_\mathrm{m}}{\varepsilon}. \qquad (3.118)$$

A comparison between (3.102) and (3.118) reveals that the foregoing analytical framework, developed for studying mean fluid motion due to modulated sound field, is equally applicable to problems involving difference-frequency signal generation provided that the effective modulation envelope is taken as

$$\mathcal{M}(\tau) \;=\; \sqrt{A_1^2 + A_2^2 + 2A_1A_2\cos\!\big(\tilde{\omega}_\mathrm{m}\tau + \varphi_1 - \varphi_2\big)}. \qquad (3.119)$$

Relationship (3.119) thus enables the difference-frequency problem to be considered as a *special (steady-state) case* of the present analysis in situations where the ratio between the companion frequencies, featured in the difference-frequency problem, is $1 + O(\varepsilon)$ (whereby $\tilde{\omega}_\mathrm{m}\!=\!O(1)$) as in e.g. [66].

3.5.4 Analytical solutions

Strongly dissipative fluid

To close the linearized system (3.90) (resp. (3.108)) in terms of averaged acoustic quantities, one must compute $\tilde{I}_{\mathrm{E}}$ and $\tilde{I}^*_{\mathrm{E}}$ (resp. $\tilde{I}_{\mathrm{L}}$ and $\tilde{I}^*_{\mathrm{L}}$) beforehand. Even though the latter task generally requires the solution to the "original" nonlinear set (3.79), this difficulty can be circumvented in certain situations. One such example is the case of a strongly dissipative fluid where

$$\varepsilon < \varepsilon\tilde{\delta}, \qquad \tilde{\delta} \;=\; \tilde{\mu}_{\mathrm{B}} + \tfrac{4}{3}\tilde{\mu} + \tilde{\kappa}\frac{\beta_{\mathrm{T}}^2}{\mathrm{c}_{\mathrm{p}}^2}, \tag{3.120}$$

i.e. where the non-linear effects (as quantified via the Mach number) are "small" relative to dissipation effects. In soft tissues, for instance, one finds that $\tilde{\delta} \approx 2 \div 5$ (see [59, 9]) which makes the foregoing hypothesis relevant to medical ultrasound applications. On the basis of (3.120) the nonlinear acoustic field $\tilde{\rho}$ solving (3.46) and (3.79)can be expanded, in terms of the perturbation parameter $1/\tilde{\delta}<1$, via the method of successive approximations as $\tilde{\rho} = \tilde{\rho}_1 + \tilde{\rho}_2 + o(\tilde{\rho}_2)$ where

$$\begin{aligned}
\tilde{\rho}_1 \;&=\; \sin(t-z)\,\mathcal{M}(\varepsilon(t-z))\,\exp\Big(-\frac{\varepsilon\tilde{\delta}}{2}z\Big), \\
\tilde{\rho}_2 \;&=\; \frac{1}{\tilde{\delta}}\frac{\beta}{2}\sin(2(t-z))\,\mathcal{M}^2(\varepsilon(t-z))\left[\exp\Big(-\varepsilon\tilde{\delta}z\Big) - \exp\Big(-2\varepsilon\tilde{\delta}z\Big)\right],
\end{aligned} \tag{3.121}$$

are the respectively the first- and second-order approximations of the mass density fluctuation. By way of (3.121), one finds that

$$\tilde{I}^*_{\mathrm{E}} - \tilde{I}_{\mathrm{E}} \;=\; \left\langle \Big(\frac{\partial\tilde{\rho}}{\partial t}\Big)^2 - \tilde{\rho}^2 \right\rangle_{\mathrm{E}} \;=\; O\Big(\max\Big\{\varepsilon^2, \tilde{\delta}^{-2}\Big\}\Big) \tag{3.122}$$

which, on substitution into (3.101), yields the differential equation for intensity

$$\frac{\partial\tilde{I}_{\mathrm{E}}}{\partial\tau} + \frac{\partial\tilde{I}_{\mathrm{E}}}{\partial\zeta} + \tilde{\delta}\tilde{I}_{\mathrm{E}} \;=\; O\Big(\max\Big\{\varepsilon, \tilde{\delta}^{-1}\Big\}\Big). \tag{3.123}$$

Equalities (3.123) and (3.102), specifying the behavior of $\tilde{I}_{\mathrm{E}}$, can be conveniently rewritten as the initial value problem in terms of τ–ζ and ζ and shown to have the closed-form solution

$$\tilde{I}_{\mathrm{E}} \;=\; \tfrac{1}{2}\exp\Big(-\tilde{\delta}\zeta\Big)\,\mathcal{M}^2(\tau-\zeta) \,+\, O\Big(\max\Big\{\varepsilon, \tilde{\delta}^{-2}\Big\}\Big). \tag{3.124}$$

To provide further specificity to the problem, consider next the case where the diffusivity of sound is dominated by the viscosity term, namely

$$\tilde{\delta} \;\approx\; \tilde{\mu}_{\mathrm{B}} + \tfrac{4}{3}\tilde{\mu} \quad\Longrightarrow\quad \frac{\beta_{\mathrm{T}}}{\mathrm{c_p}} \ll 1, \tag{3.125}$$

a hypothesis which applies to many liquids due to smallness of thermal expansion coefficient. By way of (3.122), (3.124) and (3.125), field equations (3.90) can be reduced as

$$\begin{aligned}
\frac{\partial\langle\tilde{\rho}\rangle_{\mathrm{E}}}{\partial\tau} + \frac{\partial\langle\tilde{j}_z\rangle_{\mathrm{E}}}{\partial\zeta} \;&=\; 0,\\
\frac{\partial\langle\tilde{j}_z\rangle_{\mathrm{E}}}{\partial\tau} + \frac{\partial\langle\tilde{\rho}\rangle_{\mathrm{E}}}{\partial\zeta} \;&=\; -\,\varepsilon\beta\frac{\partial\tilde{I}_{\mathrm{E}}}{\partial\zeta} \,+\, O\Big(\max\Big\{\varepsilon^2, \varepsilon\,\alpha^{-2}, \varepsilon\frac{\beta_{\mathrm{T}}}{\mathrm{c_p}}\Big\}\Big),\\
\frac{\partial\langle\tilde{S}\rangle_{\mathrm{E}}}{\partial\tau} \;&=\; 2\tilde{\alpha}\tilde{I}_{\mathrm{E}} \,+\, O\Big(\max\Big\{\varepsilon\,\tilde{\alpha}, \tilde{\alpha}^{-1}, \tilde{\kappa}\frac{\beta_{\mathrm{T}}^2}{\mathrm{c_p^2}}\Big\}\Big),
\end{aligned} \tag{3.126}$$

where the ultrasound intensity is given by

$$\tilde{I}_{\mathrm{E}} \;=\; \tfrac{1}{2}e^{-2\tilde{\alpha}\zeta}\mathcal{M}^2(\tau-\zeta), \qquad\quad \tilde{\alpha} = \tfrac{1}{2}\tilde{\delta} > 1. \tag{3.127}$$

While the approximation error in (3.126) may not always be negligible, however when $\tilde{\alpha}^{-1} \approx 0.2 \div 0.5$ [59, 9] or when $\beta_{\mathrm{T}}/\mathrm{c_p} \approx 0.1$, numerical results in Section 3.5.5 demonstrate that the above field equations are indeed capable of capturing the essence of wave motion in a strongly dissipative fluid for the problem under consideration. Here it is noted that the key simplification carried by (3.126) lies in the fact that the balances of mass and momentum are now uncoupled from entropy equation (3.126c). In this setting one may conveniently solve (3.126a) and (3.126b), subject to boundary conditions (3.91) and (3.96), by reparameterizing the problem in terms of $\tau-\zeta$ and ζ. On dropping the residual terms for brevity, the resulting solution reads

$$\begin{aligned}
\langle\tilde{\rho}\rangle_{\mathrm{E}} \;&=\; \langle\tilde{\rho}\rangle_{\mathrm{E},\infty} - \frac{\varepsilon\beta}{8}e^{-2\tilde{\alpha}\zeta}\left(3\mathcal{M}^2(\tau-\zeta) + \tilde{\alpha}^{-1}\frac{\partial\mathcal{M}^2}{\partial\tau}(\tau-\zeta) + \mathcal{K}(\tau-\zeta)\right),\\
\langle\tilde{j}_z\rangle_{\mathrm{E}} \;&=\; \langle\tilde{\rho}\rangle_{\mathrm{E},\infty} - \frac{\varepsilon\beta}{8}e^{-2\tilde{\alpha}\zeta}\left(\mathcal{M}^2(\tau-\zeta) + \tilde{\alpha}^{-1}\frac{\partial\mathcal{M}^2}{\partial\tau}(\tau-\zeta) - \mathcal{K}(\tau-\zeta)\right),
\end{aligned} \tag{3.128}$$

where

$$\langle\tilde{\rho}\rangle_{\mathrm{E},\infty} = \lim_{\zeta\to\infty}\langle\tilde{\rho}\rangle_{\mathrm{E}} \;=\; \frac{\varepsilon\beta}{8}\left(\mathcal{M}^2(\tau-\zeta) + \tilde{\alpha}^{-1}\frac{\partial\mathcal{M}^2}{\partial\tau}(\tau-\zeta) - \mathcal{K}(\tau-\zeta)\right) \tag{3.129}$$

signifies the far-field density fluctuation, and

$$\mathcal{K}(\tau-\zeta) \;=\; \tilde{\alpha}\, e^{-\tilde{\alpha}(\tau-\zeta)} \int_0^{\tau-\zeta} e^{\tilde{\alpha}\tau'} \mathcal{M}^2(\tau')d\tau'. \tag{3.130}$$

For completeness, the entropy solution of the initial value problem given by (3.126c) and the quiescent-past condition can be computed as

$$\langle \tilde{S} \rangle_{\mathrm{E}} \;=\; \tilde{\alpha} e^{-2\tilde{\alpha}\zeta} \int_0^{\tau} \mathcal{M}^2(\tau'-\zeta)\; d\tau'. \tag{3.131}$$

On the basis of (3.127) and (3.128), one may further compute the pressure fluctuation by taking the "fast" time average of (3.41) whereby

$$\langle \tilde{p} \rangle_{\mathrm{E}} \;=\; \langle \tilde{\rho} \rangle_{\mathrm{E}} + \frac{\varepsilon(\beta-1)}{2} e^{-2\tilde{\alpha}\zeta} \mathcal{M}^2(\tau-\zeta). \tag{3.132}$$

The Lagrangian counterparts of (3.128), (3.131) and (3.132) can be easily computed by employing the relationships (3.111) and (3.112) and the Lagrangian "fast" time average of (3.41).

Solution for example modulation envelope. With reference to (3.46) consider the case involving time-harmonic excitation for $t>0$, namely

$$\mathcal{M}(\varepsilon t) \;=\; H(\varepsilon t)\, \sin(\tilde{\omega}_{\mathrm{m}}\, \varepsilon t), \tag{3.133}$$

where $\tilde{\omega}_{\mathrm{m}} \equiv \omega_{\mathrm{m}}/\varepsilon \;= O(1)$, and H is the Heaviside function. In this case, the ARF featured on the right-hand side of (3.90b) can be computed as

$$\tilde{f}_z^{\mathrm{E}} \;=\; -\varepsilon\beta \frac{\partial \tilde{I}_{\mathrm{E}}}{\partial \zeta} \;=\; \tfrac{1}{2}\varepsilon\beta\, \tilde{\alpha}\, H(\tau-\zeta)\, e^{-2\tilde{\alpha}\zeta} \left[1 - \cos(2\tilde{\omega}_{\mathrm{m}}(\tau-\zeta)) + \tfrac{\tilde{\omega}_{\mathrm{m}}}{\tilde{\alpha}} \sin(2\tilde{\omega}_{\mathrm{m}}(\tau-\zeta))\right], \tag{3.134}$$

while (3.130) can be integrated to obtain

$$\mathcal{K}(\tau-\zeta) = \tfrac{1}{2} H(\tau-\zeta) \left[1 - \frac{\cos(2\tilde{\omega}_{\mathrm{m}}(\tau-\zeta)) + \frac{2\tilde{\omega}_{\mathrm{m}}}{\tilde{\alpha}} \sin(2\tilde{\omega}_{\mathrm{m}}(\tau-\zeta))}{1+\left(\frac{2\tilde{\omega}_{\mathrm{m}}}{\tilde{\alpha}}\right)^2} - \frac{\left(\frac{2\tilde{\omega}_{\mathrm{m}}}{\tilde{\alpha}}\right)^2}{1+\left(\frac{2\tilde{\omega}_{\mathrm{m}}}{\tilde{\alpha}}\right)^2} e^{-\tilde{\alpha}(\tau-\zeta)}\right]. \tag{3.135}$$

As a result, the far-field component (3.129) of density perturbation can be computed as

$$\langle \tilde{\rho} \rangle_{\mathrm{E},\infty} \;=\; \varepsilon\beta\, H(\tau-\zeta) \left[\frac{\tilde{\omega}_{\mathrm{m}}}{4\tilde{\alpha}} \sqrt{\frac{1+\left(\frac{\tilde{\omega}_{\mathrm{m}}}{\tilde{\alpha}}\right)^2}{1+\left(\frac{2\tilde{\omega}_{\mathrm{m}}}{\tilde{\alpha}}\right)^2}}\, \sin\!\big(2\tilde{\omega}_{\mathrm{m}}(\tau-\zeta) - \phi_1\big) + \frac{\left(\frac{\tilde{\omega}_{\mathrm{m}}}{2\tilde{\alpha}}\right)^2}{1+\left(\frac{2\tilde{\omega}_{\mathrm{m}}}{\tilde{\alpha}}\right)^2} e^{-\tilde{\alpha}(\tau-\zeta)}\right], \tag{3.136}$$

where

$$\phi_1 \;=\; \sin^{-1}\left[\tfrac{\tilde{\omega}_{\rm m}}{\tilde{\alpha}}\;\Big[\Big(1+\big(\tfrac{\tilde{\omega}_{\rm m}}{\tilde{\alpha}}\big)^2\Big)\Big(1+\big(\tfrac{2\tilde{\omega}_{\rm m}}{\tilde{\alpha}}\big)^2\Big)\Big]^{-1/2}\right].$$

With (3.133)–(3.136) at hand, the "fast" time averages of the featured acoustic quantities can be easily computed from (3.128), (3.131) and (3.132). As an illustration, Fig. 3.2 plots the averaged perturbations of mass density and pressure versus ζ for $\tau=8,\ \varepsilon=1.5\times10^{-3},\ \tilde{\alpha}=1.28\dot{3},\ \beta=3.5$, and $\tilde{\omega}_{\rm m}=\{0.2\dot{7},1.0\dot{7},4\}$. Assuming the (carrier) ultrasound frequency of 1 MHz, the latter sample modulation frequencies translate respectively into 0.4, 1.6 and 6 kHz, which are well inside the range used in medical ultrasound applications [17, 42, 18, 15]. For completeness, included in the diagram are the variations of both Eulerian and Lagrangian "fast" time averages, noting that $\zeta-\zeta_{\rm o}=O(\varepsilon^2)=O(10^{-6})$ whereby the two scales are visually indistinguishable. With reference to (3.128a) and (3.132), one may also note that the distinction between the Eulerian averages of mass density and pressure decays exponentially as $e^{-2\tilde{\alpha}\zeta}$ which is reflected in the display. A similar comment can be made regrading the difference between the Eulerian and Lagrangian "fast" time averages. From the physical standpoint, the segments in Fig. 3.2 where $\langle\tilde{p}\rangle_{\rm E},\langle\tilde{\rho}\rangle_{\rm E},\langle\tilde{p}\rangle_{\rm L}$ and $\langle\tilde{\rho}\rangle_{\rm L}$ visually coincide can be identified with regions where the intensity of the acoustic field $\tilde{I}_{\rm E}=o(1)$, see (3.111), (3.112), (3.127) and (3.132).

Comparison with quasi-static solution. To provide the basis for comparison with existing solutions, it is useful to recall that the past treatments [45, 46, 9] by rule account for the modulation effects via a "quasi-static" approximation which assumes the ARF to take the form of a *product* between the *non-modulated solution* and *squared modulation envelope* (i.e. the modulation envelope for intensity). In the context of (3.126a), (3.126b), (3.127) and (3.133), such hypothesis leads to the system of differential equations

$$\frac{\partial\langle\tilde{\rho}\rangle_{\rm E}^{\rm qs}}{\partial\tau}+\frac{\partial\langle\tilde{j}_z\rangle_{\rm E}^{\rm qs}}{\partial\zeta} \;=\; 0, \tag{3.137}$$

$$\frac{\partial\langle\tilde{j}_z\rangle_{\rm E}^{\rm qs}}{\partial\tau}+\frac{\partial\langle\tilde{p}\rangle_{\rm E}^{\rm qs}}{\partial\zeta} \;=\; \tilde{f}_{z,{\rm qs}}^{\rm E}, \qquad \tilde{f}_{z,{\rm qs}}^{\rm E} \;=\; \varepsilon\beta\tilde{\alpha}\,e^{-2\tilde{\alpha}\zeta}\,H(\tau)\,\sin^2(\tilde{\omega}_{\rm m}\tau), \tag{3.138}$$

where superscript "qs" indicates quasi-static solution; the residual terms are omitted for brevity, and the ARF in (3.138) namely $\tilde{f}_{z,{\rm qs}}^{\rm E}$ should be compared to (3.134), see

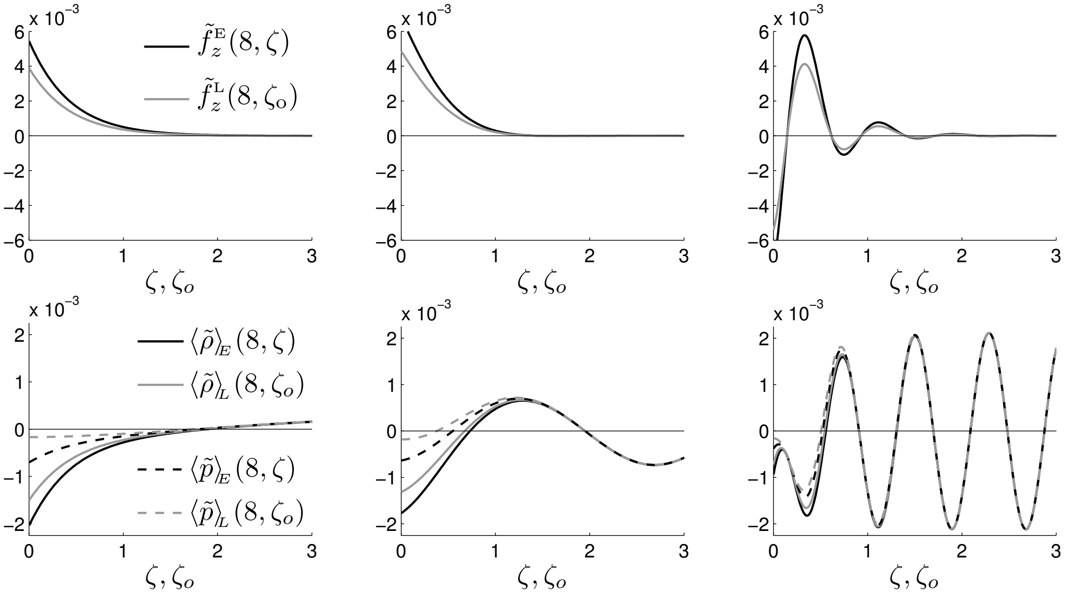

Figure 3.2: Acoustic radiation force (top panels) and averaged solution (bottom panels) in a strongly dissipative fluid, $\tilde{\alpha} = 1.28\dot{3}$, due to harmonically-modulated ultrasound excitation for $\tau = 8$, $\varepsilon = 1.5\times 10^{-3}$, and $\beta = 3.5$: variation with distance from the transducer face for "low" modulation frequency $\tilde{\omega}_{\mathrm{m}} = 0.2\dot{7}$ (left column), "intermediate" frequency $\tilde{\omega}_{\mathrm{m}} = 1.0\dot{7}$ (middle column), and "high" frequency $\tilde{\omega}_{\mathrm{m}} = 4$ (right column).

also (3.126a) and (3.126b). For further reference, the mass density solution of (3.137) and (3.138) under the "left" boundary condition (3.96) and radiation condition (3.91) can be computed as

$$\begin{aligned}\langle\tilde{\rho}\rangle_{\mathrm{E}}^{\mathrm{qs}} \;=\; & \frac{\varepsilon\beta}{4\Big(1+\big(\frac{\tilde{\omega}_{\mathrm{m}}}{\tilde{\alpha}}\big)^2\Big)}\Bigg[H(\tau)\Big\{\big(\tfrac{\tilde{\omega}_{\mathrm{m}}}{\tilde{\alpha}}\big)^2\big(\mathcal{H}-e^{-2\tilde{\alpha}\zeta}\big)-2e^{-2\tilde{\alpha}\zeta}\sin^2(\tilde{\omega}_{\mathrm{m}}\tau)\Big\} \\ & + \; H(\tau-\zeta)\;\tfrac{\tilde{\omega}_{\mathrm{m}}}{\tilde{\alpha}}\sin(2\tilde{\omega}_{\mathrm{m}}(\tau-\zeta))\Bigg],\end{aligned} \tag{3.139}$$

where

$$\mathcal{H} = \tfrac{1}{2}\Big[H(\tau-\zeta)e^{-2\tilde{\alpha}(\tau-\zeta)} + H(\zeta-\tau)e^{-2\tilde{\alpha}(\zeta-\tau)} + H(\tau+\zeta)e^{-2\tilde{\alpha}(\tau+\zeta)}\Big].$$

To highlight the differences between the proposed model and its predecessor, Fig. 3.3 compares the acoustic radiation force $\tilde{f}_z^{\mathrm{E}}$ as in (3.134) and mass density perturbation

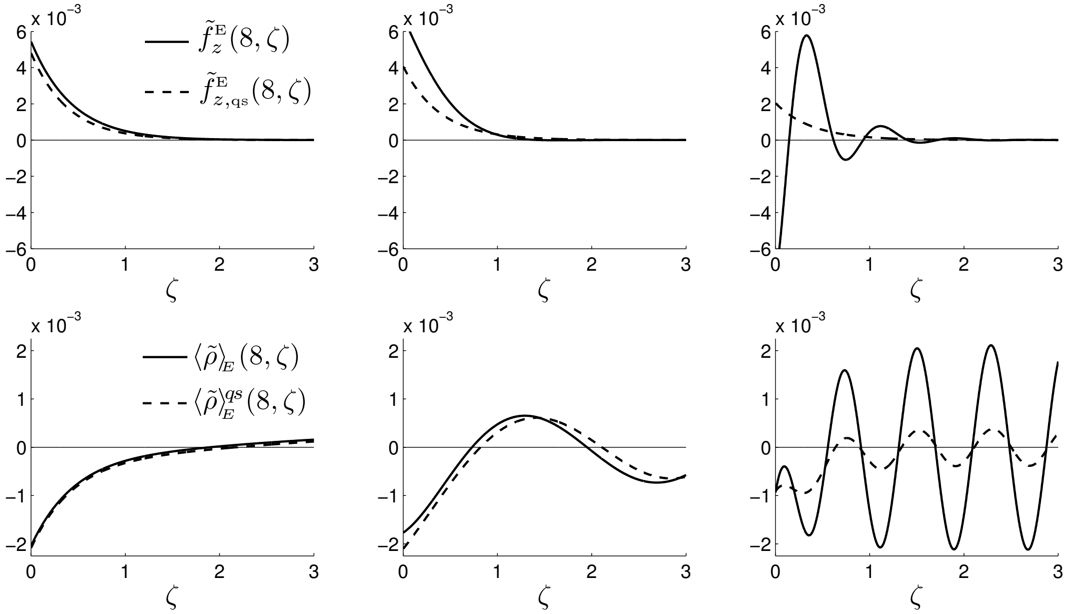

Figure 3.3: Comparison between the modulated-signal solution ($\tilde{f}_z^{\mathrm{E}}$, $\langle\tilde{\rho}\rangle_{\mathrm{E}}$) and its quasi-static predecessor ($\tilde{f}_{z,\mathrm{qs}}^{\mathrm{E}}$, $\langle\tilde{\rho}\rangle_{\mathrm{E}}^{\mathrm{qs}}$) in a strongly dissipative fluid, $\tilde{\alpha} = 1.28\dot{3}$, due to harmonically-modulated ultrasound excitation for $\tau = 8$, $\varepsilon = 1.5 \times 10^{-3}$, and $\beta = 3.5$: variation with distance from the transducer face for "low" modulation frequency $\tilde{\omega}_{\mathrm{m}} = 0.2\dot{7}$ (left column), "intermediate" frequency $\tilde{\omega}_{\mathrm{m}} = 1.0\dot{7}$ (middle column), and "high" frequency $\tilde{\omega}_{\mathrm{m}} = 4$ (right column).

$\langle\tilde{\rho}\rangle_{\mathrm{E}}$ stemming from (3.128a), (3.133), (3.135) and (3.136), with their quasi-static approximations $\tilde{f}_{z,\mathrm{qs}}^{\mathrm{E}}$ and $\langle\tilde{\rho}\rangle_{\mathrm{E}}^{\mathrm{qs}}$, see (3.138) and (3.139). For consistency with Fig. 3.2, the results are plotted versus ζ for $\tau = 8$, $\varepsilon = 1.5 \times 10^{-3}$, $\tilde{\alpha} = 1.28\dot{3}$, $\beta = 3.5$, and $\tilde{\omega}_{\mathrm{m}} = \{0.2\dot{7}, 1.0\dot{7}, 4\}$. As expected, the differences between the two solutions become more pronounced with increasing frequency. In this regard, the results at $\tilde{\omega}_{\mathrm{m}} = 4$ are especially instructive as they demonstrate the inability of the quasi-static approach to capture the physics of problem (non-monotonicity of the ARF distribution, amplitude of the induced response) at higher modulation frequencies. Assuming the (carrier) ultrasound frequency of 1 MHz, $\tilde{\omega}_{\mathrm{m}} = 4$ again translates into the modulation frequency of 6kHz which makes the latter example directly relevant to medical ultrasound applications [17, 42, 18].

For completeness, the left panel in Fig. 3.7 plots $\langle\tilde{\rho}\rangle_{\mathrm{E}}$ from the bottom right panel in Fig. 3.3 over a "large" ζ-scale as to capture the solution's wave front at $\zeta = \tau = 8$. The result indicates that for sufficiently large τ, there exists an "intermediate" spatial region, sufficiently removed from both the transducer face and the wave front, where the solution is nearly harmonic in terms of ζ. The analysis of (3.128a) and (3.136) in fact demonstrates that this intermediate behavior permits approximation

$$\langle\tilde{\rho}\rangle_{\mathrm{E}}(\tau,\zeta) \;\approx\; \mathcal{A}\,\sin(2\tilde{\omega}_{\mathrm{m}}(\tau-\zeta)-\phi_1),$$

which is obtained by dropping the exponential-decay terms $e^{-2\tilde{\alpha}\zeta}$ and $e^{-\tilde{\alpha}(\tau-\zeta)}$ from the solution. An analogous analysis of (3.139) further reveals that $\langle\tilde{\rho}\rangle_{\mathrm{E}}^{\mathrm{qs}} \approx \mathcal{A}^{\mathrm{qs}}\sin(2\tilde{\omega}_{\mathrm{m}}(\tau-\zeta))$ over the same region, thereby permitting an explicit comparison between the "intermediate" solution amplitudes $\mathcal{A}$ and $\mathcal{A}^{\mathrm{qs}}$ as shown in the right panel of Fig. 3.7. From the display, one may observe that notable differences between the proposed solution and its quasi-static approximation appear beyond $\tilde{\omega}_{\mathrm{m}}/\tilde{\alpha} > 0.8$ which can be used as a back-of-the-envelope upper bound, in terms of modulation frequency, where the quasi-static model ceases to apply. As a point of reference it is noted that the modulation frequencies in Fig. 3.2, ordered from lowest to highest, translate into respective $\tilde{\omega}_{\mathrm{m}}/\tilde{\alpha}$ ratios equaling roughly 0.2, 0.8 and 3.0.

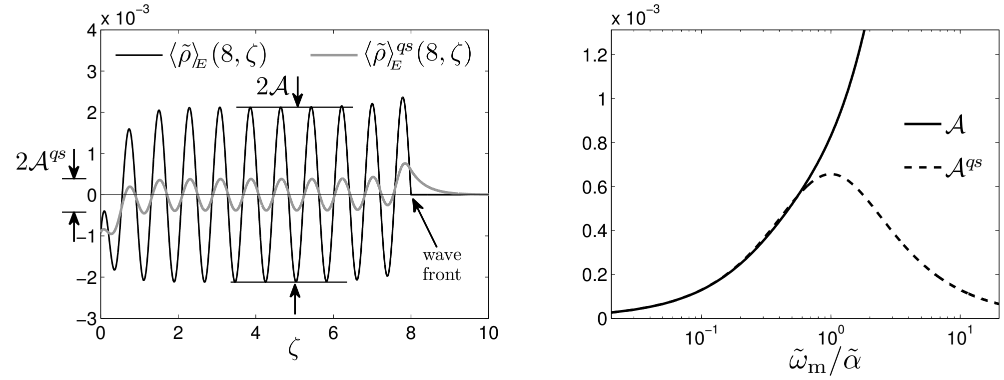

Figure 3.4: Left panel – variation of $\langle\tilde{\rho}\rangle_{\mathrm{E}}$ and $\langle\tilde{\rho}\rangle_{\mathrm{E}}^{\mathrm{qs}}$ between transducer face ($\zeta = 0$) and wave front ($\zeta = \tau$) indicating the existence of an "intermediate range" solution that is nearly harmonic with ζ; right panel – "intermediate range" solution amplitude given by the present model ($\mathcal{A}$) and quasi-static approximation ($\mathcal{A}^{\mathrm{qs}}$) versus modulation frequency.

Lossless fluid

As pointed out earlier, inspection of (3.90) and (3.101) reveals an interesting and yet not recognized phenomenon of the existence of the ARF in a lossless fluid where $\tilde{\delta}=0$. For this problem the analytical solution for intensity $\tilde{I}_{\mathrm{E}}$, and consequently that for the ARF in (3.90), can be obtained from (3.101) for *any* modulation envelope satisfying the assumptions made in conjunction with boundary condition (3.46). On employing the additional hypothesis that $\beta_{\mathrm{T}}/\mathrm{c_p} \ll 1$ as in Section 3.5.4, (3.90a) and (3.90b) can be solved independently from (3.90c) to find

$$\begin{aligned}\langle\tilde{\rho}\rangle_{\mathrm{E}}^{\mathrm{lf}} &= \frac{\varepsilon\beta}{4}\left(-\mathcal{M}^2(\tau-\zeta)+\zeta\frac{\partial\mathcal{M}^2}{\partial\tau}(\tau-\zeta)\right),\\ \langle\tilde{j}_z\rangle_{\mathrm{E}}^{\mathrm{lf}} &= \frac{\varepsilon\beta}{4}\zeta\frac{\partial\mathcal{M}^2}{\partial\tau}(\tau-\zeta),\end{aligned} \tag{3.140}$$

as a mean solution in terms of the mass density and mass flux. Consistent with the experimental findings in e.g. [43], (3.140) demonstrate that the mean motion can be generated in a lossless fluid by the application of a *modulated* sound field. It is however noted that (3.140) apply only for small to "moderate" values of ζ, where the implicit hypothesis about $\langle\tilde{\rho}\rangle_{\mathrm{E}}$ and $\langle\tilde{j}_z\rangle_{\mathrm{E}}$ behaving as $O(\varepsilon)$ still holds. Two additional restrictions implicit to (3.140) are that: one cannot have $M(\tau)=\mathcal{C}$ (where $\mathcal{C}>0$ is a constant) for it violates the quiescent past hypothesis, nor $M(\tau)=\mathcal{C}\,H(\tau)$ because it violates the smoothness assumption made on $\mathcal{M}$.

By virtue of (3.140) and averaged (3.41), the mean pressure fluctuations in a lossless fluid can be computed as

$$\langle\tilde{p}\rangle_{\mathrm{E}}^{\mathrm{lf}} = \frac{\varepsilon}{4}\left((\beta-2)\mathcal{M}^2(\tau-\zeta)+\beta\zeta\frac{\partial\mathcal{M}^2}{\partial\tau}(\tau-\zeta)\right). \tag{3.141}$$

On substituting (3.119) into (3.141) and taking $\varphi_1=\varphi_2$ for simplicity, one may further obtain the *difference-frequency* component of pressure, generated in a lossless fluid by two collinear sound beams, as

$$\langle\tilde{p}\rangle_{\mathrm{E,d}}^{\mathrm{lf}} = \frac{\varepsilon}{4}\Big((\beta-2)\big[A_1^2+A_2^2+2A_1A_2\cos\big(\tilde{\omega}_{\mathrm{m}}(\tau-\zeta)\big)\big]-2\beta\zeta\tilde{\omega}_{\mathrm{m}}A_1A_2\sin\big(\tilde{\omega}_{\mathrm{m}}(\tau-\zeta)\big)\Big). \tag{3.142}$$

The difference-frequency generation of mean air motion via the nonlinear interaction of two elevated-intensity sound beams was investigated theoretically and experimentally in [43], who in particular examined the amplitude of the difference-frequency wave at a Mach number $\varepsilon \approx 10^{-3}$. In order to compare (3.142) with the expression given in [43], one should however note that the ratio between the companion frequencies in the latter study was notably different from unity (implying $\tilde{\omega}_{\mathrm{m}} \gg 1$), whereas (3.142) postulates this ratio to be $1+O(\varepsilon)$, i.e that $\tilde{\omega}_{\mathrm{m}}=O(1)$. When $\tilde{\omega}_{\mathrm{m}} \gg 1$, the second term in (3.142) clearly dominates the expression, and the fluctuation amplitude of (3.142) can be "blindly" approximated as

$$A_{\mathrm{d}}^{\mathrm{lf}} \;=\; \tfrac{1}{2}\,\varepsilon\,\beta\,\zeta\,\tilde{\omega}_{\mathrm{m}}\,A_1\,A_2. \tag{3.143}$$

Noting that i) $\beta=(\gamma+1)/2$ for gases, and ii) the root-mean-square values of the amplitudes of the incipient (time-harmonic) sound fields are given by $P_{\mathrm{i}} = A_{\mathrm{i}}/\sqrt{2}$ ($\mathrm{i} = 1, 2$), the scaling scheme in Table 2.1 and (3.18) allow one to recover the dimensional form of (3.143), which happens to *coincide* with the result in [43]. This comparison not only illustrates the applicability of the concept of the ARF towards studying the phenomenon of difference-frequency signal generation, but also verifies the existence of the ARF in a lossless homogeneous fluid due to modulation of an ultrasound signal.

3.5.5 Numerical model and verification

In light of major differences between the present model and its quasi-static predecessor seen in Figs. 3.3 and 3.7, it is next critical to verify the former numerically via suitable computational scheme that operates on the "original" i.e. non-averaged field equations. Without loss of generality, the ensuing numerical analysis is focused on the harmonic modulation envelope (3.133) and Eulerian system (3.79); the computational treatment of its Lagrangian analogue (3.103) can be established in a similar fashion, and is omitted for brevity.

Governing equations for the numerical treatment

To facilitate the numerical treatment of nonlinear field equations (3.79), one may employ expansions (3.26), (3.93) and (3.41) to arrive to the governing system

$$\begin{aligned} \frac{\partial\tilde{\rho}}{\partial t}+\frac{\partial\tilde{j}_z}{\partial z} &= 0, \\ \frac{\partial\tilde{j}_z}{\partial t}+\frac{\partial\tilde{\rho}}{\partial z}+\varepsilon\frac{\beta_{\mathrm{T}}}{\mathrm{c_p}}\frac{\partial\tilde{S}}{\partial z}+\varepsilon\frac{\partial\tilde{j}_z^{\,2}}{\partial z}+\varepsilon(\beta-1)\frac{\partial\tilde{\rho}^2}{\partial z}-2\varepsilon\tilde{\alpha}\frac{\partial^2\tilde{j}_z}{\partial z^2} &= \mathcal{R}_1, \\ \frac{\partial\tilde{S}}{\partial t}-\tilde{\kappa}\frac{\beta_{\mathrm{T}}}{\mathrm{c_p}}\Big(1-\varepsilon\Big(1+\frac{\beta_{\mathrm{T}}}{\mathrm{c_p}}\Big)\tilde{\rho}\Big)\frac{\partial^2\tilde{\rho}}{\partial z^2}+\varepsilon\tilde{j}_z\frac{\partial\tilde{S}}{\partial z}-2\varepsilon\tilde{\alpha}\Big(\frac{\partial\tilde{j}_z}{\partial z}\Big)^2 &= \mathcal{R}_2, \end{aligned} \tag{3.144}$$

written in terms of $\tilde{\rho}$, mass flux $\tilde{j}_z=(1+\varepsilon\tilde{\rho})\tilde{v}_z$ and $\tilde{S}$. It can be shown that the residuals R_1 and R_2 are such that they are *at most* $O(\varepsilon)$ relative to the leading terms in the respective field equations when computing either $\tilde{\rho}$, $\tilde{j}_z$ and $\tilde{S}$, their time averages, or ultrasound intensity.

For an application of the (Lagrangian) kinematic boundary condition (3.46) to Eulerian system (3.144), it can be shown via Taylor series expansion, relationship $z = z_{\mathrm{o}}+\varepsilon\hat{\tilde{u}}_z$, and (3.144a) that

$$\tilde{j}_z(t,z) \overset{\varepsilon^2}{=} \tilde{j}_z(t,z_{\mathrm{o}})+\varepsilon\frac{\partial\tilde{j}_z}{\partial z}(t,z_{\mathrm{o}})\hat{\tilde{u}}_z(t,z_{\mathrm{o}}) \overset{\varepsilon^2}{=} \tilde{j}_z(t,z_{\mathrm{o}})-\varepsilon\frac{\partial\hat{\tilde{\rho}}}{\partial t}(t,z_{\mathrm{o}})\hat{\tilde{u}}_z(t,z_{\mathrm{o}})$$

which, combined with the relationship

$$\tilde{j}_z(t,z) = \hat{\tilde{j}}_z(t,z_{\mathrm{o}}) = \hat{\tilde{v}}_z(t,z_{\mathrm{o}})+\varepsilon\hat{\tilde{\rho}}(t,z_{\mathrm{o}})\frac{\partial\hat{\tilde{u}}_z}{\partial t}(t,z_{\mathrm{o}})$$

yields

$$\tilde{j}_z(t,z_{\mathrm{o}}) \overset{\varepsilon^2}{=} \hat{\tilde{v}}_z(t,z_{\mathrm{o}}) + \varepsilon\frac{\partial(\hat{\tilde{u}}_z\hat{\tilde{v}}_z)}{\partial t}(t,z_{\mathrm{o}}). \tag{3.145}$$

On the basis of (3.46), (3.133) and (3.145), the kinematic boundary condition for (3.144) can be written as

$$\tilde{j}_z(t,0) \overset{\varepsilon^2}{=} H(\varepsilon t)\Big[\sin(t)\sin(\tilde{\omega}_{\mathrm{m}}\varepsilon t)-\varepsilon\cos(2t)\sin^2(\tilde{\omega}_{\mathrm{m}}\varepsilon t)\Big]. \tag{3.146}$$

In a similar fashion, the zero-heat-flux boundary condition (3.47) can be expressed using (3.26) and (3.93) as

$$\frac{\partial\tilde{\rho}}{\partial z}(t,0) = O(\varepsilon) \tag{3.147}$$

which, together with the radiation condition and the quiescent-past assumption, completes the formulation of the problem.

Finite difference scheme

The solution to (3.144) under the above boundary and initial conditions can be conveniently sought by selecting a regular grid of nodal points $(t_i = (i-1)h_t,\ z_k = (k-1)h)$ $(i = 1, 2, \dots I,\ k = 1, 2, \dots K)$ over the spatiotemporal domain $(t, z) \in [0, T] \times [0, z_{\max}]$ and approximating the featured partial derivatives via finite differences. For simplicity, one may further take $z_{\max} > T$ such that all quantities of interest are identically zero for $z = z_K$ and $t \leqslant T$ by virtue of the radiation condition and inherent causality of the solution. On adopting the forward difference scheme to deal with temporal derivatives, one such discretized system can be written as

$$
\begin{aligned}
\frac{\bar{\rho}_k^{i+1} - \bar{\rho}_k^{i}}{h_t} + \frac{\bar{j}_k^{i} - \bar{j}_{k-1}^{i}}{h} &= 0, \\
\frac{\bar{j}_k^{i+1} - \bar{j}_k^{i}}{h_t} + \frac{\bar{\rho}_{k+1}^{i+1} - \bar{\rho}_k^{i+1}}{h} + \varepsilon \frac{\beta_{\mathrm{T}}}{\mathrm{c_p}} \frac{\bar{S}_{k+1}^{i+1} - \bar{S}_k^{i+1}}{h} + \Pi_k^i &= 0, \\
\frac{\bar{S}_k^{i+1} - \bar{S}_k^{i}}{h_t} + \Sigma_k^i &= 0,
\end{aligned}
\tag{3.148}
$$

for $i = \overline{1, I-1}$, $k = \overline{1, K}$, where $\bar{\rho}_k^i$, $\bar{j}_k^i$ and $\bar{S}_k^i$ are the nodal approximations of $\tilde{\rho}$, $\tilde{j}_z$ and $\tilde{S}$ at (t_i, z_k), while Π_k^i and Σ_k^i denote respectively the remaining terms on the left-hand sides of (3.144b) and (3.144c), computed respectively via forward differences and central differences applied to $\partial(\cdot)/\partial z$ and $\partial^2(\cdot)/\partial z^2$ at (t_i, z_k). The above time-marching scheme, which entails the sequential evaluation of (3.148c), (3.148a) and (3.148b) for each i, makes use of (3.146) and (3.147) discretized as

$$
\bar{j}_1^i \;=\; \sin(t_i)\sin(\tilde{\omega}_{\mathrm{m}} \varepsilon t_i) - \varepsilon \cos(2t_i)\sin^2(\tilde{\omega}_{\mathrm{m}} \varepsilon t_i), \qquad \bar{\rho}_1^i - \bar{\rho}_0^i = 0, \quad i = \overline{1, I}
$$

to obtain a numerical solution to the problem.

Even though the stability of (3.148) which include nonlinear terms can not be explicitly analyzed, one may note that the $O(1)$-leading terms in (3.148a) and (3.148b) constitute a closed linear system that can be shown, via von Neumann stability analysis [67], to form a stable scheme in terms of $\bar{\rho}$ and $\bar{j}$ when $h_t < h$ – a restriction that is assumed hereon.

Approximation accuracy

To determine the accuracy of (3.148) it can be shown, by substituting Taylor expansions of $\tilde{\rho}$, $\tilde{j}_z$ and $\tilde{S}$ about (t_i, z_k) into the featured algebraic system, that the scheme has accuracy $O(h)$. As a result, one should nominally have $h \ll \varepsilon$ to capture the contribution of the $O(\varepsilon)$-terms in (3.148), including those comprising Π_k^i and Σ_k^i, as they are central to the (numerical) computation of "fast"-time averages $\langle\tilde{\rho}\rangle_{\mathrm{E}}$, $\langle\tilde{j}_z\rangle_{\mathrm{E}}$ and $\langle\tilde{S}\rangle_{\mathrm{E}}$, as well as that of ultrasound intensity $\tilde{I}_{\mathrm{E}}$. Here it can be shown, however, that: (A) the "fast" time averages of (3.148) approximate (3.90) with an $O(\varepsilon h)$-residual, and (B) the ultrasound intensity, computed numerically on the basis (3.148), satisfies (3.101) with an $O(h)$-residual. As a result, one finds that choosing $\varepsilon < h = o(1)$ is sufficient to compute the *leading* behavior of both $(\tilde{\rho}, \tilde{j}_z, \tilde{S}) = O(1)$, $(\langle\tilde{\rho}\rangle_{\mathrm{E}}, \langle\tilde{j}_z\rangle_{\mathrm{E}}, \varepsilon\langle\tilde{S}\rangle_{\mathrm{E}}) = O(\varepsilon)$, and ultrasound intensity $\tilde{I}_{\mathrm{E}} = O(1)$. For simplicity of the computational treatment, one may further take $h = \pi/N$ and $h_t = \pi/N_t$, where N and $N_t > N$ are suitably chosen integers.

To demonstrate claim (A), one may substitute $\tilde{\rho}$, $\tilde{j}_z$, $\tilde{S}$ into (3.148), employ Taylor series expansion about (t_i, z_k), and apply the "fast" time average (3.74) to find that the resulting equations are the same as (3.90) with an $O(h\varepsilon)$-residual. The proof of claim (B), on the other hand, entails calculations as in Section 3.5.1, applied to the discretized system (3.148). For brevity of presentation, however, this proof is enclosed in Appendix A.6.

Numerical computation of "fast" time averages

Owing to the fact that the numerical solution does not differentiate between "slow" and "fast" time as its analytical companion, the key remaining question is how to compute the "fast" time average, (3.74), of the featured field quantities within the framework of the finite difference scheme (3.148). To help resolve the problem, one may make reference to Section 3.5.1 and recall that the "fast" time averages $\langle\tilde{\rho}\rangle_{\mathrm{E}}$ and $\langle\tilde{j}_z\rangle_{\mathrm{E}}$ are $O(\varepsilon)$, whereas the entropy average, $\langle\tilde{S}\rangle_{\mathrm{E}}$, is $O(1)$. In this setting the solution to the continuum parent of (3.148), namely (3.144), can be conveniently synthesized in terms of the rescaled (Eulerian) state vector

$$\boldsymbol{\mathcal{Q}}(t,z) \;=\; [Q^{\tilde{\rho}}, Q^{\tilde{j}_z}, \varepsilon Q^{\tilde{S}}](t,z) \;\equiv\; [\tilde{\rho}, \tilde{j}_z, \varepsilon\tilde{S}](t,z).$$

On differentiating between "slow" and "fast" spatiotemporal variables as in Section 3.4.3, $\boldsymbol{\mathcal{Q}}$ can alternatively be written as

$$\boldsymbol{\mathcal{Q}}(t,z) = \boldsymbol{\mathcal{R}}(t,z,\tau,\zeta), \quad \tau = \varepsilon t,\ \zeta = \varepsilon z, \quad \boldsymbol{\mathcal{R}}(t{+}2\pi,\cdot,\cdot,\cdot) = \boldsymbol{\mathcal{R}}(t,\cdot,\cdot,\cdot), \quad \frac{\partial \boldsymbol{\mathcal{R}}}{\partial z} = -\frac{\partial \boldsymbol{\mathcal{R}}}{\partial t}.$$

In this setting, the "ordinary" time average of $\boldsymbol{\mathcal{Q}}$ (that is computable from the numerical solution) can be written by virtue of (3.74) and Taylor expansion as

$$\begin{aligned} \frac{1}{2\pi}\int_{t-\pi}^{t+\pi} \boldsymbol{\mathcal{Q}}(t',z)\ dt' &= \frac{1}{2\pi}\int_{t-\pi}^{t+\pi} \boldsymbol{\mathcal{R}}(t',z,\varepsilon t',\varepsilon z)\ dt' \\ &= \langle \boldsymbol{\mathcal{Q}}\rangle_{\mathrm{E}}(\tau,\zeta) + \frac{\varepsilon}{2\pi}\int_{-\pi}^{\pi} \tilde{t}\,\frac{\partial \boldsymbol{\mathcal{R}}}{\partial \tau}(\tilde{t}+t,z,\varepsilon t,\varepsilon z)\ d\tilde{t}\ +\ O(\varepsilon^2), \qquad \tilde{t} = t'-t, \end{aligned} \tag{3.149}$$

which demonstrates that the residual between the "ordinary" and "fast" time averages of $\boldsymbol{\mathcal{Q}}$ is $O(\varepsilon)$. Given the fact that $\langle \boldsymbol{\mathcal{Q}}\rangle_{\mathrm{E}}$ is $O(\varepsilon)$ as well, the question still remains how to compute the latter quantity, up to the leading order, directly from $\boldsymbol{\mathcal{Q}}$. To this end, one may evaluate the repeated average of (3.149) as

$$\begin{aligned} \frac{1}{4\pi^2}\int_{t-\pi}^{t+\pi}\int_{t'-\pi}^{t'+\pi} \boldsymbol{\mathcal{Q}}(t'',z)\,dt''\,dt' \ &=\ \langle \boldsymbol{\mathcal{Q}}\rangle_{\mathrm{E}}(\tau,\zeta)\ +\ \frac{\varepsilon}{2\pi}\int_{-\pi}^{\pi}\tilde{t}\,\frac{\partial\langle \boldsymbol{\mathcal{Q}}\rangle_{\mathrm{E}}}{\partial \tau}(\tau,\zeta)\ d\tilde{t}\ +\ O(\varepsilon^2) \\ &=\ \langle \boldsymbol{\mathcal{Q}}\rangle_{\mathrm{E}}(\tau,\zeta) + O(\varepsilon^2), \end{aligned} \tag{3.150}$$

which shows that *double* "ordinary" time average of $\boldsymbol{\mathcal{Q}}$ approximates $\langle \boldsymbol{\mathcal{Q}}\rangle_{\mathrm{E}}$ with an $O(\varepsilon^2)$-error. In what follows, averages (3.149) and (3.150) will be denoted respectively by ${}_1\langle\cdot\rangle_{\mathrm{E}}$ and ${}_2\langle\cdot\rangle_{\mathrm{E}}$.

To expose the accuracy of (3.150) in the context of the featured finite difference scheme, one may recall that $h_t = \pi/N_t$ and employ Taylor series expansion of $\boldsymbol{\mathcal{Q}}$ at relevant nodal points to find

$$\begin{aligned} \frac{1}{2\pi}\int_{t_i-\pi}^{t_i+\pi} \boldsymbol{\mathcal{Q}}(t',z)\ dt' &= \frac{1}{2\pi}\sum_{\ell=i-N_t}^{i+N_t-1}\int_{t_\ell}^{t_\ell+h_t} \boldsymbol{\mathcal{Q}}(t',z)\ dt' \\ &= \frac{h_t}{2\pi}\sum_{\ell=i-N_t}^{i+N_t-1}\left(\boldsymbol{\mathcal{Q}}(t_\ell,z) + \frac{\partial \boldsymbol{\mathcal{Q}}}{\partial t}(t_\ell,z)\frac{h_t}{2} + \ldots\right). \end{aligned} \tag{3.151}$$

On manipulating the "ordinary" time average of $\partial^m \boldsymbol{\mathcal{Q}}/\partial t^m$ as in (3.149) and employing Taylor series expansion, it can be shown that

$$\int_{t_i-\pi}^{t_i+\pi} \frac{\partial^m \boldsymbol{\mathcal{Q}}}{\partial t^m}(t',z)\,dt' = O(\varepsilon)\ \Longrightarrow \sum_{\ell=i-N_t}^{i+N_t-1}\left(\frac{\partial^m \boldsymbol{\mathcal{Q}}}{\partial t^m}(t_\ell,z)\,h_t + \frac{\partial^{m+1}\boldsymbol{\mathcal{Q}}}{\partial t^{m+1}}(t_\ell,z)\,\frac{h_t^2}{2} + \ldots\right) \overset{\varepsilon}{=} 0,$$

for $m \geqslant 1$. A recursive use of the latter equality starting with $m=1$ demonstrates that

$$\sum_{\ell=i-N_t}^{i+N_t-1} \frac{\partial^m \boldsymbol{\mathcal{Q}}}{\partial t^m}(t_\ell, z)\, h_t \;=\; O(\max\{\varepsilon, h_t^\infty\}) \;\overset{\varepsilon}{=}\; 0, \quad m \geqslant 1,$$

which, on substitution into (3.151), yields

$$_1\langle \boldsymbol{\mathcal{Q}} \rangle_{\mathrm{E}}^{\mathrm{num}}(t_i, z) \;\equiv\; \frac{h_t}{2\pi} \sum_{\ell=i-N_t}^{i+N_t-1} \boldsymbol{\mathcal{Q}}(t_\ell, z) \;=\; \frac{1}{2\pi} \int_{t_i-\pi}^{t_i+\pi} \boldsymbol{\mathcal{Q}}(t', z)\, dt' \;+\; O(\varepsilon h_t). \qquad (3.152)$$

To approximate the left-hand side of (3.150) numerically, (3.152) can be averaged anew without increasing the order of the residual, which finally yields

$$_2\langle \boldsymbol{\mathcal{Q}} \rangle_{\mathrm{E}}^{\mathrm{num}}(t_i, z) \;\equiv\; \frac{h_t^2}{4\pi^2} \sum_{j=i-N_t}^{i+N_t-1} \sum_{\ell=j-N_t}^{j+N_t-1} \boldsymbol{\mathcal{Q}}(t_\ell, z) \;=\; \langle \boldsymbol{\mathcal{Q}} \rangle_{\mathrm{E}}(\tau_i, \zeta) + O(\max\{\varepsilon^2, \varepsilon h_t\}), \; (3.153)$$

as a finite-difference formula for computing $\langle \boldsymbol{\mathcal{Q}} \rangle_{\mathrm{E}}$, where $\tau_i = \varepsilon t_i$.

Numerical results

To verify the proposed analytical developments, (3.148) are integrated numerically with the spatial and temporal discretization parameters set to $N = \pi/h = 8$ and $N_t = \pi/h_t = 12$, respectively. The thermo-mechanical properties of the fluid are taken as $\tilde{\kappa} = 0.06$, $\beta_{\mathrm{T}}/\mathrm{c_p} = 0.13$, $\beta = 3.5$, and $\tilde{\alpha} = 1.28\dot{3}$. The left panels in Fig. 3.5 show a comparison between the analytical "fast" time average $\langle\tilde{\rho}\rangle_{\mathrm{E}}$ and twice-averaged finite difference solution, $_2\langle\bar{\rho}\rangle_{\mathrm{E}}^{\mathrm{num}}$, versus distance from the transducer face for $\tau = 5$, $\varepsilon = 1.5 \times 10^{-3}$ and $\tilde{\omega}_{\mathrm{m}} = \{0.2\dot{7}, 1.0\dot{7}, 4\}$. From additional numerical computations it was found that already small discrepancies between $\langle\tilde{\rho}\rangle_{\mathrm{E}}$ and $_2\langle\bar{\rho}\rangle_{\mathrm{E}}^{\mathrm{num}}$, seen in the display, are mostly due to neglected entropy term $(\beta_{\mathrm{T}}/\mathrm{c_p})\,\partial\langle\tilde{S}\rangle_{\mathrm{E}}/\partial\zeta$ in the balance of linear momentum (in particular there is no visible difference between $\langle\tilde{\rho}\rangle_{\mathrm{E}}$ and $_2\langle\bar{\rho}\rangle_{\mathrm{E}}^{\mathrm{num}}$ when $\beta_{\mathrm{T}}/\mathrm{c_p} = 4 \times 10^{-2}$). As expected the mean density fluctuations $\langle\tilde{\rho}\rangle_{\mathrm{E}}$, induced by the ARF, are indeed small i.e. $O(\varepsilon)$, recalling that $\tilde{\rho} = O(1)$ according to (3.18). For completeness, the right panels in Fig. 3.5 compare the *non-averaged* finite-difference solution $\bar{\rho}$ versus its single average $_1\langle\bar{\rho}\rangle_{\mathrm{E}}^{\mathrm{num}}$ and double average $_2\langle\bar{\rho}\rangle_{\mathrm{E}}^{\mathrm{num}}$. Consistent with (3.149), the once-averaged numerical solution exhibits an $O(\varepsilon)$-difference relative to its twice-averaged counterpart, and thus relative to $\langle\tilde{\rho}\rangle_{\mathrm{E}}$. From the latter set of results, it is further obvious that the "ordinary" time average ${}_1\langle\tilde{\rho}\rangle_{\rm E}$, developed for the treatment of non-modulated (elevated-intensity) sound fields, is indeed inadequate when dealing with the modulated sound problem.

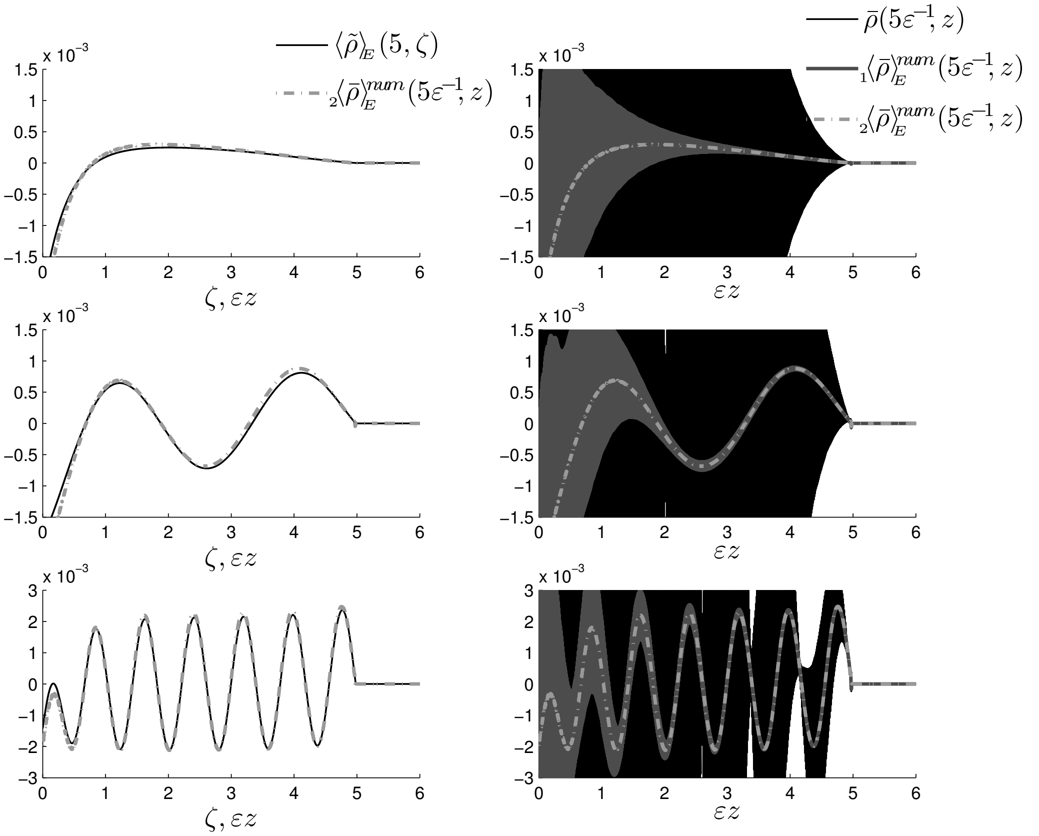

Figure 3.5: Left panels: comparison between the analytical "fast" time average $\langle\tilde{\rho}\rangle_{\rm E}$ and twice-averaged numerical solution ${}_2\langle\bar{\rho}\rangle_{\rm E}^{\rm num}$. Right panels: non-averaged finite-difference solution, $\bar{\rho}$, versus its single average ${}_1\langle\bar{\rho}\rangle_{\rm E}^{\rm num}$ and double average ${}_2\langle\bar{\rho}\rangle_{\rm E}^{\rm num}$. The comparisons are made at $\tau = 5$, $\varepsilon = 1.5{\times}10^{-3}$, $\tilde{\alpha} = 1.28\dot{3}$ and $\beta = 3.5$, assuming modulation frequencies $\tilde{\omega}_{\rm m} = 0.2\dot{7}$ (top row), $\tilde{\omega}_{\rm m} = 1.0\dot{7}$ (middle row), and $\tilde{\omega}_{\rm m} = 4$ (bottom row).

3.6 Acoustic radiation force: focused beam

This section is devoted to the derivation of the acoustic radiation force for the focused ultrasound configuration. With reference to Fig. 3.2, it is noted that the geometry of the domain (except that affiliated with transducer's boundary Γ) does not enter the problem of ARF generation, and will hereon be considered arbitrary. The only restriction on the domain is that it should be sufficiently large so that the wave reflections from its boundaries are sufficiently weak, i.e. that their Mach number is significantly smaller than ε within the focal region.

3.6.1 Eulerian formulation

To facilitate the computation of the ARF in the Eulerian frame of reference, one may recall (3.27) and (3.30) and decompose the Cauchy stress tensor (3.29) as $\tilde{\boldsymbol{\sigma}} = \tilde{\boldsymbol{\sigma}}^{\text{lin}} + \tilde{\boldsymbol{\sigma}}^{\text{non}}$, where

$$\tilde{\boldsymbol{\sigma}}^{\text{lin}} \;=\; (1-2\varepsilon\tilde{G})(\nabla\cdot\tilde{\boldsymbol{u}})\boldsymbol{I} \,+\, 2\varepsilon\tilde{G}\nabla^{\text{S}}\tilde{\boldsymbol{u}} \,-\, \varepsilon\frac{\beta_{\text{T}}}{\text{c}_{\text{p}}}\tilde{S}\boldsymbol{I} \,+\, \varepsilon(\tilde{\mu}_{\text{B}}-\tfrac{2}{3}\tilde{\mu})\Big(\nabla\cdot\frac{\partial\tilde{\boldsymbol{u}}}{\partial t}\Big)\boldsymbol{I} \,+\, 2\varepsilon\tilde{\mu}\nabla^{\text{S}}\frac{\partial\tilde{\boldsymbol{u}}}{\partial t}, \tag{3.154}$$

and $\tilde{\boldsymbol{\sigma}}^{\text{non}}$ denote respectively its *linear* and *nonlinear* components. With reference to (3.19) and (3.154), one may now apply the "fast" time average (3.74a) to the rearranged balance of linear momentum (3.20b) as

$$\Big\langle \frac{\partial^2\tilde{\boldsymbol{u}}}{\partial t^2} - \nabla\cdot\tilde{\boldsymbol{\sigma}}^{\text{lin}} \Big\rangle_{\text{E}} \;=\; \Big\langle \nabla\cdot\tilde{\boldsymbol{\sigma}}^{\text{non}} - \varepsilon\tilde{\boldsymbol{v}}\cdot\nabla\tilde{\boldsymbol{v}} - \varepsilon\tilde{\rho}\Big(\frac{\partial\tilde{\boldsymbol{v}}}{\partial t} + \varepsilon\tilde{\boldsymbol{v}}\cdot\nabla\tilde{\boldsymbol{v}}\Big) - \varepsilon\frac{\partial}{\partial t}\Big(\nabla^{\text{T}}\tilde{\boldsymbol{u}}\cdot\frac{\partial\tilde{\boldsymbol{u}}}{\partial t} + \varepsilon\tilde{\boldsymbol{g}}\Big)\Big\rangle_{\text{E}} \tag{3.155}$$

whose right-hand side signifies the sought ARF. Here $\tilde{\boldsymbol{g}} = O(1)$ is the residual in the expansion $\tilde{\boldsymbol{v}} = (\boldsymbol{I}+\varepsilon\nabla^{\text{T}}\tilde{\boldsymbol{u}})\cdot(\partial\tilde{\boldsymbol{u}}/\partial t)+\varepsilon^2\tilde{\boldsymbol{g}}$, see also (3.19); like other variables, this residual is periodic in "fast" time so that $\langle\partial\tilde{\boldsymbol{g}}/\partial t\rangle_{\text{E}} = O(\varepsilon)$. As can be seen from (3.155), the acoustic radiation force stems from both constitutive and geometric nonlinearities of the problem - a feature that will be examined in greater detail shortly.

With reference to (3.74), let $\langle\tilde{\boldsymbol{u}}\rangle_{\text{E}}(\chi_{\text{i}},\zeta,\tau)$ denote the "fast" time average of the displacement vector, and let

$$\begin{aligned} \boldsymbol{\mathcal{L}}\langle\tilde{\boldsymbol{u}}\rangle_{\text{E}} \;=\; (\mathcal{L}_{\text{i}},\mathcal{L}_z)\langle\tilde{\boldsymbol{u}}\rangle_{\text{E}} \;:=\; & \varepsilon^2\frac{\partial^2\langle\tilde{\boldsymbol{u}}\rangle_{\text{E}}}{\partial\tau^2} - (1-\varepsilon\tilde{G})\nabla\nabla\cdot\langle\tilde{\boldsymbol{u}}\rangle_{\text{E}} - \varepsilon\tilde{G}\nabla^2\langle\tilde{\boldsymbol{u}}\rangle_{\text{E}} \\ & - \varepsilon^2(\tilde{\mu}_{\text{B}}+\tfrac{1}{3}\tilde{\mu})\nabla\nabla\cdot\frac{\partial\langle\tilde{\boldsymbol{u}}\rangle_{\text{E}}}{\partial\tau} - \varepsilon^2\tilde{\mu}\nabla^2\frac{\partial\langle\tilde{\boldsymbol{u}}\rangle_{\text{E}}}{\partial\tau}, \end{aligned} \tag{3.156}$$

be an extension of the (linear) Navier operator for viscoelastic solids, where

$$\nabla\langle\cdot\rangle_{\text{E}} \;=\; \Big(\frac{\partial}{\partial x_{\text{i}}},\,\frac{\partial}{\partial z}\Big)\langle\cdot\rangle_{\text{E}} \;=\; \Big(\varepsilon^{\lambda}\frac{\partial}{\partial\chi_{\text{i}}},\,\varepsilon^{\vartheta}\frac{\partial}{\partial\zeta}\Big)\langle\cdot\rangle_{\text{E}}. \tag{3.157}$$

With the aid of (3.76) and (3.156), (3.155) can be rewritten in component form as

$$\begin{aligned}\mathcal{L}_{\mathrm{i}}\langle\tilde{\boldsymbol{u}}\rangle_{\mathrm{E}} \;+\; \varepsilon^{1+\lambda}\,\frac{\beta_{\mathrm{T}}}{\mathrm{c_p}}\frac{\partial\langle\tilde{S}\rangle_{\mathrm{E}}}{\partial\chi_{\mathrm{i}}} \;&=\; \tilde{f}^{\mathrm{E}}_{\mathrm{i}}, \qquad \mathrm{i}=1,2\\ \mathcal{L}_{z}\langle\tilde{\boldsymbol{u}}\rangle_{\mathrm{E}} \;+\; \varepsilon^{1+\vartheta}\,\frac{\beta_{\mathrm{T}}}{\mathrm{c_p}}\frac{\partial\langle\tilde{S}\rangle_{\mathrm{E}}}{\partial\zeta} \;&=\; \tilde{f}^{\mathrm{E}}_{z},\end{aligned} \tag{3.158}$$

where $\tilde{f}^{\mathrm{E}}_{\mathrm{i}}$ and $\tilde{f}^{\mathrm{E}}_{z}$ and are the respective Cartesian components of the ARF. On recalling the definition of the scaled ($O(1)$) instantaneous quantities $\tilde{\mathrm{u}}_{\mathrm{i}}, \tilde{\mathrm{u}}_{z}, \tilde{\mathrm{v}}_{\mathrm{i}}$ and $\tilde{\mathrm{v}}_{z}$ in (3.54), one finds from (3.20b) that

$$\begin{aligned}\tilde{f}^{\mathrm{E}}_{\mathrm{i}} \;&\overset{\varepsilon^{1+\lambda+\vartheta}}{=}\; \varepsilon^{\lambda}\frac{\partial\langle\tilde{\sigma}^{\mathrm{non}}_{\mathrm{ji}}\rangle_{\mathrm{E}}}{\partial\chi_{\mathrm{j}}} + \varepsilon^{\vartheta}\frac{\partial\langle\tilde{\sigma}^{\mathrm{non}}_{z\mathrm{i}}\rangle_{\mathrm{E}}}{\partial\zeta} - \varepsilon^{1+\lambda}\Big\langle\tilde{\rho}\frac{\partial\tilde{\mathrm{v}}_{\mathrm{i}}}{\partial t}\Big\rangle_{\mathrm{E}} - \varepsilon^{1+\lambda}\Big\langle\tilde{\mathrm{v}}_{z}\frac{\partial\tilde{\mathrm{v}}_{\mathrm{i}}}{\partial z}\Big\rangle_{\mathrm{E}},\\ \tilde{f}^{\mathrm{E}}_{z} \;&\overset{\varepsilon^{2+\vartheta}}{=}\; \varepsilon^{\lambda}\frac{\partial\langle\tilde{\sigma}^{\mathrm{non}}_{\mathrm{j}z}\rangle_{\mathrm{E}}}{\partial\chi_{\mathrm{j}}} + \varepsilon^{\vartheta}\frac{\partial\langle\tilde{\sigma}^{\mathrm{non}}_{zz}\rangle_{\mathrm{E}}}{\partial\zeta} - \varepsilon\Big\langle\tilde{\rho}\Big(\frac{\partial\tilde{\mathrm{v}}_{z}}{\partial t}+\varepsilon\tilde{\mathrm{v}}_{z}\frac{\partial\tilde{\mathrm{v}}_{z}}{\partial z}\Big)\Big\rangle_{\mathrm{E}}\\ &\qquad - \varepsilon^{2}\frac{\partial}{\partial\tau}\Big\langle\frac{\partial\tilde{\mathrm{u}}_{z}}{\partial t}\frac{\partial\tilde{\mathrm{u}}_{z}}{\partial z}\Big\rangle_{\mathrm{E}} - \varepsilon\Big\langle\tilde{\mathrm{v}}_{z}\frac{\partial\tilde{\mathrm{v}}_{z}}{\partial z}\Big\rangle_{\mathrm{E}} - \varepsilon^{1+2\lambda}\Big\langle\tilde{\mathrm{v}}_{\mathrm{j}}\frac{\partial\tilde{\mathrm{v}}_{z}}{\partial\chi_{\mathrm{j}}}\Big\rangle_{\mathrm{E}},\end{aligned} \tag{3.159}$$

where $\mathrm{i},\mathrm{j} = 1,2$; $\tilde{\sigma}^{\mathrm{non}}_{\mathrm{ji}}, \tilde{\sigma}^{\mathrm{non}}_{\mathrm{j}z}$ and $\tilde{\sigma}^{\mathrm{non}}_{zz}$ are the Cartesian components of $\tilde{\boldsymbol{\sigma}}^{\mathrm{non}}$; Einstein summation convention is assumed over repeated index j, and "$\overset{\varepsilon^{n}}{=}$" denotes equality with an $O(\varepsilon^{n})$ residual. By virtue of (3.27) and (3.29), one finds that

$$\begin{aligned}\langle\tilde{\sigma}^{\mathrm{non}}_{\mathrm{ji}}\rangle_{\mathrm{E}} \;&\overset{\varepsilon^{1+\vartheta}}{=}\; \varepsilon\,\frac{B+2C+1}{2}\Big\langle\Big(\frac{\partial\tilde{\mathrm{u}}_{z}}{\partial z}\Big)^{2}\Big\rangle_{\mathrm{E}}\delta_{\mathrm{ji}},\\ \langle\tilde{\sigma}^{\mathrm{non}}_{\mathrm{i}z}\rangle_{\mathrm{E}} = \langle\tilde{\sigma}^{\mathrm{non}}_{z\mathrm{i}}\rangle_{\mathrm{E}} \;&\overset{\varepsilon^{1+\lambda+\vartheta}}{=}\; -\varepsilon^{1+\lambda}\,\frac{C-2}{2}\Big\langle\frac{\partial\tilde{\mathrm{u}}_{z}}{\partial z}\Big(\frac{\partial\tilde{\mathrm{u}}_{z}}{\partial\chi_{\mathrm{i}}}+\frac{\partial\tilde{\mathrm{u}}_{\mathrm{i}}}{\partial z}\Big)\Big\rangle_{\mathrm{E}},\\ \langle\tilde{\sigma}^{\mathrm{non}}_{zz}\rangle_{\mathrm{E}} \;&\overset{\varepsilon^{1+\vartheta}}{=}\; \varepsilon\,\frac{B+5}{2}\Big\langle\Big(\frac{\partial\tilde{\mathrm{u}}_{z}}{\partial z}\Big)^{2}\Big\rangle_{\mathrm{E}},\end{aligned}$$

where δ_{ji} denotes the Kronecker delta. On substituting this result into (3.159) and noting via (3.19) and (3.20a) that

$$\begin{aligned}\Big\langle\tilde{\rho}\Big(\frac{\partial\tilde{\mathrm{v}}_{z}}{\partial t}+\varepsilon\tilde{\mathrm{v}}_{z}\frac{\partial\tilde{\mathrm{v}}_{z}}{\partial z}\Big)\Big\rangle_{\mathrm{E}} \;&\overset{\varepsilon^{1+2\lambda}}{=}\; \varepsilon\frac{\partial\langle\tilde{\rho}\tilde{\mathrm{v}}_{z}\rangle_{\mathrm{E}}}{\partial\tau} + \Big\langle\tilde{\mathrm{v}}_{z}\Big(\frac{\partial\tilde{\mathrm{v}}_{z}}{\partial z}+\varepsilon^{2\lambda}\frac{\partial\tilde{\mathrm{v}}_{\mathrm{j}}}{\partial\chi_{\mathrm{j}}}+\varepsilon\frac{\partial\tilde{\rho}\tilde{\mathrm{v}}_{z}}{\partial z}\Big)\Big\rangle_{\mathrm{E}} + \varepsilon\Big\langle\tilde{\rho}\tilde{\mathrm{v}}_{z}\frac{\partial\tilde{\mathrm{v}}_{z}}{\partial z}\Big\rangle_{\mathrm{E}}\\ &\overset{\varepsilon^{1+\vartheta}}{=}\; \varepsilon\frac{\partial\langle\tilde{\rho}\tilde{\mathrm{v}}_{z}\rangle_{\mathrm{E}}}{\partial\tau} + \tfrac{1}{2}\varepsilon^{\vartheta}\frac{\partial\langle\tilde{\mathrm{v}}_{z}^{2}\rangle_{\mathrm{E}}}{\partial\zeta} + \varepsilon^{2\lambda}\Big\langle\tilde{\mathrm{v}}_{z}\frac{\partial\tilde{\mathrm{v}}_{\mathrm{j}}}{\partial\chi_{\mathrm{j}}}\Big\rangle_{\mathrm{E}},\\ \Big\langle\tilde{\mathrm{v}}_{z}\frac{\partial\tilde{\mathrm{v}}_{\mathrm{i}}}{\partial z}\Big\rangle_{\mathrm{E}} \;&\overset{\varepsilon^{\vartheta}}{=}\; -\Big\langle\frac{\partial\tilde{\mathrm{v}}_{z}}{\partial z}\tilde{\mathrm{v}}_{\mathrm{i}}\Big\rangle_{\mathrm{E}} \overset{\varepsilon^{\vartheta}}{=} \Big\langle\frac{\partial\tilde{\rho}}{\partial t}\tilde{\mathrm{v}}_{\mathrm{i}}\Big\rangle_{\mathrm{E}} \overset{\varepsilon^{\vartheta}}{=} -\Big\langle\tilde{\rho}\frac{\partial\tilde{\mathrm{v}}_{\mathrm{i}}}{\partial t}\Big\rangle_{\mathrm{E}},\\ \tilde{\rho} \;&\overset{\varepsilon^{\vartheta}}{=}\; -\frac{\partial\tilde{\mathrm{u}}_{z}}{\partial z},\end{aligned}$$

the components of the ARF can be rewritten as

$$\begin{aligned}
\tilde{f}^{\mathrm{E}}_{\mathrm{i}} &\overset{\varepsilon^{1+\lambda+\vartheta}}{=} \varepsilon^{1+\lambda}\,\frac{B+2C+1}{2}\,\frac{\partial\langle\tilde{\rho}^2\rangle_{\mathrm{E}}}{\partial\chi_{\mathrm{i}}}, \qquad \mathrm{i}=1,2\\
\tilde{f}^{\mathrm{E}}_{z} &\overset{\varepsilon^{1+2\vartheta}}{=} -\,\varepsilon^{1+2\lambda}\frac{C-2}{2}\,\frac{\partial}{\partial\chi_{\mathrm{j}}}\left\langle\frac{\partial\tilde{\mathrm{u}}_z}{\partial z}\left(\frac{\partial\tilde{\mathrm{u}}_z}{\partial\chi_{\mathrm{j}}}+\frac{\partial\tilde{\mathrm{u}}_{\mathrm{j}}}{\partial z}\right)\right\rangle_{\mathrm{E}} + \varepsilon^{1+\vartheta}\,\frac{B+5}{2}\,\frac{\partial\langle\tilde{\rho}^2\rangle_{\mathrm{E}}}{\partial\zeta}\\
&\qquad -\,\varepsilon^{1+\vartheta}\frac{\partial\langle\tilde{\mathrm{v}}_z^2\rangle_{\mathrm{E}}}{\partial\zeta} - \varepsilon^{1+2\lambda}\frac{\partial\langle\tilde{\mathrm{v}}_z\tilde{\mathrm{v}}_{\mathrm{j}}\rangle_{\mathrm{E}}}{\partial\chi_{\mathrm{j}}}.
\end{aligned} \tag{3.160}$$

For a further reduction of $\tilde{f}^{\mathrm{E}}_z$, one may find from (3.19), (3.20a), (3.70) and (3.71) that

$$\tilde{\mathrm{v}}_z \overset{\varepsilon}{=} \frac{\partial\tilde{\mathrm{u}}_z}{\partial t} \overset{\varepsilon^{\vartheta}}{=} -\frac{\partial\tilde{\mathrm{u}}_z}{\partial z} \overset{\varepsilon^{\vartheta}}{=} \tilde{\rho} \tag{3.161}$$

which, in conjunction with (3.20b) and (3.154), yields

$$\begin{aligned}
\frac{\partial}{\partial\chi_{\mathrm{j}}}\left\langle\frac{\partial\tilde{\mathrm{u}}_z}{\partial z}\frac{\partial\tilde{\mathrm{u}}_z}{\partial\chi_{\mathrm{j}}}\right\rangle_{\mathrm{E}} &\overset{\varepsilon^{\vartheta}}{=} -\frac{\partial}{\partial\chi_{\mathrm{j}}}\left\langle\tilde{\mathrm{u}}_z\frac{\partial^2\tilde{\mathrm{u}}_z}{\partial z\partial\chi_{\mathrm{j}}}\right\rangle_{\mathrm{E}} \overset{\varepsilon^{\vartheta}}{=} -\frac{\partial}{\partial\chi_{\mathrm{j}}}\left\langle\tilde{\mathrm{u}}_z\frac{\partial\tilde{\mathrm{v}}_{\mathrm{j}}}{\partial t}\right\rangle_{\mathrm{E}} \overset{\varepsilon^{\vartheta}}{=} \frac{\partial\langle\tilde{\mathrm{v}}_z\tilde{\mathrm{v}}_{\mathrm{j}}\rangle_{\mathrm{E}}}{\partial\chi_{\mathrm{j}}},\\
\frac{\partial}{\partial\chi_{\mathrm{j}}}\left\langle\frac{\partial\tilde{\mathrm{u}}_z}{\partial z}\frac{\partial\tilde{\mathrm{u}}_{\mathrm{j}}}{\partial z}\right\rangle_{\mathrm{E}} &\overset{\varepsilon^{\vartheta}}{=} \frac{\partial}{\partial\chi_{\mathrm{j}}}\left\langle\tilde{\rho}\frac{\partial\tilde{\mathrm{u}}_{\mathrm{j}}}{\partial t}\right\rangle_{\mathrm{E}} \overset{\varepsilon^{\vartheta}}{=} \frac{\partial\langle\tilde{\mathrm{v}}_z\tilde{\mathrm{v}}_{\mathrm{j}}\rangle_{\mathrm{E}}}{\partial\chi_{\mathrm{j}}}.
\end{aligned} \tag{3.162}$$

By virtue of (3.161) and (3.162), (3.160) simplifies to

$$\begin{aligned}
\tilde{f}^{\mathrm{E}}_{\mathrm{i}} &\overset{\varepsilon^{1+\lambda+\vartheta}}{=} \varepsilon^{1+\lambda}\,\frac{B+2C+1}{2}\,\frac{\partial\tilde{I}_{\mathrm{E}}}{\partial\chi_{\mathrm{i}}}, \qquad \mathrm{i}=1,2\\
\tilde{f}^{\mathrm{E}}_{z} &\overset{\varepsilon^{1+2\vartheta}}{=} -\,\varepsilon^{1+2\lambda}\,(C-1)\,\frac{\partial\langle\tilde{\mathrm{v}}_z\tilde{\mathrm{v}}_{\mathrm{j}}\rangle_{\mathrm{E}}}{\partial\chi_{\mathrm{j}}} + \varepsilon^{1+\vartheta}\,\frac{B+3}{2}\,\frac{\partial\tilde{I}_{\mathrm{E}}}{\partial\zeta},
\end{aligned} \tag{3.163}$$

where

$$\tilde{I}_{\mathrm{E}} := \langle\tilde{\rho}^2\rangle_{\mathrm{E}} \overset{\varepsilon}{=} \langle\tilde{p}^2\rangle_{\mathrm{E}}, \qquad \tilde{p} = -\tfrac{1}{3}\mathrm{tr}\tilde{\boldsymbol{\sigma}}. \tag{3.164}$$

Note that the introduction of intensity-like quantity $\tilde{I}_{\mathrm{E}} = \varepsilon^{-2}I_{\mathrm{E}} = O(1)$, $I_{\mathrm{E}} = \langle(\rho-1)^2\rangle_{\mathrm{E}}$ is motivated by the fact that the existing studies focus primarily on the z-component of the ARF that is commonly expressed in terms of the *intensity of the ultrasound field* in the z-direction [7, 9]. Given transducer geometry and output, the latter quantity is computable *a priori*, with an $O(\varepsilon^{\vartheta})$ error, as the mean squared acoustic pressure [68], see also Appendix A.4 as an example.

Entropy contribution. To close the averaged system of equations (3.158), one must bring into consideration the balance of energy (3.20c) due to the presence of mean specific entropy $\langle\tilde{S}\rangle_{\mathrm{E}}$ in the system. Accordingly the "fast" time average of (3.20c) can be computed via (3.30) and (3.31) as

$$\varepsilon\frac{\partial\langle\tilde{S}\rangle_{\mathrm{E}}}{\partial\tau} \overset{\varepsilon^{1+\vartheta}}{=} -\varepsilon\Big\langle\tilde{\mathrm{v}}_z\frac{\partial\tilde{S}}{\partial z}\Big\rangle_{\mathrm{E}} - \varepsilon\tilde{\kappa}\Big\langle(\tilde{T}+\tilde{\rho})\frac{\partial^2\tilde{T}}{\partial z^2}\Big\rangle_{\mathrm{E}} + \varepsilon\Big(\tilde{\mu}_{\mathrm{B}}+\tfrac{4}{3}\tilde{\mu}\Big)\Big\langle\Big(\frac{\partial\tilde{\mathrm{v}}_z}{\partial z}\Big)^2\Big\rangle_{\mathrm{E}}. \tag{3.165}$$

To simplify the right-hand side of the (3.165), it is noted via (3.20c) and (3.71) that

$$\frac{\partial\tilde{S}}{\partial z} \overset{\varepsilon^{\vartheta}}{=} -\frac{\partial\tilde{S}}{\partial t} \overset{\varepsilon^{\vartheta}}{=} -\tilde{\kappa}\frac{\partial^2\tilde{T}}{\partial z^2}. \tag{3.166}$$

Using the latter result together with (3.20a), (3.26), (3.71) and (3.161), the averaged energy equation (3.165) reduces to

$$\frac{\partial\langle\tilde{S}\rangle_{\mathrm{E}}}{\partial\tau} \overset{\varepsilon^{\vartheta}}{=} \tilde{\delta}\,\tilde{I}^*_{\mathrm{E}}, \tag{3.167}$$

where

$$\tilde{\delta} := \tilde{\mu}_{\mathrm{B}}+\tfrac{4}{3}\tilde{\mu}+\frac{\beta_{\mathrm{T}}^2}{\mathrm{c}_{\mathrm{p}}^2}\tilde{\kappa} \tag{3.168}$$

is the so-called *diffusivity of sound* (see Section 3.5.1 in the context of Newtonian fluids), and

$$\tilde{I}^*_{\mathrm{E}} := \Big\langle\Big(\frac{\partial\tilde{\rho}}{\partial t}\Big)^2\Big\rangle_{\mathrm{E}}. \tag{3.169}$$

Boundary conditions. With the averaged balance laws (3.158) and (3.167) written in terms of $\langle\tilde{\boldsymbol{u}}\rangle_{\mathrm{E}}$ and $\langle\tilde{S}\rangle_{\mathrm{E}}$ now in place, the next step is to compute the "fast" time averages of the boundary conditions (3.43) and (3.45) which simulate the action of an oscillating transducer. In terms of the kinematic quantities, one finds from (3.43), (3.73) and (3.74) that

$$\left.\begin{array}{l} \langle\hat{\tilde{\boldsymbol{u}}}\rangle_{\mathrm{L}}\big|_{\Gamma} = 0 \\ \langle\hat{\tilde{\boldsymbol{u}}}\rangle_{\mathrm{L}} \overset{\varepsilon}{=} \langle\tilde{\boldsymbol{u}}\rangle_{\mathrm{E}} \end{array}\right\} \quad\Longrightarrow\quad \langle\tilde{\boldsymbol{u}}\rangle_{\mathrm{E}}\big|_{\Gamma} \overset{\varepsilon}{=} 0. \tag{3.170}$$

In general, (3.170) is complemented by an appropriate set of (mean) boundary conditions germane to the "macro" domain of interest, e.g. the radiation condition at infinity. For clarity, it is emphasized that these "macro" boundary conditions do not enter the computation of the ARF (i.e. the apparent mean body force) as long as the Mach number affiliated with such reflections, arriving at the focal region, is significantly smaller than ε.

With reference to the thermal boundary condition (3.45), one may note that the mean specific entropy solves the *initial value problem* given by (3.167) and the quiescent past condition. From this observation, it is clear that the "fast" time average of (3.45) does not enter the formulation and is hereon disregarded. This peculiar feature of the mean solution stems from the fact that the characteristic diffusion time (reckoned with reference to the "macro" length scale ζ) is much larger than its modulation counterpart. In particular, one finds from (3.165) that $\tilde{\kappa}\langle\nabla^2\tilde{T}\rangle_{\mathrm{E}} = o(\partial\langle\tilde{S}\rangle_{\mathrm{E}}/\partial\tau)$, even though $\tilde{\kappa}\nabla^2\tilde{T} = O(\partial\tilde{S}/\partial t)$ in terms of the instantaneous behavior. In this setting, it is also noted that the system given by (3.158) and (3.167) is *semi-coupled* in that $\langle\tilde{S}\rangle_{\mathrm{E}}$ can be solved independently from (3.167), and then substituted into (3.158) as an additional source term.

3.6.2 Lagrangian formulation

To study the generation of the ARF in the Lagrangian frame of reference, one needs to apply (3.74b) to the balance of linear momentum (3.22b). Following the same procedure as in Section 3.6.1, the "fast" time average of (3.22b) can be computed as

$$\begin{aligned} \mathcal{L}_{\mathrm{i}}\langle\hat{\tilde{\boldsymbol{u}}}\rangle_{\mathrm{L}} \;+\; \varepsilon^{1+\lambda}\frac{\beta_{\mathrm{T}}}{\mathrm{c_p}}\frac{\partial\langle\hat{\tilde{S}}\rangle_{\mathrm{L}}}{\partial\chi_{\mathrm{io}}} \;&=\; \tilde{f}^{\mathrm{L}}_{\mathrm{i}}, \qquad \mathrm{i}=1,2 \\ \mathcal{L}_{z}\langle\hat{\tilde{\boldsymbol{u}}}\rangle_{\mathrm{L}} \;+\; \varepsilon^{1+\vartheta}\frac{\beta_{\mathrm{T}}}{\mathrm{c_p}}\frac{\partial\langle\hat{\tilde{S}}\rangle_{\mathrm{L}}}{\partial\zeta_{\mathrm{o}}} \;&=\; \tilde{f}^{\mathrm{L}}_{z}, \end{aligned} \tag{3.171}$$

where $\mathcal{L}_{\mathrm{i}}\langle\cdot\rangle_{\mathrm{L}}$ and $\mathcal{L}_{z}\langle\cdot\rangle_{\mathrm{L}}$ are given by the Lagrangian version of (3.156), while $\tilde{f}^{\mathrm{L}}_{\mathrm{i}}$ and $\tilde{f}^{\mathrm{L}}_{z}$ are the respective Lagrangian components of the ARF. On decomposing the first Piola-Kirchhoff stress tensor (3.35) as $\hat{\tilde{\boldsymbol{P}}} = \hat{\tilde{\boldsymbol{P}}}^{\mathrm{lin}} + \hat{\tilde{\boldsymbol{P}}}^{\mathrm{non}}$ where $\hat{\tilde{\boldsymbol{P}}}^{\mathrm{lin}}$ is the Lagrangian statement of (3.154) and $\hat{\tilde{\boldsymbol{P}}}^{\mathrm{non}}$ denotes its nonlinear part, one finds from (3.22b) and (3.35)–(3.36) that

$$\begin{aligned} \tilde{f}^{\mathrm{L}}_{\mathrm{i}} \;&=\; \varepsilon^{\lambda}\frac{\partial\langle\hat{\tilde{P}}^{\mathrm{non}}_{\mathrm{ji}}\rangle_{\mathrm{L}}}{\partial\chi_{\mathrm{jo}}} \;+\; \varepsilon^{\vartheta}\frac{\partial\langle\hat{\tilde{P}}^{\mathrm{non}}_{z\mathrm{i}}\rangle_{\mathrm{L}}}{\partial\zeta_{\mathrm{o}}}, \\ \tilde{f}^{\mathrm{L}}_{z} \;&=\; \varepsilon^{\lambda}\frac{\partial\langle\hat{\tilde{P}}^{\mathrm{non}}_{\mathrm{j}z}\rangle_{\mathrm{L}}}{\partial\chi_{\mathrm{jo}}} \;+\; \varepsilon^{\vartheta}\frac{\partial\langle\hat{\tilde{P}}^{\mathrm{non}}_{zz}\rangle_{\mathrm{L}}}{\partial\zeta_{\mathrm{o}}}. \end{aligned} \tag{3.172}$$

where

$$
\begin{aligned}
\langle \hat{\tilde{P}}^{\mathrm{non}}_{\mathrm{ji}} \rangle_{\mathrm{L}} \quad &\overset{\varepsilon^{1+\vartheta}}{=} \quad \varepsilon \frac{B+2C+1}{2} \left\langle \left(\frac{\partial \hat{\tilde{\mathrm{u}}}_z}{\partial z_{\mathrm{o}}} \right)^2 \right\rangle_{\mathrm{L}} \delta_{\mathrm{ji}}, \\
\langle \hat{\tilde{P}}^{\mathrm{non}}_{\mathrm{i}z} \rangle_{\mathrm{L}} \quad &\overset{\varepsilon^{1+\lambda+\vartheta}}{=} \quad -\varepsilon^{1+\lambda} \frac{C}{2} \left\langle \frac{\partial \hat{\tilde{\mathrm{u}}}_z}{\partial z_{\mathrm{o}}} \left(\frac{\partial \hat{\tilde{\mathrm{u}}}_z}{\partial \chi_{\mathrm{io}}} + \frac{\partial \hat{\tilde{\mathrm{u}}}_{\mathrm{i}}}{\partial z_{\mathrm{o}}} \right) \right\rangle_{\mathrm{L}} + \varepsilon^{1+\lambda} \left\langle \frac{\partial \hat{\tilde{\mathrm{u}}}_z}{\partial z_{\mathrm{o}}} \frac{\partial \hat{\tilde{\mathrm{u}}}_z}{\partial \chi_{\mathrm{io}}} \right\rangle_{\mathrm{L}}, \\
\langle \hat{\tilde{P}}^{\mathrm{non}}_{z\mathrm{i}} \rangle_{\mathrm{L}} \quad &\overset{\varepsilon^{1+\lambda+\vartheta}}{=} \quad -\varepsilon^{1+\lambda} \frac{C}{2} \left\langle \frac{\partial \hat{\tilde{\mathrm{u}}}_z}{\partial z_{\mathrm{o}}} \left(\frac{\partial \hat{\tilde{\mathrm{u}}}_z}{\partial \chi_{\mathrm{io}}} + \frac{\partial \hat{\tilde{\mathrm{u}}}_{\mathrm{i}}}{\partial z_{\mathrm{o}}} \right) \right\rangle_{\mathrm{L}} + \varepsilon^{1+\lambda} \left\langle \frac{\partial \hat{\tilde{\mathrm{u}}}_z}{\partial z_{\mathrm{o}}} \frac{\partial \hat{\tilde{\mathrm{u}}}_{\mathrm{i}}}{\partial z_{\mathrm{o}}} \right\rangle_{\mathrm{L}}, \\
\langle \hat{\tilde{P}}^{\mathrm{non}}_{zz} \rangle_{\mathrm{L}} \quad &\overset{\varepsilon^{1+\vartheta}}{=} \quad \varepsilon \frac{B+3}{2} \left\langle \left(\frac{\partial \hat{\tilde{\mathrm{u}}}_z}{\partial z_{\mathrm{o}}} \right)^2 \right\rangle_{\mathrm{L}}.
\end{aligned}
$$

Substitution of the latter result into (3.172) yields

$$
\begin{aligned}
\tilde{f}^{\mathrm{L}}_{\mathrm{i}} &\overset{\varepsilon^{1+\lambda+\vartheta}}{=} \varepsilon^{1+\lambda} \frac{B+2C+1}{2} \frac{\partial}{\partial \chi_{\mathrm{io}}} \left\langle \left(\frac{\partial \hat{\tilde{\mathrm{u}}}_z}{\partial z_{\mathrm{o}}} \right)^2 \right\rangle_{\mathrm{L}}, \qquad \mathrm{i} = 1, 2 \\
\tilde{f}^{\mathrm{L}}_{z} &\overset{\varepsilon^{1+2\vartheta}}{=} -\varepsilon^{1+2\lambda} \frac{C}{2} \frac{\partial}{\partial \chi_{\mathrm{jo}}} \left\langle \frac{\partial \hat{\tilde{\mathrm{u}}}_z}{\partial z_{\mathrm{o}}} \left(\frac{\partial \hat{\tilde{\mathrm{u}}}_z}{\partial \chi_{\mathrm{jo}}} + \frac{\partial \hat{\tilde{\mathrm{u}}}_{\mathrm{j}}}{\partial z_{\mathrm{o}}} \right) \right\rangle_{\mathrm{L}} + \varepsilon^{1+2\lambda} \frac{\partial}{\partial \chi_{\mathrm{jo}}} \left\langle \frac{\partial \hat{\tilde{\mathrm{u}}}_z}{\partial z_{\mathrm{o}}} \frac{\partial \hat{\tilde{\mathrm{u}}}_z}{\partial \chi_{\mathrm{jo}}} \right\rangle_{\mathrm{L}} \\
&\qquad + \varepsilon^{1+\vartheta} \frac{B+3}{2} \frac{\partial}{\partial \zeta_{\mathrm{o}}} \left\langle \left(\frac{\partial \hat{\tilde{\mathrm{u}}}_z}{\partial z_{\mathrm{o}}} \right)^2 \right\rangle_{\mathrm{L}}.
\end{aligned}
\tag{3.173}
$$

On introducing the intensity-like quantity

$$
\tilde{I}_{\mathrm{L}} \; := \; \langle \hat{\tilde{\rho}}^2 \rangle_{\mathrm{L}}, \tag{3.174}
$$

employing the fact that $\hat{\tilde{\rho}} \overset{\varepsilon^{\vartheta}}{=} -\partial \hat{\tilde{\mathrm{u}}}_z / \partial z_{\mathrm{o}}$, and making use of the Lagrangian analogue of (3.161) and (3.162), one may simplify (3.173) as

$$
\begin{aligned}
\tilde{f}^{\mathrm{L}}_{\mathrm{i}} &\overset{\varepsilon^{1+\lambda+\vartheta}}{=} \varepsilon^{1+\lambda} \frac{B+2C+1}{2} \frac{\partial \tilde{I}_{\mathrm{L}}}{\partial \chi_{\mathrm{io}}}, \qquad \mathrm{i} = 1, 2 \\
\tilde{f}^{\mathrm{L}}_{z} &\overset{\varepsilon^{1+2\vartheta}}{=} -\varepsilon^{1+2\lambda} (C-1) \frac{\partial \langle \hat{\tilde{\mathrm{v}}}_z \hat{\tilde{\mathrm{v}}}_{\mathrm{j}} \rangle_{\mathrm{L}}}{\partial \chi_{\mathrm{jo}}} \; + \; \varepsilon^{1+\vartheta} \frac{B+3}{2} \frac{\partial \tilde{I}_{\mathrm{L}}}{\partial \zeta_{\mathrm{o}}}.
\end{aligned}
\tag{3.175}
$$

Entropy contribution and boundary conditions. To close (3.171), the "fast" time average of the balance of energy (3.22c) can be computed with the aid of (3.22a), (3.22b) and (3.34)–(3.38) as

$$
\varepsilon \frac{\partial \langle \hat{\tilde{S}} \rangle_{\mathrm{L}}}{\partial \tau} \overset{\varepsilon^{1+\vartheta}}{=} -\varepsilon \tilde{\kappa} \left\langle \hat{\tilde{T}} \frac{\partial^2 \hat{\tilde{T}}}{\partial {z_{\mathrm{o}}}^2} \right\rangle_{\mathrm{L}} + \varepsilon \Big(\tilde{\mu}_{\mathrm{B}} + \tfrac{4}{3} \tilde{\mu} \Big) \left\langle \left(\frac{\partial \hat{\tilde{\mathrm{v}}}_z}{\partial z_{\mathrm{o}}} \right)^2 \right\rangle_{\mathrm{L}}. \tag{3.176}
$$

By way of (3.22a), (3.22b), (3.34)–(3.38) and (3.65), one may show that (3.176) reduces to

$$\frac{\partial \langle \hat{\tilde{S}} \rangle_{\mathrm{L}}}{\partial \tau} \overset{\varepsilon^{\vartheta}}{=} \tilde{\delta}\, \tilde{I}^{*}_{\mathrm{L}}, \tag{3.177}$$

where $\tilde{\delta}$ is the diffusivity of sound given by (3.168) and

$$\tilde{I}^{*}_{\mathrm{L}} \;:=\; \left\langle \left(\frac{\partial \hat{\tilde{\rho}}}{\partial t} \right)^{2} \right\rangle_{\mathrm{L}}. \tag{3.178}$$

Averaged balance equations (3.171) and (3.177) govern the mean response of a solid in the Lagrangian frame of reference, expressed in terms of the displacement vector and specific entropy. This system is complemented by the (mean) kinematic boundary condition on the transducer's face, which can be found on the basis of (3.43) and (3.74b) to read

$$\langle \hat{\tilde{\boldsymbol{u}}} \rangle_{\mathrm{L}} \big|_{\Gamma} \;=\; 0. \tag{3.179}$$

For completeness it is noted, making reference to the discussion concluding Section 3.6.1, that the thermal boundary condition (3.45) does not enter the problem, and that (3.179) is in general accompanied by a suitable set of "macro" boundary conditions dependent on the geometry of the domain.

3.6.3 Reduced expression of the ARF in terms of intensity derivatives

As examined in Section 3.6.1, spatial description of the ARF depends not only on the intensity of the sound beam $\tilde{I}_{\mathrm{E}}$, but also on quantity $\partial \langle \tilde{\mathrm{v}}_z \tilde{\mathrm{v}}_{\mathrm{j}} \rangle_{\mathrm{E}} / \partial \chi_{\mathrm{j}}$ which requires additional knowledge of the velocity field, produced by the modulated ultrasound beam. A similar comment applies to the results in Section 3.6.2 where the radiation body force is expressed in terms of $\tilde{I}_{\mathrm{L}}$ and $\partial \langle \hat{\tilde{\mathrm{v}}}_z \hat{\tilde{\mathrm{v}}}_{\mathrm{j}} \rangle_{\mathrm{L}} / \partial \chi_{\mathrm{jo}}$. Fortunately, in most situations $\partial \langle \tilde{\mathrm{v}}_z \tilde{\mathrm{v}}_{\mathrm{j}} \rangle_{\mathrm{E}} / \partial \chi_{\mathrm{j}}$ (resp. $\partial \langle \hat{\tilde{\mathrm{v}}}_z \hat{\tilde{\mathrm{v}}}_{\mathrm{j}} \rangle_{\mathrm{L}} / \partial \chi_{\mathrm{jo}}$) can be related to the derivatives of $\tilde{I}_{\mathrm{E}}$ (resp. $\tilde{I}_{\mathrm{L}}$) as shown next, for simplicity, in the Lagrangian frame of reference. In particular, on multiplying the z-component of (3.22b) by $\partial \hat{\tilde{\mathrm{u}}}_z / \partial z_{\mathrm{o}}$, one finds from (3.35)–(3.37) that

$$\begin{aligned}
\frac{\partial \hat{\tilde{\mathrm{u}}}_z}{\partial z_{\mathrm{o}}} \frac{\partial^2 \hat{\tilde{\mathrm{u}}}_z}{\partial t^2} \overset{\varepsilon^{1+\vartheta}}{=} \; & \frac{\partial \hat{\tilde{\mathrm{u}}}_z}{\partial z_{\mathrm{o}}} \frac{\partial^2 \hat{\tilde{\mathrm{u}}}_z}{\partial {z_{\mathrm{o}}}^2} + \varepsilon^{2\lambda} \frac{\partial \hat{\tilde{\mathrm{u}}}_z}{\partial z_{\mathrm{o}}} \frac{\partial^2 \hat{\tilde{\mathrm{u}}}_{\mathrm{i}}}{\partial z_{\mathrm{o}} \partial \chi_{\mathrm{io}}} + \varepsilon \frac{B+3}{2} \frac{\partial \hat{\tilde{\mathrm{u}}}_z}{\partial z_{\mathrm{o}}} \frac{\partial}{\partial z_{\mathrm{o}}} \Big(\frac{\partial \hat{\tilde{\mathrm{u}}}_z}{\partial z_{\mathrm{o}}} \Big)^2 \\
& - \varepsilon \frac{\beta_{\mathrm{T}}}{\mathrm{c_p}} \frac{\partial \hat{\tilde{\mathrm{u}}}_z}{\partial z_{\mathrm{o}}} \frac{\partial \hat{\tilde{S}}}{\partial z_{\mathrm{o}}} + \varepsilon \big(\tilde{\mu}_{\mathrm{B}} + \tfrac{4}{3} \tilde{\mu} \big) \frac{\partial \hat{\tilde{\mathrm{u}}}_z}{\partial z_{\mathrm{o}}} \frac{\partial^2 \hat{\tilde{\mathrm{v}}}_z}{\partial {z_{\mathrm{o}}}^2}.
\end{aligned} \tag{3.180}$$

To compute the "fast" time average of (3.180), it is necessary to evaluate the average of each term. To this end, the Lagrangian counterpart of (3.161), namely

$$\hat{\tilde{\mathrm{v}}}_z \;=\; \frac{\partial\hat{\tilde{\mathrm{u}}}_z}{\partial t} \;\overset{\varepsilon^{\vartheta}}{=}\; -\frac{\partial\hat{\tilde{\mathrm{u}}}_z}{\partial z_{\mathrm{o}}} \;\overset{\varepsilon^{\vartheta}}{=}\; \hat{\tilde{\rho}}, \tag{3.181}$$

together with (3.174) allows one to deal with the acceleration term in (3.180) as

$$\left\langle\frac{\partial\hat{\tilde{\mathrm{u}}}_z}{\partial z_{\mathrm{o}}}\frac{\partial^2\hat{\tilde{\mathrm{u}}}_z}{\partial t^2}\right\rangle_{\mathrm{L}} \;=\; \varepsilon\frac{\partial}{\partial\tau}\left\langle\frac{\partial\hat{\tilde{\mathrm{u}}}_z}{\partial z_{\mathrm{o}}}\frac{\partial\hat{\tilde{\mathrm{u}}}_z}{\partial t}\right\rangle_{\mathrm{L}} - \tfrac{1}{2}\varepsilon^{\vartheta}\frac{\partial}{\partial\zeta_{\mathrm{o}}}\left\langle\left(\frac{\partial\hat{\tilde{\mathrm{u}}}_z}{\partial t}\right)^2\right\rangle_{\mathrm{L}} \;\overset{\varepsilon^{2\vartheta}}{=}\; -\varepsilon\frac{\partial\tilde{I}_{\mathrm{L}}}{\partial\tau} - \tfrac{1}{2}\varepsilon^{\vartheta}\frac{\partial\tilde{I}_{\mathrm{L}}}{\partial\zeta_{\mathrm{o}}}. \tag{3.182}$$

Similarly, the first term on the right-hand side of (3.180) can be computed via (3.174) and (3.181) as

$$\left\langle\frac{\partial\hat{\tilde{\mathrm{u}}}_z}{\partial z_{\mathrm{o}}}\frac{\partial^2\hat{\tilde{\mathrm{u}}}_z}{\partial {z_{\mathrm{o}}}^2}\right\rangle_{\mathrm{L}} \;=\; \tfrac{1}{2}\varepsilon^{\vartheta}\frac{\partial}{\partial\zeta_{\mathrm{o}}}\left\langle\left(\frac{\partial\hat{\tilde{\mathrm{u}}}_z}{\partial z_{\mathrm{o}}}\right)^2\right\rangle_{\mathrm{L}} \;\overset{\varepsilon^{2\vartheta}}{=}\; \tfrac{1}{2}\varepsilon^{\vartheta}\frac{\partial\tilde{I}_{\mathrm{L}}}{\partial\zeta_{\mathrm{o}}}, \tag{3.183}$$

while (3.22b), (3.71) and (3.181) can be used to show that

$$\left\langle\frac{\partial\hat{\tilde{\mathrm{u}}}_z}{\partial z_{\mathrm{o}}}\frac{\partial^2\hat{\tilde{\mathrm{u}}}_{\mathrm{i}}}{\partial z_{\mathrm{o}}\partial\chi_{\mathrm{io}}}\right\rangle_{\mathrm{L}} \overset{\varepsilon^{\vartheta}}{=} \frac{\partial}{\partial\chi_{\mathrm{io}}}\left\langle\frac{\partial\hat{\tilde{\mathrm{u}}}_z}{\partial t}\frac{\partial\hat{\tilde{\mathrm{u}}}_{\mathrm{i}}}{\partial t}\right\rangle_{\mathrm{L}} - \left\langle\frac{\partial^2\hat{\tilde{\mathrm{u}}}_z}{\partial z_{\mathrm{o}}\partial\chi_{\mathrm{io}}}\frac{\partial\hat{\tilde{\mathrm{u}}}_{\mathrm{i}}}{\partial z_{\mathrm{o}}}\right\rangle_{\mathrm{L}} \overset{\varepsilon^{\vartheta}}{=} \frac{\partial\langle\hat{\tilde{\mathrm{v}}}_z\hat{\tilde{\mathrm{v}}}_{\mathrm{i}}\rangle_{\mathrm{L}}}{\partial\chi_{\mathrm{io}}} + \left\langle\frac{\partial^2\hat{\tilde{\mathrm{u}}}_{\mathrm{i}}}{\partial t^2}\frac{\partial\hat{\tilde{\mathrm{u}}}_{\mathrm{i}}}{\partial t}\right\rangle_{\mathrm{L}} \overset{\varepsilon^{\vartheta}}{=} \frac{\partial\langle\hat{\tilde{\mathrm{v}}}_z\hat{\tilde{\mathrm{v}}}_{\mathrm{i}}\rangle_{\mathrm{L}}}{\partial\chi_{\mathrm{io}}}. \tag{3.184}$$

The term multiplying $(B+3)/2$ is negligible because

$$\left\langle\frac{\partial\hat{\tilde{\mathrm{u}}}_z}{\partial z_{\mathrm{o}}}\frac{\partial}{\partial z_{\mathrm{o}}}\left(\frac{\partial\hat{\tilde{\mathrm{u}}}_z}{\partial z_{\mathrm{o}}}\right)^2\right\rangle_{\mathrm{L}} \;=\; \tfrac{2}{3}\varepsilon^{\vartheta}\frac{\partial}{\partial\zeta_{\mathrm{o}}}\left\langle\left(\frac{\partial\hat{\tilde{\mathrm{u}}}_z}{\partial z_{\mathrm{o}}}\right)^3\right\rangle_{\mathrm{L}} \;\overset{\varepsilon^{\vartheta}}{=}\; 0. \tag{3.185}$$

On the other hand, the entropy term can be shown via (3.34), the Lagrangian statement of (3.166) and (3.181) to read

$$\left\langle\frac{\partial\hat{\tilde{\mathrm{u}}}_z}{\partial z_{\mathrm{o}}}\frac{\partial\hat{\tilde{S}}}{\partial z_{\mathrm{o}}}\right\rangle_{\mathrm{L}} \;\overset{\varepsilon^{\vartheta}}{=}\; -\tilde{\kappa}\left\langle\frac{\partial\hat{\tilde{\mathrm{u}}}_z}{\partial z_{\mathrm{o}}}\frac{\partial^2\hat{\tilde{T}}}{\partial {z_{\mathrm{o}}}^2}\right\rangle_{\mathrm{L}} \;\overset{\varepsilon^{\vartheta}}{=}\; \tilde{\kappa}\frac{\beta_{\mathrm{T}}}{\mathrm{c_p}}\left\langle\frac{\partial\hat{\tilde{\mathrm{u}}}_z}{\partial z_{\mathrm{o}}}\frac{\partial^3\hat{\tilde{\mathrm{u}}}_z}{\partial {z_{\mathrm{o}}}^3}\right\rangle_{\mathrm{L}} \;\overset{\varepsilon^{\vartheta}}{=}\; -\tilde{\kappa}\frac{\beta_{\mathrm{T}}}{\mathrm{c_p}}\tilde{I}^*_{\mathrm{L}}. \tag{3.186}$$

Finally, the viscosity term can be written using (3.181) as

$$\left\langle\frac{\partial\hat{\tilde{\mathrm{u}}}_z}{\partial z_{\mathrm{o}}}\frac{\partial^2\hat{\tilde{\mathrm{v}}}_z}{\partial {z_{\mathrm{o}}}^2}\right\rangle_{\mathrm{L}} \;\overset{\varepsilon^{\vartheta}}{=}\; -\left\langle\hat{\tilde{\rho}}\frac{\partial^2\hat{\tilde{\rho}}}{\partial t^2}\right\rangle_{\mathrm{L}} \;\overset{\varepsilon^{\vartheta}}{=}\; \tilde{I}^*_{\mathrm{L}}. \tag{3.187}$$

Combining (3.182)–(3.187), the "fast" time average of (3.180) reduces to

$$\varepsilon^{1-2\lambda}\frac{\partial\tilde{I}_{\mathrm{L}}}{\partial\tau} \;+\; \varepsilon^{\vartheta-2\lambda}\frac{\partial\tilde{I}_{\mathrm{L}}}{\partial\zeta_{\mathrm{o}}} \;+\; \varepsilon^{1-2\lambda}\tilde{\delta}\tilde{I}^*_{\mathrm{L}} \;+\; \frac{\partial\langle\hat{\tilde{\mathrm{v}}}_z\hat{\tilde{\mathrm{v}}}_{\mathrm{i}}\rangle_{\mathrm{L}}}{\partial\chi_{\mathrm{io}}} \;\overset{\varepsilon^{2\vartheta-2\lambda}}{=}\; 0, \tag{3.188}$$

which allows the $\partial\langle\hat{\tilde{\mathrm{v}}}_z\hat{\tilde{\mathrm{v}}}_{\mathrm{i}}\rangle_{\mathrm{L}}/\partial\chi_{\mathrm{io}}$ term, which enters the ARF expression, to be expressed in terms of intensity derivatives. From (3.175) and (3.188), one in particular finds that the ARF formula in the Lagrangian frame of reference admits vector representation

$$\tilde{\boldsymbol{f}}^{\mathrm{L}} \overset{\varepsilon^{1+\vartheta+(\lambda,\vartheta)}}{=} \varepsilon(C-1-\beta)\nabla_{\mathrm{o}}\tilde{I}_{\mathrm{L}} + \varepsilon^2(C-1)\Big(\tilde{\delta}\tilde{I}^*_{\mathrm{L}} + \frac{\partial\tilde{I}_{\mathrm{L}}}{\partial\tau}\Big)\boldsymbol{e}_z, \qquad \nabla_{\mathrm{o}} = \Big(\varepsilon^{\lambda}\frac{\partial}{\partial\chi_{\mathrm{io}}}, \varepsilon^{\vartheta}\frac{\partial}{\partial\zeta_{\mathrm{o}}}\Big), \tag{3.189}$$

where $\tilde{\boldsymbol{f}}^{\mathrm{L}} = (\tilde{f}^{\mathrm{L}}_{\mathrm{i}}, \tilde{f}^{\mathrm{L}}_z)$; $\boldsymbol{e}_z$ is the unit vector in the z-direction; $\beta = -(B+3)/2$ is the coefficient of (acoustic) nonlinearity introduced in (3.42), and symbol "$\varepsilon^{1+\vartheta+(\lambda,\vartheta)}$" indicates that $\tilde{f}^{\mathrm{L}}_{\mathrm{i}}$ and $\tilde{f}^{\mathrm{L}}_z$ are approximated with respective accuracies $O(\varepsilon^{1+\lambda+\vartheta})$ and $O(\varepsilon^{1+2\vartheta})$. In a similar fashion, the Eulerian expression for the radiation body force can be obtained as

$$\tilde{\boldsymbol{f}}^{\mathrm{E}} \overset{\varepsilon^{1+\vartheta+(\lambda,\vartheta)}}{=} \varepsilon(C-1-\beta)\nabla\tilde{I}_{\mathrm{E}} + \varepsilon^2(C-1)\Big(\tilde{\delta}\tilde{I}^*_{\mathrm{E}} + \frac{\partial\tilde{I}_{\mathrm{E}}}{\partial\tau}\Big)\boldsymbol{e}_z, \qquad \nabla = \Big(\varepsilon^{\lambda}\frac{\partial}{\partial\chi_{\mathrm{i}}}, \varepsilon^{\vartheta}\frac{\partial}{\partial\zeta}\Big). \tag{3.190}$$

With reference to (3.189) and (3.190), it is noted that the restriction $\lambda > \frac{1}{4}$ introduced in (3.49) becomes important at this point. In particular when $\lambda < \frac{1}{4}$, the $O(\varepsilon^2)$ axial component of the ARF (which is proportional to $C-1$ and is the main focus of biomedical applications) becomes smaller than its approximation accuracy $O(\varepsilon^{1+2\vartheta}) = O(\varepsilon^{1+2\min\{1,2\lambda\}})$. In this case (3.189) and (3.190) cease to be useful and their "mother" counterparts, given respectively by (3.175) and (3.163), should be used instead.

3.6.4 Comments on the result

Eulerian vs. Lagrangian formulation. From the results in Sections 3.6.1 and 3.6.2, it is apparent that there is no formal difference between the Lagrangian and Eulerian formulations of the boundary value problem governing the *mean* displacement and specific entropy. Given the fact that the analysis of the ARF is essentially a second-order problem, this equivalence is however far from obvious, and could not have been asserted without a detailed analysis. Indeed, it is noted that the parity between the mean Lagrangian and Eulerian formulations is strongly dependent on the choice of independent variables. In particular, one finds from (3.19) and (3.164) that

$$\langle\hat{\tilde{\mathrm{v}}}_z\rangle_{\mathrm{L}} = \varepsilon\frac{\partial\langle\hat{\tilde{\mathrm{u}}}_z\rangle_{\mathrm{L}}}{\partial\tau}, \qquad \langle\tilde{\mathrm{v}}_z\rangle_{\mathrm{E}} \overset{\varepsilon^{1+2\lambda}}{=} \varepsilon\frac{\partial\langle\tilde{\mathrm{u}}_z\rangle_{\mathrm{E}}}{\partial\tau} + \varepsilon\Big\langle\tilde{\mathrm{v}}_z\frac{\partial\tilde{\mathrm{u}}_z}{\partial z}\Big\rangle_{\mathrm{E}} \overset{\varepsilon^{1+\vartheta}}{=} \varepsilon\frac{\partial\langle\tilde{\mathrm{u}}_z\rangle_{\mathrm{E}}}{\partial\tau} + \varepsilon\tilde{I}_{\mathrm{E}},$$

which demonstrates that the Lagrangian and Eulerian variants of the boundary value problems written in terms of $\langle\tilde{\boldsymbol{v}}\rangle$ and $\langle\tilde{S}\rangle$ (in lieu of $\langle\tilde{\boldsymbol{u}}\rangle$ and $\langle\tilde{S}\rangle$) are in fact different. For completeness, it is noted that similar differences (between the Eulerian and Lagrangian averages of the same quantity) appear when dealing with the mean mass density or pressure in nonlinear acoustics, which leads to a well studied distinction between the so-called Rayleigh and Langevin radiation pressures on an obstacle exposed to elevated-intensity ultrasound [7, 69].

Limiting case of plane-wave propagation. For verification purposes, it is important to consider the limiting case of plane waves, and compare it with the solution in Section 3.5. On the basis of the foregoing developments, the sought plane-wave limit can be immediately computed by setting $\partial(\cdot)/\partial\chi_{\mathrm{i}} = 0$ and $\vartheta = 1$. Under this restriction, one finds by way of the Eulerian statement of (3.188) and (3.190) that (3.158) reduces to

$$\mathcal{L}_z\langle\tilde{\boldsymbol{u}}\rangle_{\mathrm{E}} \;+\; \varepsilon^2\frac{\beta_{\mathrm{T}}}{\mathrm{c_p}}\frac{\partial\langle\tilde{S}\rangle_{\mathrm{E}}}{\partial\zeta} \;\overset{\varepsilon^3}{=}\; \varepsilon^2\beta\Big(\tilde{\delta}\,\tilde{I}^*_{\mathrm{E}} + \frac{\partial\tilde{I}_{\mathrm{E}}}{\partial\tau}\Big),$$

where the acoustic radiation force, given by the term on the right-hand side, coincides with the result (3.116), obtained assuming propagation of modulated plane waves through a Newtonian fluid.

Computation of intensity-like quantities. Taking (3.190) as an example, it is clear that a prerequisite for computing the ARF is the knowledge of intensity-like quantities $\tilde{I}_{\mathrm{E}}(\boldsymbol{x},t) = \langle\tilde{\rho}^2\rangle_{\mathrm{E}}$ and $\tilde{I}^*_{\mathrm{E}}(\boldsymbol{x},t) = \langle(\partial\tilde{\rho}/\partial t)^2\rangle_{\mathrm{E}}$ within the focal region. This in turn requires solving the original nonlinear system (3.20), at the ultrasound time scale, for a given set of transducer characteristics and tissue properties. Due to the smallness of the germane shear modulus, however, $\tilde{I}_{\mathrm{E}}$ and $\tilde{I}^*_{\mathrm{E}}$ are in ARF applications commonly computed from an approximate ultrasound solution which solves the *linearized* version of (3.20) for a *viscous fluid* [10, 11], see also Appendix A.4. In dealing with the modulated beam problem, it can be in particular shown (see Chapter 4) that

$$\tilde{I}_{\mathrm{E}}(\boldsymbol{x},t) \;=\; \tilde{I}_{\mathrm{E,nm}}(\boldsymbol{x})\,\mathcal{M}^2(\varepsilon t - \varepsilon z), \qquad \tilde{I}^*_{\mathrm{E}}(\boldsymbol{x},t) \;=\; \tilde{I}^*_{\mathrm{E,nm}}(\boldsymbol{x})\,\mathcal{M}^2(\varepsilon t - \varepsilon z), \tag{3.191}$$

under the premise of linear approximation, where $\tilde{I}_{\mathrm{E,nm}}$ and $\tilde{I}^*_{\mathrm{E,nm}}$ are time-invariant intensity fields corresponding to the non-modulated beam problem. To incorporate the non-linear effects into the computation of $\tilde{I}_{\rm E}$ and $\tilde{I}^*_{\rm E}$, the underpinning ultrasound solution (in this case $\tilde{\rho}$) can alternatively be solved from the so-called KZK equation for viscous fluids [39, 9, 7], which approximates (3.20) within the focal region under the premise of quasi-plane waves, given by (3.54) with $\lambda = \frac{1}{2}$. An extension of the KZK equation to modulated ultrasound fields, that is beyond the scope of this section, is examined in Chapter 4. In either (linear or nonlinear) approach, the featured approximations of $\tilde{I}_{\rm E}$ and $\tilde{I}^*_{\rm E}$ are accordingly computed i) independent of the shear modulus, and ii) assuming acoustic tissue properties (wave speed and attenuation) that are representative of a given tissue type. This very feature is the driving force behind the use of the ARF for the local shear modulus interrogation in soft tissues that is, in contrast to their acoustic properties, found to vary sharply for a variety of cancers.

Relationship between $\tilde{I}_{\rm E}$ and $\tilde{I}^*_{\rm E}$. In situations where $\tilde{I}_{\rm E}$ and $\tilde{I}^*_{\rm E}$ are computed on the basis of the *linear* acoustic solution, it follows from (3.43) and linearity of the problem that $\partial\tilde{\rho}/\partial t(\boldsymbol{x},t) \overset{\varepsilon}{=} \tilde{\rho}(\boldsymbol{x},t+\pi/2)$ whereby $\tilde{I}_{\rm E} \overset{\varepsilon}{=} \tilde{I}^*_{\rm E}$. If the two quantities are computed from a *non-linear* solution (e.g. that solving the KZK equation), on the other hand, one may expand the resulting mass density fluctuations in "fast" time Fourier series as

$$\tilde{\rho} \;=\; \sum_{k=1}^{\infty} \tilde{\rho}^{(k)}, \tag{3.192}$$

where $\tilde{\rho}^{(k)}$ denotes the kth solution component with dominant dimensionless frequency equaling k, so that $\partial\tilde{\rho}^{(k)}/\partial t(\boldsymbol{x},t) \overset{\varepsilon}{=} k\,\tilde{\rho}^{(k)}(\boldsymbol{x},t+\pi/2)$. On recalling the definition of the "fast" time average (3.74a), one finds that

$$\begin{aligned} I_{\rm E} = \Big\langle\Big(\sum_{k=1}^{\infty}\tilde{\rho}^{(k)}\Big)^2\Big\rangle_{\rm E} \;&=\; \sum_{k=1}^{\infty}\tilde{I}^{(k)}_{\rm E}, \qquad \tilde{I}^{(k)}_{\rm E} = \big\langle\big(\tilde{\rho}^{(k)}\big)^2\big\rangle_{\rm E}, \\ \tilde{\delta}\tilde{I}^*_{\rm E} \;\overset{\varepsilon}{=}\; \tilde{\delta}\Big\langle\Big(\sum_{k=1}^{\infty}k\,\tilde{\rho}^{(k)}\Big)^2\Big\rangle_{\rm E} \;&=\; \sum_{k=1}^{\infty}\tilde{\delta}k^2\tilde{I}^{(k)}_{\rm E}. \end{aligned} \tag{3.193}$$

At this point one may note that a linear plane wave, propagating at frequency k in an isotropic Kelvin-Voigt material whose constitutive behavior is given by (3.154), will experience exponential decay $e^{-\varepsilon\tilde{\alpha}^{(k)}z}$ in the direction of propagation, where $\tilde{\alpha}^{(k)} = \frac{1}{2}\tilde{\delta}k^2$ and $\tilde{\delta}$ is given by (3.168), see [70, 71]. Accordingly, one finds from (3.193) that

$$\tilde{\delta}\tilde{I}^*_{\rm E} \;\overset{\varepsilon}{=}\; \sum_{k=1}^{\infty}2\tilde{\alpha}^{(k)}\tilde{I}^{(k)}_{\rm E} \;:=\; 2\tilde{\alpha}\tilde{I}_{\rm E}, \qquad \tilde{\alpha} \;=\; \frac{1}{\tilde{I}_{\rm E}}\sum_{k=1}^{\infty}\tilde{\alpha}^{(k)}\tilde{I}^{(k)}_{\rm E}, \tag{3.194}$$

where $\tilde{\alpha}$ denotes an *effective attenuation coefficient* for the nonlinear ultrasound problem at hand, that accounts for disparate attenuation rates affiliated with higher-order harmonics and scales as $\tilde{\alpha} = \alpha/\varepsilon = O(1)$, see (3.14).

Compact formulation of the mean equation of motion. As examined in Sec. 3.6.4, there is formally no difference between the averaged governing equations written in the Eulerian and Lagrangian frames of reference, as long as the formulation is written in terms of $\langle \tilde{\boldsymbol{u}} \rangle$ and $\langle \tilde{S} \rangle$. In this case it is no longer necessary to track both formulations, and one may proceed with the Eulerian description only. On dispensing with all scaling and residuals (but keeping everything dimensionless), the balance of linear momentum (3.158) can be rewritten by virtue of (3.18), (3.164), (3.167), (3.190) and (3.194) as

$$\boldsymbol{\mathcal{L}}\langle \boldsymbol{u} \rangle_{\mathrm{E}} \;=\; \boldsymbol{f}^{\mathrm{E}}_{\mathrm{pot}} \;+\; \boldsymbol{f}^{\mathrm{E}}_{\mathrm{dir}}, \tag{3.195}$$

where the *potential* and *directional* body force fields are given respectively by

$$\boldsymbol{f}^{\mathrm{E}}_{\mathrm{pot}} \;=\; \nabla\Big((C{-}1{-}\beta)I_{\mathrm{E}} - \frac{\beta_{\mathrm{T}}}{\mathrm{c_p}}\int_0^t 2\alpha I_{\mathrm{E}}\, dt'\Big), \qquad \boldsymbol{f}^{\mathrm{E}}_{\mathrm{dir}} \;=\; (C{-}1)\Big(2\alpha I_{\mathrm{E}} + \frac{\partial I_{\mathrm{E}}}{\partial t}\Big)\boldsymbol{e}_z. \tag{3.196}$$

Here $\nabla = (\partial/\partial x_{\mathrm{i}},\, \partial/\partial z)$, and the scaling-free Navier operator is given by

$$\boldsymbol{\mathcal{L}}\langle \boldsymbol{u} \rangle_{\mathrm{E}} \;=\; \frac{\partial^2 \langle \boldsymbol{u} \rangle_{\mathrm{E}}}{\partial t^2} \;-\; (1{-}G)\nabla\nabla\cdot\langle \boldsymbol{u} \rangle_{\mathrm{E}} \;-\; G\nabla^2\langle \boldsymbol{u} \rangle_{\mathrm{E}} \;-\; (\mu_{\mathrm{B}}{+}\tfrac{1}{3}\mu)\nabla\nabla\cdot\frac{\partial \langle \boldsymbol{u} \rangle_{\mathrm{E}}}{\partial t} \;-\; \mu\nabla^2\frac{\partial \langle \boldsymbol{u} \rangle_{\mathrm{E}}}{\partial t}. \tag{3.197}$$

Note that the entropy term, featured in (3.158), is treated as a source term and accordingly moved to the right-hand side of (3.195) which is composed of two distinct components. The first one, given by a potential force, causes only irrotational motion (in the absence of domain boundaries), while the second component, representing the body force in the direction of the ultrasound beam, also causes shear motion. Since the local interrogation of the tissue's shear modulus is of primary interest in many ARF applications, the potential part of the mean body force is usually disregarded, and the term "ARF" is reserved for its directional component [9, 12, 22].

Tissue homogeneity. The basic premise underpinning the proposed formula for the ARF is that the tissue-like solid is *homogeneous* as examined in Section 3.1. In the context of (3.196), however, it is important to recognize that the featured restriction of tissue homogeneity *applies only to the focal region*, see Fig. 3.2. In particular if the tissue is heterogeneous outside of the focal region, formulas (3.196) still apply, except for the fact that the "global" tissue heterogeneity must be accounted for when computing the intensity field I_{E}. In ultrasound applications, the latter difficulty is often circumvented by making use of the linear acoustic approximation of I_{E} and the fact that the small-amplitude sound speed varies little between a wide range of soft tissues [7].

Generation of shear waves. From (3.195), one may decompose the mean displacement field as

$$\langle \boldsymbol{u} \rangle_{\mathrm{E}} \;=\; \langle \boldsymbol{u} \rangle_{\mathrm{E}}^{\mathrm{pot}} \;+\; \langle \boldsymbol{u} \rangle_{\mathrm{E}}^{\mathrm{dir}}, \tag{3.198}$$

where $\langle \boldsymbol{u} \rangle_{\mathrm{E}}^{\mathrm{pot}}$ and $\langle \boldsymbol{u} \rangle_{\mathrm{E}}^{\mathrm{dir}}$ are generated respectively by $\boldsymbol{f}_{\mathrm{pot}}^{\mathrm{E}}$ and $\boldsymbol{f}_{\mathrm{dir}}^{\mathrm{E}}$. Clearly, $\langle \boldsymbol{u} \rangle_{\mathrm{E}}^{\mathrm{pot}}$ is an irrotational field and thus associated with *long-wavelength* compressional waves. To understand the nature of $\langle \boldsymbol{u} \rangle_{\mathrm{E}}^{\mathrm{dir}}$, on the other hand, one finds by way of (3.157) and (3.196) that $|\nabla \cdot \boldsymbol{f}_{\mathrm{dir}}^{\mathrm{E}}| / \, \| \nabla \times \boldsymbol{f}_{\mathrm{dir}}^{\mathrm{E}} \| = O(\varepsilon^{\vartheta - \lambda}) \ll 1$ when $\frac{1}{4} < \lambda < 1$. On employing the Helmholtz potential representation of the linear visco-elastodynamic field $\langle \boldsymbol{u} \rangle_{\mathrm{E}}^{\mathrm{dir}}$ as in [72], it can be shown that the latter motion is predominantly solenoidal, i.e. associated with *short-wavelength* shear wave motion, whereby

$$\frac{\partial^2 \langle \boldsymbol{u} \rangle_{\mathrm{E}}^{\mathrm{dir}}}{\partial t^2} \;-\; G \nabla^2 \langle \boldsymbol{u} \rangle_{\mathrm{E}}^{\mathrm{dir}} \;-\; \mu \nabla^2 \frac{\partial \langle \boldsymbol{u} \rangle_{\mathrm{E}}^{\mathrm{dir}}}{\partial t} \;=\; \boldsymbol{f}_{\mathrm{dir}}^{\mathrm{E}}, \tag{3.199}$$

again omitting the accuracy of approximation for simplicity. The z-component of (3.199), that is commonly used to describe the propagation of shear waves generated emanating from the focal region [9], can accordingly be written as

$$\frac{\partial^2 \langle u_z \rangle_{\mathrm{E}}^{\mathrm{dir}}}{\partial t^2} \;-\; G \nabla_{\perp}^2 \langle u_z \rangle_{\mathrm{E}}^{\mathrm{dir}} \;-\; \mu \nabla_{\perp}^2 \frac{\partial \langle u_z \rangle_{\mathrm{E}}^{\mathrm{dir}}}{\partial t} \;=\; f_{z,\mathrm{dir}}^{\mathrm{E}}, \qquad f_{z,\mathrm{dir}}^{\mathrm{E}} = (C-1)\Big(2\alpha I_{\mathrm{E}} + \frac{\partial I_{\mathrm{E}}}{\partial t} \Big), \tag{3.200}$$

in the case of a modulated ultrasound beam, where the Laplacian operator is approximated by its transverse component $\nabla_{\perp}^2 = \partial^2 / \partial x_{\mathrm{i}} \partial x_{\mathrm{i}} = \nabla^2 + O(\varepsilon^{2\vartheta})$. In an experimental setting, $\langle u_z \rangle_{\mathrm{E}}$ (i.e. the total axial motion) is typically monitored by a low-intensity, imaging ultrasound transducer (or an array thereof) [15, 10, 73]. In many situations, $\langle u_z \rangle_{\mathrm{E}}^{\mathrm{dir}}$ can be extracted from $\langle u_z \rangle_{\mathrm{E}}$ via either suitable high-pass filtering in the radial wavenumber domain, or natural separation in the time domain for short pulses [10] which permits the use of (3.200). If, on the other hand, the extraction of $\langle u_z \rangle_{\mathrm{E}}^{\mathrm{dir}}$ is not possible, the observations of $\langle u_z \rangle_{\mathrm{E}}$ must be interpreted via the *coupled* system (3.195). In this case, however, the specification of the ARF entails three additional material parameters, namely the coefficient of acoustic nonlinearity β given by (3.42, the coefficient of thermal expansion β_{T}, and the specific heat capacity at constant pressure $\mathrm{c_p}$.

Comparison with the existing model. The existing theory of the ARF [39] dealing with focused beams is derived assuming *Newtonian fluid* as the propagation medium, and *non-modulated* ultrasound field. To study the problem of ARF generation and consequent shear wave motion in soft tissues due to modulated ultrasound, on the other hand, the foregoing theory is modified in a somewhat heuristic fashion by: i) transplanting the ARF, computed for Newtonian fluids, to soft solids, and ii) multiplying the ARF computed for non-modulated ultrasound field by the squared modulation envelope, see [9]. Formally, these two modifications result in the mean balance of linear momentum whose statement in the z-direction can be written as

$$\frac{\partial^2 \langle w_z \rangle_{\mathrm{E}}^{\mathrm{dir}}}{\partial t^2} \;-\; G\nabla_{\perp}^2 \langle w_z \rangle_{\mathrm{E}}^{\mathrm{dir}} \;-\; \mu\,\nabla_{\perp}^2 \frac{\partial \langle w_z \rangle_{\mathrm{E}}^{\mathrm{dir}}}{\partial t} \;=\; g_{z,\mathrm{dir}}^{\mathrm{E}}, \qquad g_{z,\mathrm{dir}}^{\mathrm{E}} = 2\alpha I_{\mathrm{E,nm}}\,\mathcal{M}^2(\varepsilon t), \tag{3.201}$$

where $\langle w_z \rangle_{\mathrm{E}}^{\mathrm{dir}}$ is an approximation of the mean response due to modulated ultrasound beam, and $I_{\mathrm{E,nm}}$ the intensity of the non-modulated ultrasound field [9]. To facilitate the comparison between (3.200) and (3.201), the emphasis is hereon made on the linear approximation of the intensity field which permits, by way of (3.191), the respective body force terms to be written as

$$\begin{aligned} f_{z,\mathrm{dir}}^{\mathrm{E}} &= (C-1)\,2\,I_{\mathrm{E,nm}}\Big(\alpha\,\mathcal{M}^2(\varepsilon t - \varepsilon z) + \varepsilon\,\mathcal{M}'(\varepsilon t - \varepsilon z)\mathcal{M}(\varepsilon t - \varepsilon z)\Big), \\ g_{z,\mathrm{dir}}^{\mathrm{E}} &= 2\alpha I_{\mathrm{E,nm}}\,\mathcal{M}^2(\varepsilon t), \end{aligned} \tag{3.202}$$

where $\mathcal{M}(\cdot)$ is the prescribed modulation envelope, and $I_{\mathrm{E,nm}} = I_{\mathrm{E,nm}}(\boldsymbol{x})$. In this setting, the key differences between the proposed model and its predecessor can be summarized as follows.

- With reference to (3.195) and (3.198), $f_{z,\mathrm{dir}}^{\mathrm{E}}$ and $\langle u_z \rangle_{\mathrm{E}}^{\mathrm{dir}}$ in (3.200) represent the respective directional components of the radiation body force and induced mean displacement in the z-direction. From the discussion in [9], it is unclear whether the quantities herein denoted by $g_{z,\mathrm{dir}}^{\mathrm{E}}$ and $\langle w_z \rangle_{\mathrm{E}}^{\mathrm{dir}}$ in (3.201) in fact signify the *total* quantities or their *directional* components. For the sake of discussion, it is hereon assumed that the latter is the case. In situations where one is unable to extract $\langle u_z\rangle_{\mathrm{E}}^{\mathrm{dir}}$ from the experimental observations of $\langle u_z\rangle_{\mathrm{E}}$, however, one must consider the coupled system (3.195) that includes the potential component of the radiation body force, $\boldsymbol{f}_{\mathrm{pot}}^{\mathrm{E}}$, see (3.196).

- In the case of no modulation ($\mathcal{M}\equiv 1$), the expressions for $f_{z,\mathrm{dir}}^{\mathrm{E}}$ and $g_{z,\mathrm{dir}}^{\mathrm{E}}$ are identical except for the factor $(C-1)$, where C is the hyperelastic nonlinearity coefficient given by (3.28). Given the facts that the formula for $g_{z,\mathrm{dir}}^{\mathrm{E}}$ is derived assuming *Newtonian fluid* as the propagation medium and that $C\to 2$ in the limit of a Newtonian fluid, see (3.39), one finds that $(C-1)$ (rather than unity) is the appropriate coefficient for the ARF in tissue-like *solids* described as an elastic material with heat conduction and viscosity [48].

- Owing to the presence of argument $\varepsilon t-\varepsilon z$, the radiation body force $f_{z,\mathrm{dir}}^{\mathrm{E}}$ *propagates* within the focal zone with the speed of small-amplitude compressional waves (recall the normalization scheme in Table 2.1). In contrast, the previous approximation $g_{z,\mathrm{dir}}^{\mathrm{E}}$ assumes the radiation force to take the form of a *standing wave* by enforcing the separation of variables in terms of $\boldsymbol{x}$ and t. For completeness, it is noted that the analogous finding has been reported in the context of elevated-intensity plane waves propagating through a Newtonian fluid [19] (also see Section 3.5.1). In the applications of the ARF, the featured propagation effect (i.e. the difference between $\mathcal{M}(\varepsilon t-\varepsilon z)$ and $\mathcal{M}(\varepsilon t)$) becomes important at modulation frequencies on the order of 10 kHz where the change in the phase of $f_{z,\mathrm{dir}}^{\mathrm{E}}$ within the focal zone becomes meaningful, see [17, 42] for examples of the use of such modulation frequencies.

- In comparison with $g_{z,\mathrm{dir}}^{\mathrm{E}}$, the expression for the ARF given by $f_{z,\mathrm{dir}}^{\mathrm{E}}$ contains an additional, *modulation-driven term* which is proportional to the time derivative of ultrasound intensity, see also (3.200). Making reference to (3.202), it is noted that this term is of the same order as the first, *attenuation-driven term* due to the fact that $\alpha = O(\varepsilon)$, see (3.14). The presence of the modulation-driven term allows one to control the magnitude of the ARF by changing the frequency of modulation (which directly affects the magnitude of $\mathcal{M}'$). In general, this term becomes important when the ratio between the modulation and ultrasound frequencies (i.e. the dimensionless modulation frequency) is on the order of, or larger than, the ultrasound attenuation per wavelength (i.e. the dimensionless attenuation coefficient). In the context of plane waves, it was shown [19] (also see Section 3.5.1) that the modulation-driven contribution to the ARF can be used to explain and simulate the phenomenon of difference-frequency generation [43] of the mean motion in lossless fluids where $\alpha = 0$. In the literature, the phenomena of difference-frequency generation and ARF were long thought to be unrelated owing to the common notion that the ARF vanishes in homogeneous lossless media [21], as indicated by the expression for $g^{\mathrm{E}}_{z,\mathrm{dir}}$ in (3.202).

For completeness, this section concludes by noting that the recent studies in [21, 22] provide a trial expression for the ARF in soft tissues assuming that: i) the ultrasound field is not modulated, ii) the displacement field takes the *a priori* form $\boldsymbol{w}(\boldsymbol{x},t) = W(\boldsymbol{x})\cos(t-z)\,\boldsymbol{e}_z$ where $W(\boldsymbol{x})$ is a "slowly" varying scalar function, and iii) there is no heat generation. With such hypotheses, the authors obtain a counterpart of (3.201) in terms of the total displacement field $\langle w_z\rangle_{\mathrm{E}}$, featuring the radiation body force as $g^{\mathrm{E}}_z = g^{\mathrm{E}}_{z,\mathrm{pot}} + g^{\mathrm{E}}_{z,\mathrm{dir}}$, where $g^{\mathrm{E}}_{z,\mathrm{pot}} \propto (C-1-\beta)\nabla(W^2)\cdot\boldsymbol{e}_z$ and $g^{\mathrm{E}}_{z,\mathrm{dir}} \propto (C-1)\partial(W^2)/\partial z$ represent respectively the *potential* and *directional* component of the ARF. Despite the apparent semblance between this result and (3.195)–(3.196), the explicit comparison between g^{E}_z [22] and f^{E}_z stemming from (3.196) is not possible owing to the fact that the unidirectional displacement field $\boldsymbol{w}(\boldsymbol{x},t)$ does not satisfy the balance of linear momentum, nor it incorporates the specifics of the focused ultrasound beam geometry used to generate the ARF.

3.6.5 Analytical example

To illustrate the effect of modulation on the ARF, it is first necessary to specify the distribution of ultrasound intensity affiliated with the modulated beam problem. For simplicity, consider the axisymmetric Gaussian beam source as in [39, 9] that is modulated according to (3.43). In this case, the linear solution for ultrasound intensity can be computed from the non-modulated analytical result in [39] and (3.191) as

$$I_{\mathrm{E}}(\boldsymbol{x},t) \;=\; I_{\mathrm{E,nm}}(\boldsymbol{x})\,\mathcal{M}^2(\varepsilon t-\varepsilon z) \;=\; \frac{I_{\mathrm{o}}\,\mathcal{M}^2(\varepsilon t-\varepsilon z)}{f^2(z)}\exp\!\left(-2\alpha z-\frac{2r^2}{a^2 f^2(z)}\right), \qquad (3.203)$$

where

$$f(z) = \sqrt{\left(1-\frac{z}{d}\right)^2+\left(\frac{2z}{a^2}\right)^2},$$

$r=\sqrt{x_1^2+x_2^2}$ denotes the radial coordinate, d is the focal distance, and a and I_o signify respectively the beam width (signifying the effective transducer aperture, see Fig. 3.2) and peak ultrasound intensity at the transducer's face. To study the variation of the ARF with modulation frequency, $\mathcal{M}$ is taken as

$$\mathcal{M}(\varepsilon t) \;=\; H(t)\sin(\omega_\mathrm{m}t), \qquad \omega_\mathrm{m}=O(\varepsilon), \tag{3.204}$$

where H denotes the Heaviside step function. On the basis of (3.202)–(3.204), one finds that $f^\mathrm{E}_{z,\mathrm{dir}}$ and $g^\mathrm{E}_{z,\mathrm{dir}}$ will in general contain multitude of frequency components, including the static i.e. "DC" component (recall that $\sin^2\! y=0.5(1-\cos 2y)$). To cater for biomedical applications and to facilitate the comparison with earlier works [39, 9], the remainder of this section focuses on the *dominant oscillatory component* of the ARF and thus induced displacement, namely that at frequency $2\omega_\mathrm{m}$. For simplicity of presentation the Fourier transform of any time-dependent quantity g, evaluated at $2\omega_\mathrm{m}$, is denoted by $\mathcal{F}g$.

Material and ultrasound parameters. In what follows, the computations are effected assuming carrier ultrasound frequency $\Omega=2\pi\times 10^6$ rad/sec (1 MHz), mass density $\varrho_\mathrm{o}=1000\,\mathrm{kg/m^3}$, compressional wave speed $c_\mathrm{o}=1500\,\mathrm{m/s}$, transducer aperture $a=42$ (1 cm), focal depth $d=209$ (5 cm), frequency of modulation $\omega_\mathrm{m}=10^{-3}$ (1 kHz), attenuation $\alpha=1.4\times10^{-3}$ (0.5 dB/cm/MHz), shear viscosity $\mu=0.28\times10^{-3}$ (0.1 Pa·s), and shear modulus $G=2.2\times10^{-5}$ (50 kPa) that are similar to the respective values in [9]. To make a reasonable assumption on the nonlinearity coefficient C, on the other hand, one may recall the experimental investigation in [35] which estimates the Landau's third-order elastic moduli in agarose-based, tissue mimicking phantoms as

$$A^{\text{Landau}}\in[-108,-51]\,\mathrm{kPa}, \qquad B^{\text{Landau}}\in[-28,-9]\,\mathrm{GPa}, \qquad C^{\text{Landau}}\in[18,71]\,\mathrm{GPa}.$$

To assess the validity of the above estimates, it can be shown that the coefficient of acoustic nonlinearity introduced in (3.42) reads $\beta=-1.5-(\varrho_\mathrm{o}c_\mathrm{o}^2)^{-1}(A^{\text{Landau}}+3B^{\text{Landau}}+C^{\text{Landau}})$, and takes mean values $\beta\in[3.4,3.8]$ for the three phantoms tested in [35]. Consistent with the observations of acoustic nonlinearities in soft tissues, this range of β compares favorably with the known value for water, $\beta_\text{water}=3.5$ [7]. From the definition of Landau moduli [7] and (3.28), on the other hand, one finds that

$$C \;=\; -\,(\varrho_\mathrm{o}c_\mathrm{o}^2)^{-1}\Big(A^{\text{Landau}}+2B^{\text{Landau}}\Big) \quad\Longrightarrow\quad C\in[8,25].$$

In light of this result, the ensuing computations assume $C = 8$ as a representative value.

Results. To illustrate the effect of ultrasound modulation on the ARF, Fig. 3.6 plots the variation of $\mathcal{F}f^{\mathrm{E}}_{z,\mathrm{dir}}$ and $\mathcal{F}g^{\mathrm{E}}_{z,\mathrm{dir}}$, at the geometric focus ($r = 0$, $z = d$), versus the modulation frequency ω_{m}. As can be seen from the display, there are two key differences between the two solutions. First, $f^{\mathrm{E}}_{z,\mathrm{dir}}$ is notably higher than its predecessor (even at $\omega_{\mathrm{m}} = 0$) due to the presence of coefficient $C-1$ multiplying the radiation force in soft tissues. Second, the proposed solution exhibits marked variation with modulation frequency, which is in contrast to the frequency-invariant formula given by $g^{\mathrm{E}}_{z,\mathrm{dir}}$. With reference to (3.202), the latter difference arises from i) argument $(\varepsilon t - \varepsilon z)$, rather than (εt), of the modulation function featured in $f^{\mathrm{E}}_{z,\mathrm{dir}}$, and ii) the presence of the "derivative term" $\mathcal{M}'\mathcal{M}$ as an additional effect of modulation in the new solution. Concerning the discrepancy in the magnitude of the two ARF estimates, it is noted that in both [9] and [15], the amplitude of the *observed* mean displacements in tissue-mimicking phantoms generated by the ARF is roughly *five times* that predicted by the (visco-)elastodynamic solution assuming $g^{\mathrm{E}}_{z,\mathrm{dir}}$ for the body force. This result indeed suggests that an account for the multiplier $C-1$ may be critical in capturing the phenomenon of the ARF in soft tissues.

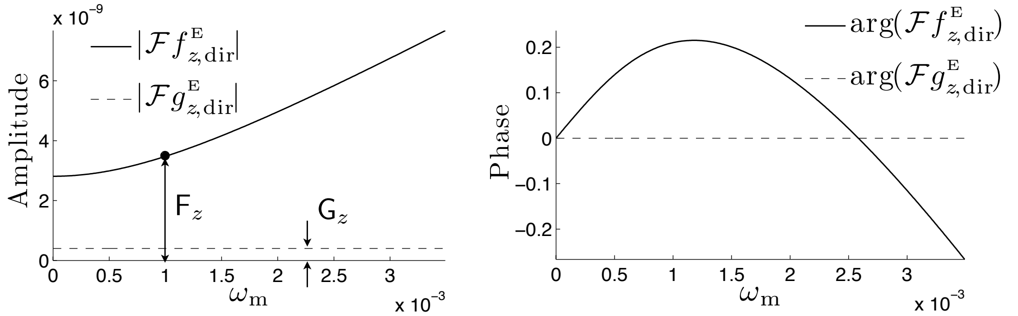

Figure 3.6: ARF versus modulation frequency: comparison between the current model ($\mathcal{F}f^{\mathrm{E}}_{z,\mathrm{dir}}$) and its predecessor ($\mathcal{F}g^{\mathrm{E}}_{z,\mathrm{dir}}$) in terms of the body force amplitude (left panel) and phase (right panel) at the focal point.

For completeness, the spatial variation of the radiation body force $\mathcal{F}f^{\mathrm{E}}_{z,\mathrm{dir}}$ and induced axial displacement $\mathcal{F}\langle u_z\rangle^{\mathrm{dir}}_{\mathrm{E}}$ is shown in Fig. 3.7. Here $\langle u_z\rangle^{\mathrm{dir}}_{\mathrm{E}}$ is computed with the aid of the Hankel integral transform, which reduces (3.200) to the equation of a damped harmonic oscillator, see [9] for details. From the display, one may observe both

i) spatial variation in the *phase* of the ARF (not predicted by the previous theory), and ii) the localization of shear waves near the the focal depth, $z = d$, that is in agreement with earlier result, cf. [9]. To further highlight the differences between the current approach and existing theory, Fig. 3.8 compares $\langle u_z\rangle_{\rm E}^{\rm dir}$ solving (3.200) with its predecessor $\langle w_z\rangle_{\rm E}^{\rm dir}$ solving (3.201), each normalized by the magnitude of the respective body force at the focal point (see Fig. 3.6 for the definition of F_z and G_z). The result demonstrates that, despite the normalization by the peak body force, $\langle u_z\rangle_{\rm E}^{\rm dir}/\mathsf{F}_z$ and $\langle w_z\rangle_{\rm E}^{\rm dir}/\mathsf{G}_z$ are still distinct due to the mismatch in the peak-normalized spatiotemporal variations of $f_{z,\rm dir}^{\rm E}$ and $g_{z,\rm dir}^{\rm E}$ evident from (3.202).

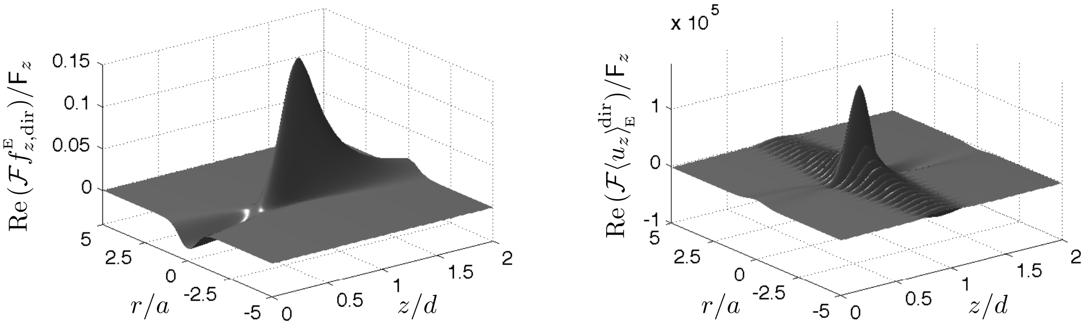

Figure 3.7: Acoustic radiation force $\mathcal{F} f_{z,\rm dir}^{\rm E}$ (left panel) and induced axial displacement $\mathcal{F}\langle u_z\rangle_{\rm E}^{\rm dir}$ (right panel) in the (r, z) plane at $\omega_{\rm m} = 10^{-3}$.

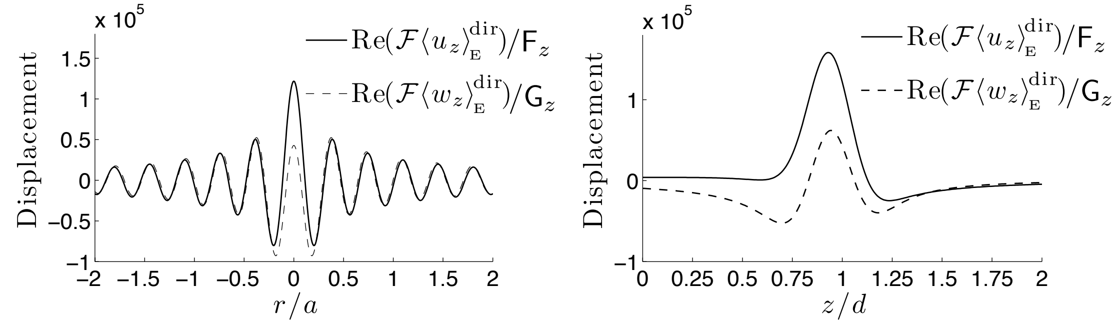

Figure 3.8: Normalized distribution of axial displacements, $\mathcal{F}\langle u_z\rangle_{\rm E}^{\rm dir}/\mathsf{F}_z$ and $\mathcal{F}\langle w_z\rangle_{\rm E}^{\rm dir}/\mathsf{G}_z$, in the radial direction (left panel) and axial direction (right panel) through the focal point.

3.7 Summary

This study establishes a rigorous asymptotic treatment of the ARF and “slow” motion in both Newtonian fluids (due to plane wave) and tissue-like solids (due to focused beam) in situations when the amplitude of elevated-intensity sound field is modulated using frequencies that are, relative to the frequency of sound, on the order of the Mach number. In simple terms, the ARF represents an effective body force for the balance of linear momentum governing the propagation of mean quantities, such as velocity and mass density for the plane wave problem, or displacement field for the focused beam configuration. The problem is tackled via a scaling paradigm wherein the axial and temporal coordinate are each split into a “fast” and “slow” component with the dual aim of: i) canceling the leading linear terms from the field equations describing the propagation of elevated-intensity ultrasound, and ii) accounting for the effect of ultrasound modulation. In addition, the transverse coordinates are scaled by the width of the focal region for the focused beam case. The key advancement in the proposed framework over previous analyses revolves around the *dual-time scale* treatment of the temporal variable, which allows one to parse out the contribution of ultrasound and its modulation in the nonlinear solution. In this setting the *mean* motion and affiliated (linear) field equations are effectively extracted from those describing the nonlinear, modulated ultrasound problem through the introduction of a “fast” time average of the germane state variables. For completeness the problem is tackled from both Eulerian and Lagrangian viewpoints, which are shown to provide different expressions for the ARF for the plane wave case, while lead to similar results for the focused configuration provided that the formulation is written in terms of the mean tissue displacement and mean specific entropy. The key aspect here is the choice of problem variables, which may either lead to the frame dependence (as for the plane wave case) or frame independence (as for the focused configuration). On developing a finite difference solution to the original nonlinear problem for the plane wave configuration, it is further shown that the featured “fast” time averages can be computed (up to the leading term) as a double “ordinary” time average of the simulated nonlinear response. As an illustration, the developments are complemented by the analytical solution for sinusoidal modulation envelope which both exposes the limitations of an earlier quasi-static approximation and demonstrates the possibility of non-zero mean motion in a lossless (albeit non-linear) fluid when a modulated, elevated-intensity ultrasound field is propagated through it. The results for the focused beam configuration are compared with the existing formula for the ARF that is derived assuming i) Newtonian fluid as the propagation medium, ii) non-modulated ultrasound field, and iii) heuristic modification to account for the effects of modulation. The comparison reveals a number of key features of the ARF that are brought to light by the new formulation. In particular, it is found that:

- The effective body force for the mean balance of linear momentum is shown to be comprised of a *potential term* (that includes the effects of thermal expansion), and a *directional term* that is typically referred to as the ARF. In this setting, the analysis of the mean tissue *shear* motion via the concept of the ARF requires suitable spatial filtering of the observed displacement field, which eliminates the compressional waves.
- Even in the case of no modulation the featured formula for the ARF, as derived for tissue-like solids, has an *additional multiplier* relative to its predecessor computed for Newtonian fluids. From the limited experimental data on tissue-mimicking phantoms it appears that this multiplier, that bears linear relationship with the Landau's third-order elastic moduli, may be significantly larger than unity and thus explain reported discrepancies between the (indirect) experimental observations of the ARF in soft tissues and its estimates based on the premise of a Newtonian fluid;
- The newly obtained formula for the ARF contains an *additional term* that is proportional to the time rate of ultrasound intensity. This term, that carries (in part) the effect of modulation on the ARF and affiliated mean tissue motion, opens the possibilities toward enhanced spatiotemporal control of the radiation body force within the focal region, and thus more effective tissue interrogation;
- The previous analytical framework which rests on the premise of a "narrow" ultrasound beam (generated by transducers with focal numbers $\geqslant 5$) is generalized, via a systematic asymptotic treatment, to permit significantly wider class of ultrasound beams (with focal numbers $\geqslant 1$) that are more representative of biomedical applications entailing the use of the ARF;

Assuming a set of ultrasound and soft-tissue parameters that are relevant to germane biomedical applications, the above findings are illustrated through the example of a modulated ultrasound beam generated by the axisymmetric Gaussian source.

Chapter 4

Nonlinear acoustics of the focused ultrasound beam

4.1 Introduction

The development of modern diagnostic techniques that make use of the *acoustic radiation force* [7] such as vibro-acoustography [17], shear wave elasticity imaging [9], and acoustic radiation force impulse imaging [11], poses the challenge of effective computation of the nonlinear acoustic solution affiliated with modulated, high-intensity focused ultrasound. For this class of applications, the acoustic radiation force (i.e. the effective body force on a tissue), which is the primary quantity of interest, can be effectively computed given the spatiotemporal intensity distribution of the nonlinear acoustic field [39, 9, 19, 20]. The radiation force thus generated is noteworthy within the focal region of the ultrasound beam, where the amplitude of the pressure wave reaches extreme values and the nonlinear effects are most pronounced. Owing to its compact support, such body force is effectively used for local tissue interrogation in terms of its shear stiffness properties [17, 9, 11, 10, 14]. Here it is noted, however, that the ultrasound field generating the radiation force is often *modulated* with either transient or steady-state signal to i) facilitate the monitoring of tissue's response [10, 14, 17], ii) expose the rate effects in tissue's constitutive behavior [11, 37], and iii) minimize the risk of tissue damage from heating effects [9, 74]. In many such testing configurations, the dominant frequency of modulation is on the order of $10^2 \div 10^4\,\mathrm{Hz}$ that, while significant in terms of the induced constitutive and inertial response in the tissue, is still small relative to the frequency of ultrasound. Even for such "slow" modulation rates, however, the customary *quasi-static* approximation of the acoustic solution [9] may not be able to capture all features of the modulated sound field and may cause significant discrepancies, as shown in Section 3.5 via the example of plane waves.

One common way to compute the nonlinear acoustic solution for any transient modulation is to use the so-called Khokhlov-Zabolotskaya-Kuznetsov (KZK) equation [9]. The KZK equation, proposed in [24, 25], has been studied and used widely over the past two decades [26, 27, 75, 76, 28, 39, 31, 77, 29, 78], and recently celebrated its 40th anniversary [79]. In the literature, the KZK equation is also known as the nonlinear parabolic wave equation, since it uses the so-called parabolic approximation which is applicable for nearly-planar waves inside the focal region. Originally, the KZK equation was developed to describe the nonlinear wave propagation in thermo-viscous fluids in situations when the effects of diffraction, nonlinearities, and attenuation are small and of the same order of magnitude. Demonstrating its relevance to ultrasound waves in soft tissues, the KZK equation was since extended to deal with finite-amplitude compressional waves in solids [80, 81]. In the context of medical ultrasound, one drawback of the original formula resides in the fact that the attenuation coefficient for thermo-viscous fluids, which is built into the KZK equation, is proportional to the squared carrier frequency. This is unfortunately not the case in soft tissues, where the featured relationship is approximately linear at (MHz) ultrasound frequencies [59]. To deal with the problem, a more comprehensive version of the KZK equation featuring the hereditary integral to describe the effects of attenuation was proposed in [9].

The KZK equation can be solved numerically in a number of ways, including the time domain algorithm [28], the frequency domain algorithm [26], and the hybrid time-frequency domain approach [82]. Naturally, each method has its unique features that make it suitable for specific class of configurations. For instance, the time domain algorithm is efficient for short transient signals (i.e. short modulation envelopes), while both the frequency domain method and the hybrid approach are more suitable when dealing with time-harmonic modulation. In the case of "low-frequency" ultrasound modulation that is of interest in this study, however, the time domain solution of the KZK equation may be inefficient due to extended length of the signal, while the frequency domain algorithms may be inappropriate when the frequency spectrum of the modulated signal is complex. To overcome the problem, this study deploys a *dual-time scale* approach (as in the treatment of the acoustic radiation force due to modulated sound, see Sections 3.5 and 3.6) to obtain the KZK-type equation which caters for "slowly" modulated ultrasound fields. In this case the introduction of two distinct time scales, namely the "fast" time to track ultrasound oscillations and the "slow" time to describe the effects of modulation, allows the solution methodology to absorb all advantages of the frequency domain approach (as in the case of time-harmonic modulation), and, at the same time, to obtain the solution for any transient modulation envelope. For completeness, the asymptotic analysis deploys separate scaling parameters to describe the effects of diffraction (i.e. focusing) and modulation, thus allowing the model to i) account for a wide range of transducer geometries, and ii) be degenerated to the quasi-static approximation [9] as a limiting case for low frequencies.

To establish the validity of the dual-time scale approach at high modulation frequencies, the results of the dual-time approximation are compared with the time domain simulations. Despite both approaches can be implemented without using the parabolic approximation, the reduced diffraction model (in both cases) is chosen for the purpose of validation due to simplicity of implementation of the time domain algorithm. At the same time, if one would compare the predictions of the dual-time method with the experimental results, the "full" diffraction can be used without introducing any extra computational complexity.

4.2 Preliminaries

This focus of this study is an intermediate asymptotic behavior of the nonlinear balance laws governing the propagation of high-intensity, focused acoustic field in situations where the germane time-harmonic excitation is *modulated* by a "low"-frequency envelope. To provide specificity for the analysis, the smallness of the (dominant) frequency of modulation is specified by requiring the ratio between the latter and the carrier frequency to be $o(1)$. As examined in [39, 9, 20] among others, the spatiotemporal distribution of acoustic intensity stemming from the solution to such intermediate asymptotics problem constitutes the basis for the computation of the induced acoustic radiation force and affiliated heating effects.

With the reference to Section 3.3, it is noted that the assumptions on the smallness of the Mach number, attenuation coefficient and shear modulus remain valid for this Chapter, however, the scaling of the modulation frequency is performed in a different manner. It is assumed that the (dominant) dimensionless frequency of the modulation envelope is $O(\varepsilon^\eta)$, where $\eta > 0$ is the parameter that accounts for a wide range of modulation frequencies ($\eta = 1$ was used in the previous Chapter, as stated in Section 3.3). In the biomedical applications of focused ultrasound, MHz-rate sound field is often modulated with a kHz-rate envelope [17], which implies that $\eta \approx 1$. Keeping η as an independent parameter, however, allows one to cater for even higher modulation frequencies and, at the same time, to find a threshold modulation frequency beyond which the customary quasi-static approximation [9] breaks down. In this setting, one may rewrite (3.14b) as

$$\tilde{\omega}_{\mathrm{m}} \;=\; \frac{\omega_{\mathrm{m}}}{\varepsilon^\eta} \;=\; O(1), \tag{4.1}$$

where ω_{m} is the dimensionless modulation frequency, and $\tilde{\omega}_{\mathrm{m}}$ denotes its rescaled counterpart.

Note that the developments are presented in the Eulerian frame of reference, and the subscript “$_{\mathrm{E}}$” is omitted for brevity (e.g. for the intensity field).

Governing equations for the nonlinear wave propagation. For a consistent calculations of the radiation force, the assumptions as well as the governing equations for the ultrasound wave propagation are taken similar as for the derivation of the ARF formula (see Section 3.6). With the reference to Section 3.3, the balance of linear momentum, expanded up to sufficient order of accuracy reads

$$(1-\varepsilon\nabla\cdot\tilde{\boldsymbol{u}})\frac{\partial\tilde{\boldsymbol{v}}}{\partial t} + \varepsilon\tilde{\boldsymbol{v}}\cdot\nabla\tilde{\boldsymbol{v}} \;\overset{\varepsilon^2}{=}\; \nabla\cdot\tilde{\boldsymbol{\sigma}}, \tag{4.2}$$

where

$$\begin{aligned}
\tilde{\boldsymbol{\sigma}} &\overset{\varepsilon^2}{=} \big(1-2\varepsilon\tilde{G}\big)\nabla\cdot\tilde{\boldsymbol{u}}\,\boldsymbol{I} + 2\varepsilon\tilde{G}\nabla^{\mathrm{S}}\tilde{\boldsymbol{u}} + \varepsilon\Big[\tfrac{1}{2}(B+3C+D-2)(\nabla\cdot\tilde{\boldsymbol{u}})^2 - \tfrac{1}{2}(C+D)\nabla^{\mathrm{S}}\tilde{\boldsymbol{u}}:\nabla^{\mathrm{S}}\tilde{\boldsymbol{u}} \\
&+ \nabla\tilde{\boldsymbol{u}}:\nabla^{\mathrm{T}}\tilde{\boldsymbol{u}} + \tfrac{1}{2}\nabla\tilde{\boldsymbol{u}}:\nabla\tilde{\boldsymbol{u}}\Big]\boldsymbol{I} - \varepsilon\Big[(C+D-2)\,\nabla\cdot\tilde{\boldsymbol{u}}\,\boldsymbol{I} - D\nabla^{s}\tilde{\boldsymbol{u}}\Big]\cdot\nabla^{s}\tilde{\boldsymbol{u}} \\
&+ \varepsilon\Big(\tilde{\mu}_{\mathrm{B}} - \tfrac{2}{3}\tilde{\mu} + \tilde{\kappa}\frac{\beta_{\mathrm{T}}^2}{\mathrm{c}_{\mathrm{p}}^2}\Big)(\nabla\cdot\tilde{\boldsymbol{v}})\,\boldsymbol{I} + 2\varepsilon\tilde{\mu}\nabla^{\mathrm{S}}\tilde{\boldsymbol{v}}, \qquad (4.3) \\
\tilde{\boldsymbol{v}} &\overset{\varepsilon^2}{=} (\boldsymbol{I} + \varepsilon\nabla^{\mathrm{T}}\tilde{\boldsymbol{u}})\cdot\frac{\partial\tilde{\boldsymbol{u}}}{\partial t}
\end{aligned}$$

are respectively the expansion of the Cauchy stress tensor and kinematic relation between velocity and displacement.

Scaling. This paragraph incorporates the geometry and relevant spatiotemporal proportions of the focused ultrasound beam, which allow for the simplification of nonlinear field equations (4.2)–(4.3) by way of rescaling. By using the focal zone size estimations as in Section 3.4, one may similarly rescale transverse coordinates as

$$\chi_{\mathrm{i}} = \varepsilon^{\lambda}\,x_{\mathrm{i}}, \qquad \frac{\partial\tilde{f}}{\partial\chi_{\mathrm{i}}} = O(\tilde{f}), \qquad \frac{\partial\tilde{f}}{\partial x_{\mathrm{i}}} = \varepsilon^{\lambda}\,\frac{\partial\tilde{f}}{\partial\chi_{\mathrm{i}}}, \qquad \mathfrak{i} = 1,2, \tag{4.4}$$

while the displacement vector can be rewritten as

$$\tilde{\mathbf{u}}(\chi_{\mathrm{i}},z,t) = (\tilde{u}_{\mathrm{i}},\tilde{u}_z)(x_{\mathrm{i}},z,t) = (\varepsilon^{\lambda}\tilde{\mathrm{u}}_{\mathrm{i}},\tilde{\mathrm{u}}_z)(\chi_{\mathrm{i}},z,t), \qquad \tilde{\mathrm{u}}_{\mathrm{i}},\tilde{\mathrm{u}}_z = O(1). \tag{4.5}$$

On extending the analysis for dealing with the effects of ultrasound modulation, one may conveniently split the temporal variable t into the "fast" and "slow" components, and introduce the retarded "fast" time (to cancel the leading terms in (4.2) that describe plane wave motion, see also Section 3.4), so that any quantity of interest can be alternatively written as

$$\tilde{f}(\chi_{\mathrm{i}},z,t) = \tilde{h}(\chi_{\mathrm{i}},\zeta,\tau,t'_{\mathrm{f}}) = \tilde{h}(\chi_{\mathrm{i}},\zeta,\tau,t'_{\mathrm{f}}+2\pi), \tag{4.6}$$

where $t'_{\mathrm{f}} = t - z$ denotes retarded "fast" time, $\tau = \varepsilon^{\eta}t_{\mathrm{s}} = \varepsilon^{\eta}t$ is rescaled "slow" time, ε^{η} factor comes from (4.1), and $\zeta = \varepsilon^{\vartheta}z_{\mathrm{s}} = \varepsilon^{\vartheta}z$ ($\vartheta = \min\{1, 2\lambda, \eta\}$) is rescaled "slow" axial coordinate. Here the "fast" time tracks the ultrasound oscillations and implies the periodicity condition in (4.6), the "slow" time describes the modulation-scale variations, while the "slow" axial coordinate reflects the slow changes in the amplitude of the solution in space. By way of the chain rule, one may show that

$$\frac{\partial\tilde{h}}{\partial t} = \frac{\partial\tilde{h}}{\partial t'_{\mathrm{f}}} + \varepsilon^{\eta}\frac{\partial\tilde{h}}{\partial\tau}, \qquad \frac{\partial\tilde{h}}{\partial z} = -\frac{\partial\tilde{h}}{\partial t'_{\mathrm{f}}} + \varepsilon^{\vartheta}\frac{\partial\tilde{h}}{\partial\zeta}, \tag{4.7}$$

where the magnitudes of all derivates on the right hand side are $O(1)$, which is necessary for further asymptotic analysis.

4.3 KZK-type equation for the modulated sound beam

To facilitate the development of the KZK-type equation for modulated sound beams, all "tilde" quantities examined so far can be considered to be functions of $(\chi_{\mathrm{i}},\zeta,\tau,t'_{\mathrm{f}})$ as in (4.6). With reference to (4.5) and (4.7), the balance of linear momentum (4.2) can accordingly be written as

$$\begin{aligned} \frac{\partial^2\tilde{\mathrm{u}}_{\mathrm{i}}}{\partial t'^2_{\mathrm{f}}} &\overset{\varepsilon^{\vartheta}}{=} -\frac{\partial^2\tilde{\mathrm{u}}_z}{\partial t'_{\mathrm{f}}\partial\chi_{\mathrm{i}}}, \qquad \mathrm{i}=1,2 \\ \varepsilon^{2\eta}\frac{\partial^2\tilde{\mathrm{u}}_z}{\partial\tau^2} - \varepsilon^{2\vartheta}\frac{\partial^2\tilde{\mathrm{u}}_z}{\partial\zeta^2} + 2\varepsilon^{\eta}\frac{\partial^2\tilde{\mathrm{u}}_z}{\partial t'_{\mathrm{f}}\partial\tau} &\overset{\varepsilon^{\nu+\vartheta}}{=} -2\varepsilon^{\vartheta}\frac{\partial^2\tilde{\mathrm{u}}_z}{\partial t'_{\mathrm{f}}\partial\zeta} - \varepsilon^{2\lambda}\frac{\partial^2\tilde{\mathrm{u}}_{\mathrm{i}}}{\partial t'_{\mathrm{f}}\partial\chi_{\mathrm{i}}} \\ &\quad + \varepsilon\beta\frac{\partial}{\partial t'_{\mathrm{f}}}\Big(\frac{\partial\tilde{\mathrm{u}}_z}{\partial t'_{\mathrm{f}}}\Big)^2 + \varepsilon\tilde{\delta}\frac{\partial^3\tilde{\mathrm{u}}_z}{\partial t'^3_{\mathrm{f}}}, \end{aligned} \tag{4.8}$$

where the acoustic nonlinearity parameter and diffusivity of sound are given by

$$\beta = -\frac{B+3}{2}, \qquad \tilde{\delta} = \tilde{\mu}_{\mathrm{B}} + \tfrac{4}{3}\tilde{\mu} + \tilde{\kappa}\frac{\alpha_{\mathrm{T}}^2}{\mathrm{c}_{\mathrm{p}}^2}. \tag{4.9}$$

Next, one may differentiate (4.8b) with respect to t'_{f}, make use of (4.8a), and introduce acoustic pressure as $\tilde{p} = -\frac{1}{3}\mathrm{tr}\tilde{\boldsymbol{\sigma}} \overset{\varepsilon^{\vartheta}}{=} \partial\tilde{\mathrm{u}}_z/\partial t'_{\mathrm{f}}$ to obtain

$$\varepsilon^{2\eta}\frac{\partial^2\tilde{p}}{\partial\tau^2} - \varepsilon^{2\vartheta}\frac{\partial^2\tilde{p}}{\partial\zeta^2} + 2\varepsilon^{\eta}\frac{\partial^2\tilde{p}}{\partial t'_{\mathrm{f}}\partial\tau} + 2\varepsilon^{\vartheta}\frac{\partial^2\tilde{p}}{\partial t'_{\mathrm{f}}\partial\zeta} \overset{\varepsilon^{\nu+\vartheta}}{=} \varepsilon^{2\lambda}\sum_{\mathrm{i}}\frac{\partial^2\tilde{p}}{\partial\chi_{\mathrm{i}}^2} + \varepsilon\beta\frac{\partial^2\tilde{p}^2}{\partial t'^2_{\mathrm{f}}} + \varepsilon\tilde{\delta}\frac{\partial^3\tilde{p}}{\partial t'^3_{\mathrm{f}}}. \tag{4.10}$$

Equation (4.10) governs the nonlinear propagation of the modulated ultrasound field, where the pressure field is expressed as $\tilde{p} = \tilde{p}(\chi_{\mathrm{i}},\zeta,\tau,t'_{\mathrm{f}})$. To simplify the problem, the solution of (4.10) can alternatively be sought in the form

$$\tilde{p}(\chi_{\mathrm{i}},\zeta,\tau,t'_{\mathrm{f}}) = \bar{\tilde{p}}(\chi_{\mathrm{i}},\zeta',\tau',t'_{\mathrm{f}}), \tag{4.11}$$

where

$$
\begin{aligned}
\zeta' \;&=\; \varepsilon^{\nu-\vartheta}\zeta \qquad &&=\; \varepsilon^{\nu}\, z_{\mathrm{s}}, \\
\tau' \;&=\; \tau - \varepsilon^{\eta-\vartheta}\zeta \;&&=\; \varepsilon^{\eta}(t_{\mathrm{s}} - z_{\mathrm{s}}),
\end{aligned}
\tag{4.12}
$$

signify respectively the (rescaled) "slow" axial coordinate which ignores the effects of sound modulation, and retarded "slow" time. In this setting, (4.10) reduces to

$$
2\,\varepsilon^{\nu}\frac{\partial^2 \bar{\tilde{p}}}{\partial t'_{\mathrm{f}}\partial\zeta'} \;\overset{\varepsilon^{\nu+\vartheta}}{=}\; \varepsilon^{2\lambda}\sum_{\mathrm{i}}\frac{\partial^2 \bar{\tilde{p}}}{\partial \chi_{\mathrm{i}}^2} + \varepsilon\beta\,\frac{\partial^2 \bar{\tilde{p}}^2}{\partial {t'_{\mathrm{f}}}^2} + \varepsilon\tilde{\delta}\,\frac{\partial^3 \bar{\tilde{p}}}{\partial {t'_{\mathrm{f}}}^3},
\tag{4.13}
$$

where $\nu = \min\{1, 2\lambda\}$, and $\vartheta = \min\{1, 2\lambda, \eta\}$. Formula (4.13), which describes the rate of axio-temporal variations (in terms of ζ' and t'_{f}) of the acoustic pressure due to diffraction, nonlinear effects, and attenuation, is hereon referred to as the KZK-type equation for "slowly" modulated sound beams.

4.4 Comments on the result

Applicability of the "full" equation. From (4.13), it is seen that the leading behavior of the solution is markedly affected by the diffraction parameter λ. When $\lambda = \frac{1}{2}$, one recovers the scaling of the transverse coordinates as in the original KZK equation [24], where the effects of diffraction, nonlinearity, and attenuation (corresponding respectively to the three terms on the right hand side of (4.13)) are all of the same order. In the case of spherical transducers where (3.49) applies, taking $\lambda = \frac{1}{2}$ and $\varepsilon = 10^{-3}$ yields the focal ratio $\mathsf{f} = 5$, which is in the upper echelon of the f-numbers encountered in the acoustic radiation force (ARF) studies [17, 61, 62, 63]. From (4.13), on the other hand, it is clear that the approximation error surrenders *in order* to the "weakest" term in the equation as long as

$$
\nu + \vartheta \;>\; \max\{1, 2\lambda, \nu\} \qquad \Longrightarrow \qquad \nu + \min\{\nu, \eta\} \;>\; \max\{1, 2\lambda\}.
\tag{4.14}
$$

With reference to (4.1), one finds that taking $\eta > \frac{1}{2}$ for example covers (dominant) modulation frequencies of up to 30 kHz – assuming the carrier frequency of 1 MHz and the Mach number $\varepsilon = 10^{-3}$. In this case (4.13) captures the leading-order behavior of the sound field (including the effects of diffraction, nonlinearity, and dissipation) as long as $\frac{1}{4} < \lambda < \frac{3}{4}$ which, in terms of (3.49), implies $1 < \mathsf{f} < 28$ and consequently covers most ARF transducers encountered in the literature. Here it is interesting to observe that for $\frac{1}{4} < \lambda < \frac{1}{2}$ (which describes spherical transducers with $1 < \mathsf{f} < 5$), the $O(\varepsilon^{2\lambda})$ diffraction effects in (4.13) are more pronounced than their $O(\varepsilon)$ counterparts due of nonlinearity and attenuation. For completeness, it is also noted that the applicability of the original KZK equation to focused beams is discussed in [76], where the relevant criterion is expressed in terms of the width of the focal region relative to acoustic wave length, which translates to $\varepsilon^{2\lambda} \ll 1$ in the context of the present study.

Effect of ultrasound modulation. In (4.13), the effects of signal modulation are synthesized via the scaling parameter η embedded in ϑ, the retarded "fast" time t'_{f} introduced in (4.7), and the retarded "slow" time τ', see (4.12), appearing as a parameter in the governing equation (which enters the problem via the boundary condition). In general, the proposed paradigm applies as soon as $\varepsilon^{\eta} = o(1)$, i.e. for any (transient or steady-state) modulation envelope whose dominant frequency is small relative to the carrier frequency. This allows one to apply (4.13) even to short modulation pulses, whose duration is on the order of several ultrasound periods. On the other side of the spectrum, the effects of modulation disappear from the modified KZK equation when $\varepsilon^{\eta} = o(\varepsilon^{\nu})$, in which case $\vartheta = \nu$, the distinction between t_{f} and t becomes immaterial, and τ' can be replaced by τ. For such configurations, the rate of axial variation of $\tilde{p}$ caused by signal modulation is negligible relative to that due to diffraction, attenuation and nonlinear effects.

Limiting cases. At this point, it is instructive examine the limiting behavior of (4.13) when the focusing parameter λ takes either extremely small, or extremely large values. Consider first the case of "very sharp" focusing where $\lambda < \min\{\frac{\eta}{2}, \frac{1}{4}\}$ so that (4.14) is violated. For such configurations, $\nu = 2\lambda$ and the leading-order behavior of (4.13) can be shown via (4.7) and (4.12) to read

$$2\varepsilon^{2\lambda}\frac{\partial^2\bar{\tilde{p}}}{\partial t'_{\mathrm{f}}\partial\zeta'} - \varepsilon^{2\lambda}\sum_{\mathsf{i}}\frac{\partial^2\bar{\tilde{p}}}{\partial\chi_{\mathsf{i}}^2} \overset{\varepsilon^{4\lambda}}{=} \frac{\partial^2\tilde{p}}{\partial t^2} - \left(\sum_{\mathsf{i}}\frac{\partial^2\tilde{p}}{\partial x_{\mathsf{i}}^2} + \frac{\partial^2\tilde{p}}{\partial z^2}\right) \overset{\varepsilon^{4\lambda}}{=} 0. \qquad (4.15)$$

Since $\lambda < \frac{1}{4}$, however, the accuracy of (4.15) may not be satisfactory. Fortunately, this impediment can be remedied by recalling that the linear wave equation solves the full nonlinear problem with the $O(\varepsilon)$ accuracy, which allows one to formally set the approximation error of the second equality in (4.15) to "$\overset{\varepsilon}{=}$". Consequently when

$\lambda < \min\{\frac{\eta}{2}, \frac{1}{4}\}$, the acoustic pressure can be computed either via the leading terms in (4.13) or, more accurately, by solving the linear wave equation. In terms of the large values of the focusing parameter, on the other hand, it is noted that (4.13) can be degenerated (as expected) to the Burgers equation [7] by setting $\lambda \to \infty$ in which case $\nu = 1$, $\vartheta = \min\{1, \eta\}$, and the first term on the right-hand side vanishes.

Unscaled equation. The problem-driven scaling of the spatial and temporal coordinates, introduced in Section 4.2, is essential for the derivation of (4.13) as it permits one to estimate of the magnitude of the residual terms in the equation. This scaling, however, does not play a role in solving (4.13) either analytically or numerically, and can be removed for simplicity. With reference to (4.4), (4.7) and (4.11), (4.13) can accordingly be written in terms of the unscaled quantities as

$$2\frac{\partial^2 \bar{p}}{\partial t'_{\mathrm{f}} \partial z_{\mathrm{s}}} \;=\; \nabla_\perp^2 \bar{p} + \beta \frac{\partial^2 \bar{p}^2}{\partial t_{\mathrm{f}}'^2} + \delta \frac{\partial^3 \bar{p}}{\partial t_{\mathrm{f}}'^3}, \tag{4.16}$$

where

$$\bar{p}(x_{\mathrm{i}}, z_{\mathrm{s}}, t'_{\mathrm{s}}, t'_{\mathrm{f}}) \;=\; \varepsilon\, \bar{\tilde{p}}(\chi_{\mathrm{i}}, \zeta', \tau', t'_{\mathrm{f}}), \qquad \delta \;=\; \varepsilon \tilde{\delta} \;=\; \mu_{\mathrm{B}} + \tfrac{4}{3}\mu + \kappa \left(\frac{\beta_{\mathrm{T}}}{\mathrm{c_p}}\right)^2$$

are respectively the (unscaled) acoustic pressure and diffusivity of sound, $t'_{\mathrm{s}} = t_{\mathrm{s}} - z_{\mathrm{s}}$ is the retarded "slow" time, and

$$\nabla_\perp^2 \;=\; \frac{\partial^2}{\partial x_1^2} + \frac{\partial^2}{\partial x_2^2}$$

denotes the Laplacian with respect to the transverse coordinates.

Relationship with the original KZK equation. Clearly, (4.16) is closely related to the original KZK equation, which can be written as

$$2\frac{\partial^2 p}{\partial t' \partial z_{\mathrm{s}}} \;=\; \nabla_\perp^2 p + \beta \frac{\partial^2 p^2}{\partial t'^2} + \delta \frac{\partial^3 p}{\partial t'^3}, \tag{4.17}$$

where $p = p(x_{\mathrm{i}}, z_{\mathrm{s}}, t')$, $t' = t - z$ denotes the retarded time [7], and all quantities are dimensionless according to the adopted normalization scheme. Note that (4.17), which is valid for an arbitrarily modulated signal, features the retarded "total" time t' as opposed to its "fast" counterpart t'_{f} appearing in (4.16). On splitting the retarded "total" time into its "fast" ($t'_\mathrm{f} = t_\mathrm{f} - z_\mathrm{f}$) and "slow" ($t'_\mathrm{s} = t_\mathrm{s} - z_\mathrm{s}$) components according to (4.7), whereby

$$p(x_\mathrm{i}, z_\mathrm{s}, t') \;=\; \bar{p}(x_\mathrm{i}, z_\mathrm{s}, t'_\mathrm{s}, t'_\mathrm{f}), \quad \frac{\partial p}{\partial t'} \;=\; \frac{\partial \bar{p}}{\partial t'_\mathrm{f}} + \frac{\partial \bar{p}}{\partial t'_\mathrm{s}}, \quad \bar{p}(\cdot, \cdot, \cdot, t'_\mathrm{f}{+}2\pi) \;=\; \bar{p}(\cdot, \cdot, \cdot, t'_\mathrm{f}), \tag{4.18}$$

and noting by way of (4.7) that $\partial\bar{p}/\partial t'_\mathrm{s} = O(\varepsilon^\eta) = o(1)$, one immediately recovers (4.16). This is perhaps the shortest, yet less rigorous way to derive (4.16), which also supports the fact that (4.16) is applicable for all (dominant) modulation frequencies such that $\varepsilon^\eta = o(1)$. As will be shown shortly, this subtle difference in the temporal argument between (4.16) and (4.17) brings about a significant computational advantage when solving the KZK equation for "slowly" modulated ultrasound fields.

One should also note that the above short-hand derivation of (4.16) may be difficult to achieve without prior knowledge of the final result, see e.g. [9] as an example where the unmitigated account for signal modulation has eluded previous studies of nonlinear ultrasound fields. In this setting, the merit of the of the systematic developments in Sections 4.2 and 4.3 is two-fold as they: i) "shed the light" for simpler arguments, and ii) explicitly expose the parametric region (4.14) in terms of the Mach number, focal number, and modulation frequency over which the proposed parabolic approximation applies.

Realistic attenuation and dispersion. Equation (4.16) is derived for an elastic material with heat conduction and viscosity [48], a generalization of the Kelvin-Voigt solid which in particular implies that the attenuation coefficient α is proportional to the *squared* ultrasound frequency. At carrier frequencies on the order of MHz, however, the attenuation coefficient of soft tissues is typically proportional to the ultrasound frequency [59], which is incompatible with (4.16). To describe the nonlinear wave propagation in a medium with arbitrary attenuation, the analysis in [9] demonstrates that the "dissipation" term in the KZK equation (4.17) should be replaced by a suitable hereditary integral. On adopting the same approach for the "slowly" modulated beam problem, one finds

$$2\frac{\partial^2 \bar{p}}{\partial t'_\mathrm{f} \partial z_\mathrm{s}} \;=\; \nabla^2_\perp \bar{p} \;+\; \beta \frac{\partial^2 \bar{p}^2}{\partial t'^2_\mathrm{f}} \;+\; \int_0^\infty K(\xi) \frac{\partial^3 \bar{p}(\ldots, t'_\mathrm{f} - \xi)}{\partial t'^3_\mathrm{f}} \, \mathrm{d}\xi \tag{4.19}$$

to be the corresponding generalization of (4.16), where K is an appropriate viscoelastic kernel whose Fourier transform consists of the real part, which describes attenuation, and the imaginary part, which captures dispersion.

Acoustic intensity propagates. One important consequence of ultrasound modulation resides in the fact that the intensity-like quantity, defined as

$$I(x_\mathrm{i}, z_\mathrm{s}, t'_\mathrm{s}) \;=\; \frac{1}{2\pi}\int_{t'_\mathrm{f}-\pi}^{t'_\mathrm{f}+\pi} \bar{p}^2(x_\mathrm{i}, z_\mathrm{s}, t'_\mathrm{s}, \xi)\,\mathrm{d}\xi, \qquad (4.20)$$

is a function of the *retarded* "slow" time, $t'_\mathrm{s} = t_\mathrm{s} – z_\mathrm{s}$ (not just "slow" time t_s). As a result, the acoustic intensity of a modulated sound beam *propagates* in the z-direction with the phase velocity equaling unity, which signifies the speed of compressional waves. To examine the consequences of this result in terms of the linear approximation of intensity, consider the phased-array representation of an ultrasound transducer as a source distribution at $z_\mathrm{s} = 0$. In this case, one has

$$\bar{p}^\mathrm{lin}(x_\mathrm{i}, z_\mathrm{s}, t'_\mathrm{s}, t'_\mathrm{f})\Big|_{z_\mathrm{s}=0} \;=\; \bar{p}^\mathrm{lin}(x_\mathrm{i}, 0, t_\mathrm{s}, t_\mathrm{f}) \;=\; \Lambda(x_\mathrm{i}, t_\mathrm{f})\,\mathcal{M}(t_\mathrm{s}), \qquad (4.21)$$

where Λ denotes the pressure distribution on the boundary, $\mathcal{M}$ is the prescribed (amplitude) modulation envelope, and $\bar{p}^\mathrm{lin}$ is the linearized pressure distribution which solves (4.16) with $\beta = 0$. On recalling that t'_s enters (4.16) only as a parameter, one accordingly finds

$$\bar{p}^\mathrm{lin}(x_\mathrm{i}, z_\mathrm{s}, t'_\mathrm{s}, t'_\mathrm{f}) \;=\; \bar{p}^\mathrm{lin}_\mathrm{nm}(x_\mathrm{i}, z_\mathrm{s}, t'_\mathrm{f})\;\mathcal{M}(t'_\mathrm{s}), \qquad (4.22)$$

where $\bar{p}^\mathrm{lin}_\mathrm{nm}$ solves the corresponding non-modulated problem with $\mathcal{M} \equiv 1$. The substitution of (4.22) into (4.20) yields

$$I^\mathrm{lin}(x_\mathrm{i}, z_\mathrm{s}, t'_\mathrm{s}) \;=\; I^\mathrm{lin}_\mathrm{nm}(x_\mathrm{i}, z_\mathrm{s})\,\mathcal{M}^2(t'_\mathrm{s}), \quad I^\mathrm{lin}_\mathrm{nm}(x_\mathrm{i}, z_\mathrm{s}) \;=\; \frac{1}{2\pi}\int_{t'_\mathrm{f}-\pi}^{t'_\mathrm{f}+\pi} \left(\bar{p}^\mathrm{lin}_\mathrm{nm}(x_\mathrm{i}, z_\mathrm{s}, \xi)\right)^2 \mathrm{d}\xi, \qquad (4.23)$$

which explicitly demonstrates the propagating nature of the linear intensity field. In the case of very low modulation frequencies where $\varepsilon^\eta = o(\varepsilon^\nu)$, τ' (resp. t'_s) can be replaced by τ (resp. t_s) es examined earlier, whereby the linear intensity of a modulated ultrasound beam permits *standing-wave* description $I^\mathrm{lin} = I^\mathrm{lin}_\mathrm{nm}\,\mathcal{M}^2(t_\mathrm{s})$ [9], which is commonly referred to as the *quasi-static approximation.*

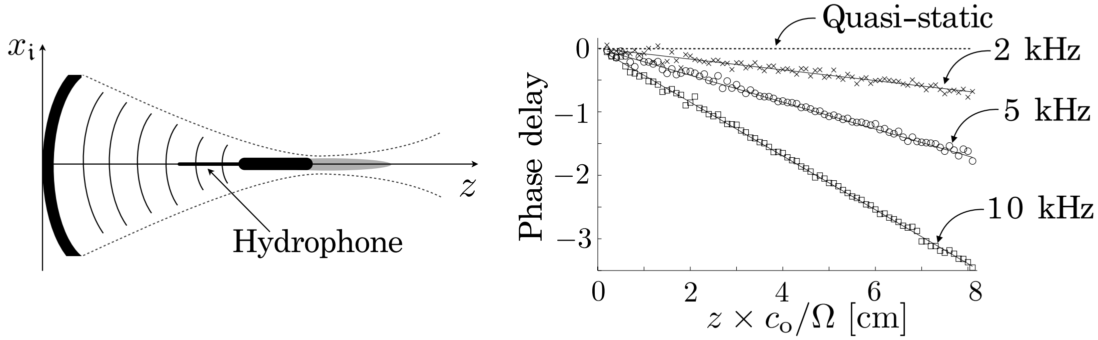

Figure 4.1: Schematics of the experimental setup for validating the propagating nature of the intensity field (left), and phase delay of the intensity versus depth for three different modulation frequencies (right). Markers indicate experimental results, solid lines under them show the theoretical prediction according to (4.23), while the dotted line shows the prediction of the quasi-static approximation.

To validate the propagating nature of the intensity experimentally, a series of tests was performed (experimental study by Chen & Fatemi, Mayo Clinic). An axisymmetric transducer was used to generate time-harmonically modulated ultrasound field in water, while response was measured along the axis of the transducer with a needle hydrophone, as shown in Fig. 4.1 (left). The phase difference between the intensity on the boundary and away from it is plotted in Fig. 4.1 (right) for different modulation frequencies. Markers correspond to the experimental data, solid lines under them show the theoretical predictions according to (4.23), while the dotted line indicates the prediction of the quasi-static approximation. As can be seen from the display, the modulation effects are clearly captured by the proposed model that features the retarded "slow" time (4.23), while the quasi-static approximation does not work for a given set of modulation frequencies. Note, however, that for modulation frequencies that are sufficiently smaller than 2 kHz, the phase difference becomes small for the problem under consideration, and quasi-static approximation provides reasonable results.

4.5 Numerical implementation of the dual-time approach

In most medical applications, the focused ultrasound field is generated by either phased transducer array or a single, convex-shaped transducer [74, 15] as shown in Fig. 4.2.

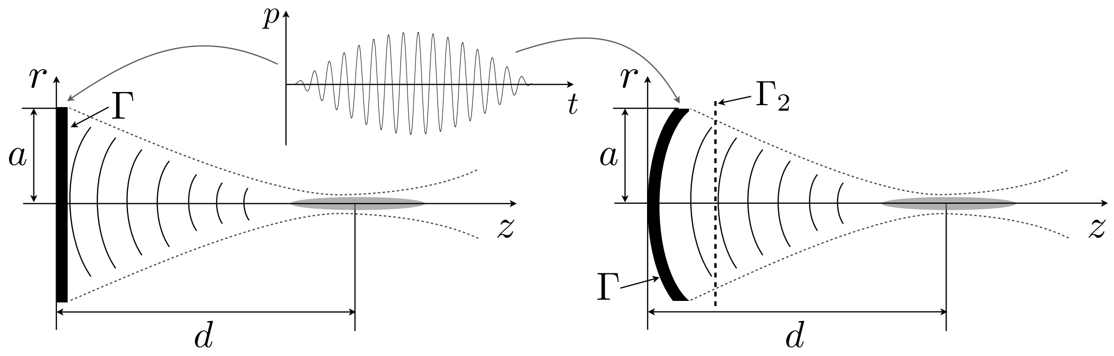

Figure 4.2: Schematics of the modulated ultrasound beam generated by phase-focused transducer array (left) and convex-shaped transducer (right).

Typical pressure signal on the boundary is also shown in Fig. 4.2, illustrating relatively short modulation envelope as measured in terms of the (carrier) ultrasound period of vibrations, T. Despite the fact that much longer signals are used in some applications [17, 15], the ensuing investigation will deploy "short" modulation envelope as a test platform to examine performance of the proposed computational scheme. With reference to Fig. 4.2, it is assumed that the transducer is axisymmetric, in which case the problem can be conveniently formulated in the cylindrical coordinate system (r, z) where z coincides with the transducer's axis. In this setting, the acoustic pressure is denoted by $p = p(r, z, t)$. For completeness, the boundary of the transducer is indicated by Γ, while its aperture and focal depth are signified respectively by a and d.

In situations entailing convex-shaped transducers, modeling of the nonlinear wave field usually requires the knowledge of the pressure over a flat surface Γ_2 given by $z = z_{\min}$, see Fig. 4.2. One way to meet such requirement is to solve the linear wave equation between Γ and Γ_2, i.e. to neglect the nonlinear contribution in this region. Since the nonlinear effects are the most pronounced in the focal zone, such approximation usually does not introduce a significant source of error. To solve the wave equation between Γ and Γ_2, one can deploy a specialization of the Rayleigh integral [83] for axisymmetric problems, which can be written in the frequency domain as

$$p_\omega(r, z) \;=\; -\,\mathrm{i}\omega \int_\Gamma \frac{e^{\mathrm{i}k|\boldsymbol{x}-\boldsymbol{\xi}|}}{|\boldsymbol{x}-\boldsymbol{\xi}|}\, v_\omega(\boldsymbol{\xi})\, r\, \mathrm{d}\Gamma_{\boldsymbol{\xi}}, \qquad \boldsymbol{x} = (r, z) \in \Gamma_2, \qquad \boldsymbol{\xi} \in \Gamma, \tag{4.24}$$

where ω denotes the component frequency; v_ω and p_ω denote respectively the Fourier transforms of the normal particle velocity v on Γ and pressure p on Γ_2; $k = \omega +$

iα is the wave number, and α is the attenuation coefficient. Even though Rayleigh integral (4.24) gives the exact solution only when Γ is planar, the error due to curved geometry of a transducer is typically small and can be neglected for sufficiently high sound frequencies [31, 84]. By way of (4.24) which describes the pressure variation over a planar surface Γ_2 due to the action a convex-shaped transducer, both configurations in Fig. 4.2 can be treated similarly from the computational point of view.

The computational treatment of (4.19) can be divided into two main parts: i) computation of the "fast"-time steady-state solutions for different values of the "slow" time (featured as a parameter), and ii) assemblage of the computed solutions to account for the "slow" time phase delay. For simplicity, it is hereon assumed that the carrier ultrasound signal is time-harmonic; however, the developments can be generalized to treat more complicated multi-frequency sources, such as modulated shock waves.

4.5.1 Steady-state solution

The first part, which deals with the steady-state solution, can be accomplished in a number of ways, as it requires only the solution of the KZK equation with suitable boundary condition. Since the solution is periodic in "fast" time, the *spectral method with operator splitting* can be applied, see e.g. [26, 7]. In particular, the solution of (4.19) is expanded in Fourier series as

$$\bar{p}(r,z,t'_\mathrm{s},t'_\mathrm{f}) \;=\; \sum_{n=1}^{\infty} \mathrm{Re}\Big(\bar{p}_n(r,z,t'_\mathrm{s})\, e^{-\mathrm{i}nt'_\mathrm{f}}\Big), \tag{4.25}$$

where $\bar{p}_n$ is the complex amplitude of the nth harmonic, and "Re" signifies the real part. The operator splitting method suggests first to solve the linear part of (4.19), and then treat the nonlinear contribution independently for each increment in z. In this case, two separate algorithms for linear propagation and nonlinear interaction can be used for each step in z.

Linear propagation. By substituting (4.25) into (4.19) and considering only the linear part, one has

$$\frac{\partial \bar{p}_n}{\partial z} \;=\; \frac{\mathrm{i}}{2n}\nabla_\perp^2 \bar{p}_n \;-\; \tfrac{1}{2}n^2 K_n\, \bar{p}_n, \tag{4.26}$$

where K_n denotes the Fourier transform of kernel K, evaluated at frequency n. For fluids $K_n = const.$, but if the attenuation coefficient is proportional to frequency, as is the case for most soft tissues, then $K_n \propto 1/n$. Equation (4.26) can be conveniently solved by way of the Hankel transform with respect to the radial coordinate as

$$\bar{p}_n(r, z_2, t'_{\mathrm{s}}) = \mathcal{H}^{-1}\left[\exp\left(\left(-\frac{\mathrm{i}}{2n}\gamma^2 - \tfrac{1}{2}n^2 K_n\right)(z_2 - z_1)\right)\mathcal{H}[\bar{p}_n(r, z_1, t'_{\mathrm{s}})]\right] := B_n[\bar{p}_n(r, z_1, t'_{\mathrm{s}})], \tag{4.27}$$

where z_2 and z_1 denote two distinct values of the axial coordinate; $\mathcal{H}$ is the zeroth-order Hankel transform

$$\mathcal{H}[f(r)](\gamma) \;=\; \int_0^\infty f(r) J_0(\gamma r) r \,\mathrm{d}r, \tag{4.28}$$

J_0 is the Bessel function of order zero, and B_n "propagates" the nth harmonic linearly in the z direction from z_1 to z_2. For computational purposes, Hankel transform (4.28) is discretized as

$$\begin{aligned} \sum_{i=1}^{N_r} \mathcal{H}_{ji}[f(r_i)] \;&=\; \sum_{i=1}^{N_r} \int_{r_{i-1/2}}^{r_{i+1/2}} f(r_i) J_0(\gamma_j r) r \,\mathrm{d}r \\ &=\; \sum_{i=1}^{N_r} f(r_i) \frac{J_1(\gamma_j r_{i+1/2}) r_{i+1/2} - J_1(\gamma_j r_{i-1/2}) r_{i-1/2}}{\gamma_j}, \end{aligned} \tag{4.29}$$

where r_i $(i = 1 \ldots N_r)$ and γ_j $(j = 1 \ldots N_\gamma)$ denote respectively the discrete values of r and γ; $r_{i\pm1/2} = \frac{1}{2}(r_i + r_{i\pm1})$; J_1 is the first-order Bessel function; $r_0 = 0$, and $r_{N_r+1} = (3r_{N_r} - r_{N_r-1})/2$. The forward and inverse Hankel transform operators, computed on the basis of (4.29), are used to approximate (4.27) which solves the linear part of (4.19). This method of using the Hankel transform (or 2D Fourier transform for non-axisymmetric problems) to solve parabolic wave equation (4.26) is usually referred to as the angular spectrum method [85]. In many applications, (4.29) is superseded by either discrete Hankel transform or the fast Hankel transform algorithm [86]. However, the advantage of (4.29) lies in its simplicity (with comparable performance, as will be shown later) and compatibility with nonuniform meshes, which, for instance, allow for finer discretization of the focal region. Moreover, the Hankel transform is needed only for precomputing the linear operator B_n in (4.27), and consequently does not significantly affect the overall computational efficiency. For this reason, further improvements of (4.29) are beyond the scope of this study.

For completeness, it is noted that the angular spectrum method can also be used to account for the "full" diffraction and dispense with the parabolic approximation without notable increase in computational time. In the "full" diffraction model, $\nabla_\perp^2$ in (4.19) is superseded by ∇^2 which, in the context of (4.26), results in the augmentation of the right-hand side by the extra term $\mathrm{i}/(2n)\,\partial^2\bar{p}_n/\partial z^2$, which completes the linear wave equation part of the model. In this case, the "full"-diffraction analogue of (4.27) reads

$$\bar{p}_n(r,z_2,t_\mathrm{s}') \;=\; \mathcal{H}^{-1}\Biggl[\exp\Biggl(-\mathrm{i}n\Bigl(1-\sqrt{1-\Bigl(\frac{\gamma}{n}\Bigr)^2+\mathrm{i}nK_n}\Bigr)(z_2-z_1)\Biggr)\mathcal{H}[\bar{p}_n(r,z_1,t_\mathrm{s}')]\Biggr], \tag{4.30}$$

which differs from (4.27) only by a multiplication factor between the inverse and forward Hankel transform operators, and thus takes similar amount of time to compute.

Nonlinear interaction. To deal with the nonlinear term, one may substitute (4.25) into (4.19) and consider only the nonlinear term on the right hand side, since the linear diffraction and attenuation terms are already accounted via (4.27). The resulting ordinary differential equation for the nth harmonic reads

$$\frac{\partial\bar{p}_n}{\partial z} \;=\; -\,\frac{\mathrm{i}n\beta}{4}\left[\sum_{k=1}^{n-1}\bar{p}_{n-k}\bar{p}_k \;+\; 2\sum_{k=1}^{\infty}\bar{p}_{n+k}\bar{p}_k^*\right], \qquad n=1,2\ldots \tag{4.31}$$

where the "star" symbol denotes complex conjugation. In the numerical implementation, the number of relevant harmonics N_h is finite, in which case the assembly of (4.31) for $n=1...N_\mathrm{h}$ makes a system of nonlinear equations, which is solved numerically using the 4th order Runge-Kutta scheme. More details about the spectral method can be found elsewhere in the literature, see e.g. [26, 7].

It is well known that the number of harmonics significantly affects computational efficiency, since the computational time increases as $O(N_\mathrm{h}^2)$ [7]. When dealing with focused ultrasound beams, the nonlinear effects are pronounced only in the focal region; as a result, it is not necessary to keep the interactions of all N_h harmonics before the focal zone if the source is time-harmonic. For this reason, an adjustable number of harmonics is deployed in the computational scheme. Initially (near the source), the interaction and propagation of only $N_\mathrm{h}=2$ harmonics is computed. When the amplitude of the second harmonic (the maximum amplitude over all lateral points) reaches the critical value, however, the number of harmonics is doubled to $N_\mathrm{h}=4$ to ensure the smallness of numerical error. When the fourth harmonic reaches the critical value, the number of harmonics is doubled again, and so on. The key aspect here is how to select the threshold values for the magnitude each harmonic, so that the overall error is minimal. For signals with "smooth" decaying frequency spectrum, that are typically produced by the nonlinear distortion of a time-harmonic wave, one can deploy

$$\|\bar{p}_{N_\mathrm{h}}\| > \ell_1 \, \|\bar{p}_{N_\mathrm{h}-1}\| \tag{4.32}$$

as the criterion for doubling the number of harmonics, where $\|\bar{p}_n(r, z, t'_\mathrm{s})\|$ denotes the L^∞-norm of $\bar{p}_n$ with respect to the radial coordinate for z and t'_s fixed. In other words, when the amplitude of the N_hth harmonic becomes larger than prescribed fraction ℓ_1 of the amplitude of the $(N_\mathrm{h}-1)$th harmonic, the number of harmonics is doubled. Somewhat similar treatment, aimed to increase the efficiency by varying the number of harmonics, can be found e.g. in [87], where an absolute threshold value is used on the right hand side of (4.32).

In situations when the nonlinear effects are accumulated locally, e.g. in the focal region, there is no reason to track diminishing high-order harmonics everywhere in the domain. In this case, one can neglect small values of the pressure harmonics outside of the focal region, which can potentially lead to both reduced computation time and lesser memory requirements. Since the typical frequency spectrum of a nonlinear wave is a decaying function of n ($|\bar{p}_n| \propto n^{-1}$ for the shock wave), the threshold of relevance for every harmonic should decay at a similar or faster rate. On the other hand, an item that is relevant in many applications is the *product* between the attenuation coefficient, which usually grows with n, and the intensity of a given harmonic (e.g. the computation of heating or the radiation body force generated by the focused sound field). On the basis of the above considerations, this study assumes

$$\|\bar{p}_n\| < \frac{\ell_2}{n^2}\, p_\mathrm{o} \qquad \longrightarrow \qquad \bar{p}_n = 0 \tag{4.33}$$

as the threshold criterion, where ℓ_2 is a small parameter and p_o is the maximum pressure amplitude near the transducer's boundary. The efficiency and accuracy of using (4.32) and (4.33) is examined in what follows.

4.5.2 Numerical examples

This section is focused on the numerical examples, which illustrate the procedures described at the beginning of the section. To this end, it is assumed that the ultrasound field is generated by a spherically-shaped transducer (see the right panel in Fig. 4.2), where the aperture radius and focal depth are given respectively by $a \times c_{\rm o}/\Omega = 1\,\text{cm}$ and $d \times c_{\rm o}/\Omega = 4\,\text{cm}$. The physical parameters of the medium are $c_{\rm o} = 1500\,\text{m/s}$ for the sound speed, $\varrho_{\rm o} = 1000\,\text{kg/m}^3$ for the mass density, $\beta = 3.5$ for the nonlinearity parameter and $\alpha \times c_{\rm o}^{-1} = 0.5\,\text{dB/(cm}\cdot\text{MHz)}$ for the attenuation coefficient per unit frequency [59]. The carrier ultrasound frequency is taken as $\Omega/(2\pi) = 2\,\text{MHz}$, while the velocity amplitude at the boundary is chosen as $v_{\rm o} \times c_{\rm o} = 0.365\,\text{m/s}$, which corresponds approximately to the intensity of $I_{\rm o} \times \varrho_{\rm o} c_{\rm o}^3 = 10\,\text{W/cm}^2$. To minimize the reflections from the radial boundary of the computational domain, the radius of the latter is set at $r_{\rm max} \times c_{\rm o}/\Omega = 5\,\text{cm}$ (counting on the attenuation to mitigate the problem), while the maximum axial coordinate is taken as $z_{\rm max} \times c_{\rm o}/\Omega = 6\,\text{cm}$. The maximum value of the Hankel transform parameter, which determines the upper bound for integration with respect to γ, is taken as $\gamma_{\rm max} \times \Omega/c_{\rm o} = 100\,\text{cm}^{-1}$.

Linear propagation. First, the error analysis of the linear wave propagation is performed. The linear solution can be computed via the combination of (4.24) and (4.30) using two different approaches: i) by varying z_2 from $z_1 + \Delta z$ to $z_{\rm max}$ (with step Δz) while keeping $z_1 \in \Gamma_2$ fixed, or ii) by the recursive use of (4.30) with $z_2 = z_1 + \Delta z$, starting from $z_1 \in \Gamma_2$. In what follows the first approach is referred to as the "leap" algorithm, while the second approach is called the "incremental" algorithm. In general, the leap approach is more accurate, while the incremental procedure is suitable for solving nonlinear problems (the leap algorithm is not). To quantify the approximation error, Rayleigh integral (4.24) can be evaluated along the axis of a spherically-shaped transducer (assuming uniform time-harmonic excitation over Γ) in closed form as

$$I(r\!=\!0, z) \;\approx\; \frac{1}{2}\,|p_\Omega(0,z)|^2 \;=\; \frac{v_{\rm o}^2}{2}\left(\frac{d}{z-d}\left|\frac{1}{k}\left(e^{\mathrm{i}kz} - e^{\mathrm{i}k\sqrt{d^2+(z-d)^2+2d(z-d)\cos\theta}}\right)\right|\right)^2 \tag{4.34}$$

in terms of the intensity I of the beam, where constant $v_{\rm o}$ denotes the amplitude of the normal velocity on Γ, $k = 1 + \mathrm{i}\alpha$ is the wave number, and $\theta = \sin^{-1}(a/d)$. In what follows, the error of numerical approximation is defined as the $L^2([z_{\rm min}, z_{\rm max}])$ distance between the analytical solution (4.34) and the corresponding numerical result, normalized by the L^2 norm of (4.34). The variation of such defined error for both leap and incremental algorithms with respect to the discretization parameters $N_r = r_{\rm max}/\Delta r + 1$

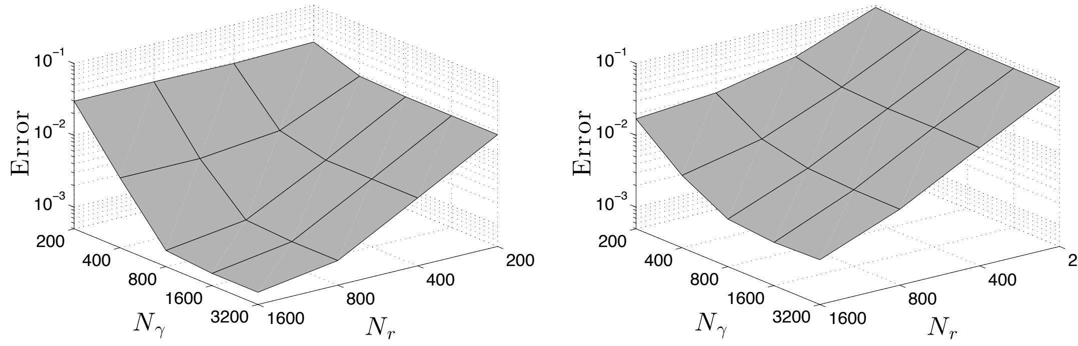

Figure 4.3: Variation of the error of leap (left) and incremental (right) algorithms with respect to N_r and N_γ.

(in terms of the radial coordinate) and $N_\gamma = \gamma_{\max}/\Delta\gamma + 1$ (in terms of the Hankel transform parameter) is plotted in Fig. 4.3. It is clearly seen that the leap algorithm is more accurate for all values of N_r and N_γ in the graph. In addition, the dependence on N_γ reduces drastically for $N_\gamma > N_r$, in which case the error is practically controlled by N_r. Accordingly, the ensuing examples assume $N_\gamma \approx 2N_r$ for simplicity of numerical analysis. Here it is noted that the assumption $N_\gamma = O(N_r)$ makes the featured technique comparable (in terms of computational time) with the discrete Hankel transform algorithm, where $N_\gamma = N_r$ is always the case [85]. On the other hand, due to the fact that the Hankel-transformed numerical solution is propagated analytically via (4.27) in the z-direction, the error of neither leap nor incremental algorithm changes with the discretization parameter $N_z = z_{\max}/\Delta z + 1$ of the axial coordinate ($N_z = 200$ for all examples in this section). For completeness, it is noted that the error in Fig. 4.3 does not converge to zero with increasing N_r and N_z due to: i) numerical integration of (4.24) that is deployed to compute the boundary conditions over the "starting" planar surface Γ_2, and ii) truncation of the computational domain in terms of r.

To illustrate and better understand the magnitude of the numerical error in Fig. 4.3, the left panel in Fig. 4.4 compares the intensity profile along the z-axis given by (4.34) with the "leap" numerical evaluation of (4.30) assuming $N_r = 800$ and $N_\gamma = 1600$. For future reference, this result is compared to the equivalent numerical treatment ($N_r = 800$, $N_\gamma = 1600$) of the parabolic approximation (4.27) plotted in the right panel of Fig. 4.4, which demonstrates that the error committed by the parabolic approximation

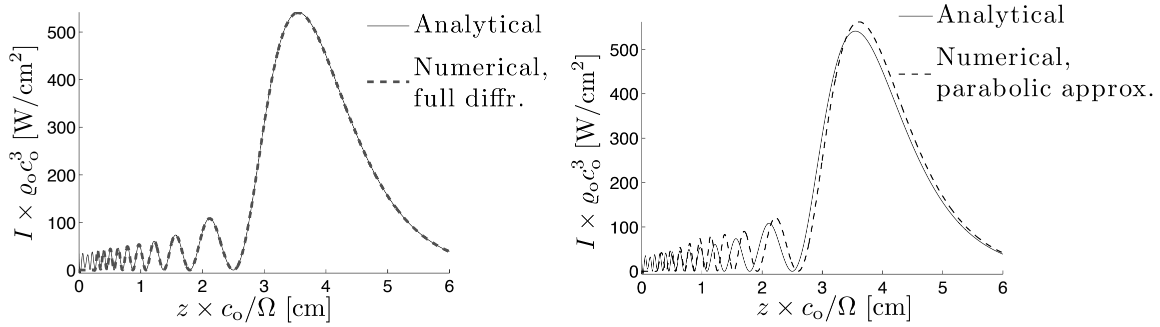

Figure 4.4: Comparison between the intensity along the axis of the spherically-shaped transducer given by the analytical solution (4.34) and numerical approximation with parabolic wave equation.

(13%) exceeds the numerical inaccuracies (0.11%) by two decades.

Nonlinear interaction. To study the effect of threshold parameters ℓ_1 and ℓ_2 featured in (4.32) and (4.33), the computation of the pressure field is performed (assuming input parameters as in the beginning of this section) by way of the full diffraction model (4.30) for the linear part, and nonlinear correction (4.31). The discretization parameters are taken as $N_r = 800$, $N_\gamma = 1600$ and $N_z = 200$, while the summation in (4.31) is truncated after first $N_\mathrm{h} = 64$ harmonics. To highlight the nonlinear effects, the $L^2([z_{\min}, z_{\max}])$ solution error is computed in terms of

$$Q(r\!=\!0, z) \;=\; \sum_{n=1}^{N_\mathrm{h}} \alpha_n |\bar{p}_n(r\!=\!0, z)|^2, \tag{4.35}$$

which signifies the distribution of heat sources along the $z-$axis caused by the acoustic field (note that (4.35) is also necessary for the computation of the acoustic radiation force [39, 9]). Here the reference "exact" solution is defined as the numerical solution with $\ell_1 = \ell_2 = 0$, limiting the computation to $N_\mathrm{h} = 64$ harmonics as stated before. The left panel in Fig. 4.5 plots the featured L^2 error versus ℓ_1 and ℓ_2. As can be seen from the display, the error is somewhat more sensitive to ℓ_2, and practically vanishes when $\ell_1 = \ell_2 = O(10^{-3})$. To provide a point of reference, it is noted the error committed by the linear approximation is (for the given configuration) 16%, while the largest error committed by the nonlinear solution (observed for $\ell_1 = \ell_2 = 10^{-1}$) is 3.4%. In

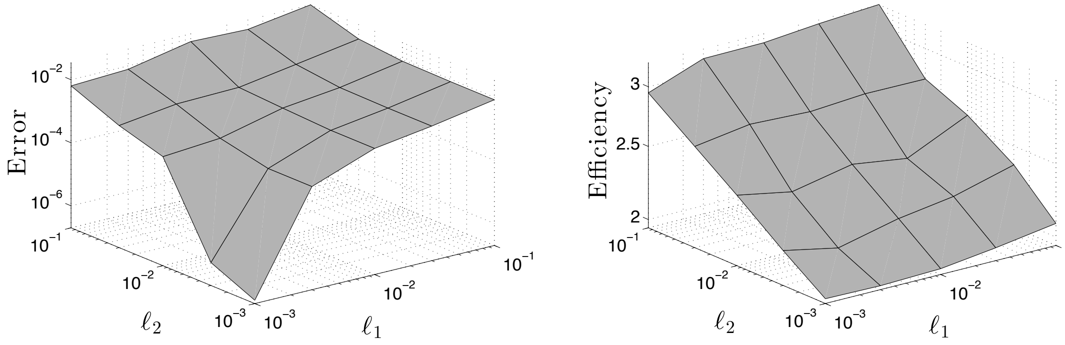

Figure 4.5: Variations of the error (left) and efficiency (right) of the nonlinear solution versus parameters ℓ_1 and ℓ_2.

this setting the approximation error affiliated with $\ell_1 = \ell_2 = 10^{-3}$ is assumed to be sufficiently small for future computations.

For completeness, the right panel in Fig. 4.5 describes the corresponding variation of *solution efficiency*, defined as the ratio between the computational time for the reference solution ($\ell_1 = \ell_2 = 0$) and its counterpart with generic $\ell_1 \geqslant 0$ and $\ell_2 \geqslant 0$. For example, the efficiency of 2.5 means that the numerical solution with given ℓ_1 and ℓ_2 can be computed 2.5 times faster than the reference "exact" model. From the graph, it is evident that the solution efficiency is mostly controlled by ℓ_2, and reaches the value of approximately two for errors as small as $O(10^{-6})$. Note that the "roughness" of the efficiency surface in Fig. 4.5 can be explained by the smallness of the computational time, whereby any concurrent active processes (however non-taxing) may affect the runtime measurements. In the context of ℓ_2, it is also important to note that the sparsity of the solution, introduced in (4.31) via (4.33), provides for significant reduction in memory requirements. For the example under consideration, the reference solution with $\ell_1 = \ell_2 = 0$ requires 230 MB of memory only to store the result (i.e. all participating $\bar{p}_n$ as functions of radius and depth), while its counterpart with $\ell_1 = \ell_2 = 10^{-3}$ drops this requirement down to 17 MB. Despite the fact that the former memory requirement is not nearly sufficient to make meaningful limitation for simulations on modern computers, a certain assembly of such solutions (and thus more memory) is necessary for the description of the modulated ultrasound as will be examined next.

4.5.3 "Slow" time phase shift

Equation (4.19) is applicable to arbitrary forms of modulated ultrasound (such as amplitude-modulated sound or the dual-beam configuration with differing frequencies), as soon as the dominant modulation frequency is significantly smaller than the carrier ultrasound frequency. For brevity of discussion, only the amplitude modulated ultrasound will be examined in this section. Hereon, it is also assumed that the modulation envelope $0 \leqslant \mathcal{M}(t) \leqslant 1$ is a function of time only, i.e. that the boundary conditions over Γ are in-phase modulated. Here is important to note that the modulation envelope carries exclusively the "slow" variation, i.e. that

$$\mathcal{M}(t) \;:=\; \mathcal{M}(t_\mathrm{s}) \tag{4.36}$$

as examined in Section 4.4. In this setting, the "slow" time phase shift characterizing the solution of (4.19) for a given modulation envelope could be accounted for by computing a set of steady-state solutions with different values of the "slow" time t_s on the boundary. This, however, may not be the most efficient way due to relatively fine discretization of the "modulation" time and inapplicability of the solution to other modulation envelopes.

An alternative and more effective approach toward computing the solution of (4.19), however, is to precompute a set of steady-state solutions assuming different *amplitude values* of the modulation envelope on Γ. With reference to (4.18), such precomputed solutions are then *phase-delayed* by the amount z in order to compute the sought pressure response $p(r,z,t)$. In this case, the procedure of "constructing" the modulated solution (for any modulation envelope) can be formulated as:

- Select a set of representative amplitudes of the modulation envelope $0 < A_1 \ldots < A_k < \ldots < A_{N_A} = 1$ (recall that $0 \leqslant \mathcal{M}(t) \leqslant 1$);
- For each A_k, $k = 1, \ldots N_A$, compute the corresponding steady-state solutions $\bar{p}_n^k$ $(n = 1, 2, \ldots)$ via the spectral method with operator splitting as described in Section 4.5.2;
- Given the values of z and t for which the pressure solution is to be computed, evaluate $\mathcal{M}(t-z)$;

- Interpolate between the precomputed solutions $\bar{p}_n^k,\ k = 1, \dots N_A$ to obtain the solution $p(r, z, t)$ that corresponds to the particular modulation amplitude equaling $\mathcal{M}(t–z)$. In other words, the solution is computed on the basis of (4.18) and (4.25) as
$$p(r, z, t) \ = \ \sum_{n=1}^{N_\mathrm{h}} \mathrm{Re}\Big(\bar{p}_n(r, z, t-z)\, e^{-\mathrm{i}n(t-z)}\Big) \tag{4.37}$$
where $\bar{p}_n(r, z, t–z)$, affiliated with the modulation amplitude $\mathcal{M}(t-z)$, is obtained by the interpolation of $\bar{p}_n^k$.

This procedure is illustrated in the left panel of Fig. 4.6 for an example modulation envelope given by
$$\mathcal{M} \ = \ H(t)\, H(\pi/\omega_\mathrm{m} - t)\ \sin(\omega_\mathrm{m} t), \tag{4.38}$$
where ω_m is the modulation frequency, and H denotes the Heaviside function. The black dots in the left panel in Fig. 4.6 indicate positions on the modulation envelope where the solution precomputed (corresponding to amplitudes $0 < A_1 \dots < A_k < \dots < A_{N_A} = 1$), while for all other locations i.e. modulation amplitudes corresponding to arbitrary $t-z$ (shown by the small grey dot), an appropriate interpolation between precomputed solutions is used.

To investigate the effect of the number of modulation amplitudes N_A (at which the solution is precomputed) on the result, Fig. 4.6 (right panel) shows the variation of the error versus N_A for several interpolation methods: linear interpolation, piecewise cubic Hermite interpolating polynomial (PCHIP), and cubic spline interpolation. In the diagram, the error is defined as the $L^2([0, t_\mathrm{max}])$ of the pressure-versus-time signal at the focus, defined as the distance from the “exact” solution, computed using $N_A = 64$ amplitudes and spline interpolation (since this is the most accurate interpolation). This particular choice of the error is deemed appropriate since the temporal dependence is an important feature of modulated ultrasound. To study the convergence of the solution, the right panel in Fig. 4.6 also shows the linear data fit for the featured interpolation methods. The resulting convergence power for linear interpolation is 1.27, for PCHIP is 1.38, while for the spline interpolation it is 2.45. Note that the error analysis presented in this paragraph is modulation envelope-specific, i.e. depends on the choice of the modulation envelope (it also depends on other parameters, such as the amplitude of the boundary condition). This result, however specific, allows one

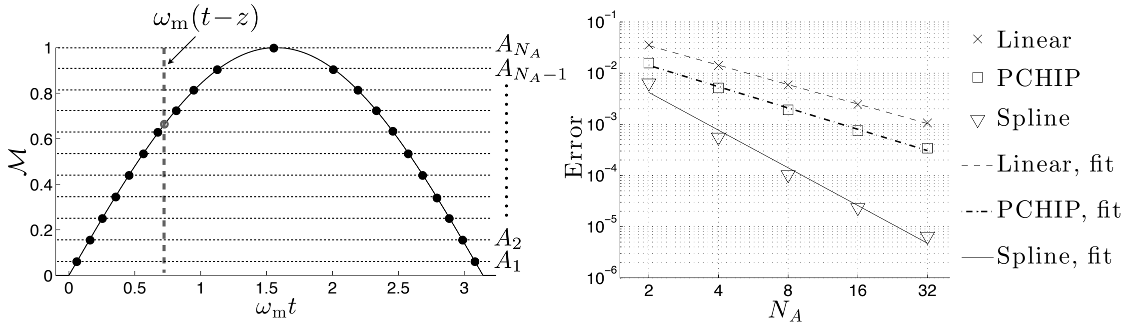

Figure 4.6: Schematics of the interpolation procedure for example modulation envelope (left) and approximation error versus number of computed solutions N_A for different interpolation methods (right) assuming $\omega_{\mathrm{m}} = 0.05$.

to establish the "hierarchy" between competing interpolation methods and expose the order of magnitude of the interpolation errors. For instance, it is not clear from the onset that $N_A = 4$ is sufficient to construct the numerical solution with reasonable accuracy, say $O(10^{-3})$ via spline interpolation. In light of the results in Fig. 4.6, $N_A = 8$ with spline interpolation is selected for the ongoing computations, which will be used to compare the dual-time approach with time-domain simulations. At this point, the memory savings through the introduction of threshold parameter ℓ_2, see (4.33), become important. For instance, the solution with $N_A = 32$ ($\ell_2 = 10^{-3}$) requires only 320 MB of memory to store all precomputed solutions $\bar{p}_n^k$, while the "full" solution ($\ell_2 = 0$) would take more than 7 GB to accomplish the same task. For the particular example under consideration, the solution with $\ell_2 = 0$ could still be computed numerically on a personal computer; however, more involved problems with different beam geometries and finer meshes, as well as three-dimensional (non-axisymmetric) extensions of the method, would require significant computational resources.

Other types of modulation. By building on the procedure for dealing with amplitude-modulated beams described in Section 4.5.3, one can also establish an approach to model the dual-beam systems (see e.g. [17]), where the pressure signal on the boundary can be written as

$$p \;=\; p_1(r)e^{-\mathrm{i}t} \;+\; p_2(r)e^{-\mathrm{i}(1+\Delta\omega)t} \;=\; \big(p_1(r) \;+\; p_2(r)e^{-\mathrm{i}\Delta\omega t_{\mathrm{s}}}\big)e^{-\mathrm{i}t_{\mathrm{f}}} \;=\; \mathcal{M}(r,t_{\mathrm{s}})e^{-\mathrm{i}t_{\mathrm{f}}}. \tag{4.39}$$

Here $p_1(r)$ and $p_2(r)$ are the pressure distributions associated with the inner and outer transducer; $\Delta\omega$ denotes the difference frequency; and $\mathcal{M}(r,t_\mathrm{s})$ is the modulation envelope, which, in this case, is also a function of the radial coordinate r. To treat generic situations where $\mathcal{M}=\mathcal{M}(r,t_\mathrm{s})$, one has to solve the steady-state problem for a representative set of values of the "slow" time variable (as opposed to a set of *modulation amplitude* values for the amplitude-modulated case), so that the modulation envelope function $\mathcal{M}(r,t_\mathrm{s})$ is discretized accurately. Then, the "slow" time phase shift can be included (similarly as for the amplitude-modulated case) by interpolating between the precomputed solutions. This class of problems is clearly more demanding in terms of the computational and memory requirements, since a larger set of solutions has to be precomputed. However, since the modulation envelope is inherently periodic in terms of "slow" time for the dual beam case (4.39), the discretization of only one period of the modulation envelope is necessary, which can be achieved using reasonably small amount of sampling points. Note that care should be taken when interpolating between the solutions that correspond to complex-valued modulation envelopes as that in (4.39). In particular, it was found that such envelopes are more effectively interpolated in terms of their amplitude and phase, rather than their real and imaginary components.

4.5.4 Full diffraction versus parabolic approximation

As examined earlier, the featured dual-time approach deploys the "full" diffraction model (4.30) for the linear part of the solution, and parabolic approximation in (4.19) as a tool to account for the nonlinear interaction. Here, the linear part of the solution is simulated without parabolic approximation because the "full" diffraction model (4.30) carries virtually the same computational cost as its parabolic-approximation counterpart (4.27). To highlight the effect of using (4.30) in lieu of (4.27) on the overall (nonlinear) solution, Fig. 4.7 compares the dual-time solutions of (4.19) computed via the two competing linear treatments. Consistent with the results shown in Fig. 4.4, the solution that relies on the parabolic approximation (4.27) overestimates the intensity computed more accurately via (4.30).

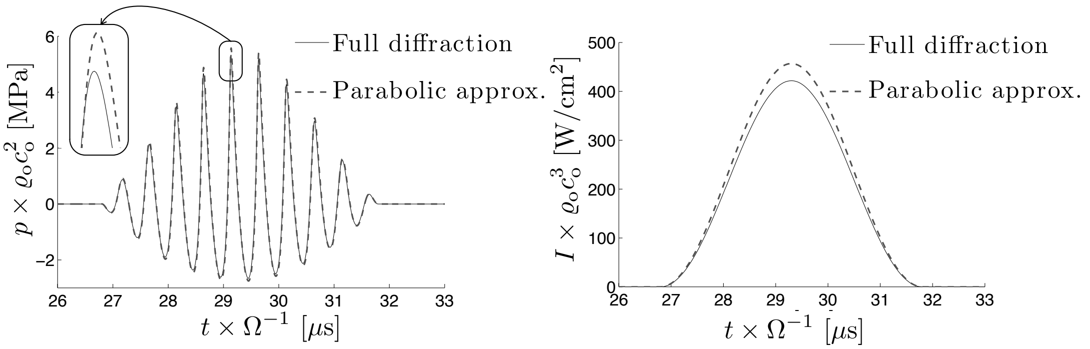

Figure 4.7: Comparison of the pressure signals (left panel) and intensities (right panel) at the focal point $(0, d)$, whose linear parts are computed respectively via the full diffraction model (4.30) and parabolic approximation (4.27). The modulation frequency is $\omega_{\mathrm{m}} = 0.05$.

4.6 Time-domain solution of the KZK equation

To examine the performance of the proposed dual-time approach, used to derive (4.19), this section summarizes an algorithm used to obtain the numerical solution of the KZK equation in the *time domain* for the case of modulated ultrasound excitation. To this end, the governing equation can be written as

$$2\frac{\partial^2 p}{\partial t' \partial z_{\mathrm{s}}} \;=\; \nabla_{\perp}^2 p \;+\; \beta\frac{\partial^2 p^2}{\partial t'^2} \;+\; \int_0^{\infty} K(\xi)\,\frac{\partial^3 p(\ldots, t'-\xi)}{\partial t'^3}\,\mathrm{d}\xi, \tag{4.40}$$

where the "total" time derivatives are used instead of their "fast" counterparts, as was done in (4.19). To deal with the hereditary integral in (4.40) numerically, one may compute the contribution from dissipation separately from that of diffraction and nonlinear interaction for each increment in z. In this setting, the lossless version of equation (4.40) can be integrated with respect to z and t' over the rectangular area $[z_1, z_2] \times [t'_1, t'_2]$ to obtain

$$\begin{aligned} p(r, z_2, t'_2) &= p(r, z_1, t'_2) + p(r, z_2, t'_1) - p(r, z_1, t'_1) + \tfrac{1}{2}\nabla_{\perp}^2 \int_{z_1}^{z_2}\int_{t'_1}^{t'_2} p\,\mathrm{d}t'\,\mathrm{d}z_{\mathrm{s}} \\ &\quad + \tfrac{1}{2}\beta \int_{z_1}^{z_2} \Big(\frac{\partial p^2}{\partial t'}(t'_2) - \frac{\partial p^2}{\partial t'}(t'_1)\Big)\,\mathrm{d}z_{\mathrm{s}}. \end{aligned} \tag{4.41}$$

In the numerical scheme, the double integral is approximated as

$$\int_{z_1}^{z_2}\!\!\int_{t'_1}^{t'_2} p\,\mathrm{d}t'\,\mathrm{d}z \;\approx\; \tfrac{1}{4}\Big[p(r,z_2,t'_2)+p(r,z_1,t'_2)+p(r,z_2,t'_1)+p(r,z_1,t'_1)\Big](z_2\!-\!z_1)(t'_2\!-\!t'_1), \tag{4.42}$$

while the central difference scheme is used to discretize both the (transverse) Laplacian and the time derivatives in (4.41). To avoid solving the nonlinear equation for each step, the one-dimensional integral in (4.41) is approximated using the value of the time derivative at z_1 only. Equations (4.41) and (4.42) are the basis for the implicit (Crank-Nicolson) numerical scheme used in this study to solve lossless version of (4.40) in the time domain, since they permit computation the solution at the next "elevation" $z_2 = z_1 + \Delta z$, knowing the result for "elevation" z_1. More detailed description of the time-domain schemes for solving the KZK equation can be found e.g. in [28, 7]. The next task is to incorporate the dissipation effects (and affiliated dispersion effects) associated with the hereditary integral in (4.40). To this end, one has to solve

$$2\frac{\partial p}{\partial z} \;=\; \int_0^\infty K(\xi)\frac{\partial^2 p(r,z,t'-\xi)}{\partial t'^2}\,\mathrm{d}\xi \tag{4.43}$$

numerically for an increment in space $\Delta z = z_2 - z_1$. Equation (4.43) can be conveniently solved using the Fourier transform $\mathcal{F}$ with respect to the temporal coordinate as

$$p(r,z_2,t') \;=\; \mathcal{F}^{-1}\Big[\exp\big(-\tfrac{1}{2}\omega^2 K_\omega(z_2\!-\!z_1)\big)\mathcal{F}[p(r,z_1,t')]\Big], \tag{4.44}$$

where ω denotes the transform parameter and K_ω is the Fourier transform of K, evaluated at frequency ω. In this setting (4.44) can be solved by an application of the fast Fourier transform algorithm for each step Δz or, alternatively, by precomputing the featured linear operator and applying it for each increment. A variant of the latter approach was deployed in [31] to account for the acoustic wave dissipation in soft tissues entailing short pulses in the time domain. For the purposes of this study, it is noted that for both soft tissues, where $K_\omega = 2\alpha/|\omega|$ (α is the attenuation coefficient per unit frequency) and fluids, where $K_\omega = \delta = \text{const.}$, the right-hand side of (4.44) can be reduced to a single integral. On substituting $K_\omega = 2\alpha/|\omega|$ into (4.44), changing the order of integration and evaluating of the inner integral analytically, one finds that

$$p(r,z_2,t') \;=\; \frac{1}{\pi\alpha(z_2\!-\!z_1)}\int_{-\infty}^{\infty}\Big(1+\Big(\frac{s-t'}{\alpha(z_2\!-\!z_1)}\Big)^2\Big)^{-1} p(r,z_1,s)\,\mathrm{d}s, \tag{4.45}$$

which can be approximated as

$$p(r,z_2,t'_j) \;=\; \sum_{i=1}^{N_t}\frac{1}{\pi}\left[\tan^{-1}\!\left(\frac{t'_{i+1/2}-t'_j}{\alpha(z_2-z_1)}\right)-\tan^{-1}\!\left(\frac{t'_{i-1/2}-t'_j}{\alpha(z_2-z_1)}\right)\right]p(r,z_1,t'_i),\quad j=1...N_t. \tag{4.46}$$

Here $t'_{i+1/2}$ is the midpoint between t'_i and t'_{i+1}, and N_t denotes the number of discretization points in time. The analogue of (4.45) for fluids reads

$$p(r,z_2,t') \;=\; \frac{1}{\sqrt{2\pi\delta(z_2-z_1)}}\int_{-\infty}^{\infty}\exp\!\left(-\frac{(s-t')^2}{2\delta(z_2-z_1)}\right)p(r,z_1,s)\,\mathrm{d}s, \tag{4.47}$$

which can be discretized as

$$p(r,z_2,t'_j) \;=\; \sum_{i=1}^{N_t}\frac{1}{2}\left[\mathrm{erf}\!\left(\frac{(t'_{i+1/2}-t'_j)}{\sqrt{2\delta(z_2-z_1)}}\right)-\mathrm{erf}\!\left(\frac{(t'_{i-1/2}-t'_j)}{\sqrt{2\delta(z_2-z_1)}}\right)\right]p(r,z_1,t'_i),\quad j=1...N_t \tag{4.48}$$

in terms of the error function. Note that (4.45) and (4.47) represent the convolution of the solution at z_1 with the fundamental solution of (4.43) for different kernels K. Also note that since (4.44) is valid for every (even large) z_2-z_1, this approach does not introduce any restriction on the discretization of the axial coordinate z. In general, the consecutive use of (4.41), (4.42) and (4.44) can be used to compute the time-domain solution of (4.40) for any kernel K. For the purposes of this study that focuses on the validation of the the dual-time approach, however, simplified relation (4.46) is used instead of more generic (4.44).

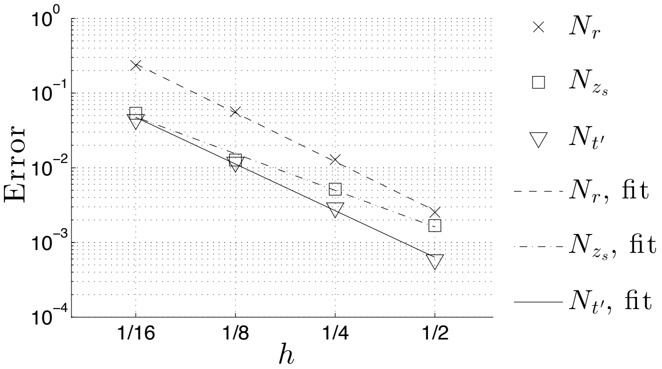

Figure 4.8: Approximation error versus the “coarsening” factor h (markers) and corresponding linear fit (lines) for three types of refinement: radial coordinate (N_r), axial coordinate (N_z), and temporal coordinate ($N_{t'}$).

To ensure that the error of numerical approximation is acceptable, the convergence rate of the time-domain scheme is investigated. For consistency, the physical parameters of the medium are chosen to be the same as in Section 4.5.3, while the focused source is modeled as a phased array for simplicity. The focusing is achieved by applying a time delay distribution $t_d = -r^2/(2d)$ to a piston source along the boundary $\Gamma = \{(r,z)\colon z=0,\, r\leqslant a\}$, see the left panel in Fig. 4.2. The computational domain is taken as $r_{\max}\times c_{\rm o}/\Omega = 2.5\,\text{cm}$, $z_{\max}\times c_{\rm o}/\Omega = 4\,\text{cm}$, and $t'_{\max}/\Omega = 8\ \mu\text{s}$ (the length of the signal is $5\ \mu\text{s}$), while the reference "exact" solution is taken as the numerical result with the mesh parameters given by $N_r = 1600$ (points along r), $N_z = 1600$ (points along z) and $N'_t = 8000$ (points along t'). In what follows, the solution error is defined as the $L^2[0,t'_{\max}]$ norm of the distance between the computed pressure signal and the "exact" solution at the focal point, normalized by the L^2 norm of the "exact" solution. Fig. 4.8 plots the variation of the error versus the coarsening factor h, defined as the ratio between the deployed mesh size and that used for the "exact" solution. For example $h=\frac{1}{4}$ in terms of N_r corresponds to the solution with $N_r = \frac{1}{4}\times 1600 = 400$ points in the radial direction, while the remaining mesh parameters are kept the same as for the "exact" solution, i.e. $N_z = 1600$ and $N'_t = 8000$. To determine the convergence rate, Fig. 4.8 also shows the linear fit to the data, where the slopes (convergence powers) are 2.17 for the N_r data, 1.63 for N_z data, and 2.08 for $N_{t'}$ data. Note that these slopes are in agreement with the order of the finite-difference approximation. In particular, the central difference scheme (used to discretize the transverse Laplacian) has accuracy $O(N_r^{-2})$; the Crank-Nicolson scheme for the diffraction term is accurate to $O(N_z^{-2}) + O(N_{t'}^{-2})$; the dissipation term computed through (4.46) gives $O(N_{t'}^{-2})$ error, while the nonlinear term is approximated with $O(N_z^{-1}) + O(N_{t'}^{-2})$ accuracy. For this reason, the fitted slopes in Fig. 4.8 are close to 2 for the N_r and $N_{t'}$ data, while the N_z data are characterized by a slope less than two due to pollution by additional source of error due to discretization of the nonlinear term. Also note that, for a given example problem, the observed computational time increases roughly linearly with each of the mesh parameters N_r, N_z and $N_{t'}$. To have the approximation error on the order of 10^{-3}, one can extrapolate the results shown in Fig. 4.8 to obtain the required mesh parameters $N_r = 1200$, $N_z = 800$, and $N_{t'} = 4000$.

4.7 Comparison with time-domain simulations

To expose the performance of the dual-time approach, this section is devoted to the comparison between the numerical solution of (4.19), described in Section 4.5, and the time-domain solution of (4.40) summarized in Section 4.6. In light of the discussion in Section 4.5.4, the dual-time approach results are hereon computed using parabolic approximation (4.27) for consistency with time-domain simulations. To achieve a meaningful comparison between the two techniques, the numerical error committed by each method should be sufficiently small. For the time-domain simulations, the spatial grid is generated using $N_r = 1200$ radial, $N_z = 800$ axial and $N_{t'} = 4000$ temporal points, taking $\omega_{\rm m} = 0.05$ as the modulation frequency in (4.38). For other modulation frequencies, both the length of the signal and $N_{t'}$ are increased linearly with $\omega_{\rm m}$, so that the number of points per oscillation period is conserved. According to Fig. 4.8, the expected relative error for time-domain simulations is in this case $O(10^{-3})$. To facilitate the comparison between the two approaches in terms of their efficiency, spatial discretization for the dual-time approach is effected using the same number of points in the z- and r- directions, namely $N_r = 1200$ and $N_z = 800$. The remaining parameters of the dual-time scheme are taken as in Section 4.5 so that, with reference to Figs. 4.3, 4.5 and 4.6, the expected numerical approximation error is again $O(10^{-3})$. For completeness, it is noted that both dual-time and time-domain solutions are implemented in Matlab 2011b, while the simulations are run on an Apple Mac Pro computer equipped with a single 2.8 GHz Quad-Core Intel Xeon processor and 8 GB of 1066 MHz DDR3 memory.

Boundary conditions. To achieve the focusing effect by way of a planar source, specific time delay distribution must be imposed along the transducer's boundary. For the problem under consideration, the pressure boundary condition generating the focused, modulated ultrasound beam can be written as

$$p(r, z\!=\!0, t) \;=\; p_{\rm o}\, \mathcal{M}(t\!+\!r^2/(2d))\, \cos(t\!+\!r^2/(2d)), \tag{4.49}$$

where the time delay $-r^2/(2d)$ is applied to both the modulation envelope and the carrier signal. Unfortunately, explicit computational treatment of the boundary condition (4.49) via the dual-time approach is not convenient, since the modulation envelope does not only vary with time as in (4.36), but also with the radial coordinate r. To

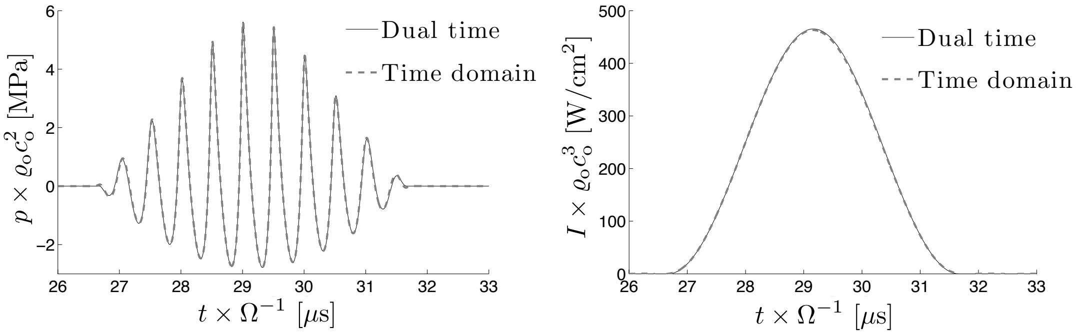

Figure 4.9: Comparison between the pressure (left) and the intensity (right) in the focus computed using the dual-time approach and the time domain calculations.

deal with the problem, one may however recall that $\mathcal{M}' = O(\omega_{\rm m}\mathcal{M})$ where $\omega_{\rm m}$ is the dominant modulation frequency, and expand the modulation term in (4.49) in Taylor series to find

$$p(r, z\!=\!0, t) \;=\; p_{\rm o}\,\mathcal{M}(t)\,\cos(t\!+\!r^2/(2d))\Big[1 + O\big(\omega_{\rm m} r^2/(2d)\big)\Big], \qquad (4.50)$$

which can be used as an approximation of (4.49) for sufficiently small modulation frequencies. The advantage of (4.50) lies in its suitability for dual-time computations, described in Section 4.5. With the above developments in place, the time-domain solution of the KZK equation is computed using (4.49) as the boundary condition, while corresponding result of the dual-time numerical scheme is computed assuming simplified boundary condition (4.50).

Error analysis. Fig. 4.9 shows a comparison in terms of time histories the nonlinear pressure signal (left panel) and intensity (right panel) at the focal point, computed via the dual-time approach and the time-domain algorithm under respective boundary conditions (4.50) and (4.49). Here the intensity is computed using the “fast” time average of the squared pressure signal [20] for dual-time simulations, and low-pass filtering of the averaged p^2 quantity for time-domain calculations. As can be seen from the display, both pressure and intensity variations are virtually indistinguishable. However, there is a small difference between the two sets of numerical results, that is concentrated near the edges of the modulation envelope.

To quantify the misfit between solutions, two distance measures are introduced, referred to as the "pressure" error and "intensity" error. As before, each error is defined as the $L^2([0, t_{\max}])$ distance between two signals normalized by the $L^2([0, t_{\max}])$ norm of the dual-time signal. Fig. 4.10 plots the featured error measures versus the modulation frequency ω_{m}, together with a linear fit to the pressure error data. The slope of the fitted line is approximately 1.1; however, if a straight line was fitted only to the first three data points ($\omega_{\mathrm{m}} = 0.025 \div 0.1$), the fitted slope becomes much closer to unity. This result is consistent with the fact that both the terms that are neglected in (4.19) (relative to (4.40)) and the approximation error of the boundary condition (4.50) (relative to (4.49)) are $O(\omega_{\mathrm{m}})$, whereby the theoretical slope value for the error in pressure data is unity. One may also note from Fig. 4.10 that for sufficiently low modulation frequencies, the intensity error is smaller than its pressure counterpart. This likely happens because of the presence of ultrasound-scale phase difference between the two solutions (mostly due to diffraction and attenuation), which may significantly affect the pressure signal while having minimal effect on the intensity. For completeness, it should be noted that the filtering, used to compute the intensity from time-domain data, works poorly for high modulation frequencies (since the modulation frequency becomes closer to the carrier ultrasound frequency), which explains higher intensity error at high modulation frequencies.

Range of applicability. If one accepts the error in the nonlinear solution as high as few percent, the data in Fig. 4.10 indicate that the dual-time approach is applicable to modulation frequencies of up to $\omega_{\mathrm{m}} = 0.05$ (recall that $\Omega = 2\pi \times 2$ MHz for the problem under consideration). In contrast, the quasi-static approximation [9], which lacks z "slow" time shift, simulates the nonlinear solution with commensurate accuracy for modulation frequencies up to only $\omega_{\mathrm{m}} = 0.0005$.

Effect of the approximate boundary condition. The results in Fig. 4.10 reflect two sources of discrepancies, namely those arising from: i) the KZK equation, and ii) the boundary conditions. To better understand the discrepancies caused exclusively by the introduction of the dual-time treatment, it is instructive to compare the results of the dual-time method to time-domain simulations of the KZK equation under identical

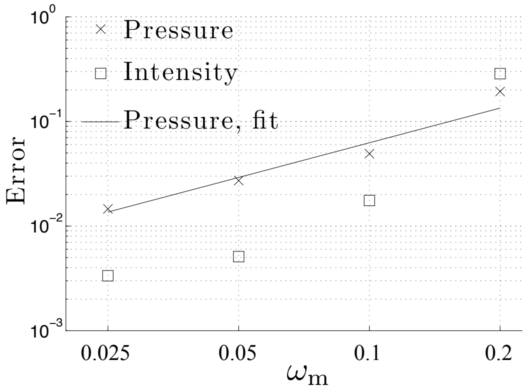

Figure 4.10: Variation of the discrepancy between dual-time approach and time domain simulations versus modulation frequency.

boundary conditions given by (4.50). In this setting, the respective time-domain simulations of (4.40) under (4.49) and (4.50) were found to exhibit similar behavior; however, the apparent modulation envelope experienced by the solution at the focus in the second case (corresponding to (4.50)) is delayed by approximately 0.5 μs. With reference to Fig. 4.9, this time delay makes the discrepancy between the dual-time approach and time domain calculations more pronounced, when identical boundary condition (4.50) is used.

To understand the 0.5 μs time shift in the time-domain solution of (4.40) and (4.50) relative to the corresponding "mother" solution of (4.40) and (4.49), one may estimate the modulation envelope that is experienced by the solution at the focus using ray theory. In this case, the *effective* amplitude modulation imposed on the solution at focus $(0,d)$ by boundary conditions (4.49) and (4.50) can be computed respectively as

$$\begin{aligned}\overline{\mathcal{M}}_1 &= \frac{1}{a^2}\int_0^a \mathcal{M}\Big(t+r^2/(2d)-\sqrt{d^2+r^2}\Big)2r\,\mathrm{d}r\\ &\approx \mathcal{M}\big(t-z_1\big) - \mathcal{M}'\big(t-z_1\big)\frac{1}{a^2}\int_0^a\big(\sqrt{d^2+r^2}-r^2/(2d)-z_1\big)2r\,\mathrm{d}r\\ &= \mathcal{M}\big(t-z_1\big) - \mathcal{M}'\big(t-z_1\big)\frac{1}{a^2}\Big[\tfrac{2}{3}\big((d^2+a^2)^{3/2}-d^3\big)-\frac{a^4}{4d}-z_1a^2\Big]\\ &= \mathcal{M}\big(t-z_1\big) - \mathcal{M}'\big(t-z_1\big)\Big[d-z_1+O\Big(\frac{a^4}{24d^3}\Big)\Big],\end{aligned} \tag{4.51}$$

and

$$
\begin{aligned}
\overline{\mathcal{M}}_2 &= \frac{1}{a^2}\int_0^a \mathcal{M}\Big(t-\sqrt{d^2+r^2}\Big)2r\,\mathrm{d}r \\
&\approx \mathcal{M}\big(t-z_2\big) \;-\; \mathcal{M}'\big(t-z_2\big)\frac{1}{a^2}\int_0^a \big(\sqrt{d^2+r^2}-z_2\big)2r\,\mathrm{d}r \\
&= \mathcal{M}\big(t-z_2\big) \;-\; \mathcal{M}'\big(t-z_2\big)\frac{1}{a^2}\Big[\tfrac{2}{3}\big((d^2+a^2)^{3/2}-d^3\big)-z_2a^2\Big] \\
&= \mathcal{M}\big(t-z_2\big) \;-\; \mathcal{M}'\big(t-z_2\big)\Big[d+\frac{a^2}{4d}-z_2+O\Big(\frac{a^4}{24d^3}\Big)\Big],
\end{aligned}
\tag{4.52}
$$

where z_1 and z_2 are the parameters to be determined next. In (4.51) and (4.52), the approximation sign indicates truncated Taylor series expansion whose residual is proportional to higher-order derivatives of $\mathcal{M}$ and is thus negligible for sufficiently low modulation frequencies. On the basis of (4.51) and (4.52), one finds that

$$
z_1 = d, \qquad\qquad z_2 = d + a^2/4d \tag{4.53}
$$

provide the best approximation of the *effective* modulation envelopes experienced by the solution at $(0,d)$ due to respective boundary conditions (4.49) and (4.50). With reference to (4.18), it is noted that the dual-time method imposes the modulation phase shift $-d$ on the pressure solution at $(0,d)$, which happens to coincide (to the leading order) with the result in (4.51) when $z_1 = d$ according to (4.53). This is precisely the reason why the result of time-domain simulations assuming (4.49) as the boundary condition is in good agreement with the output of the dual-time method. On the other hand, one finds that $a^2/(4d)/\Omega \approx 0.42$ μs for the problem under consideration, which explains the 0.5 μs phase shift observed in time-domain simulations under reduced boundary condition (4.50). In support of the results obtained in (4.51) and (4.53), Fig. 4.11 shows a comparison between the dual-time result, *phase-shifted* by $a^2/(4d)$, and time-domain simulations in terms of the pressure signal and intensity at $(0,d)$, all computed assuming the reduced boundary condition (4.50). In this case, the misfit between the solutions is more pronounced (relative to Fig. 4.9) as there is visible difference between the pressure signals near the edges of the modulation envelope, as well as notable overestimation of the peak intensity by the dual-time method. By comparing the onset of the respective pressure signals in Fig. 4.9 and Fig. 4.11, one can also observe the featured time delay $a^2/(4d)$.

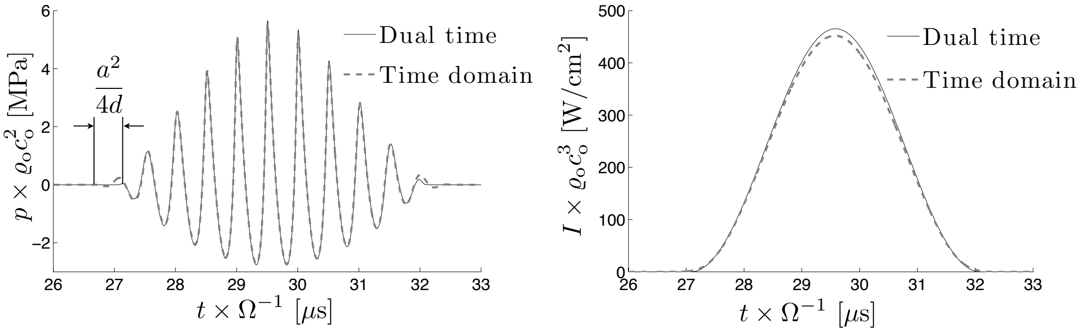

Figure 4.11: Comparison between the pressure (left) and the intensity (right) in the focus computed using the dual-time approach with the effective modulation envelope and the time domain calculations.

One should also note that the error measure used in this study is very specific, as it is limited to the time response at the focal point $(0, d)$. This is the reason why the time domain solution with (4.49) is described better by the dual-time method than the corresponding time-domain calculations assuming (4.50). If one would consider the pressure signal at another depth $z \neq d$, the phase cancellation as in (4.51) may not occur and the dual-time solution may be closer to the time-domain simulations with (4.50). In any case, the discrepancy in the phase along the boundary is on the order of $a^2/(2d) \approx 0.8$ μs, and when such time scales are negligible compared to the modulation time scale, the distinction between (4.49) and (4.50) is immaterial and the dual-time algorithm approximates the time-domain solution at an arbitrary depth.

Efficiency. As can be seen from Fig. 4.10, the error committed by the dual-time method is admissible, by being on the order of several percent or less, for modulation frequencies below $\omega_\mathrm{m} = 0.05$. At the same time, the dual-time method used to solve (4.40) is both memory-wise and computationally more efficient than its time-domain companion. For instance, it takes only 6 minutes and 20 seconds to precompute $N_A = 8$ nonlinear steady-state solutions for the example problem considered in this section ($\omega_\mathrm{m} = 0.05$), with additional 50 seconds being needed to precompute the linear propagation operator (4.29). In contrast, the time-domain solution of the same problem requires 1 hour and 38 minutes of computation. Note that the spatial grid is chosen to be the same for two methods for objective comparison of their efficiency; however, such fine discretization is not necessary for the dual-time approach, whereby the reduction in the spatial mesh size (with minimal accuracy degradation) may lead to even faster dual-time computations. One additional advantage of the dual-time approach is that with N_A (nonlinear) steady-state solutions at hand, one can recover the pressure signal at an arbitrary point in space, for any modulation envelope, via suitable interpolation and phase shifting of the former as examined in Section 4.5. In the time-domain solution, on the other hand, one has to recompute the solution for each modulation envelope; in addition, the affiliated computational effort increases (roughly linearly) with the length of the signal if the same number of points per ultrasound-scale oscillation is used.

Concerning the memory usage, the sparsity of the dual-time approach introduced through (4.33) allows one to manage the memory in a very efficient way. For the problem under consideration, it takes only 655 MB to store $N_A = 8$ nonlinear solutions. In contrast, storing the time-domain solution at every point in space would require approximately 30 GB of memory for $\omega_{\mathrm{m}} = 0.05$ (note that the latter memory requirement increases linearly with modulation frequency). Even though the above computing and memory requirements of the time-domain solution are not an issue for the example under consideration, the time-domain treatment of problems entailing either larger computational domains or non-axisymmetric geometries may be significantly more taxing. In conclusion, it is noted that the dual-time approach is equally applicable to linear simulations in which case only one steady-state solution must be precomputed (since the solution scales with the amplitude of boundary excitation), while the time-domain algorithm for the linear case requires almost the same computational effort as that for the nonlinear case.

4.8 Summary

In this Chapter, a KZK-type model is proposed to describe the nonlinear wave propagation affiliated with modulated, high-intensity focused ultrasound under the premise that the ratio between the dominant modulation frequency and the carrier frequency is $o(1)$. Such ultrasound fields, which bear particular relevance to the applications of acoustic radiation force in medical diagnosis, may be difficult to simulate, mostly due to extended temporal length of the modulation signal which makes the full-time simulations computationally expensive. Compounding the problem, the customary quasi-static approximation (which caters for this class of problems) may not be able to accurately capture the effects of ultrasound modulation when the dominant modulation frequency on the order of $10^2 \div 10^4$ Hz as in a number of diagnostic applications. To deal with the impediment, an intermediate asymptotics approach, which exploits the simplicity of the quasi-static solution while rigorously taking into account the leading-order modulation effects, is suggested. The technique is based on the dual-time scale analysis, where the temporal variable is split into its "fast" (i.e. ultrasound) and "slow" (i.e. modulation) components, which makes the solution periodic in "fast" time. A KZK-type equation, which effectively describes the nonlinear wave propagation of the modulated ultrasound field, is obtained for this case. The solution to this equation, while being similar in form to the quasi-static approximation, carries an important distinction in that it features the phase delay in "slow" time due to finite wavelength of the compressional wave at modulation frequency. For generality, the analysis deploys separate scaling parameters to describe the effects of diffraction and modulation, allowing the model both to absorb a wide range of transducer geometries and to recover the quasi-static approximation as a limiting case for low modulation frequencies. The accuracy of the dual-time approximation for high modulation frequencies is investigated by comparing the output signal for the example axisymmetric focused modulated sound beam problem with the time domain simulations of the KZK equation. To obtain the result using the dual-time approach, the solution at an arbitrary point in space and time is obtained by i) precomputing a finite set of nonlinear steady-state solutions, and ii) suitably interpolating and phase-shifting the latter to incorporate the effects of modulation. Here the "reference" nonlinear solutions are computed via the spectral method with operator splitting. In particular, the linear part of the KZK equation is solved in the frequency domain via the angular spectrum method, while the spectral method is utilized to capture the nonlinear interaction. The performance of the dual-time approximation, applied to the nonlinear parabolic wave equation (i.e. the KZK equation), is exposed by comparing the output signal for the example axisymmetric problem with time-domain simulations of the KZK equation. In the time-domain algorithm, the effects of nonlinearity and diffraction are computed via a Crank-Nicolson scheme wherein the nonlinear term is approximated using central differences. The dissipation for the case of soft tissues, where the attenuation coefficient is proportional to the excitation frequency, is taken into account via convolution with the fundamental solution of a diffusion-type equation. With the two alternative computational schemes at hand, a numerical analysis is performed to ensure that the relative error is low ($O(10^{-3})$ in this study) for each approach. A comparison between the respective pressure signals reveals that the discrepancy between the two solutions is on the order of few percent when the ratio between the dominant modulation frequency and carrier ultrasound frequency is $\omega_{\mathrm{m}} = 0.05$, and decreases monotonically with diminishing ω_{m}. The observed rate of decay is found to be slightly stronger than unity, where the latter signifies the expected (theoretical) value. In terms of the solution efficiency, the dual-time approach is shown to outperform its time-domain companion in terms of both computational cost and memory usage. The principal reason for the improved performance resides in the fact that only a few, $O(10)$, steady-state nonlinear solutions are required to "construct" the temporal variation of the nonlinear solution everywhere in the domain (assuming arbitrary "slow" modulation envelope). Overall, the dual-time method is capable of effectively describing the modulated sound field in situations when the modulation frequency is notably smaller than the carrier frequency of ultrasound ($\omega_{\mathrm{m}} \leqslant 0.05$), yet sufficient to render the time-domain computations inefficient. Due to its effectiveness, the dual-time approach opens the possibilities for simulating nonlinear wave propagation in large computational domains under arbitrary (three-dimensional) transducer geometries.

Chapter 5

Measurement of the nonlinear elastic coefficient C via acoustic radiation force

5.1 Introduction

The theory of continuum mechanics demonstrates that the strain energy density in an isotropic, nonlinear elastic solid can be described by two second-order moduli (e.g. the usual bulk modulus and shear modulus) and three independent third-order moduli for sufficiently small strains (see e.g. [88, 23, 7]). Among linear elastic constants, the bulk modulus is known to vary a little for most soft tissues, while the shear modulus is very sensitive to a tissue type and is commonly used to characterize the tissue and distinguish unhealthy grows (see e.g. [22, 16, 10]). One relevant technique is the shear wave elasticity imaging, introduced by [9], where the focused ultrasound is used to push inside the tissue with the radiation force and generate the shear waves locally within the focal region, then, the shear modulus is estimated from the shear wave particle velocity data. Regarding the third-order elastic moduli, to the author's knowledge, only two of them were studied thoroughly in the context of soft tissues. The first, that characterizes the nonlinear behavior with respect to volumetic deformations (denoted by B) and is used to describe shock pressure waves, was studied by the acoustic community (e.g. see [7]).

The second, that describes nonlinear shear deformations (D) is typically utilized as an additional information to the shear modulus, and is examined mostly by people in elasticity imaging (see e.g. [89]). The third coefficient, which is responsible for the nonlinear coupling between volumetric and deviatoric modes of deformation (coefficient C), has not received mounting attention in the literature, perhaps, due to the facts that tissue is assumed water-like (no shear resistance) for ultrasound waves [7] and incompressible for static deformations [89]. Those assumptions automatically disregard shear-bulk mode of nonlinear interaction and remove the dependence on the third nonlinearity modulus C. One should note, however, that there is at least one work, which deals with the measurement of all three elastic nonlinearity coefficients in tissue-mimicking phantoms [35].

In Chapter 3, it was found that the magnitude of the acoustic radiation force (ARF) in an isotropic tissue-like solid, generated by the action of focused ultrasound field, is related linearly to the third-order modulus C. Prompted by recently developed theory of the ARF in tissue-like solids (see [20] or Chapter 3), this chapter aims to: i) locally estimate the third-order modulus C from the amplitude of the shear waves generated by the ARF; ii) cross-validate thus obtained estimates of C via an independent measurement technique, and iii) examine the level of variability of C in selected tissue-mimicking phantoms.

One effective (independent) way to measure the third-order moduli is the technique known as acoustoelasticity [33, 34, 7] that exploits the variation of (small-strain) elastic wave speed with the level of pre-existing (finite) static deformation. In this study, acoustoelasticity experiments were performed on uniaxially-stressed tissue-mimicking phantoms wherein the small-strain shear waves were generated by the ARF. Equipped with the newly established theory of the ARF in soft solids, the value of C is independently assessed by matching the amplitude of the observed and modeled shear wave motion. The results demonstrate that the phantoms tested, while clearly exhibiting nonlinear elastic behavior, differ significantly in magnitude of the back-calculated third-order modulus C. The estimates of the latter coefficient obtained respectively via acoustoelasticity and the theory of the ARF have shown significant degree of consistency.

5.2 Acoustoelasticity: Eulerian approach

In situations when the isotropic nonlinear elastic material undergoes finite static deformations, it becomes apparently anisotropic, as viewed through the prism of linear waves, due to the contribution of nonlinear effects. Thus observed anisotropy can be quantified by measuring the small-amplitude wave speed e.g. in different directions, where it was found to scale (in terms of its square) with the magnitude of the static deformation. This phenomenon is utilized by the acoustoelasticity technique for the purpose of measuring the nonlinear elastic behavior of various materials [34, 7].

This section aims to establish the relevant formulas of acoustoelasticity. In particular, it seeks to derive the expressions for the shear wave velocities in a uniaxially prestressed, nonlinear tissue-like material. Note that the discussion in this section is focused on the special case of soft solids, and the developments are presented exclusively in the Eulerian frame of reference (as opposed to Lagrangian, see e.g. [7]). The consideration of the limiting case of soft solids allows one to simplify the problem from the beginning and to obtain the acoustoelasticity formulas in a more elegant manner, avoiding unnecessary complications. In the last part of the section, the featured theoretical developments are used to measure the coefficients of nonlinear elasticity in tissue-mimicking phantoms on the basis of the ultrasound measurements of shear wave propagation performed at the Mayo Clinic.

5.2.1 Preliminaries

As a starting point, consider a case of a nonlinear elastic material with heat conduction and viscosity – a constitutive model that was used in the development of the acoustic radiation force (see Chapter 3). By adopting the notation from Section 3.2, the governing equation for the wave propagation in the prestressed material (the balance of linear momentum) can be written in the Eulerian frame of reference as

$$\rho\Big(\frac{\partial \boldsymbol{v}}{\partial t} + \boldsymbol{v}\cdot\nabla\boldsymbol{v}\Big) \;=\; \nabla\cdot\boldsymbol{\sigma} + \boldsymbol{f}, \tag{5.1}$$

where $\boldsymbol{f}$ is the body force vector, $\boldsymbol{\sigma}$ is the Cauchy stress tensor, which is given by

$$\boldsymbol{\sigma} \;=\; \rho\boldsymbol{F}\cdot\left[\frac{\partial\bar{U}}{\partial I_1}\boldsymbol{I} + \frac{\partial\bar{U}}{\partial I_2}\Big(I_1\boldsymbol{I} - \boldsymbol{E}\Big) + \frac{\partial\bar{U}}{\partial I_3}\Big(I_2\boldsymbol{I} - I_1\boldsymbol{E} + \boldsymbol{E}^2\Big)\right]\cdot\boldsymbol{F}^{\mathrm{T}} + \boldsymbol{J}:\nabla\boldsymbol{v}, \tag{5.2}$$

and $\bar{U}$ denotes the internal energy expressed in terms of the invariants of the Green-Lagrangian strain tensor (see (3.8)). For the purpose of deriving the acoustoelasticity expressions, it is next instructive to expand (5.1) and (5.2) in Taylor series, assuming the smallness of the displacement field, but retaining *all* second-order terms. On setting $\boldsymbol{u} = O(\psi)$, where $\psi \ll 1$, one may approximate the internal energy as

$$\bar{U} \overset{\psi^4}{=} \tfrac{1}{2}(K+\tfrac{4}{3}G)I_1^2 - 2GI_2 + \tfrac{1}{6}BI_1^3 + CI_1I_2 + DI_3, \quad I_n = O(\psi^n), \quad n = 1,2,3, \tag{5.3}$$

where the bulk and shear moduli are denoted respectively by K and G, the third-order moduli are signified by B, C, and D, while

$$I_1(\boldsymbol{E}) = \mathrm{tr}(\boldsymbol{E}), \qquad I_2(\boldsymbol{E}) = \tfrac{1}{2}\big[(\mathrm{tr}(\boldsymbol{E}))^2 - \mathrm{tr}(\boldsymbol{E}^2)\big], \qquad I_3(\boldsymbol{E}) = \det(\boldsymbol{E}) \tag{5.4}$$

are the invariants of the Green-Lagrangian strain tensor, and $\overset{\psi^n}{=}$ indicates the approximation with $O(\psi^n)$ residual. The deformation gradient, strain tensor, mass density, the first and the second strain invariants, and the viscous part of the Cauchy stress tensor can respectively be expanded up to a sufficient order of accuracy as

$$\begin{aligned}
\boldsymbol{F} &= (\boldsymbol{I} - \nabla^{\mathrm{T}}\boldsymbol{u})^{-1} \overset{\psi^2}{=} \boldsymbol{I} + \nabla^{\mathrm{T}}\boldsymbol{u},\\
\boldsymbol{E} &= \tfrac{1}{2}(\boldsymbol{F}^{\mathrm{T}}\!\cdot\boldsymbol{F} - \boldsymbol{I}) \overset{\psi^3}{=} \tfrac{1}{2}\Big(\nabla\boldsymbol{u} + \nabla^{\mathrm{T}}\boldsymbol{u} + \nabla\boldsymbol{u}\cdot\nabla\boldsymbol{u} + \nabla^{\mathrm{T}}\boldsymbol{u}\cdot\nabla^{\mathrm{T}}\boldsymbol{u} + \nabla\boldsymbol{u}\cdot\nabla^{\mathrm{T}}\boldsymbol{u}\Big),\\
\rho &= \det(\boldsymbol{F})^{-1} \overset{\psi^2}{=} 1 - \nabla\cdot\boldsymbol{u},\\
I_1 &\overset{\psi^3}{=} \nabla\cdot\boldsymbol{u} + \nabla^{\mathrm{T}}\boldsymbol{u}\!:\!\nabla\boldsymbol{u} + \tfrac{1}{2}\nabla\boldsymbol{u}\!:\!\nabla\boldsymbol{u},\\
I_2 &\overset{\psi^3}{=} \tfrac{1}{2}\Big((\nabla\cdot\boldsymbol{u})^2 - \nabla^{\mathrm{S}}\boldsymbol{u}\!:\!\nabla^{\mathrm{S}}\boldsymbol{u}\Big),\\
\boldsymbol{J}\!:\!\nabla\boldsymbol{v} &\overset{\psi^3}{=} \Big(\mu_{\mathrm{B}} - \tfrac{2}{3}\mu + (\bar{\mu}_{\mathrm{B}} - \tfrac{2}{3}\bar{\mu})\nabla\cdot\boldsymbol{u}\Big)\frac{\partial\nabla\cdot\boldsymbol{u}}{\partial t}\,\boldsymbol{I} + 2(\mu + \bar{\mu}\nabla\cdot\boldsymbol{u})\,\frac{\partial\nabla^{\mathrm{S}}\boldsymbol{u}}{\partial t},
\end{aligned} \tag{5.5}$$

where $\nabla^{\mathrm{S}}\boldsymbol{u} = \tfrac{1}{2}(\nabla\boldsymbol{u} + \nabla^{\mathrm{T}}\boldsymbol{u})$ denotes small strain tensor or symmetric part of the displacement gradient. Note that the last equation in (5.5) is obtained by expanding the general form of $\boldsymbol{J}$, that satisfies material objectivity principle and accounts for material isotropy (see [48]) in Taylor series, while $\bar{\mu}_{\mathrm{B}}$ and $\bar{\mu}$ signify respectively the dependence of bulk and shear viscosities on the applied volumetric strain. Using the energy function (5.3) and the expansions (5.5), the Cauchy stress tensor (5.2) can be reduced to

$$\begin{aligned}\boldsymbol{\sigma} \overset{\psi^3}{=}\; & (K-\tfrac{2}{3}G)\nabla\cdot\boldsymbol{u}\,\boldsymbol{I} + 2G\nabla^{\mathrm{S}}\boldsymbol{u} + \Big\{\tfrac{1}{2}(B+3C+D-2K+\tfrac{4}{3}G)(\nabla\cdot\boldsymbol{u})^2 \\ & - \tfrac{1}{2}(C+D)\nabla^{\mathrm{S}}\boldsymbol{u}:\nabla^{\mathrm{S}}\boldsymbol{u} + (K-\tfrac{2}{3}G)(\nabla^{\mathrm{T}}\boldsymbol{u}:\nabla\boldsymbol{u} + \tfrac{1}{2}\nabla\boldsymbol{u}:\nabla\boldsymbol{u})\Big\}\boldsymbol{I} \\ & - (C+D-2K+\tfrac{10}{3}G)\nabla\cdot\boldsymbol{u}\nabla^{\mathrm{S}}\boldsymbol{u} + (D+8G)\nabla^{\mathrm{S}}\boldsymbol{u}\cdot\nabla^{\mathrm{S}}\boldsymbol{u} - G\nabla\boldsymbol{u}\cdot\nabla^{\mathrm{T}}\boldsymbol{u} \\ & + \Big(\mu_{\mathrm{B}} - \tfrac{2}{3}\mu + (\bar{\mu}_{\mathrm{B}} - \tfrac{2}{3}\bar{\mu})\nabla\cdot\boldsymbol{u}\Big)\frac{\partial\nabla\cdot\boldsymbol{u}}{\partial t}\boldsymbol{I} + 2(\mu + \bar{\mu}\nabla\cdot\boldsymbol{u})\frac{\partial\nabla^{\mathrm{S}}\boldsymbol{u}}{\partial t}.\end{aligned} \tag{5.6}$$

Note that (5.6) is very similar to (3.27) in Section 3.3.4, however, the difference lies in avoiding the assumption about smallness of the shear modulus and viscosities, which makes (5.6) more general. Also note that all coefficients in (5.6) are functions of entropy at this point, however, they become constants for isentropic motion. To expand the left hand side of (5.1), one may recall unscaled analog of (3.19) and mass density relation in (5.5), which together give

$$\rho\Big(\frac{\partial\boldsymbol{v}}{\partial t} + \boldsymbol{v}\cdot\nabla\boldsymbol{v}\Big) \overset{\psi^3}{=} \frac{\partial^2\boldsymbol{u}}{\partial t^2}\cdot\big(\boldsymbol{I} - \nabla\cdot\boldsymbol{u}\,\boldsymbol{I} + \nabla\boldsymbol{u}\big) + 2\frac{\partial\boldsymbol{u}}{\partial t}\cdot\frac{\partial\nabla\boldsymbol{u}}{\partial t}. \tag{5.7}$$

The combination of (5.1), (5.6) and (5.7) yields to a governing equation for the displacement field, which is the basis for the acoustoelasticity.

5.2.2 Wave motion under uniaxial static precompression

The total deformation, that is relevant for acoustoelasticity measurements, can be split into two contributions: finite uniform static deformation and infinitesimal dynamic deformation, whereby the displacement field can be written as

$$\boldsymbol{u} \;=\; \boldsymbol{u}^s + \boldsymbol{u}^d, \qquad \frac{\partial\boldsymbol{u}^s}{\partial t} \;\equiv\; 0, \tag{5.8}$$

where $\boldsymbol{u}^s$ denotes the static deformation and $\boldsymbol{u}^d$ stands for the dynamic part. Furthermore, the static deformation is considered to be uniaxial, so that

$$\nabla\boldsymbol{u}^s \;=\; \sum_{\mathrm{i}=1}^{3}\epsilon_{\mathrm{i}}\,\boldsymbol{e}_{\mathrm{i}}\otimes\boldsymbol{e}_{\mathrm{i}}, \tag{5.9}$$

where $\epsilon_{\mathrm{i}} = \text{const.}$ $(\mathrm{i} = 1, 2, 3)$ denote the principal strains and $\boldsymbol{e}_{\mathrm{i}}$ $(\mathrm{i} = 1, 2, 3)$ are the principal direction unit vectors (i.e. the basis of the Cartesian coordinate system). Here it is noted that since $G/K = O(10^{-6}) \ll 1$ for soft tissues, the volumetric strain (under uniaxial state of stress) is very small, compared to the deviatoric part, however, as will be shown shortly, it can not be neglected. For a consistent treatment of the problem, let

$$\bar{\varepsilon} = G/K \tag{5.10}$$

denote the small parameter, so that the volumetric strain $\epsilon_v = \sum_{\mathrm{i}=1}^{3} \epsilon_{\mathrm{i}} = O(\bar{\varepsilon}\epsilon)$, while $\epsilon_{\mathrm{i}} = O(\epsilon)$ ($\mathrm{i} = 1, 2, 3$), where ϵ is the magnitude of the axial static strain. Note that the static deformation is assumed moderately small, so that the equations of linear elasticity can be used to relate stress and strain, and infinitesimal stain tensor can be used. Also note that the temperature distribution is assumed to be uniform, and thermal losses (due to dynamic motion $\boldsymbol{u}^d$) are neglected. In this case, the entropy variations can be omitted, and all parameters in (5.6) are taken as constants (as opposed to functions of entropy). In addition to that, the third-order elastic constants vary a lot in magnitude for soft materials. It is shown experimentally in [35], that for tissue-mimicking phantoms

$$B/K \;=\; O(1), \qquad C/K \;=\; O(1), \qquad D/G \;=\; O(1), \tag{5.11}$$

where the last relation can be rewritten as $D/K = O(\bar{\varepsilon})$. So that the bulk modulus K, coefficients B and C have GPa-scale values, while the shear modulus G and coefficient D are $O(\text{kPa})$ for tissue-mimicking materials. Based on this study, it is further assumed that (5.11) holds for materials that are relevant for the current study. Finally, the magnitudes of the viscosities μ and μ_{B}, as well as $\bar{\mu}$ and $\bar{\mu}_{\mathrm{B}}$ are assumed to be commensurate in magnitude, which ensures that the terms proportional to $\bar{\mu}$ and $\bar{\mu}_{\mathrm{B}}$ can be neglected for small volumetric strains.

With the aid of (5.8)–(5.11) and hypothesis $\boldsymbol{u}^d \ll 1$ (so that one can linearize with respect to $\boldsymbol{u}^d$), the Cauchy stress tensor (5.6) can be rewritten as

$$\begin{aligned}
\boldsymbol{\sigma} \;=\; & \Big[K\nabla\cdot\boldsymbol{u}^d + (3K-C)\sum_{\mathrm{i}=1}^{3} \epsilon_{\mathrm{i}} \frac{\partial u_{\mathrm{i}}^d}{\partial x_{\mathrm{i}}}\Big]\boldsymbol{I} + \Big(2G - (C-2K)\epsilon_v\Big)\nabla^{\mathrm{S}}\boldsymbol{u}^d \\
& -\; (C-2K)\nabla\cdot\boldsymbol{u}^d \sum_{\mathrm{i}=1}^{3} \epsilon_{\mathrm{i}}\, \boldsymbol{e}_{\mathrm{i}}\otimes\boldsymbol{e}_{\mathrm{i}} + \tfrac{1}{2}(D+8G)\sum_{\mathrm{i}=1}^{3}\epsilon_{\mathrm{i}}\Big[\Big(\nabla u_i^d + \frac{\partial \boldsymbol{u}^d}{\partial x_{\mathrm{i}}}\Big)\otimes\boldsymbol{e}_{\mathrm{i}} + \boldsymbol{e}_{\mathrm{i}}\otimes\Big(\nabla u_i^d + \frac{\partial \boldsymbol{u}^d}{\partial x_{\mathrm{i}}}\Big)\Big] \\
& -\; G\sum_{\mathrm{i}=1}^{3}\epsilon_{\mathrm{i}}(\nabla u_i^d \otimes \boldsymbol{e}_{\mathrm{i}} + \boldsymbol{e}_{\mathrm{i}} \otimes \nabla u_i^d) + \big(\mu_{\mathrm{B}} - \tfrac{2}{3}\mu\big)\frac{\partial \nabla\cdot\boldsymbol{u}^d}{\partial t}\,\boldsymbol{I} + 2\mu\,\frac{\partial \nabla^{\mathrm{S}}\boldsymbol{u}^d}{\partial t} + \text{const.}
\end{aligned} \tag{5.12}$$

where the constant term represents the uniform static stress, "$\otimes$" denotes tensor product, and x_{i} ($\mathrm{i} = 1, 2, 3$) are the Cartesian coordinates. By taking the divergence of (5.12), and using (5.7), (5.8) and (5.11), the balance of linear momentum (5.1) can be finally rewritten as

$$\begin{aligned}
\frac{\partial^2 \boldsymbol{u}^d}{\partial t^2} &= K\nabla\nabla\cdot\boldsymbol{u}^d + \big(G - \tfrac{1}{2}(C-2K)\epsilon_v\big)\nabla^2\boldsymbol{u}^d + (3K-C)\sum_{\mathrm{i}=1}^{3}\epsilon_{\mathrm{i}}\frac{\partial\nabla u_{\mathrm{i}}^d}{\partial x_{\mathrm{i}}} \\
&- (C-2K)\sum_{\mathrm{i}=1}^{3}\epsilon_{\mathrm{i}}\frac{\partial\nabla\cdot\boldsymbol{u}^d}{\partial x_{\mathrm{i}}}\,\boldsymbol{e}_{\mathrm{i}} + \tfrac{1}{2}(D+8G)\sum_{\mathrm{i}=1}^{3}\epsilon_{\mathrm{i}}\frac{\partial^2\boldsymbol{u}^d}{\partial {x_{\mathrm{i}}}^2} + \tfrac{1}{2}(D+4G)\sum_{\mathrm{i}=1}^{3}\epsilon_{\mathrm{i}}\nabla^2 u_{\mathrm{i}}^d\,\boldsymbol{e}_{\mathrm{i}} \\
&+ \big(\mu_{\mathrm{B}}+\tfrac{1}{3}\mu\big)\frac{\partial\nabla\nabla\cdot\boldsymbol{u}^d}{\partial t} + \mu\,\frac{\partial\nabla^2\boldsymbol{u}^d}{\partial t} - \big(\mu_{\mathrm{B}}+\tfrac{1}{3}\mu\big)\sum_{\mathrm{i}=1}^{3}\epsilon_{\mathrm{i}}\frac{\partial^2\nabla\cdot\boldsymbol{u}^d}{\partial x_{\mathrm{i}}\partial t}\,\boldsymbol{e}_{\mathrm{i}} - \mu\sum_{\mathrm{i}=1}^{3}\epsilon_{\mathrm{i}}\frac{\partial\nabla^2 u_{\mathrm{i}}^d}{\partial t}\,\boldsymbol{e}_{\mathrm{i}} \\
&+ \sum_{\mathrm{i}=1}^{3} f_{\mathrm{i}}(1-\epsilon_{\mathrm{i}})\,\boldsymbol{e}_{\mathrm{i}}. \qquad (5.13)
\end{aligned}$$

Note that the approximation accuracy is omitted in both (5.12) and (5.13) for brevity, and only the leading terms (based on (5.11)) are taken into account. Equation (5.13) governs the propagation of the infinitesimally small distortion, described by the displacement vector $\boldsymbol{u}^d$, in the uniaxially stressed nonlinear visco-elastic material. An interesting outcome of (5.13) lies in the fact that, in addition to the elastic contribution, both the viscous terms and the body force are affected by the prestressing. This observation might be relevant for modeling of the ARF-induced motion in the prestressed material, while it is not included in the classical description of the acoustoelasticity (see e.g. [7]).

5.2.3 Plane shear wave propagation under uniaxial loading

To analyse the propagation of the planar shear waves in the prestressed nonlinear elastic material, let's take the displacement vector in the form $\boldsymbol{u}^d = (0, 0, u_z^d(x))$, where $\boldsymbol{x} = (x_1, x_2, x_3) = (x, y, z)$ denotes the coordinate vector written in two alternative forms. With such premise and an assumption of no body forces, equation (5.13) can be reduced to

$$\frac{\partial^2 u_z^d}{\partial t^2} = \Big(G(1+4\epsilon_1+2\epsilon_3) - \tfrac{1}{2}(C-2K)\epsilon_v + \tfrac{1}{2}D(\epsilon_1+\epsilon_3) + \mu(1-\epsilon_3)\frac{\partial}{\partial t}\Big)\frac{\partial^2 u_z^d}{\partial x^2}. \qquad (5.14)$$

As can be seen from (5.14), the shear wave speed depends on the static strains and two third-order moduli. Note that since $C = O(\bar{\varepsilon}^{-1}G)$, according to (5.11) and (5.10), and

$\epsilon_v = O(\bar{\varepsilon}\epsilon)$, their product is on the order of $O(G\epsilon)$, which is comparable to other terms in (5.14).

To specify the problem further, consider two independent uniaxial loadings: i) stress is applied along x axis, i.e. parallel to the direction of shear wave propagation, and ii) stress is applied along y axis, i.e. perpendicular to the direction of shear wave propagation. By denoting the magnitude of the uniaxial stress by σ (positive for compression), the static strains for the parallel configuration are given by

$$\epsilon_v \;=\; -\frac{\sigma}{3K}, \qquad \epsilon_1 \;=\; -\frac{\sigma}{E} \;\approx\; -\frac{\sigma}{3G}, \qquad \epsilon_2 \;=\; \epsilon_3 \;=\; \nu\frac{\sigma}{E} \;\approx\; \frac{\sigma}{6G}, \tag{5.15}$$

where E is the Young's modulus, ν is the Poisson's ratio, and (5.10) is used to obtain approximate expressions. By substituting (5.15) into (5.14), the "parallel" shear modulus can be computed as

$$G_{||} \;=\; G + \frac{\sigma}{6}\Big[\frac{C}{K} - \frac{D}{2G} - 8\Big]. \tag{5.16}$$

In situations when the stress is applied along y direction, i.e. perpendicular to the direction of shear wave propagation, the static strains are given by

$$\epsilon_v \;=\; -\frac{\sigma}{3K}, \qquad \epsilon_2 \;=\; -\frac{\sigma}{E} \;\approx\; -\frac{\sigma}{3G}, \qquad \epsilon_1 \;=\; \epsilon_3 \;=\; \nu\frac{\sigma}{E} \;\approx\; \frac{\sigma}{6G}, \tag{5.17}$$

while the "perpendicular" shear modulus is

$$G_{\perp} \;=\; G + \frac{\sigma}{6}\Big[\frac{C}{K} + \frac{D}{G} + 4\Big]. \tag{5.18}$$

With the reference to (5.11), it is noted that ratios C/K and D/G that enter (5.16) and (5.18) are $O(1)$, while $G/K \ll 1$. Also note that the formulas (5.16) and (5.18) can be inverted as

$$\begin{aligned} \frac{C}{K} \;&=\; 2\Big(2\frac{\partial G_{||}}{\partial\sigma} + \frac{\partial G_{\perp}}{\partial\sigma} + 2\Big), \\ \frac{D}{G} \;&=\; 4\Big(-\frac{\partial G_{||}}{\partial\sigma} + \frac{\partial G_{\perp}}{\partial\sigma} - 2\Big), \end{aligned} \tag{5.19}$$

which allow to compute two nonlinearity coefficients C and D knowing the values of bulk and shear modulus, as well as the slopes $\partial G_{||}/\partial\sigma$ and $\partial G_{\perp}/\partial\sigma$. Relations (5.19) are used in the next section to determine the ratios of C/K and D/G experimentally for tissue-mimicking phantoms.

5.2.4 Experimental results

To measure the third-order elastic moduli in a physical setting, experiments on tissue-mimicking phantoms were performed in the Department of Biomedical Engineering, Mayo Clinic College of Medicine, Rochester, Minnesota. The experimental setup (developed at the University of Minnesota) is shown in Fig. 5.1. The left image illustrates the testing procedure: the phantom is compressed uniaxially between two parallel plates; the strain is controlled by the adjustment nut and measured using caliper, and the shear wave is generated by the pulsed acoustic radiation force (ARF). In the approach, two testing configurations were used – “parallel” and “perpendicular”, which relate the direction of propagation of shear waves to the direction of applied stress. A Verasonics system (Verasonics V-1, Verasonics, Inc., Redmond, WA) equipped with a linear array transducer (L7-4, Philips Healthcare, Andover, MA) was used to generate shear waves and measure the resulting motion using plane wave imaging techniques with angular compounding [90]. Both focused and unfocused beam configurations were used. The focused push beam was generated using 96 elements (element width 0.308 mm), while the focal distance varied from 15 to 25 mm. To produce the unfocused push beam, 16 central elements, exited coherently, were used. The unfocused beam has the advantage of exciting a shear wave at shallow depths and creating a planar shear wave over a large range of depths [91]. The ultrasound toneburst used for shear wave generation had a duration of either 391 or 585 μs with a frequency of 4.09 MHz. The shear wave detection and monitoring was performed using angular compounding with 3 angles [90]. The frame rate for the acquisition was 4.167 kHz. Shear wave motion was estimated with an autocorrelation method [92]. The shear wave speeds were estimated using a method based on the Radon transform similar to the algorithm presented in [93]. A median and mean over a range of depths was calculated at each compression step. Having the shear wave velocity measured, the value of the shear modulus is then computed taking the mass density of phantom as for water. Experiments were performed in Mayo Clinic, Rochester, MN in collaboration with M. Urban, R. Kinnick and M. Fatemi.

Two sets of experiments were performed. A total of five tissue-mimicking phantoms were tested first, containing: i) paraffin, ii) polyvinyl chloride (PVC), iii) polyvinyl alcohol (PVA), iv) agarose, and v) gelatin as the “matrix” material. All phantoms were mixed with the same concentration of cotton fibers and spherical scatterers, where

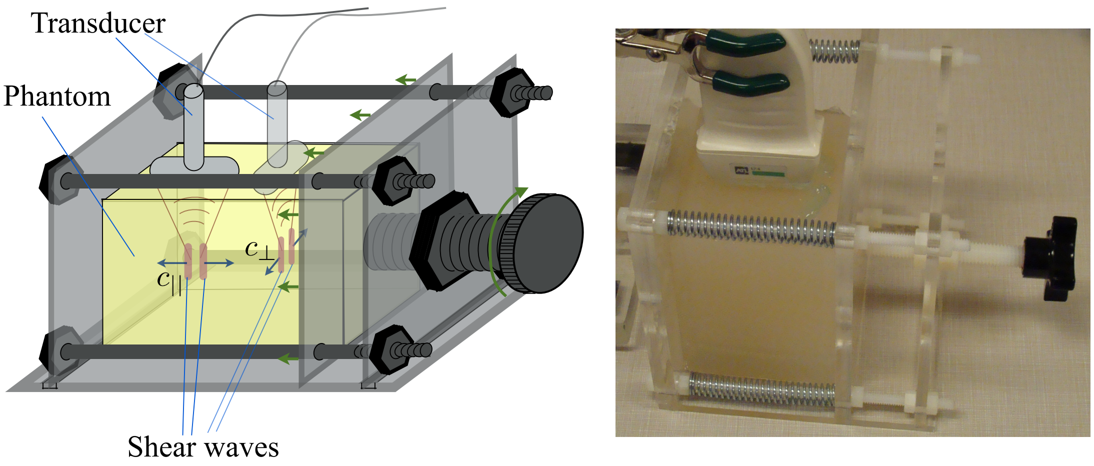

Figure 5.1: Schematics (left) and picture (right) of the experimental setup for measuring the elastic nonlinearities C and D in tissue-mimicking phantoms using acoustoelasticity.

the latter are added to aid the shear wave detection using ultrasound. The first set of experiments sought to investigate the nonlinear elastic properties of different tissue-mimicking materials. In the second set of experiments, five paraffin-based phantoms containing: i) no fibers, ii) 2% cotton fibers, iii) 4% cotton fibers, iv) 2% glass fibers, and v) 4% glass fibers, were tested. The goal of the second batch of tests was to study the effect of fibers on the nonlinear elastic properties of tissue-like materials. To visualize the microstructure, produced by fiber additives, Fig. 5.2 shows the SEM (Scanning Electron Microscope) images of all 5 paraffin-based phantoms that were tested in the second set of experiments. The imaging was done primarily by Yuping Li (Postdoctoral Associate, School of Dentistry, University of Minnesota).

Figs. 5.3 and 5.4 illustrate respectively the results obtained from the first and the second batch of experiments, where both parallel and perpendicular configurations are examined. Here σ denotes the magnitude of the applied uniaxial stress, which is computed as

$$\sigma \;=\; E\,\frac{\Delta L}{L} \;\approx\; 3G\,\frac{\Delta L}{L}, \tag{5.20}$$

where L is the initial distance between two parallel plates (see Fig. 5.1), and ΔL denotes the change in it due to applied deformation (positive for contraction). Quantity σ_{o} denotes the initial stress, which was applied in order to make two compression plates

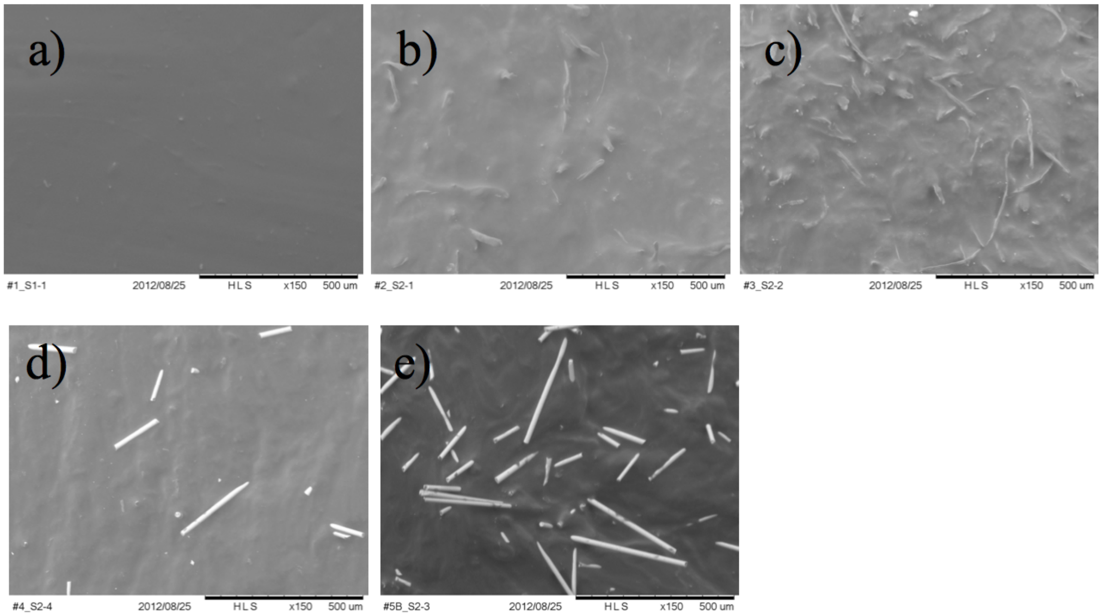

Figure 5.2: SEM images of samples of tested paraffin-based phantoms with no fibers (a), with 2% cotton fibers (b), with 4% cotton fibers (c), with 2% glass fibers (d) and with 4% glass fibers (e).

parallel at the initial configuration. The markers correspond to the experimental measurements, while lines show the linear fit. The numbers near triangles indicate the magnitude of the slopes (of the linear fit) and are used to compute the ratios C/K and D/G via (5.19). The results for all phantoms tested are summarized in Tables 5.1 and 5.2.

The results in Table 5.1 demonstrate that four out of five phantoms have somewhat similar values of the constitutive parameters, while the agarose-based phantom is very different. It is much stiffer, has much higher C/K ratio, and is the only tested material with positive coefficient D. Note, however, that there are no thermodynamic restrictions on the sign of the third-order moduli [7], so that both positive and negative values of D are acceptable. The results in Table 5.2 show that all phantoms, except for that with 4% cotton fibers, have similar values of both linear and nonlinear moduli. The one with 4% cotton fibers is notably stiffer and has higher C/K ratio. As a result, small concentrations of fibers (2%) do not make significant contribution to the nonlinear elastic behavior of the phantoms. Higher concentrations show a notable influence

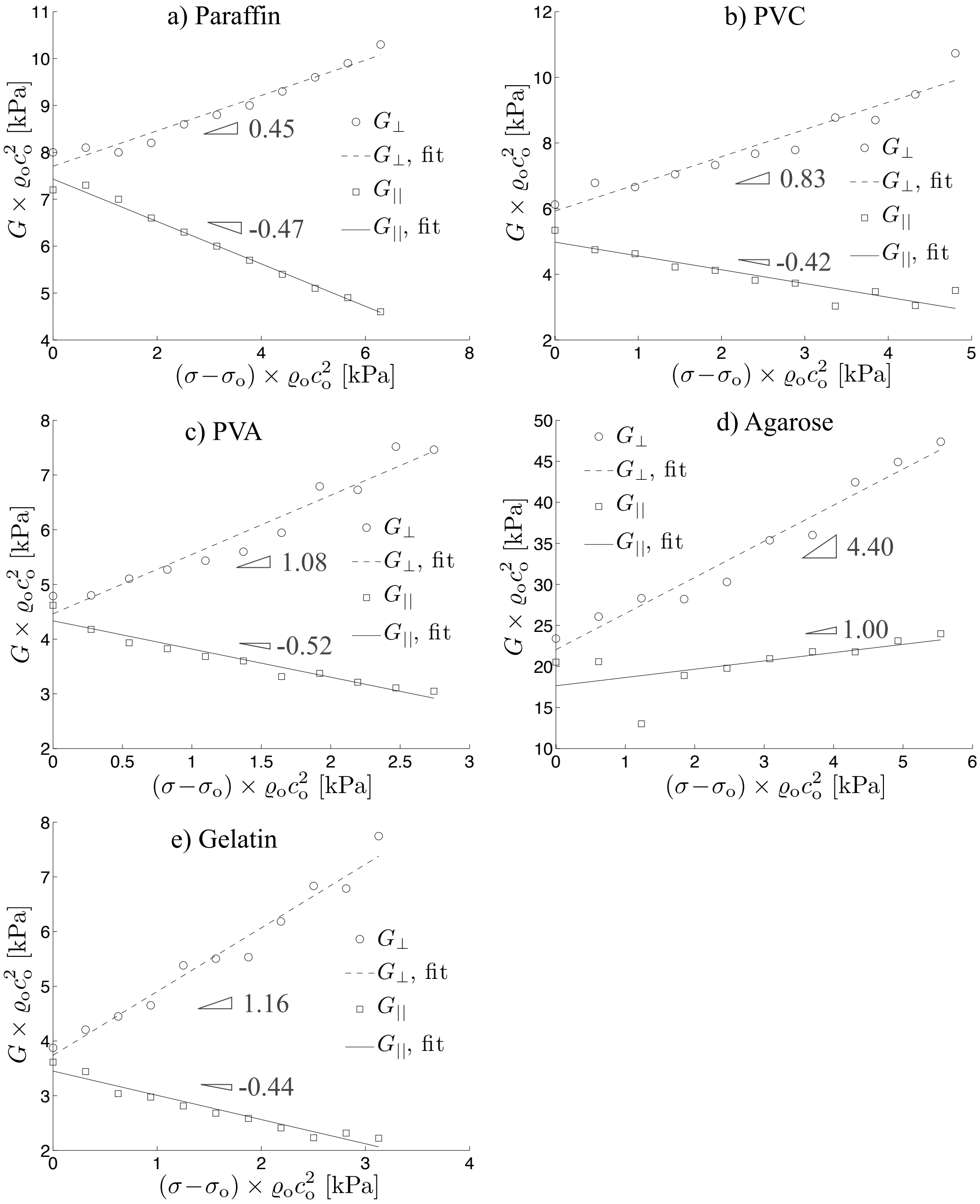

Figure 5.3: Variations of the shear modulus in the perpendicular and parallel configurations (markers) and linear fit (dashed and solid lines) for different phantoms: a) paraffin, b) PVC, c) PVA, d) agarose, and e) gelatin. The numbers indicate the magnitude of corresponding slopes.

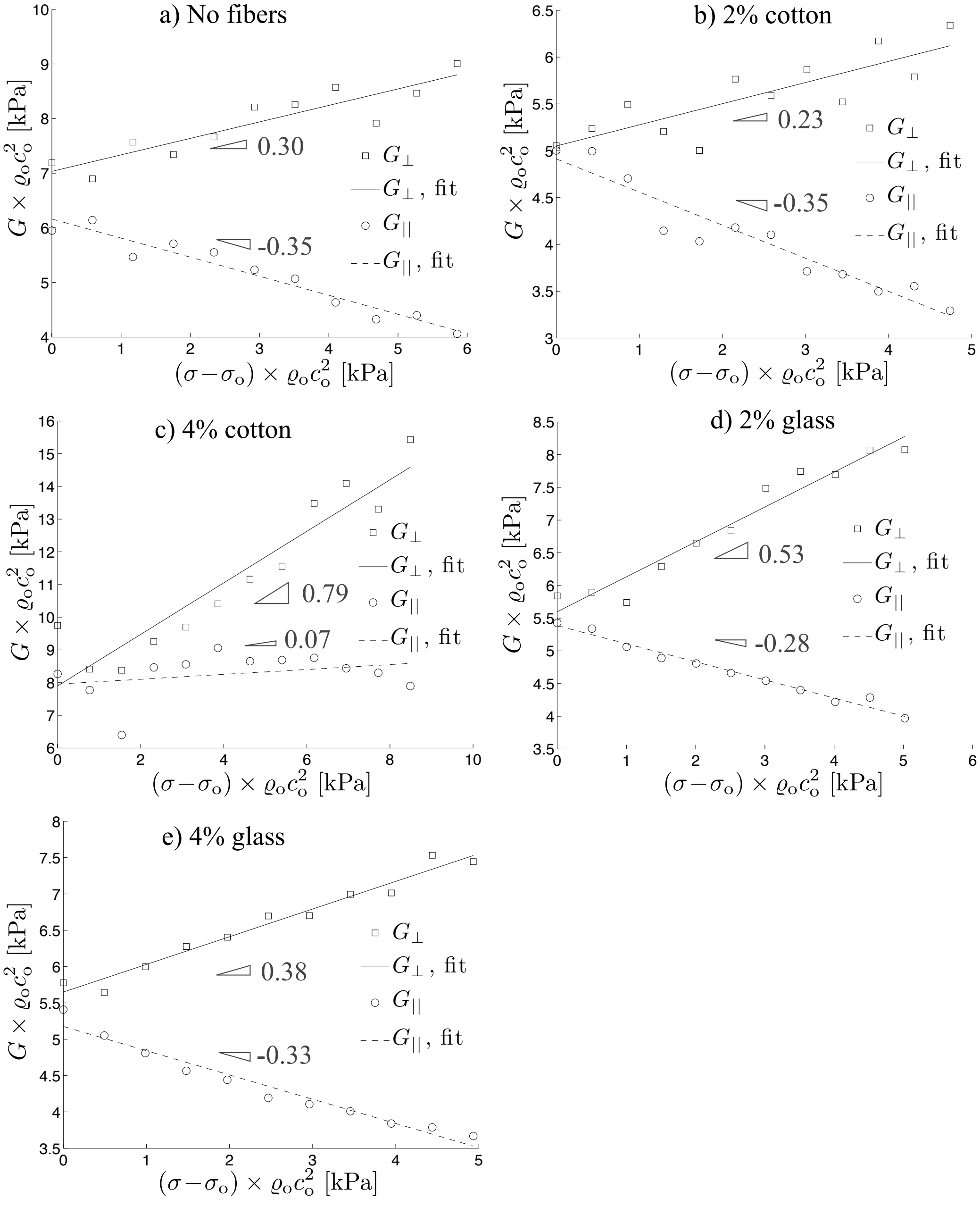

Figure 5.4: Variations of the shear modulus in the perpendicular and parallel configurations (markers) and linear fit (dashed and solid lines) for paraffin-based phantoms with different fiber content: a) no fibers, b) 2% cotton fibers, c) 4% cotton fibers, d) 2% glass fibers, and e) 4% glass fibers. The numbers indicate the magnitude of corresponding slopes.

Phantom	Paraffin	PVC	PVA	Agarose	Gelatin
$G \times \varrho_o c_o^2$ [kPa]	7.3	5.5	4.4	20	3.6
C/K	3.0	4.0	4.1	16.8	4.6
D/G	-4.3	-3.0	-1.6	5.6	-1.6

Table 5.1: Values of the shear modulus G, ratio C/K and ratio D/G for paraffin, PVC, PVA, agarose and gelatin phantoms measured using the acoustoelasticity technique.

Phantom	No fibers	2% cotton	4% cotton	2% glass	4% glass
$G \times \varrho_o c_o^2$ [kPa]	6.6	5.0	7.9	5.5	5.4
C/K	3.2	3.0	5.9	4.0	3.4
D/G	-5.4	-5.7	-5.1	-4.8	-5.1

Table 5.2: Values of the shear modulus G, ratio C/K and ratio D/G for paraffin-based phantoms with different fiber content measured using the acoustoelasticity technique.

of cotton fibers, while almost no effect is observed in terms of the glass fibers. One possible explanation of the results that correspond to the material with glass fibers is the inhomogeneity of the phantom due to uneven distribution of glass fibers caused by the gravity force during preparation. The data for the C/K ratio is the most importnat for this study since the magnitude of the directional part of the ARF linearly depends on it. The observed results for C/K provide the basis for preliminary experimental verification of the ARF formula (3.196), in terms of its dependence on the C coefficient.

5.3 Estimation of the nonlinearity parameter C from the ARF-induced shear wave amplitude

The goal of this section is to provide an algorithm for estimating the coefficient C of nonlinear tissue elasticity from the amplitude of the ARF-generated shear waves. Since the radiation force was used in the experimental setting for acoustoelasticity measurements, the observed deformation pattern for the unstressed configuration is used for the analysis in this section. At the same time, to simulate the ARF-induced shear waves, one has to solve two separate problems, namely: i) computation of the ultrasound pressure field (and then the ARF) for given transducer geometry, and ii) solution of the elasticity equations with the ARF as the body force. By making reference to (3.196) and noting that the directional part of the ARF is solely responsible for generating the shear waves, the C coefficient can be determined by comparing the amplitudes of the model prediction and observed shear wave motion. The details of this procedure are described next.

5.3.1 Calculation of the ultrasound pressure field

In order to predict the shear wave motion caused by the acoustic radiation force, one first needs to compute the body force distribution for a particular testing configuration. This entails the computation of the ultrasound pressure filed, produced by the ultrasound transducer that was used in the acoustoelasticity experiments (see Fig. 5.1). By parametrizing the active surface of the linear array with (x, y) orthogonal coordinate system, the boundary condition for the pressure field (normalized according to the scaling in Table 2.1) can be written as

$$p|_{z=0} \;=\; p_{\mathrm{o}} H(a_1 - |x|) H(a_2 - |y|) \exp\Big[-\mathrm{i}\Big(t + \frac{x^2}{2d_1} + \frac{y^2}{2d_2}\Big)\Big], \tag{5.21}$$

where p_{o} is pressure amplitude at the boundary (assumed to be uniform), a_1 and a_2 denote respectively the apertures in the x and y directions, d_1 and d_2 signify the corresponding focusing depths, and H is the Heaviside step function. Note that the z coordinate is perpendicular the transducer's face and the waves propagate in the positive z direction. Also note, that 96 elements were used to produce the phase delay along the boundary in the x direction (which produces the focusing in the (x, z) plane), and the discrete nature of the boundary condition is smeared due to the large number of elements. The focusing in the (y, z) plane is achieved by using the acoustic lens, whose action can be represented by a fixed value of d_2 in (5.21).

Due to the fact that the magnitude of the pressure signal p_{o} on the boundary of the ultrasound transducer has not been measured in the experimental study, it is taken as an unknown parameter. In this situation, the lack of the knowledge of p_{o} makes the nonlinear treatment of the ultrasound wave propagation unsuitable. As a result, the (linear) Helmholtz equation (with dissipation) is used for calculations of the ultrasound pressure field in this section. By way of the two-dimensional Fourier transform, the solution of the Helmholtz equation can be written as

$$p(x,y,z) \;=\; \mathcal{F}^{-1}_{k_x k_y}\Big[\exp\Big(\mathrm{i}\,z\,\sqrt{(1+\mathrm{i}\alpha)^2-k_x^2-k_y^2}\Big)\mathcal{F}_{xy}[p(x,y,0)]\Big], \tag{5.22}$$

where $\mathcal{F}_{xy}$ denotes the forward Fourier transform with respect to x and y, $\mathcal{F}^{-1}_{k_x k_y}$ is the inverse Fourier transform with respect to k_x and k_y, α is the ultrasound attenuation coefficient, while k_x and k_y signify the spatial frequencies respectively in the x and y directions. For the purpose of computing the ultrasound pressure filed, equation (5.22) is solved numerically over a rectangular spatial grid using fast Fourier transform (FFT) algorithm. Such method of solving the Helmholtz equation is typically referred as an angular spectrum method [94].

The parameters of the ultrasound source, that were used for simulating the results on tissue-mimicking phantoms (see Section 5.2.4), are taken as $a_1 \times c_{\mathrm{o}}/\Omega = 1.4784$ cm, $a_2 \times c_{\mathrm{o}}/\Omega = 0.35$ cm, $d_1 \times c_{\mathrm{o}}/\Omega = 2$ cm, $d_2 \times c_{\mathrm{o}}/\Omega = 2.5$ cm, and $\Omega = 2\pi \times 4.09 \times 10^6$ rad/s, while the medium properties are chosen as $c_{\mathrm{o}} = 1540$ m/s, $\varrho_{\mathrm{o}} = 1000$ kg/m^3. The attenuation coefficient varied notably among the phantoms, and is assigned individually to each tested material. As an illustration, Fig. 5.5 shows the normalized intensity field, computed as $\frac{1}{2}|p|^2$, for attenuation coefficient $\alpha \times c_{\mathrm{o}}^{-1} = 0.5$ dB/(cm·MHz) in the (x,z) plane for $y=0$ (left) and in the (y,z) plane for $x=0$ (right). As can be seen from the display, the intensity field (and thus the ARF) clearly obeys three-dimensional behavior, which implies that the three-dimensional elasticity equations have to be solved (with the ARF body force) in order to model the deformation (i.e. the shear waves) caused by the ARF.

5.3.2 Numerical solution of incompressible elasticity equations using triple Fourier transform in space

With the ARF body force distribution at hand, the remaining question is how to solve the 3D elasticity equations in an efficient way, which would allow for modeling of the ARF-induced deformation. As a starting point, one may set $\epsilon_{\mathrm{i}} = 0$ ($\mathrm{i} = 1,2,3$) in (5.13), i.e. represent the unstressed configuration, which leads to

$$\frac{\partial^2 \boldsymbol{u}^d}{\partial t^2} \;=\; K\nabla\nabla\cdot\boldsymbol{u}^d + G\nabla^2\boldsymbol{u}^d + \big(\mu_{\mathrm{B}}+\tfrac{1}{3}\mu\big)\frac{\partial\nabla\nabla\cdot\boldsymbol{u}^d}{\partial t} + \mu\,\frac{\partial\nabla^2\boldsymbol{u}^d}{\partial t} + \boldsymbol{f}, \tag{5.23}$$

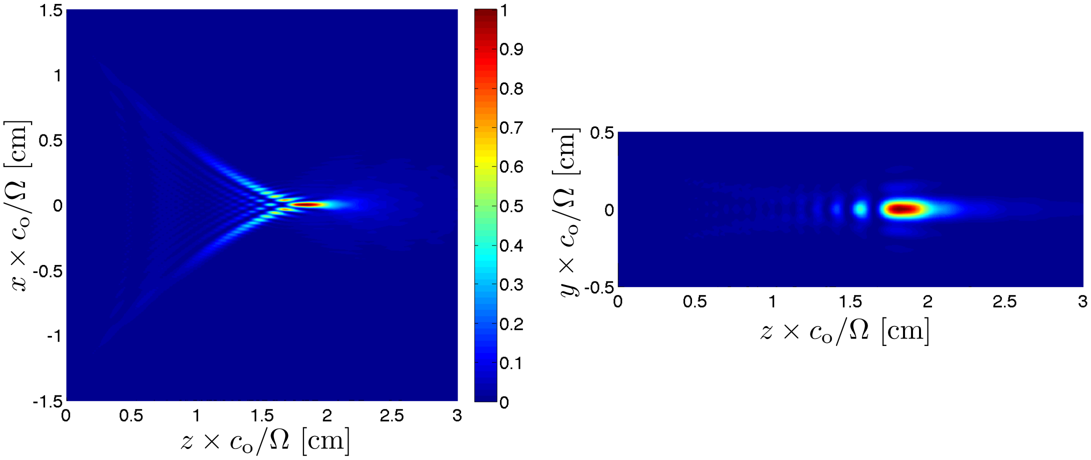

Figure 5.5: The distribution of the intensity field calculated using angular spectrum approach, normalized by its maximum value, shown in the (x, z) plane for $y = 0$ (left) and in the (y, z) plane for $x = 0$ (right).

where the body force $\boldsymbol{f}$ is the ARF, given by (3.196). By utilizing the notation ∇^{-2} for the inverse Laplace operator, equation (5.23) can be rewritten as

$$\begin{aligned}\frac{\partial^2 \boldsymbol{u}^d}{\partial t^2} &= -\nabla\check{p} + \check{G}\nabla^2\boldsymbol{u}^d + \boldsymbol{f} - \nabla^{-2}\nabla\nabla\cdot\boldsymbol{f}, \qquad \check{G} = G + \mu\frac{\partial}{\partial t}, \\ \check{p} &= -K\nabla\cdot\boldsymbol{u}^d - \left(\mu_{\mathrm{B}} + \tfrac{1}{3}\mu\right)\frac{\partial\nabla\cdot\boldsymbol{u}^d}{\partial t} - \nabla^{-2}\nabla\cdot\boldsymbol{f}.\end{aligned} \tag{5.24}$$

Motivated by the fact that $G/K = O(10^{-6})$ for materials in consideration, it is next assumed that the motion is quasi-static with respect to the compressional waves, i.e. the propagation of pressure waves is neglected. Note that this assumption poses a serious limitation for the modulation envelope, in particular, the compressional wavelength on the dominant modulation frequency should be much larger than the characteristic dimension of the source, such as the focal depth. In other words, the modulation frequencies should be such that

$$\omega_{\mathrm{m}} \ll d_1^{-1}. \tag{5.25}$$

The validity of this assumption for the particular problem at hand will be discussed later in Section 5.3.3. By expressing the quasi-static compressional behavior as

$$\frac{\partial\nabla\cdot\boldsymbol{u}^d}{\partial t} = 0, \tag{5.26}$$

and noting that $K \approx 1$ according to the scaling scheme in Table 2.1 and (5.10), equations (5.24) can be reduced to

$$\frac{\partial^2 \boldsymbol{u}^d}{\partial t^2} \;=\; \check{G}\nabla^2 \boldsymbol{u}^d + \Big(\boldsymbol{f} - \nabla^{-2}\nabla\nabla\cdot\boldsymbol{f}\Big) + \check{G}\nabla^{-2}\nabla\nabla\cdot\boldsymbol{f}, \tag{5.27}$$

where the part of the forcing term in parentheses represents divergence-free part of the body force, while the last term adds the contribution of the potential part of $\boldsymbol{f}$. Despite the second forcing term seems to be negligible compared to the first one (since it is proportional to $\check{G} \ll 1$), it can not be disregarded at this point since it represents qualitatively different type of source. On considering only the axial (i.e. z) component of the displacement vector, and applying 3D spatial Fourier transform to (5.28), one finds that

$$\frac{\partial^2 \mathcal{F}_{xyz}[u_z^d]}{\partial t^2} + \check{G}k^2\Big(\mathcal{F}_{xyz}[u_z^d] - \frac{k_z}{k^4}\boldsymbol{k}\cdot\mathcal{F}_{xyz}[\boldsymbol{f}]\Big) \;=\; \frac{k_x^2+k_y^2}{k^2}\,\mathcal{F}_{xyz}[f_{\mathrm{dir}}], \tag{5.28}$$

where $\boldsymbol{k} = (k_x, k_y, k_z)$ is the spatial frequency vector, $k^2 = \boldsymbol{k}\cdot\boldsymbol{k}$ denotes its squared amplitude, and $\mathcal{F}_{xyz}$ stands for the three-dimensional Fourier transform operator. Here, with the reference to (3.196), the total ARF vector and its directional part are given respectively by

$$\begin{aligned} f_{\mathrm{dir}} \;&=\; (C-1)\Big(2\alpha I + \frac{\partial I}{\partial t}\Big), \\ \boldsymbol{f} \;&=\; \nabla\Big((C-1-\beta)I - \frac{\beta_{\mathrm{T}}}{\mathrm{c_p}}\int_0^t 2\alpha I\,\mathrm{d}t'\Big) \;+\; (C-1)\Big(2\alpha I + \frac{\partial I}{\partial t}\Big)\,\boldsymbol{e}_z. \end{aligned} \tag{5.29}$$

According to (4.23), the intensity of the modulated ultrasound, computed using the linear model, can be written as

$$I \;=\; \tfrac{1}{2}|p|^2\,\mathcal{M}^2(t-z), \tag{5.30}$$

where p the ultrasound pressure field, which is computed using angular spectrum approach (see Section 5.3.1), and $\mathcal{M}$ is the modulation envelope. Noting that the derivation of (5.28) required an assumption on the smallness of the dominant modulation frequency (see (5.25)), one may utilize similar argument to moderate the computational complexity by using the quasi-static approximation for the intensity, i.e.

$$I \;\approx\; \tfrac{1}{2}|p|^2\,\mathcal{M}^2(t) \;=\; I_{\mathrm{nm}}\,\mathcal{M}^2(t), \tag{5.31}$$

which is valid as soon as (5.25) holds. By substituting (5.31) into (5.29), combining the result with (5.28), and using (5.26), one may express the axial component of the displacement field as

$$\begin{aligned} u_z^d \;=\; & \mathcal{F}^{-1}_{k_xk_yk_z}\Bigg[\bigg\{\frac{\mathrm{i}k_z}{k^2}\Big((C-1-\beta)\,\mathcal{M}^2(t) - 2\alpha\frac{\beta_\mathrm{T}}{\mathrm{c_p}}\int_0^t \mathcal{M}^2(t')\,\mathrm{d}t'\Big) \\ &+ \frac{k_z^2}{k^4}(C-1)\big(2\alpha\,\mathcal{M}^2(t) + \big(\mathcal{M}^2\big)'(t)\big) \\ &+ \frac{k_x^2+k_y^2}{k^2}(C-1)\int_{-\infty}^t \mathcal{G}(t-t')\big(2\alpha\,\mathcal{M}^2(t') + \big(\mathcal{M}^2\big)'(t')\big)\,\mathrm{d}t'\bigg\}\,\mathcal{F}_{xyz}[I_\mathrm{nm}]\Bigg], \end{aligned} \tag{5.32}$$

where $\mathcal{G}$ is the Green's function for a linear oscillator, and is given by

$$\mathcal{G}(t) \;=\; H(t)e^{-\frac{1}{2}k^2\mu\,t}\frac{\sin\!\big(\breve{\kappa}\,t\big)}{\breve{\kappa}}, \qquad \breve{\kappa} = \sqrt{Gk^2 - \tfrac{1}{4}k^4\mu^2}, \tag{5.33}$$

Note that the Green's function (5.33) is also applicable for the overdamped case when $k^2 > 4G/\mu^2$. If one is interested in the particle velocity field instead of the displacement field, then (5.32) can be differentiated with respect to time to obtain

$$\begin{aligned} v_z^d \;=\; & \mathcal{F}^{-1}_{k_xk_yk_z}\Bigg[\bigg\{\frac{\mathrm{i}k_z}{k^2}\Big((C-1-\beta)\,\big(\mathcal{M}^2\big)'(t) - 2\alpha\frac{\beta_\mathrm{T}}{\mathrm{c_p}}\mathcal{M}^2(t)\Big) \\ &+ \frac{k_z^2}{k^4}(C-1)\big(2\alpha\,\big(\mathcal{M}^2\big)'(t) + \big(\mathcal{M}^2\big)''(t)\big) \\ &+ \frac{k_x^2+k_y^2}{k^2}(C-1)\int_{-\infty}^t \mathcal{G}(t-t')\big(2\alpha\,\big(\mathcal{M}^2\big)'(t') + \big(\mathcal{M}^2\big)''(t')\big)\,\mathrm{d}t'\bigg\}\,\mathcal{F}_{xyz}[I_\mathrm{nm}]\Bigg], \end{aligned} \tag{5.34}$$

Since the ARF-induced particle velocity field is measured in the experimental setting, (5.34) is going to be used as the basis for the computation of the axial component of the particle velocity field numerically at a given time instant. Terms in the first two lines represent the motion due to the volumetric distortion caused by the ARF and thermal expansion, while the last term with the convolution integral stays for the shear deformation produced by the directional part of the ARF (see (5.29)). Note that the motion due to the volumetric distortion is important only during the application of the ultrasound, and does not contribute to the change in distortion after the end of the ARF push. Also, there are two issues that have to be resolved in order to obtain the appropriate shear wave motion. The first issue is the computation of the convolution integral in (5.34), which, in general, can be evaluated numerically, but would add a significant amount of computational time. Alternatively, for two most relevant cases of time-harmonic and pulsed modulation, the convolution can be computed analytically. Next paragraph establishes the result for the case of pulsed modulation, which is relevant for this study since such modulation was used in the experimental setting. The second issue is the boundary conditions. Formally, Fourier transform approach, utilized in this section, gives the solution in the infinite domain without boundaries, while the problem can be better described by the infinite half-space geometry. In this case, the method of images can be applied for resolving this issue, which is examined later in this section.

Special case of the pulsed modulation envelope. In order to generate the shear waves for the acoustoelasticity experiment (see Fig. 5.1), pulsed modulation was used. For such situation, the modulation envelope can be written as

$$\mathcal{M}(t) \;=\; H(t)H(t_\mathrm{o}-t), \tag{5.35}$$

where t_o denotes the duration of the pulse. Note that (5.35) is an *idealized* modulation envelope that suits the computations, while the smooth analog of (5.35) is used in the actual setting. By substituting (5.35) into the convolution integral in (5.34), one finds that

$$\begin{aligned} \int_{-\infty}^{t} \mathcal{G}(t-t')\big(2\alpha\,(\mathcal{M}^2)'(t') + (\mathcal{M}^2)''(t')\big)\,\mathrm{d}t' \;&=\; \mathcal{D}(t) - \mathcal{D}(t-t_\mathrm{o}), \\ \mathcal{D}(t) \;&=\; H(t)e^{-\frac{1}{2}k^2\mu\,t}\Big[2\alpha\Big(1-\tfrac{1}{2}\mu k^2\breve{\kappa}\Big)\frac{\sin\!\big(\breve{\kappa}\,t\big)}{\breve{\kappa}} + \cos\!\big(\breve{\kappa}\,t\big)\Big], \end{aligned} \tag{5.36}$$

where $\breve{\kappa}$ is given in (5.33). With the aid of (5.36), the computation of the shear wave motion via (5.34) is reduced to three steps: i) the evaluation the FFT of the intensity, ii) multiplication by a constant factor, and iii) the evaluation of the inverse FFT of the result. Note that since the FFT algorithm is used, the three-dimensional transient wave propagation problem at hand can be solved reasonably fast on the regular computer.

Boundary condition. As was mentioned previously in this section, (5.34) gives the solution in the infinite space and does not account for the boundaries. Since the shear waves dissipate quickly and typically can not reach the side and bottom boundaries, the experimental configuration can be well-described by the half-space domain (see Fig. 5.1).

In this setting, one may impose the boundary condition for the solution $\breve{v}_z^d$ on the top surface of the domain (given by relation $z = 0$) as

$$\breve{v}_z^d|_{z=0} \; = \; 0. \tag{5.37}$$

Boundary condition (5.37) implies that the transducer can be associated with a rigid body, and is much less compliant than the material. To impose (5.37), one can apply the method of images, so that the solution which satisfies (5.37) can be computed as

$$\breve{v}_z^d(x, y, z) \; = \; v_z^d(x, y, z) \; - \; v_z^d(x, y, -z), \tag{5.38}$$

where v_z^d is calculated using (5.34) and $\breve{v}_z^d$ satisfies (5.37). As the result of the method of images, the lateral components of the particle velocity vector satisfy shear traction-free condition

$$\left. \frac{\partial \breve{v}_\mathrm{i}^d}{\partial z} \right|_{z=0} \; = \; 0, \qquad \mathrm{i} = 1, 2. \tag{5.39}$$

Conditions (5.37) and (5.39) are associated with using the method of images, and represent the actual boundary conditions only up to some extent. In particular, the ultrasound probe has a contact only with a part of the top surface, while (5.37) is assumed to be valid over the whole area. Friction-free contact, imposed by (5.39) is also an approximation. Such simplistic boundary condition, probably, is the largest source of the systematic error, which can not be eliminated. However, there are reasons why such degenerate boundary condition may provide good results. One argument toward applicability of (5.37) lies in the fact that most of the ARF-induced deformation occurs right under the transducer, where the effect of the top boundary is the most pronounced, and accounted by (5.37). At the same time, the lateral components of the particle velocity vector are expected to be small since the directional part of the ARF, which produces the shear deformation, acts in the z direction and generates predominantly z component of the motion. In this case, the boundary conditions for the lateral components of the particle velocity vector are irrelevant. Finally, most deformation occurs in the focal zone, i.e. at some distance away from the top surface, in which case the distortion due to boundary may not always be significant in the region of interest, which further reduces the error due to the boundary conditions.

As an illustration, Figs. 5.6 and 5.7 show the normalized axial component of the (shear wave) particle velocity field (computed using (5.34) for a given transducer's geometry and example medium parameters) before (left) and after (right) the application of the boundary condition. As can be seen from the display, the boundary condition (5.37) notably affects the solution near the surface ($z=0$), while is not crucial for the focal region ($z \times c_{\mathrm{o}}/\Omega = 2$ cm). Aslo note that the finite size of the computational domain introduces an additional error, which is accumulated mostly near its boundaries.

5.3.3 Comparison with the experimental observations

Having developed the numerical model for the ARF-induced axial component of the particle velocity field, described in Section 5.3.2, the next step is to compare the amplitude of the actual shear wave motion, observed in the test, and that is given by model predictions. The ratio between the amplitudes should provide the information about the C coefficient, which is present in the ARF formula (5.29). As a starting point, recall that the terms in (5.34) which describe the volumetric deformation do not contribute to the total motion after $t > t_{\mathrm{o}}$ (see (5.35) for the definition of t_{o}). In this case, only the convolution term in (5.34) is considered in computations, and phantom-specific parameters in the model are just α (ultrasound attenuation coefficient), G (shear modulus), μ (shear viscosity), and C (third-order modulus). Among other unknown parameters is the value of intensity on the boundary $I_{\mathrm{o}} = \frac{1}{2}|p_{\mathrm{o}}|^2$, which is, however, stayed the same for all tested materials. The geometry of the ultrasound source, as well as the compressional wave sound speed and the mass density are taken as known parameters and are described in Section 5.3.1. Since the linear approximation is used to compute the intensity field and the directional part of the ARF is proportional to $C-1$, the amplitude of the shear wave motion, computed using (5.34), is proportional to $(C-1)I_{\mathrm{o}}$. As a result of unknown I_{o}, the C coefficient can not be determined in the absolute sense, however, since I_{o} was constant for all tests, $(C-1)I_{\mathrm{o}}$ can be used to judge about the relative values of the coefficient C. The information about shear moduli G is taken from the shear wave speed measurements, and are shown in Tables 5.1 and 5.2. The shear viscosity was not measured experimentally and is determined from the decay of the shear waves. The ultrasound attenuation coefficient was not measured experimentally for the first set of tests, and is determined from the penetration depth of the generated

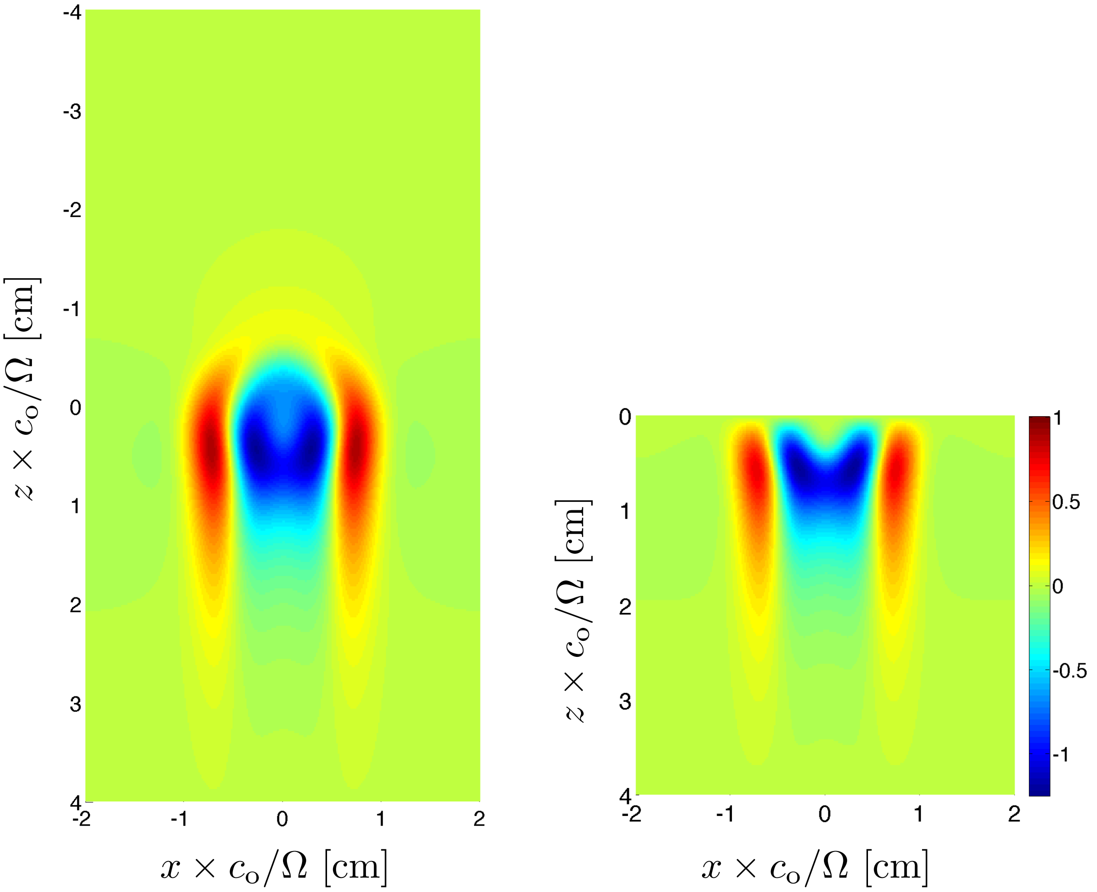

Figure 5.6: Normalized axial component of the particle velocity field, produced by the unfocused ARF in the infinite medium (left) and in the half-space (right).

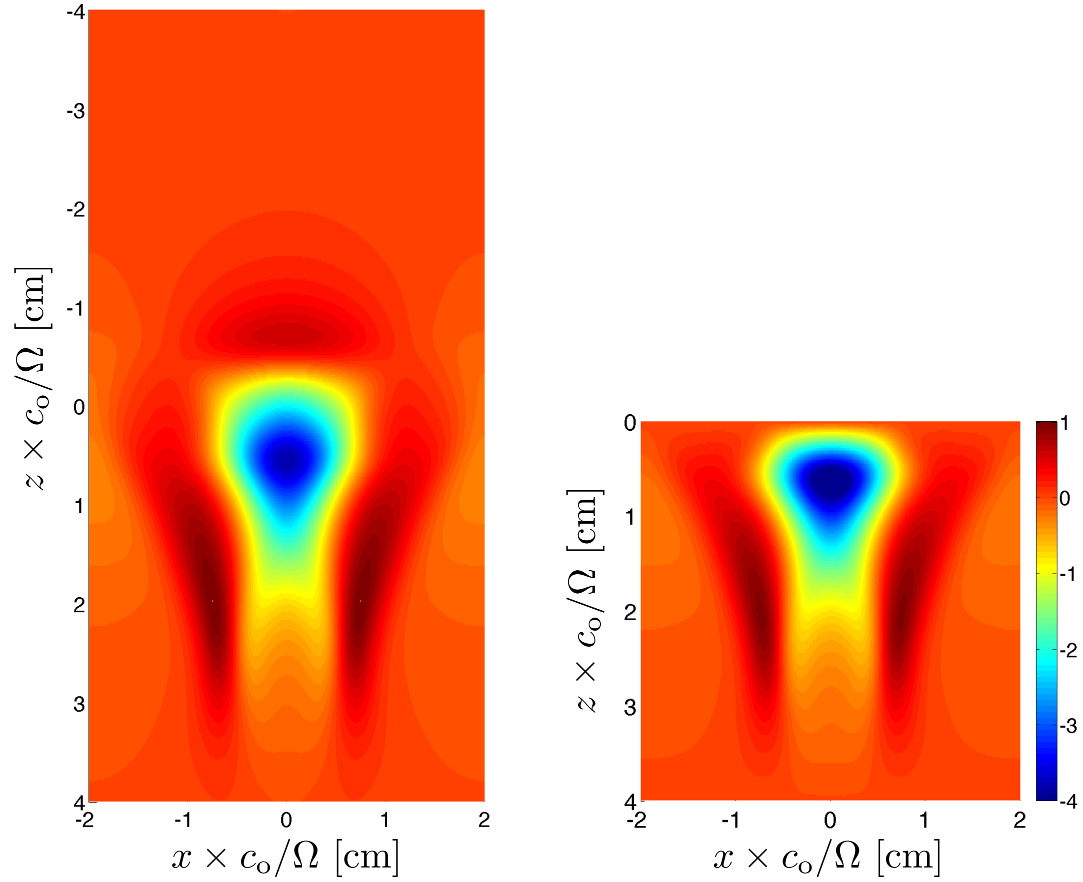

Figure 5.7: Normalized axial component of the particle velocity field, produced by the focused ARF in the infinite medium (left) and in the half-space (right).

motion. For the second set of experiments, however, the ultrasound attenuation coefficient was measured in a separate test. Note that the shear viscosity tends to add a small contribution to the amplitude of the deformation during the first stages, in which case the wrong value of the shear viscosity does not significantly affect the calculation of $(C-1)I_{\mathrm{o}}$. Unfortunately, this is not the case for the ultrasound attenuation coefficient α, since the directional part of the ARF has a term proportional to it (5.29), and makes the amplitude sensitive to α in some cases. The modulation envelope, used to excite the phantoms, had a rectangular pulse shape (5.35) with a duration of $t_{\mathrm{o}}/\Omega = 391\ \mu$s in the first set of tests and 585 μs in the second experiment. To justify an assumption (5.25), which is essential for the model development, one may note that the parameters used for computations are such that

$$3 \times 10^{-4} \;\approx\; \frac{\pi}{t_{\mathrm{o}}} \;\approx\; \omega_{\mathrm{m}} \;\ll\; d_1^{-1} \;\approx\; 3 \times 10^{-3}, \tag{5.40}$$

where ω_{m} is the dominant modulation frequency of the modulation envelope (computed here for shorter modulation signal).

Tables 5.3 and 5.4 summarize the values of the attenuation coefficient, shear viscosity and $(C-1)I_{\mathrm{o}}$ for both tests, which were determined from the comparison between the experimental data for the ARF-induced z component of the particle velocity vector and the model described in Sections 5.3.1 and 5.3.2. Due to the phantom-specific features of the experimental data and artifacts in the measurements, observations for each phantom have been processed individually, without using an universal algorithm for the solution of the inverse problem. In addition, since the acoustoelasticity envolved the measurements in two configurations (parallel and perpendicular) using two pushing modes (focused and unfocused), four data sets were used for the extraction of α, μ and $(C-1)I_{\mathrm{o}}$. As an illustration, Figs. 5.8 and 5.9 show the comparison between the raw experimental data and the model for paraffin-based phantom respectively for unfocused and focused push beams. Top panels illustrate the spatial distributions of the axial component of the particle velocity (in mm/s, same scale for left and right pictures) for a given time instant, while the bottom panels indicate the corresponding comparison along two specific directions, denoted by black solid lines on the top panels.

Comparison with acoustoelasticity tests. By using the data from Tables 5.1-5.4, one may compare the results for the third-order modulus C obtained independently from

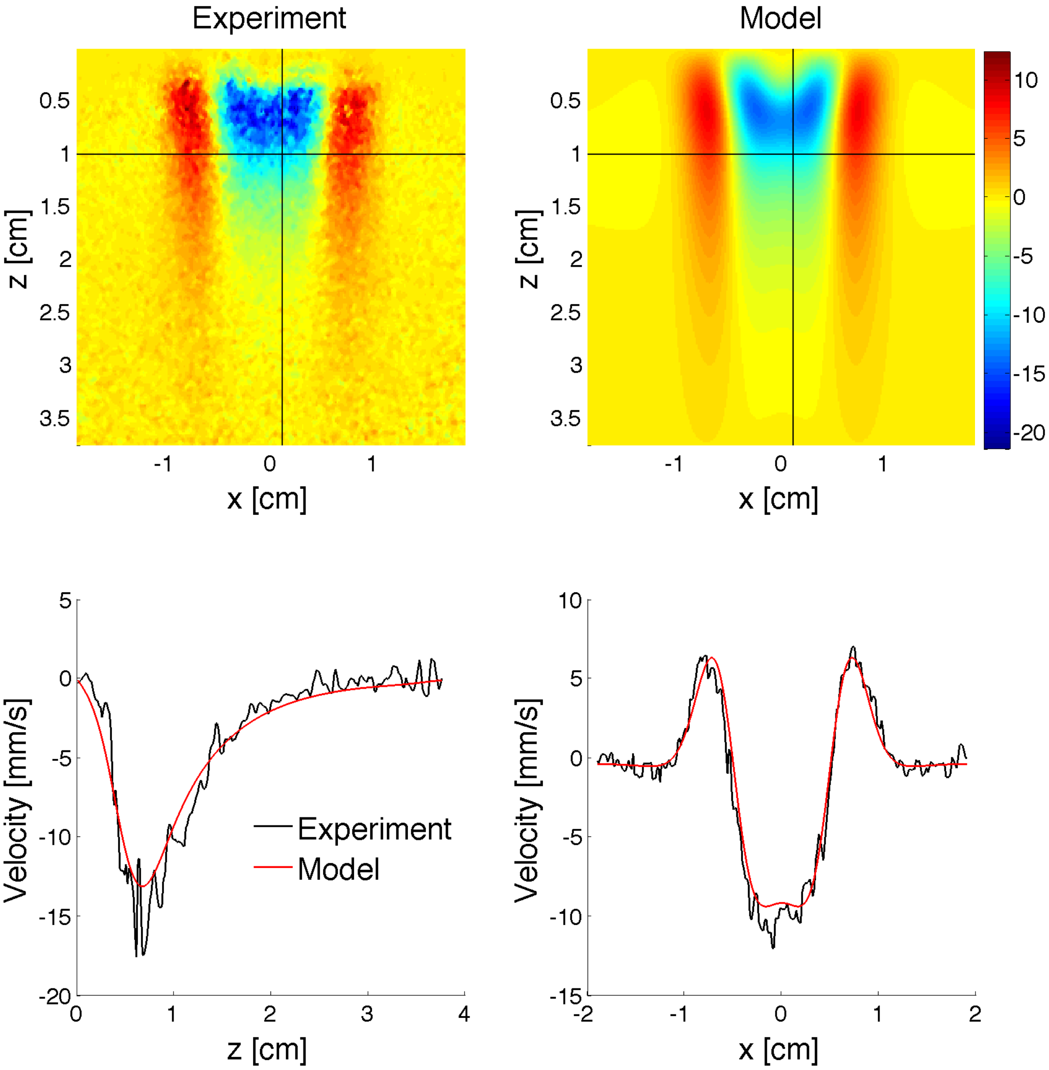

Figure 5.8: Comparison between the experimental observations and the model in terms of the axial particle velocity field for paraffin-based phantom for $t = 10\,t_{\rm o}$ and unfocused push beam. Top panels: raw experimental data (left) and the model (right) for the particle velocity field distribution (colorbar is in mm/s, the same scale for left and right pictures). Bottom panels: comparison between the observed and the modeled particle velocity fields along the cut in z direction (left) and x direction (right). Black solid lines on the top panels indicate the positions of the“cuts”.

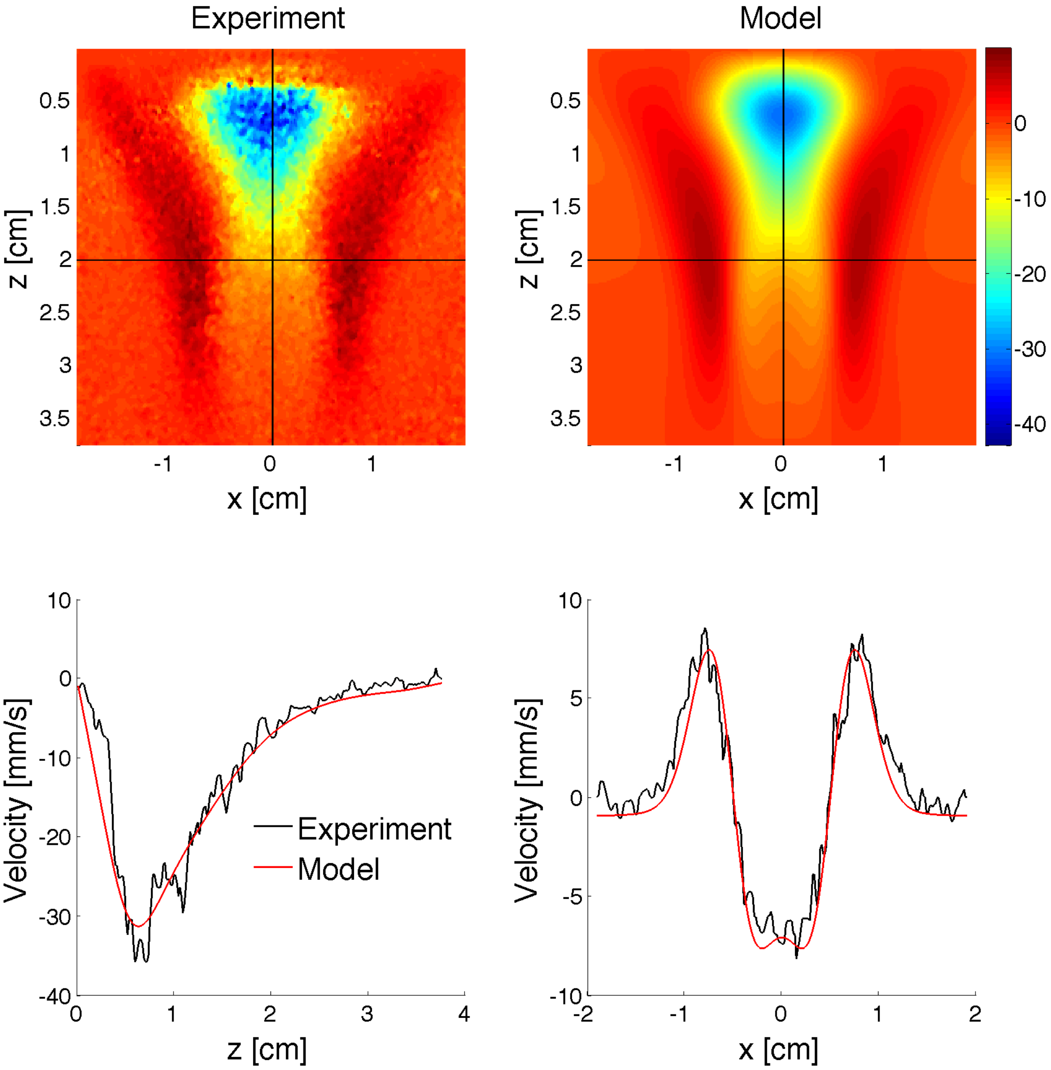

Figure 5.9: Comparison between the experimental observations and the model in terms of the axial particle velocity field for paraffin-based phantom for $t = 10\,t_o$ and focused push beam. Top panels: raw experimental data (left) and the model (right) for the particle velocity field distribution (colorbar is in mm/s, the same scale for left and right pictures). Bottom panels: comparison between the observed and the modeled particle velocity fields along the cut in z direction (left) and x direction (right). Black solid lines on the top panels indicate the positions of the“cuts”.

Phantom	Paraffin	PVC	PVA	Agarose	Gelatin
$\alpha \times c_{\mathrm{o}}^{-1}$ [dB/(cm·MHz)]	0.8	0.9	0.2	0.1	0.2
$\mu \times \Omega/(\varrho_{\mathrm{o}} c_{\mathrm{o}}^2)$ [Pa·s]	1.6	1.8	0.2	0.3	0.1
$(C-1)I_{\mathrm{o}} \times \varrho_{\mathrm{o}} c^3$ [W/cm^2]	150	150	175	700	210

Table 5.3: Values of the ultrasound attenuation coefficient α, shear viscosity μ, and $(C-1)I_{\mathrm{o}}$ for paraffin, PVC, PVA, agarose and gelatin phantoms.

Phantom	No fibers	2% cotton	4% cotton	2% glass	4% glass
$\alpha \times c_{\mathrm{o}}^{-1}$ [dB/(cm·MHz)]	1.3	1.6	2.2	1.3	1.4
$\mu \times \Omega/(\varrho_{\mathrm{o}} c_{\mathrm{o}}^2)$ [Pa·s]	1.0	1.2	1.5	1.1	1.2
$(C-1)I_{\mathrm{o}} \times \varrho_{\mathrm{o}} c^3$ [W/cm^2]	210	200	280	200	140

Table 5.4: Values of the ultrasound attenuation coefficient α, shear viscosity μ, and $(C-1)I_{\mathrm{o}}$ for paraffin-based phantoms with different fiber content.

the acoustoelasticity measurements and from the observed amplitude of the shear waves. Fig. 5.10 plots the $(C-1)I_{\mathrm{o}}$ quantity from Tables 5.3 and 5.4 (note that $I_{\mathrm{o}} = \text{const.}$ for all tested materials) versus $C-1$, computed from the results in Tables 5.1 and 5.2 (note that $K \approx 1$ according to the normalization scheme). Dashed line shows the linear fit, and has the slope of about $I_{\mathrm{o}} \times \varrho_{\mathrm{o}} c_{\mathrm{o}}^3 \approx 60$ W/cm^2, which implies that the pressure amplitude, generated at the source boundary, is $p_{\mathrm{o}} \times \varrho_{\mathrm{o}} c_{\mathrm{o}}^2 \approx 1.3$ MPa. As can be seen from Fig. 5.10, the overall agreement is acceptable, noting that the measurement errors are quite high. The most significant source of inaccuracy is the lack of knowledge of ultrasound attenuation coefficient, which affected notably three points that correspond to the materials with low attenuation (first set of experiments). The value of the slope of the fitted line is reasonable, but still unknown, which adds an additional degree of freedom to the problem and reduces the value of the obtained result. Understanding the sparsity of the diagram in Fig. 5.10, the population of the figure with more accurately determined points is one of the primary goals for the future research.

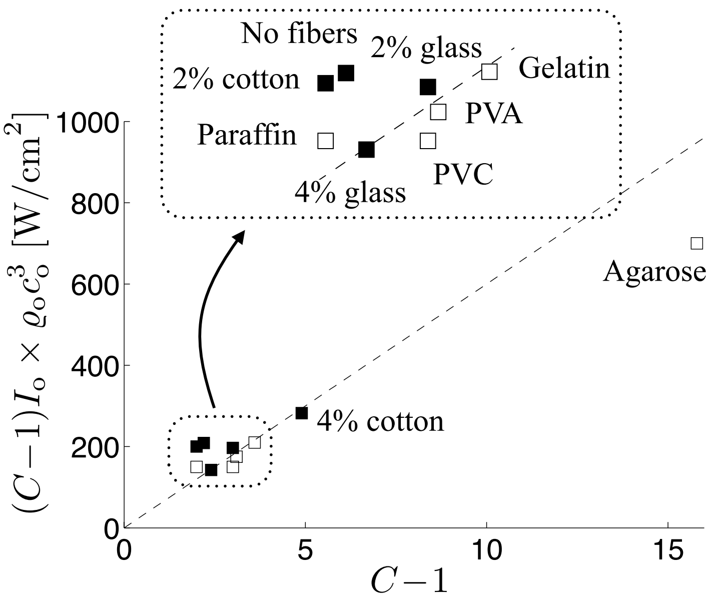

Figure 5.10: The variation of $(C-1)I_\mathrm{o}$, determined from the shear wave amplitude measurements, versus $C-1$, measured using acoustoelasticity technique (markers). Dashed line indicates a linear fit, and has the slope of approximately 60 W/cm^2.

5.4 Summary

This chapter describes the procedure for measuring the elastic nonlinearity coefficient C using the ARF-induced shear wave amplitude data, and validates the results via comparison versus those obtained from the acoustoelasticity experiments. First, the acoustoelasticity technique, applied to soft solids, is briefly described. The essence of such technique lies in the ability to measure elastic third-order moduli by determining the variation of the various wave speeds (e.g. with different directions of propagation or polarizations) with respect to applied uniform static stress. Total of ten tissue-mimicking phantoms were tested in the experimental setting for the two (out of three) independent third-order moduli. The shear waves, used for measurement of the shear wave speeds, were generated by the radiation force produced by both focused and unfocused ultrasound field in the uniaxially stressed material. Having the experimental measurements of C from the acoustoelasticity tests, next part of the chapter described the model for calculation of the ARF-induced shear motion in the unstressed material. The ultrasound field (used to quantify the radiation force) is computed for a given transducer geometry using the angular spectrum method, while the ARF-induced shear wave motion is calculated using three-dimensional spatial Fourier transform (evaluated numerically using FFT algorithm) and the method of images. By taking the values of the shear moduli from the acoustoelasticity experiments and determining the shear viscosities and ultrasound attenuation coefficients from the ARF-induced particle velocity data, the model showed an overall good agreement with the observations for all tested phantoms. Given the fact that the absolute value of the ultrasound intensity field is unknown (was not measured in the experimental setting), the comparison between the amplitude of the modeled and observed shear wave motions allowed to determine only the product $(C-1)I_{\mathrm{o}}$, where I_{o} is the magnitude of the intensity at the boundary of the transducer. The comparison between $(C-1)I_{\mathrm{o}}$, obtained from the particle velocity amplitude data, and $C-1$, computed from the acoustoelasticity results, showed a significant degree of agreement, which i) provides the experimental validation for the ARF formula, and ii) shows a possibility for imaging of tissue's nonlinear elasticity parameter C using the information about the amplitude of the ARF-induced motion.

Chapter 6

Conclusions

The Acoustic Radiation Force (ARF) is a phenomenon affiliated with the nonlinear effects of finite-amplitude wave propagation. It represents the mean momentum transfer from the sound wave to the medium, and allows for an effective computation of the mean motion induced by the sound wave. The first part of study investigates the generation of the ARF in situations when the ultrasound field is *modulated* by a low-frequency signal. The computation of the ARF due to modulated ultrasound field is facilitated by introducing the “fast” and “slow” time variables, which allow one to parse out the ultrasound-rate and modulation-rate variations in the solution. To study the mean motion induced by the ARF, the “fast” time average, computed over the period of ultrasound vibrations, is introduced. To highlight the features of the problem and validate the dual-time scale analysis, the reduced case of a plane wave excitation is considered first. By taking the constitutive model for soft tissues (under plane wave condition) as that for the Newtonian fluid, the “fast” time averages of the acoustic fields are shown to be governed by a linear system of equations featuring the ARF that rationally captures the effect of sound modulation. The developments are illustrated by the analytical solution for a sinusoidal modulation envelope which both exposes the limitations of earlier treatments and demonstrates the generation of nonzero mean motion in a lossless fluid by a modulated, high-intensity ultrasound field. To cater for practical applications of the ARF, the generation of the radiation force in soft tissues under the focused ultrasound excitation is established next. On approximating the constitutive response of soft tissues as that of a nonlinear viscoelastic solid with heat conduction, the governing equations for the mean tissue motion, featuring the new formula for the ARF, are obtained by taking the "fast" time average of the nonlinear field equations dictating the original ultrasound-scale problem. The computed radiation force has two qualitatively different terms: i) potential body force term, which is proportional to the gradient of the intensity and produces mostly compressional waves, and ii) directional body force term, which acts along the transducer's axis and generates predominantly shear motion. By comparing the result with the existing theory, it is further shown that the established formulation enriches the previous treatment by both including the role of the third-order elastic moduli, and accounting for the contribution of ultrasound modulation and thermal expansion to the sustained body force in tissue-like solids.

One prerequisite for the computation of the ARF is the knowledge of ultrasound intensity of the modulated source, which typically requires simulations of the nonlinear wave propagation problem. Unfortunately, the numerical computation of the nonlinear acoustic pressure field due to modulated excitation is complicated by the presence of two disparate time scales in the solution (namely the ultrasound time scale and it modulation counterpart). In this situation, time-domain simulations of the nonlinear acoustic field are computationally expensive due to excessive length of the signal, which may extend for hundreds or even thousands of ultrasound periods. On the other side of the spectrum, the frequency-domain approach is similarly ineffective due to richness of the frequency content of the nonlinear response. To deal with the problem, the customary quasi-plane wave scaling of the spatial coordinates that provides the basis for computing the acoustic field inside the focal region is complemented by its dual-time scale companion, where the temporal coordinate is split into its "fast" and "slow" components, allowing one to track the ultrasound-scale oscillations and modulation-scale variations separately in the solution. In this case, the nonlinear acoustic solution is governed by the KZK-type equation and can be independently discretized in the "fast" and "slow" temporal coordinates and then effectively computed in the "fast" frequency domain and "slow" time domain for any given (transient or time-harmonic) modulation envelope. The proposed developments are verified by the experimental results, time-domain numerical simulations, and illustrated via numerical examples that show the effectiveness of the hybrid (time-frequency) computational scheme.

The third part of this study utilizes the ARF developments for the purpose of determining one particular nonlinear elastic modulus C, that is present in the ARF formula, from the ARF-induced shear wave motion. To provide an alternative method for measuring the third-order moduli, first, the acoustoelasticity technique is briefly described. Acoustoelasticity is a method, that is used to measure elastic third-order moduli from the variation of the small-strain wave speed with applied uniform static stress. Acoustoelasticity experiments were performed on tissue-mimicking phantoms, which allowed to quantify two (out of three) elastic nonlinearity parameters for the tested materials. Since the ARF was used as an excitation in the acoustoelasticity tests, the obtained data was also used to determine the C coefficient from the shear wave amplitude. For the purpose of simulating each phantom's response to the ARF excitation, the value of the corresponding shear modulus was taken from the acoustoelasticity experiments, while the shear viscosity and ultrasound attenuation coefficient are deduced from the shape of the generated shear wave. The comparison between the measurements and the model demonstrated a good agreement for all tested materials in terms of both the shape and the amplitude of the generated waves. The comparison between nonlinear elasticity parameter C, obtained from the shear wave amplitude data, and observed in acoustoelasticity tests, showed a significant degree of consistency. This provides the preliminary verification for the ARF formula, which can be potentially used to facilitate the local noninvasive imaging of the tissue's nonlinear elasticity parameter C using the information about the amplitude of the ARF-induced motion.

References

[1] M. Faraday. On a peculiar class of acoustical figures; and on certain forms assumed by groups of particles upon vibrating elastic surfaces. *Phil. Trans. Roy. Soc. Lond.*, 121:299–340, 1831.

[2] Lord Rayleigh. On the circulation of air observed in Kundt's tubes, and on some allied acoustical problems. *Phil. Trans. Roy. Soc. Lond.*, 175:1–21, 1884.

[3] C. Eckart. Vortices and streams caused by sound waves. *Phys. Rev.*, 73:68–76, 1948.

[4] J. E. Percy and J. Lamb. Acoustic streaming in liquids. *Proc. Roy. Soc. Lond. A*, 226:43–50, 1954.

[5] O.V. Rudenko and S.I. Soluyan. *Theoretical Foundations of Nonlinear Acoustics.* Plenum, Consultants Bureau, New York, 1977.

[6] J. Lighthill. Acoustic streaming. *J. Sound Vibr.*, 61:391–418, 1978.

[7] M.F. Hamilton and D.T. Blackstock, editors. *Nonlinear Acoustics.* Academic Press, San Diego, California, 1998.

[8] V. Dvorak. *Pogg. Ann.*, 157:61, 1876.

[9] A.P. Sarvazyan, O.V. Rudenko, S.D. Swanson, J.B. Fowlkes, and S.Y. Emelianov. Shear wave elasticity imaging: A new ultrasonic technology of medical diagnostics. *Ultras. Med. Biol.*, 24:1419–1435, 1998.

[10] J. Bercoff, M. Tanter, and M. Fink. Supersonic shear imaging: A new technique for soft tissue elacticity mapping. *IEEE Trans. Ultrason. Ferroelect. Freq. Contr.*, 51(4):396–409, 2004.

[11] M.L. Palmeri, A.C. Sharma, R.R. Bouchard, R.W. Nightingale, and K.R. Nightingale. A finite-element method model of soft tissue response to impulsive acoustic radiation force. *IEEE Trans. Ultrason. Ferroelect. Freq. Contr.*, 52(10):1699–1712, 2005.

[12] K.R. Nightingale, S.A. McAleavey, and G.E. Trahey. Shear wave generation using acoustic radiation force: In vivo and ex vivo results. *Ultrasound Med. Biol.*, 29(12):1715–1723, 2003.

[13] F. Lizzi, R. Muratore, C. Deng, J. Ketterling, K. Alam, S. Mikaelian, and A. Kalisz. Radiation-force technique to monitor lesions during ultrasonic therapy. *Ultrasound Med. Biol.*, 29(11):1593–1605, 2003.

[14] D. Liu and E. S. Ebbini. Viscoelastic property measurement in thin tissue constructs using ultrasound. *IEEE Trans. Ultrason. Ferroelect. Freq. Contr.*, 55:368–383, 2008.

[15] B. B Guzina, K. Tuleubekov, D. Liu, and E. Ebbini. Viscoelastic characterization of thin tissues using acoustic radiation force and model-based inversion. *Phys. Med. Biol.*, 54:40894112, 2009.

[16] A. P. Sarvazyan. Diversity of biomedical applications of acoustic radiation force. *Ultrasonics*, 50:230–234, 2010.

[17] M. Fatemi and J. Greenleaf. Vibro-acoustography: An imaging modality based on ultrasound-stimulated acoustic emission. *Proc. Natl. Acad. Sci.*, 96:6603–6608, 1999.

[18] E. A. Barannik, S. A. Girnyk, V. V. Tovstiak, A. I. Marusenko, V. A. Volokhov, A. P. Sarvazyan, and S. Y. Emelianov. The influence of viscosity on the shear strain remotely induced by focused ultrasound in viscoelastic media. *J. Acoust. Soc. Am.*, 115:2358–2364, 2004.

[19] E. Dontsov and B. B. Guzina. Effect of low-frequency modulation on the acoustic radiation force in newtonian fluids. *SIAM J. Appl. Math.*, 71:356–378, 2011.

[20] E.V. Dontsov and B.B. Guzina. Acoustic radiation force in tissue-like solids due to modulated sound field. *J. Mech. Phys. Solids*, 60:1791–1813, 2012.

[21] L. Ostorvsky, A Sutin, Yu. Ilinskii, O. Rudenko, and A. Sarvazyan. Radiation force and shear motions in inhomogeneous media. *J. Acoust. Soc. Am.*, 121(3):1324–1331, 2007.

[22] A. P. Sarvazyan, O. V. Rudenko, and W. L. Nyborg. Biomedical applications of radiation force of ultrasound: historical roots and physical basis. *Ultras. Med. Biol.*, 36:1379–1394, 2010.

[23] L. D. Landau and E. M. Lifshitz. *Theory of Elacticity.* Pergamon Press, Oxford, 3rd edition, 1986.

[24] E. A. Zabolotskaya and R. V. Khokhlov. Quasi-plane waves in the nonlinear acoustics of confined beams. *Sov. Phys. Acoust.*, 15:3540, 1969.

[25] V.P. Kuznetsov. Equations of nonlinear acoustics. *Sov. Phys. Acoust.*, 15:3540, 1969.

[26] S. I. Aanonsen, T. Barkve, J. N. Tjøtta, and S. Tjøtta. Distortion and harmonic generation in the nearfield of a finite amplitude sound beam. *J. Acoust. Soc. Am.*, 75:749–768, 1984.

[27] T. S. Hart and M. F. Hamilton. Nonlinear effects in focused sound beams. *J. Acoust. Soc. Am*, 84:1488–1496, 1988.

[28] Y. S. Lee and M. F. Hamilton. Time-domain modeling of pulsed finite-amplitude sound beams. *J. Acoust. Soc. Am.*, 97:906917, 1995.

[29] D. Zhang, X. Gong, and B. Zhang. Second harmonic sound field after insertion of a biological tissue sample. *J. Acoust. Soc. Am*, 111:45–48, 2002.

[30] P. J. Westervelt. Parametric acoustic array. *J. Acoust. Soc. Am.*, 35(4):535–537, 1963.

[31] J. Tavakkoli, D. Cathignol, R. Souchon, and O. A. Sapozhnikov. Modeling of pulsed finite-amplitude focused sound beams in time domain. *J. Acoust. Soc. Am*, 104:2061–2072, 1998.

[32] E. Dontsov and B. B. Guzina. On the nonlinear parabolic wave equation for modulated ultrasound fields. *Submitted to Wave Motion.*

[33] D. S. Hugues and J. L. Kelly. Second-order elastic deformation of solids. *Phys. Rev.*, 92:1145–1149, 1953.

[34] T. Bateman, W. P. Mason, and H. J. McSkimin. Third-order elastic moduli of germanium. *J. Appl. Phys.*, 32:928–936, 1961.

[35] S. Catheline, J.L. Gennisson, and M. Fink. Measurement of elastic nonlinearity of soft solid with transient elastography. *J. Acoust. Soc. Am.*, 114:3087, 2003.

[36] E. Dontsov and B. B. Guzina. Dual-time approach to the numerical simulation of modulated nonlinear ultrasound fields. *In preparation.*

[37] J. Vappou, C. Maleke, and E.E. Konofagou. Quantitative viscoelastic parameters measured by harmonic motion imaging. *Phys. Med. Biol.*, 54:736–742, 2009.

[38] H. C. Ting and C. K. Yeh. A theoretical time-course study of acoustic tweezers. In *2007 IEEE Ultrasonics Symposium*, pages 2566–2569, 2007.

[39] O.V. Rudenko, A.P. Sarvazyan, and S.Y. Emelianov. Acoustic radiation force and streaming induced by nonlinear ultrasound in dissipative medium. *J. Acoust. Soc. Am.*, 99(5):2791–2798, 1996.

[40] T. Hasegawa and K. Yosioka. Acoustic-radiation force on a solid elastic sphere. *J. Acoust. Soc. Am.*, 56(5B):1139–1143, 1969.

[41] F. G. Mitri. Theoretical and experimental determination of the acoustic radiation force acting on an elastic cylinder in a planerogressive wave – far-field derivation approach. *New J. Phys.*, 8(138), 2006.

[42] S. Chen, M. Fatemi, and J. F. Greenleaf. Remote measurement of material properties from radiation force induced vibration of an embedded sphere. *J. Acoust. Soc. Am.*, 112:884889, 2002.

[43] A. L. Thuras, R. T. Jenkins, and H. T. O'Neil. Extraneous frequencies generated in air carrying intense sound waves. *J. Acoust. Soc. Am.*, 6:173–180, 1935.

[44] J. S. Thierman. *Sources of difference frequency sound in a dual-frequency imaging system with implications for monitoring thermal surgery.* PhD thesis, Harvard-MIT division of health sciences and technology, 2004.

[45] A.A. Karabutov, O.V. Rudenko, and O.A. Sapozhnikov. Theory of thermal self-focusing with allowance for the generation of shock waves and acoustic streaming. *Sov. Phys. Acoust.*, 34:371–374, 1988.

[46] O.V. Rudenko, M.M. Sagatov, and O.A. Sapozhnikov. Thermal self-focusing of sawtooth waves. *Sov. Phys. JETP*, 71(3):449–454, 1990.

[47] L.E. Malvern. *Introduction to the Mechanics of a Continuous Medium.* Prentice Hall, Englewood Cliffs, New Jersey, 1969.

[48] B. D. Coleman and W. Noll. The thermodynamics of elastic materials with heat conduction and viscosity. *Arch. Rational Mech. Anal.*, 12:167–178, 1963.

[49] D R Raichel. Sound propagation in voigt fluid. *J. Acoust. Soc. Am.*, 52:395–398, 1972.

[50] A. S. Ahuja. Tissue as a Voight body for propagation of ultrasound. *Ultrasonic Imaging*, 1:136–146, 1979.

[51] T. Deffieuux, G. Montaldo, M Tanter, and M Fink. Shear wave spectroscopy for in vivo quantication of human soft tissues visco-elasticity. *Medical Imaging, IEEE Transcations*, 28:313–322, 2009.

[52] G. Forgacs, R.A. Foty, Y. Shafrir, and M. S. Steinberg. Viscoelastic properties of living embryonic tissues: a quantitative study. *Biophysical Journal*, 74(5):2227 – 2234, 1998.

[53] J. F. Greenleaf, M. Fatemi, and M. Insana. Selected methods for imaging elastic properties of biological tissues. *Annu. Rev. Biomed. Eng.*, 5:57 – 78, 2003.

[54] C. Schmitt, A. Bruhat, A. H. Henni, and G. Cloutier. Viscoelastic characterization of soft tissues by Dynamic Micro-Elastography (DME) in the frequency range of 300-1500 Hz. *Ultrasonics Symposium*, pages 2044 – 2047, 2008.

[55] R. Sinkus, M. Tanter, T. Xydeas, S. Catheline, J. Bercoff, and M. Fink. Viscoelastic shear properties of in vivo breast lesions measured by MR elastography. *Magnetic Resonance Imaging*, 23(2):159 – 165, 2005.

[56] K. Sunagawa and H. Kanai. Measurement of shear wave propagation and investigation of estimation of shear viscoelasticity for tissue characterization of the arterial wall. *Journal of Medical Ultrasonics*, 32:39–47, 2005.

[57] B. D. Coleman. Thermodyamics of materials with memory. *Arch. Rational Mech. Anal.*, 17:1–46, 1964.

[58] C. Truesdell and W. Noll, editors. *The Non-Linear Field Theories of Mechanics.* Springer, Berlin, Germany, third edition, 2004.

[59] E.P. Papadakis, editor. *Ultrasonic instruments and devices: reference for modern instrumentation, techniques and technology.* Academic Press, New York, 1999.

[60] NCRP. Exposure criteria for medical diagnostic ultrasound: I. Criteria based on thermal mechanisms. Technical Report 113, National Council on Radiation Protection and Measurements, 1992.

[61] M. Fatemi and J. F. Greenleaf. Ultrasound-stimulated vibro-acoustic spectrography. *Science*, 280(5360):82–84, 1998.

[62] A. Giannoula and R. S. C. Cobbold. Propagation of shear waves generated by a modulated finite amplitude radiation force in a viscoelastic medium. *IEEE Trans. Ultrason. Ferroelect. Freq. Contr.*, 56:575–588, 2009.

[63] B. J. Fahey, S. J. Hsu, P. D. Wolf, R. C. Nelson, and G. E. Trahey. Liver ablation guidance with acoustic radiation force impulse imaging: challenges and opportunities. *Phys. Med. Biol.*, 51:3785–3808, 2006.

[64] C.E. Pearson. Dual time scales in a wave problem governed by coupled nonlinear equations. *SIAM Review*, 23:425–433, 1981.

[65] R. Z. Khasminskii and G. Yin. On averaging principles: an asymptotic expansion approach. *SIAM J. Math. Anal.*, 35:1534–1560, 2004.

[66] M. Fatemi and J.F. Greenleaf. Probing the dynamics of tissue at low frequencies with the radiation force of ultrasound. *Phys. Med. Biol.*, 45:1449–1464, 2000.

[67] J. G. Charney, R. Fjortoft, and J. von Neumann. Numerical equation of the barotropic vorticity equation. *Tellus*, 2:237–254, 1950.

[68] G.F. Pinton. *Numerical methods for nonlinear wave propagation in ultrasound.* PhD thesis, Department of Biomedical Engineering, Duke University, 2007.

[69] T. Hasegawa, T. Kido, T. Iizuka, and C. Matsuoka. A general theory of Rayleigh and Langevin radiation. *J. Acoust. Soc. Jpn. (E)*, 21:145–152, 2000.

[70] N.H. Ricker. *Transient waves in visco-elastic media.* Elsevier Scientific Publ., Amsterdam, 1977.

[71] C. Zhang. *Seismic Absorption Estimation and Compensation.* PhD thesis, The University of British Columbia, 2008.

[72] G. Caviglia and A. Morro. *Inhomogeneous Waves in Solids and Fluids.* World Scientific, Singapore, 1992.

[73] R. Sinkus, M. Tanter, T. Xydeas, S. Catheline, J. Bercoff, and M. Fink. A single-element focused transducer method for harmonic motion imaging. *Proc. 2005 IEEE Ultrasonics Symp.*, pages 17–20, 2005.

[74] K. Nightingale, M. S. Soo, R. Nightingale, and G. Trahey. Acoustic radiation force impulse imaging: in vivo demonstration of clinical feasibility. *Ultras. Med. Biol.*, 28:227–235, 2002.

[75] J.N. Tjøtta, S. Tjøtta, and E.H. Vefring. Propagation and interaction of two collinear finite amplitude sound beams. *J. Acoust. Soc. Am.*, 88:2859–2870, 1990.

[76] J.N. Tjøtta, S. Tjøtta, and E.H. Vefring. Effects of focusing on the nonlinear interaction between two collinear finite amplitude sound beams. *J. Acoust. Soc. Am.*, 89:1017–1027, 1991.

[77] M.A. Averkiou and R.O. Cleveland. Modeling of an electrohydraulic lithotripter with the KZK equation. *J. Acoust. Soc. Am*, 106:102–112, 1999.

[78] J. Wojcik, A. Nowicki, P.A. Lewin, P.E. Bloomfield, T. Kujawska, and L. Filipczyski. Wave envelopes method for description of nonlinear acoustic wave propagation. *Ultrasonics*, 44:310–329, 2006.

[79] O.V. Rudenko. The 40th anniversary of the Khokhlov-Zabolotskaya equation. *Acoust. Phys.*, 56:457466, 2010.

[80] E. A. Zabolotskaya. Sound beams in a nonlinear isotropic solid. *Sov. Phys. Acoust.*, 16:467–470, 1971.

[81] A.N. Norris and S. Kostek. Nonlinear parabolic wave equations for solids. In *Advances in nonlinear acoustics: 13th ISNA*, pages 463–471. World Scientific, Singapore, 1993.

[82] F.M. Pestorius and D.T. Blackstock. Propagation of finite amplitude noise. In *Finite-Amplitude Wave Effects in Fluids*, pages 24–29. IPC Science and Technology Press, Guildford, Surrey, England, 1974.

[83] J.W.S. Rayleigh. *The Theory of Sound*. 2nd edition, 1896.

[84] D.W. Herrin, F. Martinus, T.W. Wu, and A.F. Seybert. An assessment of the high frequency boundary element and rayleigh integral approximations. *Appl. Acoust.*, 67(8):819 – 833, 2006.

[85] P. T. Christopher and K. J. Parker. New approaches to the linear propagation of acoustic fields. *J. Acoust. Soc. Am.*, 90:507–521, 1991.

[86] A. E. Siegman. Quasi fast hankel transform. *Opt. Lett.*, 1:13–15, 1977.

[87] V. A. Khokhlova, R. Souchon, J. Tavakkoli, O. A. Sapozhnikov, and D. Cathignol. Numerical modeling of finite-amplitude sound beams: Shock formation in the near field of a cw plane piston source. *J. Acoust. Soc. Am.*, 110:95–108, 2001.

[88] T.D. Murnaghan. *Finite deformation of an elastic solid*. John Wiley and Sons, Inc., New York, 1951.

[89] J.-L. Gennisson, M. Renier, S. Catheline, C. Barriere, J. Bercoff, M. Tanter, and M. Fink. Acoustoelasticity in soft solids: Assessment of the nonlinear shear modulus with the acoustic radiation force. *J. Acoust. Soc. Am.*, 122(6):3211–3219, 2007.

[90] G. Montaldo, M. Tanter, J. Bercoff, N. Benech, and M. Fink. Coherent plane-wave compounding for very high frame rate ultrasonography and transient elastography. *IEEE Trans. Ultrason. Ferroelectr. Freq. Control*, 56:489–506, 2009.

[91] H. Zhao, P. Song, M. W. Urban, J. F. Greenleaf, and S. Chen. Shear wave speed measurement using an unfocused ultrasound beam. *Ultrasound Med. Biol.*, 38:1646–1655, 2012.

[92] C. Kasai, K. Namekawa, A. Koyano, and R. Omoto. Real-time two-dimensional blood flow imaging using an autocorrelation technique. *IEEE Trans. Son. Ultrason.*, SU-32:458–464, 1985.

[93] N. C. Rouze, M. H. Wang, M. L. Palmeri, and K. R. Nightingale. Robust estimation of time-of-flight shear wave speed using a radon sum transformation. *IEEE Trans. Ultrason. Ferroelectr. Freq. Control*, 57:2662–2670, 2010.

[94] J. W. Goodman. *Introduction to Fourier Optics.* McGraw-Hill, New York, 2nd edition, 1996.

[95] E. Fermi. *Thermodynamics.* Dover, New York, 1956.

Appendix A

A.1 Thermodynamic equality (3.11)

To obtain (3.11), recall the (nonlinear) thermoelastic part of the second Piola-Kirchhoff stress tensor

$$\boldsymbol{\Pi}_2 \;:=\; \rho^{-1}\boldsymbol{F}^{-1}\!\cdot\boldsymbol{\Sigma}\cdot\boldsymbol{F}^{-\mathrm{T}}. \tag{A.1}$$

From (3.8), the second of (3.10), and (A.1) it follows that $\boldsymbol{\Pi}_2 = \boldsymbol{\Pi}_2(\boldsymbol{E}, S)$. On invoking the chain rule and the definition of tensorial derivative "to the right", one consequently finds

$$\left(\frac{\partial \boldsymbol{\Pi}_2}{\partial S}\right)_{\boldsymbol{\Pi}_2,\mathrm{o}} \equiv \boldsymbol{0} \qquad \Longrightarrow \qquad \left(\frac{\partial \boldsymbol{\Pi}_2}{\partial S}\right)_{\boldsymbol{E},\mathrm{o}} + \left(\frac{\partial \boldsymbol{E}}{\partial S}\right)_{\boldsymbol{\Pi}_2,\mathrm{o}} \!:\! \left(\frac{\partial \boldsymbol{\Pi}_2}{\partial \boldsymbol{E}}\right)_{S,\mathrm{o}} \;=\; \boldsymbol{0}. \tag{A.2}$$

Here the fourth-order tensor $(\partial\boldsymbol{\Pi}_2/\partial\boldsymbol{E})_{S,\mathrm{o}}$ signifies the linear elasticity tensor which, with reference to the premise of isotropy and the scaling scheme in Table 2.1, reads

$$\left(\frac{\partial \boldsymbol{\Pi}_2}{\partial \boldsymbol{E}}\right)_{S,\mathrm{o}} \;=\; \big(1-2G\big)\,\boldsymbol{I}\otimes\boldsymbol{I} \;+\; 2G\,\boldsymbol{I}_4^{\mathrm{sym}}, \tag{A.3}$$

where $\boldsymbol{I}_4^{\mathrm{sym}}$ is the symmetric fourth-order identity tensor. Considering the "inverse" of the relationship $\boldsymbol{\Pi}_2 = \boldsymbol{\Pi}_2(\boldsymbol{E}, S)$ in the form of $\boldsymbol{E} = \boldsymbol{E}(\boldsymbol{\Pi}_2, T)$, on the other hand, one finds that

$$\left(\frac{\partial \boldsymbol{E}}{\partial S}\right)_{\boldsymbol{\Pi}_2,\mathrm{o}} \;=\; \left(\frac{\partial \boldsymbol{E}}{\partial T}\right)_{\boldsymbol{\Pi}_2,\mathrm{o}} \left(\frac{\partial T}{\partial S}\right)_{\boldsymbol{\Pi}_2,\mathrm{o}}. \tag{A.4}$$

From linear thermoelasticity [47] and basic thermodynamic considerations [95], it follows (by way of Table 2.1) that

$$\left(\frac{\partial \boldsymbol{E}}{\partial T}\right)_{\boldsymbol{\Pi}_2,\mathrm{o}} := \;\frac{\alpha_{\mathrm{T}}}{3}\,\boldsymbol{I}, \qquad \left(\frac{\partial T}{\partial S}\right)_{\boldsymbol{\Pi}_2,\mathrm{o}} := \;\frac{1}{\mathrm{c_p}}, \tag{A.5}$$

where α_{T} is the coefficient of volumetric thermal expansion, and $\mathrm{c_p}$ is the specific heat capacity at constant stress. On the basis of (A.1)–(A.5), one finds

$$\left(\frac{\partial \boldsymbol{\Pi}_2}{\partial S}\right)_{\boldsymbol{E},\mathrm{o}} = -\frac{\alpha_{\mathrm{T}}}{3\mathrm{c_p}}\,\boldsymbol{I}\!:\!\Big[\big(1-2G\big)\,\boldsymbol{I}\!\otimes\!\boldsymbol{I} + 2G\boldsymbol{I}_4^{\mathrm{sym}}\Big] = -\frac{\alpha_{\mathrm{T}}}{\mathrm{c_p}}\Big[1-\tfrac{4}{3}G\Big]\,\boldsymbol{I} = -\frac{\beta_{\mathrm{T}}}{\mathrm{c_p}}\,\boldsymbol{I}, \tag{A.6}$$

where $\beta_{\mathrm{T}} = \alpha_{\mathrm{T}}(1-\frac{4}{3}G) = \alpha_{\mathrm{T}}K$, and K denotes the linear elastic bulk modulus. A substitution of (A.1) into (A.6) recovers the claim.

A.2 Expansion of the thermoelastic response function

To demonstrate (3.27) one may first make use of (3.11), (3.23) and (3.24), and partially expand (3.10b) as

$$\begin{aligned}
\tilde{\boldsymbol{\Sigma}} \;=\; \frac{\boldsymbol{\Sigma}-\boldsymbol{\sigma}_{\mathrm{o}}}{\varepsilon} \;&\overset{\varepsilon^2}{=}\; (1+\varepsilon\tilde{\rho})\,\boldsymbol{F}\cdot\Bigg[\Bigg\{\frac{1}{\varepsilon}\left(\frac{\partial\bar{U}}{\partial I_1}\right)_{\mathrm{o}} + \left(\frac{\partial^2\bar{U}}{\partial {I_1}^2}\right)_{\mathrm{o}} I_1(\tilde{\boldsymbol{E}}) + \frac{\varepsilon}{2}\left(\frac{\partial^3\bar{U}}{\partial {I_1}^3}\right)_{\mathrm{o}} I_1^2(\tilde{\boldsymbol{E}}) \\
&+\; \varepsilon\left(\frac{\partial^2\bar{U}}{\partial I_1\partial I_2}\right)_{\mathrm{o}} I_2(\tilde{\boldsymbol{E}})\Bigg\}\boldsymbol{I} + \Bigg\{\left(\frac{\partial\bar{U}}{\partial I_2}\right)_{\mathrm{o}} + \varepsilon\left(\frac{\partial^2\bar{U}}{\partial I_1\partial I_2}\right)_{\mathrm{o}} I_1(\tilde{\boldsymbol{E}})\Bigg\}\Big(I_1(\tilde{\boldsymbol{E}})\boldsymbol{I}-\tilde{\boldsymbol{E}}\Big) \\
&+\; \varepsilon\left(\frac{\partial\bar{U}}{\partial I_3}\right)_{\mathrm{o}}\Big(I_2(\tilde{\boldsymbol{E}})\boldsymbol{I} - I_1(\tilde{\boldsymbol{E}})\tilde{\boldsymbol{E}} + \tilde{\boldsymbol{E}}^2\Big) - \varepsilon\,\frac{\beta_{\mathrm{T}}}{\mathrm{c_p}}\tilde{S}\,\boldsymbol{I}\Bigg]\cdot\boldsymbol{F}^{\mathrm{T}} + \tilde{p}_{\mathrm{o}}\boldsymbol{I},
\end{aligned} \tag{A.7}$$

where $\boldsymbol{\sigma}_{\mathrm{o}} = -\varepsilon\tilde{p}_{\mathrm{o}}\boldsymbol{I}$ is the initial hydrostatic stress field as postulated before. By virtue of the facts that i) $\tilde{\boldsymbol{\Sigma}}$ is homogeneous in $\tilde{\boldsymbol{u}}$, and ii) the terms that are linear in $\tilde{\boldsymbol{u}}$ are associated with the Hooke's law for an isotropic solid, one finds that

$$\left(\frac{\partial\bar{U}}{\partial I_1}\right)_{\mathrm{o}} = -\varepsilon\tilde{p}_{\mathrm{o}}, \qquad \left(\frac{\partial^2\bar{U}}{\partial {I_1}^2}\right)_{\mathrm{o}} = 1+\varepsilon\tilde{p}_{\mathrm{o}}, \qquad \left(\frac{\partial\bar{U}}{\partial I_2}\right)_{\mathrm{o}} = -2\varepsilon(\tilde{G}+\tilde{p}_{\mathrm{o}}), \tag{A.8}$$

which relates the internal energy derivatives to the initial pressure and linear elastic moduli. To keep the accuracy of approximation in (A.7) within $O(\varepsilon^2)$, it follows from (A.8) that $\tilde{\boldsymbol{E}}$ and $I_2(\tilde{\boldsymbol{E}})$ can be approximated with their $O(1)$ terms, while $I_1(\tilde{\boldsymbol{E}})$ requires expansion up to the linear i.e. $O(\varepsilon)$ term. Accordingly, one finds from (3.9) and (3.23) that

$$\tilde{\boldsymbol{E}} \;\overset{\varepsilon}{=}\; \nabla^{\mathrm{S}}\tilde{\boldsymbol{u}} = \tfrac{1}{2}(\nabla\tilde{\boldsymbol{u}} + \nabla^{\mathrm{T}}\tilde{\boldsymbol{u}}),$$

$$I_1(\tilde{\boldsymbol{E}}) \overset{\varepsilon^2}{=} \nabla\cdot\tilde{\boldsymbol{u}} + \varepsilon\big(\nabla\tilde{\boldsymbol{u}}\!:\!\nabla^{\mathrm{T}}\tilde{\boldsymbol{u}} + \tfrac{1}{2}\nabla\tilde{\boldsymbol{u}}\!:\!\nabla\tilde{\boldsymbol{u}}\big), \qquad I_2(\tilde{\boldsymbol{E}}) \overset{\varepsilon}{=} \tfrac{1}{2}\big[(\nabla\cdot\tilde{\boldsymbol{u}})^2 - \nabla^{\mathrm{S}}\tilde{\boldsymbol{u}}\!:\!\nabla^{\mathrm{S}}\tilde{\boldsymbol{u}}\big].$$

By virtue of (3.27) and (A.8), these approximations allow one to rewrite (A.7) as

$$\begin{aligned} \tilde{\boldsymbol{\Sigma}} \;&\overset{\varepsilon^2}{=}\; (1+\varepsilon\tilde{\rho})\boldsymbol{F}\cdot\Big[\Big\{\nabla\cdot\tilde{\boldsymbol{u}} + \varepsilon\big(\nabla\tilde{\boldsymbol{u}}:\nabla^{\mathrm{T}}\tilde{\boldsymbol{u}} + \tfrac{1}{2}\nabla\tilde{\boldsymbol{u}}:\nabla\tilde{\boldsymbol{u}}\big) + \tfrac{1}{2}\varepsilon B(\nabla\cdot\tilde{\boldsymbol{u}})^2 + \tfrac{1}{2}\varepsilon C\big[(\nabla\cdot\tilde{\boldsymbol{u}})^2 \\ &- \;\nabla^{\mathrm{S}}\tilde{\boldsymbol{u}}:\nabla^{\mathrm{S}}\tilde{\boldsymbol{u}}\big]\Big\}\boldsymbol{I} + \Big\{-2\varepsilon\tilde{G} + \varepsilon C\,\nabla\cdot\tilde{\boldsymbol{u}}\Big\}\Big(\nabla\cdot\tilde{\boldsymbol{u}}\,\boldsymbol{I} - \nabla^{\mathrm{S}}\tilde{\boldsymbol{u}}\Big) \qquad (\mathrm{A.9}) \\ &+ \;\varepsilon D\Big(\tfrac{1}{2}\big[(\nabla\cdot\tilde{\boldsymbol{u}})^2 - \nabla^{\mathrm{S}}\tilde{\boldsymbol{u}}:\nabla^{\mathrm{S}}\tilde{\boldsymbol{u}}\big]\,\boldsymbol{I} - \nabla\cdot\tilde{\boldsymbol{u}}\,\nabla^{\mathrm{S}}\tilde{\boldsymbol{u}} + (\nabla^{s}\tilde{\boldsymbol{u}})^2\Big) - \varepsilon\frac{\beta_{\mathrm{T}}}{\mathrm{c_p}}\tilde{S}\,\boldsymbol{I}\Big]\cdot\boldsymbol{F}^{\mathrm{T}}, \end{aligned}$$

where B, C and D are constants given by (3.28). With the aid of (3.22a), (3.23) and relationship

$$\det(\boldsymbol{F}) \;\overset{\varepsilon^2}{=}\; 1 \,+\, \varepsilon\nabla\cdot\tilde{\boldsymbol{u}},$$

the latter expression for $\tilde{\boldsymbol{\Sigma}}$ can be further expanded as

$$\begin{aligned} \tilde{\boldsymbol{\Sigma}} \;&\overset{\varepsilon^2}{=}\; \big(1-2\varepsilon\tilde{G}\big)\nabla\cdot\tilde{\boldsymbol{u}}\,\boldsymbol{I} + 2\varepsilon\tilde{G}\nabla^{\mathrm{S}}\tilde{\boldsymbol{u}} + \varepsilon\Big[\tfrac{1}{2}(B+3C+D-2)(\nabla\cdot\tilde{\boldsymbol{u}})^2 - \tfrac{1}{2}(C+D)\nabla^{\mathrm{S}}\tilde{\boldsymbol{u}}:\nabla^{\mathrm{S}}\tilde{\boldsymbol{u}} \\ &+ \;\nabla\tilde{\boldsymbol{u}}:\nabla^{\mathrm{T}}\tilde{\boldsymbol{u}} + \tfrac{1}{2}\nabla\tilde{\boldsymbol{u}}:\nabla\tilde{\boldsymbol{u}} - \frac{\beta_{\mathrm{T}}}{\mathrm{c_p}}\tilde{S}\Big]\boldsymbol{I} \;-\; \varepsilon\Big[(C+D-2)\,\nabla\cdot\tilde{\boldsymbol{u}}\,\boldsymbol{I} - D\nabla^{s}\tilde{\boldsymbol{u}}\Big]\cdot\nabla^{s}\tilde{\boldsymbol{u}}, \quad (\mathrm{A.10}) \end{aligned}$$

which recovers claim (3.27).

To compute the thermoelastic part of the first Piola-Kirchhoff stress tensor, $\hat{\tilde{\boldsymbol{\Pi}}} = \det(\hat{\boldsymbol{F}})\,\hat{\boldsymbol{F}}^{-1}\cdot\hat{\tilde{\boldsymbol{\Sigma}}}$, one may first note via the identity $\nabla\tilde{\boldsymbol{u}} = \hat{\boldsymbol{F}}^{-\mathrm{T}}\cdot\nabla\hat{\tilde{\boldsymbol{u}}}$ and (3.22a) that

$$\nabla\tilde{\boldsymbol{u}} \;\overset{\varepsilon^2}{=}\; \nabla\hat{\tilde{\boldsymbol{u}}} \,-\, \varepsilon\nabla\hat{\tilde{\boldsymbol{u}}}\cdot\nabla\hat{\tilde{\boldsymbol{u}}}, \qquad \nabla\cdot\tilde{\boldsymbol{u}} \;\overset{\varepsilon^2}{=}\; \nabla\cdot\hat{\tilde{\boldsymbol{u}}} \,-\, \varepsilon\nabla\hat{\tilde{\boldsymbol{u}}}:\nabla^{\mathrm{T}}\hat{\tilde{\boldsymbol{u}}}. \qquad (\mathrm{A.11})$$

On the basis of (A.10) and (A.11), $\hat{\tilde{\boldsymbol{\Pi}}}$ can be computed as

$$\begin{aligned} \hat{\tilde{\boldsymbol{\Pi}}} \;&\overset{\varepsilon^2}{=}\; \big(1-2\varepsilon\tilde{G}\big)\nabla\cdot\hat{\tilde{\boldsymbol{u}}}\,\boldsymbol{I} \,+\, 2\varepsilon\tilde{G}\nabla^{\mathrm{S}}\hat{\tilde{\boldsymbol{u}}} \,+\, \varepsilon\Big[\tfrac{1}{2}(B+3C+D)(\nabla\cdot\hat{\tilde{\boldsymbol{u}}})^2 - \tfrac{1}{2}(C+D)\nabla^{\mathrm{S}}\hat{\tilde{\boldsymbol{u}}}:\nabla^{\mathrm{S}}\hat{\tilde{\boldsymbol{u}}} \\ &+ \;\tfrac{1}{2}\nabla\hat{\tilde{\boldsymbol{u}}}:\nabla\hat{\tilde{\boldsymbol{u}}} - \frac{\beta_{\mathrm{T}}}{\mathrm{c_p}}\hat{\tilde{S}}\Big]\boldsymbol{I} \;-\; \varepsilon\Big[(C+D)\,\nabla\cdot\hat{\tilde{\boldsymbol{u}}}\,\boldsymbol{I} - D\nabla^{s}\hat{\tilde{\boldsymbol{u}}}\Big]\cdot\nabla^{s}\hat{\tilde{\boldsymbol{u}}} \,+\, \varepsilon\nabla\cdot\hat{\tilde{\boldsymbol{u}}}\,\nabla\hat{\tilde{\boldsymbol{u}}}. \quad (\mathrm{A.12}) \end{aligned}$$

A.3 Properties of the Eulerian state vector $\boldsymbol{R}$

With reference to (3.54), (3.69) and relationships $\chi_{\mathrm{i}} = \chi_{\mathrm{io}} + \varepsilon^{1+2\lambda}\hat{\boldsymbol{R}}^{\mathrm{u_i}}$, $\zeta = \zeta_{\mathrm{o}} + \varepsilon^{1+\vartheta}\hat{\boldsymbol{R}}^{\mathrm{u}_z}$ and $z = z_{\mathrm{o}} + \varepsilon\hat{\boldsymbol{R}}^{\mathrm{u}_z}$ where, according to the adopted convention, $\hat{\boldsymbol{R}}^{\mathrm{u_i}}(\chi_{\mathrm{io}}, \zeta_{\mathrm{o}}, z_{\mathrm{o}}, \tau, t) = \hat{\tilde{\mathrm{u}}}_{\mathrm{i}}$ and $\hat{\boldsymbol{R}}^{\mathrm{u}_z}(\chi_{\mathrm{io}}, \zeta_{\mathrm{o}}, z_{\mathrm{o}}, \tau, t) = \hat{\tilde{\mathrm{u}}}_z$, one has

$$\begin{aligned} \frac{\partial\hat{\boldsymbol{R}}}{\partial z_{\mathrm{o}}} &= \frac{\partial\boldsymbol{R}(\chi_{\mathrm{i}},\zeta,z,\tau,t)}{\partial z_{\mathrm{o}}}\bigg|_{\chi_{\mathrm{io}},\zeta_{\mathrm{o}},\tau,t} = \varepsilon^{1+2\lambda}\frac{\partial\boldsymbol{R}}{\partial\chi_{\mathrm{i}}}\frac{\partial\hat{\boldsymbol{R}}^{\mathrm{u_i}}}{\partial z_{\mathrm{o}}} + \varepsilon^{1+\vartheta}\frac{\partial\boldsymbol{R}}{\partial\zeta}\frac{\partial\hat{\boldsymbol{R}}^{\mathrm{u}_z}}{\partial z_{\mathrm{o}}} + \frac{\partial\boldsymbol{R}}{\partial z}\bigg(1+\varepsilon\frac{\partial\hat{\boldsymbol{R}}^{\mathrm{u}_z}}{\partial z_{\mathrm{o}}}\bigg), \\ \frac{\partial\hat{\boldsymbol{R}}}{\partial t} &= \frac{\partial\boldsymbol{R}(\chi_{\mathrm{i}},\zeta,z,\tau,t)}{\partial t}\bigg|_{\chi_{\mathrm{io}},\zeta_{\mathrm{o}},z_{\mathrm{o}},\tau} = \varepsilon^{1+2\lambda}\frac{\partial\boldsymbol{R}}{\partial\chi_{\mathrm{i}}}\frac{\partial\hat{\boldsymbol{R}}^{\mathrm{u_i}}}{\partial t} + \varepsilon^{1+\vartheta}\frac{\partial\boldsymbol{R}}{\partial\zeta}\frac{\partial\hat{\boldsymbol{R}}^{\mathrm{u}_z}}{\partial t} + \varepsilon\frac{\partial\boldsymbol{R}}{\partial z}\frac{\partial\hat{\boldsymbol{R}}^{\mathrm{u}_z}}{\partial t} + \frac{\partial\boldsymbol{R}}{\partial t}. \end{aligned} \qquad (\mathrm{A.13})$$

On employing (3.65) in terms of $\hat{\boldsymbol{R}}^{\mathrm{u}_z}$ and $\hat{\boldsymbol{R}}^{\mathrm{u_i}}$, (A.13b) can be rewritten as

$$\frac{\partial \hat{\boldsymbol{R}}}{\partial t} = -\frac{\partial \boldsymbol{R}}{\partial \chi_{\mathrm{i}}}\left(\varepsilon^{1+2\lambda}\frac{\partial \hat{\boldsymbol{R}}^{\mathrm{u_i}}}{\partial z_{\mathrm{o}}}\right) - \frac{\partial \boldsymbol{R}}{\partial \zeta}\left(\varepsilon^{1+\vartheta}\frac{\partial \hat{\boldsymbol{R}}^{\mathrm{u}_z}}{\partial z_{\mathrm{o}}}\right) - \frac{\partial \boldsymbol{R}}{\partial z}\left(\varepsilon\frac{\partial \hat{\boldsymbol{R}}^{\mathrm{u}_z}}{\partial z_{\mathrm{o}}}\right) + \frac{\partial \boldsymbol{R}}{\partial t}. \tag{A.14}$$

From (3.65), (A.13a) and (A.14), one immediately recovers the reciprocity claim (3.71). In a similar fashion, the use of (3.69) and the "fast"-time periodicity condition (3.66) in terms of $\hat{\boldsymbol{R}}^{\mathrm{u}_z}$ yields

$$\begin{aligned}
\hat{\boldsymbol{R}}(\boldsymbol{t}_1) &= \boldsymbol{R}\Big(\chi_{\mathrm{io}} + \varepsilon^{1+2\lambda}\hat{\boldsymbol{R}}^{\mathrm{u_i}}(\boldsymbol{t}_1),\, \zeta_{\mathrm{o}} + \varepsilon^{1+\vartheta}\hat{\boldsymbol{R}}^{\mathrm{u}_z}(\boldsymbol{t}_1),\, z_{\mathrm{o}} + \varepsilon\hat{\boldsymbol{R}}^{\mathrm{u}_z}(\boldsymbol{t}_1),\, \tau,\, t+2\pi\Big)\\
&= \boldsymbol{R}\Big(\chi_{\mathrm{io}} + \varepsilon^{1+2\lambda}\hat{\boldsymbol{R}}^{\mathrm{u_i}}(\boldsymbol{t}_0),\, \zeta_{\mathrm{o}} + \varepsilon^{1+\vartheta}\hat{\boldsymbol{R}}^{\mathrm{u}_z}(\boldsymbol{t}_0),\, z_{\mathrm{o}} + \varepsilon\hat{\boldsymbol{R}}^{\mathrm{u}_z}(\boldsymbol{t}_0),\, \tau,\, t+2\pi\Big)\\
&= \boldsymbol{R}(\chi_{\mathrm{i}}, \zeta, z, \tau, t+2\pi), \qquad \text{where} \quad \boldsymbol{t}_{\mathrm{n}} = \{\zeta_{\mathrm{o}}, \chi_{\mathrm{io}}, \zeta_{\mathrm{o}}, z_{\mathrm{o}}, \tau, t+2\pi\mathrm{n}\}, \qquad \mathrm{n}=0,1
\end{aligned}$$

which, in concert with (3.66) and (3.69), recovers the periodicity statement (3.72).

A.4 Approximate dimensions of the focal region

To effectively scale the problem quantities within the focal region, one needs an estimate of its width that, to the leading order, can be obtained via a *linear acoustic* approximation of the focused beam problem. With such premise, the signal modulation can be discarded for it has a little effect on the beam geometry. As a result, the acoustic pressure field can be conveniently computed via the Rayleigh integral as

$$p(\boldsymbol{x}) = \int_\Gamma \Lambda\, \frac{e^{\mathrm{i}kR}}{R}\, \mathrm{d}\boldsymbol{\xi}, \qquad R = |\boldsymbol{\xi} - \boldsymbol{x}|, \qquad k = 1 + \mathrm{i}\alpha, \qquad \boldsymbol{\xi} \in \Gamma, \tag{A.15}$$

where $\boldsymbol{x} = (x_1, x_2, z)$ is the observation point, α is the attenuation coefficient, Γ synthesizes the transducer geometry, and $\Lambda = \Lambda(\boldsymbol{\xi})$ is the source density over Γ. For a spherical transducer with focal depth d, (A.15) reduces to

$$\begin{aligned}
&p(\boldsymbol{x}) = d^2 \int_0^{\theta_{\max}} \Lambda_\theta \sin\theta \int_0^{2\pi} \frac{e^{\mathrm{i}kR}}{R}\, \mathrm{d}\phi\, \mathrm{d}\theta,\\
&R = d\sqrt{1 - 2\bar{r}\sin\theta\cos\phi + \bar{r}^2 - 2\bar{z}\cos\theta + \bar{z}^2}, \quad \bar{r} = \frac{\sqrt{x_1^2 + x_2^2}}{d}, \quad \bar{z} = 1 - \frac{z}{d}
\end{aligned} \tag{A.16}$$

in the spherical coordinate system (R, θ, ϕ) centered at the focal point $\boldsymbol{x}_f = (0, 0, d)$, where $\Lambda_\theta = \Lambda_\theta(\sin\theta) = \Lambda(\boldsymbol{\xi})$, θ is the angle between $\bar{z}$ and $\boldsymbol{\xi} - \boldsymbol{x}_f$, and $\theta_{\max} = \sin^{-1}(a/d) = \sin^{-1}(0.5/f)$ is the so-called "focusing" angle. As an illustration, the top panel in Fig. A.1 plots the distribution of normalized beam intensity, computed via (A.16a) as $|p(\boldsymbol{x})|^2/|p|^2_{\max}$, assuming $\Lambda = \text{const.}$, $d = 1000$ and $f = 2.5$. To better understand the behavior of (A.16a) in the focal region, one may take $\bar{r} \ll 1$ and $|\bar{z}| \ll 1$ which permits (A.16b) to be expanded as

$$R \;=\; d\big(1 - \bar{r}\sin\theta\cos\phi - \bar{z}\cos\theta\big) \;+\; O(\bar{\eta}^2 d), \qquad \bar{\eta} \;=\; \max\{\bar{r}, |\bar{z}|\}. \tag{A.17}$$

By virtue of (A.17) and identity $\int_0^{2\pi} e^{-\mathrm{i}x\cos\phi}\,\mathrm{d}\phi = 2\pi J_0(x)$ where J_0 is the zeroth-order Bessel function, (A.16a) can be simplified as

$$p(\boldsymbol{x}) \;=\; 2\pi\, d\, e^{\mathrm{i}kd} \int_0^{\theta_{\max}} \Lambda_\theta \sin\theta\, e^{-\mathrm{i}k\bar{z}d\cos\theta} J_0\big(k\,\bar{r}\,d\sin\theta\big)\,\mathrm{d}\theta \,\times\, \Big(1 + O(\max\{\bar{\eta}, \bar{\eta}^2 d\})\Big).$$

On changing the integration variable as $s = \sin\theta$ and taking $1/(2f)$ as a small parameter, one finds that

$$p(\boldsymbol{x}) = 2\pi\, d\, e^{\mathrm{i}kd(1-\bar{z})} \int_0^{1/(2f)} \Lambda_\theta\, s\, e^{\mathrm{i}k\bar{z}ds^2/2} J_0\big(k\,\bar{r}\,d\,s\big)\,\mathrm{d}s \,\times\, \Big(1 + O\Big(\max\Big\{\frac{2|\bar{z}|d}{(4f)^4}, \frac{2}{(4f)^2}, \bar{\eta}, \bar{\eta}^2 d\Big\}\Big)\Big). \tag{A.18}$$

Assuming $\Lambda_\theta = \text{const.}$, the integral in (A.18) can be evaluated analytically for either $\bar{z} = 0$ or $\bar{r} = 0$, yielding the peak-normalized intensity distributions as

$$\begin{aligned} \bar{I}_{z=d}(r) \;&\approx\; \frac{|p(\boldsymbol{x})|^2_{z=d}}{\max_{\boldsymbol{x}} |p(\boldsymbol{x})|^2_{z=d}} \approx \left[\frac{2J_1(\pi x)}{\pi x}\right]^2, \qquad x = \frac{r}{2\pi f}, \\ \bar{I}_{r=0}(z-d) \;&\approx\; \frac{|p(\boldsymbol{x})|^2_{r=0}}{\max_{\boldsymbol{x}} |p(\boldsymbol{x})|^2_{r=0}} \approx \left[\frac{\sin(\pi y)}{\pi y}\right]^2, \qquad y = \frac{z-d}{16\pi f^2}, \end{aligned} \tag{A.19}$$

where J_1 is the first-order Bessel function.

On the basis of (A.19), one is now in position to estimate the size of the focal region by taking the its *half-width* w and *half-length* l so that $\bar{I}_{z=d}(\pm\frac{1}{2}w) = 0.5$ and $\bar{I}_{r=0}(\pm\frac{1}{2}l) = 0.5$, consistent with the applications of elevated-intensity focused ultrasound [15]. From (A.19), one in particular finds that

$$w \approx 2\pi f, \qquad l \approx 14\pi f^2. \tag{A.20}$$

Note, however, that for the estimates in (A.20) to hold, one must respectively have $\max\{2/(4f)^2,\, w/d, w^2/d\} = o(1)$ and $\max\{2l/(4f)^4, 2/(4f)^2, l/d, l^2/d\} = o(1)$. Since normally $w \ll l$, one may expect (A.20a) to be more accurate. This is illustrated in the bottom panels of Fig. A.1 which compare (A.19) with the numerical solution stemming from (A.16a).

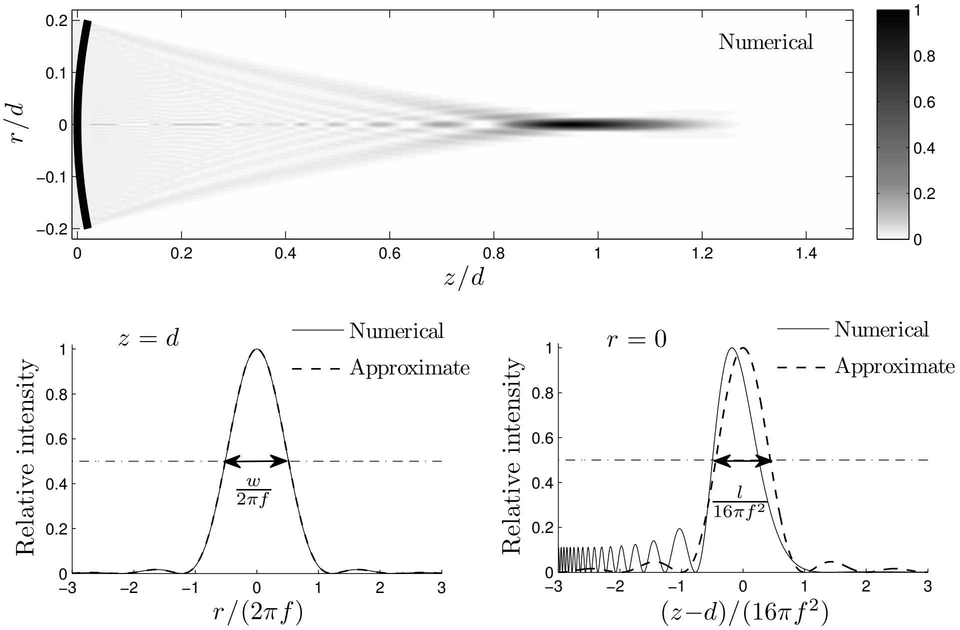

Figure A.1: Normalized intensity of the linear acoustic wave generated by a spherical ultrasound transducer with $d = 1000$, $f = 2.5$ and $\Lambda_\theta = \text{const.}$: axial cross section (top), focal plane $z = d$ (bottom left) and transducer axis $r = 0$ (bottom right).

A.5 Linearized acoustic relationship (3.161)

In invoking the first-order relationship $\tilde{v}_z \overset{\varepsilon}{=} \tilde{\rho}$, it is important to note that the plane-wave problem under consideration may not fit the assumptions (e.g. non-dissipative fluid) that are customarily made [7, 5] in justifying (3.161). To overcome this impediment, one may consider the leading behavior of (3.79a) when $\varepsilon \ll 1$ in terms of the components of the state vector $\boldsymbol{R}$, namely

$$\frac{\partial R^\rho}{\partial t} = -\frac{\partial R^{v_z}}{\partial z} + r, \qquad r = O(\varepsilon), \tag{A.21}$$

whose residual r, expressible in terms of R^ρ and R^{v_z}, inherently satisfies the periodicity condition (3.72). By applying the exact reciprocity relationship (3.71), namely $\partial R^{v_z}/\partial z = -\partial R^{v_z}/\partial t$ and computing the "fast" time average of (A.21), it can be further shown that $\langle r\rangle_{\text{E}}=0$. On integrating (A.21) with respect to "fast" time and employing (3.71), one finds

$$R^{\rho} \;=\; R^{v_z} + \int_0^t r\,dt' + \mathcal{C}(\tau,\zeta), \tag{A.22}$$

where the integral on the right-hand side is $O(\varepsilon)$ for any t since $\langle r\rangle_{\text{E}}=0$, and $\mathcal{C}(\tau,\zeta)$ is the constant of integration. An application of the "fast" time average to (A.22), together with the facts that $\langle\tilde{\rho}\rangle_{\text{E}} = O(\varepsilon)$ and $\langle\tilde{v}_z\rangle_{\text{E}} = O(\varepsilon)$ (see Section 3.5.1) shows that $\mathcal{C}(\tau,\zeta)\equiv\langle\mathcal{C}\rangle_{\text{E}}=O(\varepsilon)$. By virtue of this result, (3.70) and (A.22), one finally obtains

$$\tilde{v}_z \;\overset{\varepsilon}{=}\; \tilde{\rho}, \qquad t,z<\infty.$$

A.6 Finite-difference approximation of ultrasound intensity

To establish claim (B) from Section 3.5.5, one may express $\bar{\rho}$, $\bar{j}$ and $\bar{S}$ in (3.148) in terms of $\tilde{\rho}$, $\tilde{j}_z$, and $\tilde{S}$, multiply (3.148a) by $\tilde{j}_k^i$, and add the result to (3.148b) multiplied by $\tilde{\rho}_k^{i+1}$ to obtain

$$\begin{aligned}\frac{\Delta_{k,0}^{i,1}(\tilde{\rho})\,\tilde{j}_k^i + \Delta_{k,0}^{i,1}(\tilde{j})\,\tilde{\rho}_k^{i+1}}{h_t} &+ \frac{\Delta_{k-1,1}^{i,0}(\tilde{j})\,\tilde{j}_k^i + \Delta_{k,1}^{i+1,0}(\tilde{\rho})\,\tilde{\rho}_k^{i+1}}{h}\\ &= \left(-\varepsilon\frac{\beta_{\text{T}}}{\text{c}_{\text{p}}}\,\frac{\Delta_{k,1}^{i+1,0}(\tilde{S})}{h} + \Pi_k^i\right)\tilde{\rho}_k^{i+1} + \mathcal{R},\end{aligned} \tag{A.23}$$

where $\Delta_{q,n}^{p,m}(\tilde{\chi}) = \tilde{\chi}_{q+n}^{p+m} - \tilde{\chi}_q^p$, $\tilde{\chi}_q^p = \tilde{\chi}(t_p,z_q)$, and $\mathcal{R}$ is the residual i.e. misfit caused by substituting the exact quantities into discretized equations. The goal is to show the ultrasound intensity, computed numerically on the basis (3.148), satisfies (3.101) with an $O(h)$-residual. To this end it can be shown by employing the analysis as in Appendix A.5, that the finite difference solution approximates (3.161) with an $O(h)$ accuracy. This result, combined with (3.99), and (3.100), can be used to show that

$$\left\langle\left(-\varepsilon\frac{\beta_{\text{T}}}{\text{c}_{\text{p}}}\,\frac{\Delta_{k,1}^{i+1,0}(\tilde{S})}{h} + \Pi_k^i\right)\tilde{\rho}_k^{i+1}\right\rangle_{\text{E}} \;=\; -\,\varepsilon\tilde{\delta}\tilde{I}_{\text{E}}^*(t_i,z_k) \,+\, O(\varepsilon h). \tag{A.24}$$

On the other hand, the "fast" time average of the first term on the left-hand side of (A.23) can be computed via finite-difference approximation of (3.161) and Taylor series expansion as

$$\left\langle \frac{\Delta^{i,1}_{k,0}(\tilde{\rho})\, \tilde{j}^{i}_{k} + \Delta^{i,1}_{k,0}(\tilde{j})\, \tilde{\rho}^{i+1}_{k}}{h_t} \right\rangle_{\mathrm{E}} = \varepsilon \frac{\partial \langle \tilde{j}^{i}_{k}\, \tilde{\rho}^{i}_{k} \rangle_{\mathrm{E}}}{\partial \tau} + O(\varepsilon^2 h_t) = \varepsilon \frac{\partial \tilde{I}_{\mathrm{E}}}{\partial \tau}(t_i, z_k) + O(\varepsilon h), \tag{A.25}$$

recalling that $h_t < h$, and $\varepsilon < h$. Similarly, the second term on the left-hand side of (A.23) can be averaged as

$$\begin{aligned}
\left\langle \frac{\Delta^{i,0}_{k-1,1}(\tilde{j})\, \tilde{j}^{i}_{k} + \Delta^{i+1,0}_{k,1}(\tilde{\rho})\, \tilde{\rho}^{i+1}_{k}}{h} \right\rangle_{\mathrm{E}} &= \left\langle \frac{\Delta^{i,0}_{k-1,1}(\tilde{j})\, \tilde{j}^{i}_{k} + \Delta^{i,0}_{k,1}(\tilde{\rho})\, \tilde{\rho}^{i}_{k}}{h} \right\rangle_{\mathrm{E}} + O(\varepsilon h_t) \\
&= \sum_{m=0}^{\infty} \left\langle \frac{(-h)^m}{(m+1)!} \frac{\partial^{m+1} \tilde{j}^{i}_{k}}{\partial z^{m+1}}\, \tilde{j}^{i}_{k} + \frac{h^m}{(m+1)!} \frac{\partial^{m+1} \tilde{\rho}^{i}_{k}}{\partial z^{m+1}}\, \tilde{\rho}^{i}_{k} \right\rangle_{\mathrm{E}} + O(\varepsilon h_t) \\
&= \varepsilon \frac{\partial \tilde{I}_{\mathrm{E}}}{\partial \zeta}(t_i, z_k) + \sum_{n=1}^{\infty} \frac{(-1)^n\, h^{2n-1}}{(2n)!} \left\langle \left(\frac{\partial^n \tilde{\rho}^{i}_{k}}{\partial z^n} \right)^2 - \left(\frac{\partial^n \tilde{j}^{i}_{k}}{\partial z^n} \right)^2 \right\rangle_{\mathrm{E}} + O(\varepsilon h),
\end{aligned} \tag{A.26}$$

where the last equality makes use of the auxiliary summation index $n = (m+1)/2$ in lieu of m, and recursive use of the relationship $\langle a\, \partial b/\partial z \rangle_{\mathrm{E}} \overset{\varepsilon}{=} -\langle b\, \partial a/\partial z \rangle_{\mathrm{E}}$. To evaluate the sum in (A.26) one may compute the "fast" time average of the difference between (3.148a) multiplied by $\partial^{2p+1} \tilde{j}^{i}_{p}/\partial z^{2p+1}$ and (3.148b) multiplied by $\partial^{2p+1} \tilde{\rho}^{i+1}_{p}/\partial z^{2p+1}$ (both written in terms of $\tilde{\rho}$ and $\tilde{j}_z$), assuming $p \geqslant 0$, to find

$$\begin{aligned}
O(\varepsilon) &= \left\langle \left(\frac{\Delta^{i,1}_{k,0}(\tilde{\rho})}{h_t} + \frac{\Delta^{i,0}_{k-1,1}(\tilde{j})}{h} \right) \frac{\partial^{2p+1} \tilde{j}^{i}_{k}}{\partial z^{2p+1}} - \left(\frac{\Delta^{i,1}_{k,0}(\tilde{j})}{h_t} + \frac{\Delta^{i+1,0}_{k,1}(\tilde{\rho})}{h} \right) \frac{\partial^{2p+1} \tilde{\rho}^{i+1}_{k}}{\partial z^{2p+1}} \right\rangle_{\mathrm{E}} \\
&= \left\langle \left(\frac{\Delta^{i,1}_{k,0}(\tilde{\rho})}{h_t} + \frac{\Delta^{i,0}_{k-1,1}(\tilde{j})}{h} \right) \frac{\partial^{2p+1} \tilde{j}^{i}_{k}}{\partial z^{2p+1}} - \left(\frac{\Delta^{i-1,1}_{k,0}(\tilde{j})}{h_t} + \frac{\Delta^{i,0}_{k,1}(\tilde{\rho})}{h} \right) \frac{\partial^{2p+1} \tilde{\rho}^{i}_{k}}{\partial z^{2p+1}} \right\rangle_{\mathrm{E}} + O(\varepsilon h_t).
\end{aligned} \tag{A.27}$$

On employing the identities $\langle a\,\partial b/\partial\chi\rangle_{\mathrm{E}} \overset{\varepsilon}{=} -\langle b\,\partial a/\partial\chi\rangle_{\mathrm{E}}$ where $\chi = t, z,$ (A.27) can be expanded in Taylor series as

$$\begin{aligned}
O(\varepsilon) \;&=\; \sum_{m=0}^{\infty}\frac{1}{(m+1)!}\left\{h_t^m \left\langle \frac{\partial^{m+1}\tilde{\rho}_k^i}{\partial t^{m+1}}\frac{\partial^{2p+1}\tilde{j}_k^i}{\partial z^{2p+1}} - (-1)^m\frac{\partial^{m+1}\tilde{j}_k^i}{\partial t^{m+1}}\frac{\partial^{2p+1}\tilde{\rho}_k^i}{\partial z^{2p+1}}\right\rangle_{\mathrm{E}}\right.\\
&\quad+\;\left. h^m\left\langle(-1)^m\frac{\partial^{m+1}\tilde{j}_k^i}{\partial t^{m+1}}\frac{\partial^{2p+1}\tilde{j}_k^i}{\partial z^{2p+1}} - \frac{\partial^{m+1}\tilde{\rho}_k^i}{\partial t^{m+1}}\frac{\partial^{2p+1}\tilde{\rho}_k^i}{\partial z^{2p+1}}\right\rangle_{\mathrm{E}}\right\}\\
&=\; \sum_{m=0}^{\infty}\frac{h_t^m}{(m+1)!}\left\langle\frac{\partial^{m+1}\tilde{\rho}_k^i}{\partial t^{m+1}}\frac{\partial^{2p+1}\tilde{j}_k^i}{\partial z^{2p+1}}\right\rangle_{\mathrm{E}}\left(1-(-1)^{2m+2p+2}\right) \qquad\qquad (A.28)\\
&\quad+\;\sum_{\ell=0}^{\infty}\frac{(-1)^{\ell-p}h^{2\ell}}{(2\ell+1)!}\left\langle\left(\frac{\partial^{\ell+p+1}\tilde{\rho}_k^i}{\partial z^{\ell+p+1}}\right)^2 - \left(\frac{\partial^{\ell+p+1}\tilde{j}_k^i}{\partial z^{\ell+p+1}}\right)^2\right\rangle_{\mathrm{E}} +\; O(\varepsilon h)\\
&=\; \sum_{\ell=0}^{\infty}\frac{(-1)^{\ell-p}h^{2\ell}}{(2\ell+1)!}\left\langle\left(\frac{\partial^{\ell+p+1}\tilde{\rho}_k^i}{\partial z^{\ell+p+1}}\right)^2 - \left(\frac{\partial^{\ell+p+1}\tilde{j}_k^i}{\partial z^{\ell+p+1}}\right)^2\right\rangle_{\mathrm{E}} +\; O(\varepsilon h),
\end{aligned}$$

which makes use of the auxiliary summation index $\ell = 2m$. A recursive use of this result shows that

$$\left\langle\left(\frac{\partial^n\tilde{\rho}_k^i}{\partial z^n}\right)^2 - \left(\frac{\partial^n\tilde{j}_k^i}{\partial z^n}\right)^2\right\rangle_{\mathrm{E}} \overset{\varepsilon}{=} 0, \qquad n \geqslant 1,$$

which, together with (A.24)–(A.26), reduces the “fast” time average of (A.23) to

$$\frac{\partial\tilde{I}_{\mathrm{E}}}{\partial\tau}(t_i, z_k) + \frac{\partial\tilde{I}_{\mathrm{E}}}{\partial\zeta}(t_i, z_k) + \tilde{\delta}\tilde{I}^*_{\mathrm{E}}(t_i, z_k) \;=\; O(h) + \frac{1}{\varepsilon}\langle\mathcal{R}\rangle_{\mathrm{E}}. \qquad (A.29)$$

A comparison of (A.29) with (3.101) whose inherent residual is $O(\varepsilon)$, together with the assumption that $h > \varepsilon$, finally yields the finite-difference residual in the intensity equation as $\varepsilon^{-1}\langle\mathcal{R}\rangle_{\mathrm{E}} = O(h)$, which verifies claim (B).